Nanoscale Surface Modification studied by Reflection Anisotropy Spectroscopy

By

Paul David Lane

Submitted for the degree of Doctor of Philosophy

The University of Edinburgh

2009

Contents

Chapter 4: Ion Bombarding Copper

Chapter 5: Methanethiol on Copper

Chapter 6: Angular Effects in RAS

Abstract

The development and control of nanoscale properties is a major goal in science and technology; for the development of such technologies it is important that there are experimental techniques which allow the monitoring of development processes in real time and in a range of environments. With this in mind much effort has been invested in the development of surface sensitive optical probes. One such technique, reflection anisotropy spectroscopy (RAS), has been applied successfully to a number of different problems since its development in the mid 1980's.

RAS as a surface specific technique is very sensitive to small changes to surface morphology, electronic structure and molecular orientation. This makes RAS a useful technique to study nanoscale changes occurring at surfaces and it is applied here to three such systems, in an attempt to develop a better understanding of both the systems and the technique.

Surface defects arising from thermal processing and etching of the sample are considered and are found to have a significant effect on both the electronic structure and the morphology of the surface. The time and temperature dependences of the RAS signatures allow the monitoring of surface dynamic processes.

The deposition of a monolayer of adsorbate molecules onto the surface allows a new interface to be created. Monitoring the evolution of this surface during deposition provides information about both the substrate surface and the adsorbate covered surface; a theoretical framework has been outlined to show how the sources of anisotropy from multiple thin film layers combine to give a RAS signal.

Azimuth dependent RAS (ADRAS) is known to provide information on surface symmetry and can be used to determine molecular orientation. There are also a number of other angles which affect the RA spectrum from a sample. A tilted molecule causes a breakdown in surface symmetry; this work shows how such an effect can be observed.

Declaration

This thesis has been composed by myself and has not been submitted for any other degree or professional qualification. The work reported was carried out by myself except where otherwise acknowledged.

Paul Lane
May 2009

Acknowledgements

I am indebted to my supervisor Jamie Cole for not only giving me the opportunity to carry out this work but also for his excellent supervision and the support he offered me throughout. This work would not have been possible without his input, assistance, and expertise. His proof reading of this thesis and subsequent comments are particularly appreciated.

I would also like to thank past and present members of the group Greg Isted and David Roseburgh for their input into this project. David for the use of his code which enabled the work in Chapter 6 to be carried out, and to Greg for the numerous discussions we shared on the various aspects of the work contained in this thesis.

The experimental measurements in Chapter 5 were taken in collaboration with David Martin of the University of Liverpool, on his equipment in the Surface Science Research Centre in Liverpool. The STM images in Chapter 4 were recorded in collaboration with Renald Schaub and Marco Caffio of the University of St. Andrews. I would like to thank them all for their help in acquiring this data.

I gratefully acknowledge the support of the EPSRC who funded this research.

Last but no means least I would like to thank my family and friends for their encouragement and support throughout, in particular my mum and dad, without whom none of this would have been possible.

To every one of you: Thank you

Chapter 1: Introduction

1.1 Surface Science

It is useful to first start off by defining what is meant by a surface. A dictionary definition of a surface is "*the outermost boundary of any material body immediately adjacent to air or empty space, or to another body*" [1.1]. Mathematically this boundary is a locus of points in space, which have no size; hence a mathematical surface has no thickness.

Surface science considers a surface to be the top few atomic layers of a solid and hence surface science can be considered a branch of solid state physics; however most solid state physics ignores the surface. The reason for this is that the number of atoms at the surface are negligible compared to those in the bulk. The surface is interesting because it is where many processes occur: materials interact, symmetry breaks down, bulk band structure is perturbed and new electronic states are created.

In an age where nanoscience and nanotechnology are attracting a large amount of attention, the science occurring at surfaces takes on an even more significant role.

The study of surfaces at the nanoscale is hence a study of atomic arrangements and chemical composition. The chemical, mechanical and electronic properties of the material at the surface can be different from those of the bulk and these differences are important from a fundamental viewpoint. There are a number of applications dependent on surface science: chemical reactions, catalysis, crystal growth, colloids and semiconductor interfaces [1.2-1.4] to name a few, and it is important for the development of technologies reliant on such processes that the science of surfaces is understood.

1.2 The Study of Surfaces with Light

Light or optical photons are not the obvious choice for studying surfaces since the penetration depth of light into a material is large compared to the thickness of the surface layer. For the context of this thesis 'optical' is taken to mean electromagnetic radiation in or around the visible region of the spectrum.

There are two large advantages of optical surface probes over other types of surface probes such as electron based probes; firstly they are (usually) non-invasive, non-destructive techniques, and secondly they are not restricted to ultra high vacuum (UHV) environments.

The development of UHV systems made the study of surfaces possible, by providing a clean controlled environment [1.5]; combined with the small mean free paths of electrons within materials, surface sensitivity is obtained. The advancement of surface science beyond UHV to more realistic environments such as ambient conditions, the solid-gas interface or the solid-liquid interface, requires techniques which can operate in these conditions. Optical probes are one promising avenue [1.6].

The majority of the work contained in this thesis is concentrated in UHV environments, which would seem contradictory to the previous paragraph; so why after discussing these other environments has the work contained with in this thesis been carried out under UHV conditions? Well the best ways to test and hence understand the information obtained from new techniques is to test them in known conditions where there is already a good level of understanding. The UHV environment offers the best range of complementary techniques to aid the understanding of such techniques. Thus the work contained in this thesis attempts to understand some of the information obtained from one such technique, reflection anisotropy spectroscopy (RAS), and the differences that changes on the nanoscale make.

1.3 Thesis Layout

The aims of this thesis are to develop a better understanding of the origin and features of the RA response of the Cu(110) surface and the effect of various nanoscale changes on these features, and secondly to develop a better understanding of how the material properties and spectrometer set-up affect the anisotropic signals obtained from RAS.

Chapter two discusses the theory behind the interaction of light with surfaces and the theory of RAS as well as technical details regarding the experimental RAS apparatus used to obtain results presented in later chapters.

Chapter three discusses the other apparatus that was necessary to perform the work presented in this thesis, such as the UHV chamber and the other experimental techniques used to complement the RAS results, namely LEED and STM.

Chapter four is the first experimental chapter which is concerned with ion bombarding of the Cu(110) surface and how the nanoscale effects of the ion bombarding affect the RA response of the system at different temperatures. The chapter starts off with an overview of previous RAS studies of the Cu(110) surface and later considers the effects of steps on such a system.

Chapter five considers the deposition of methanethiol onto the surface of Cu(110) and the RA response of the system, before heating the surface to cause the dissociation of the molecule, leaving a sulphur adlayer on the surface. Attempts to model such a system see the derivation of a 4-phase model for the RA response and the application of effective medium theory to sub-monolayer coverages of molecular adsorbates.

Chapter six considers the angular effects in RAS, and presents a simulated study of tilted molecules and how they affect the observed spectrum. The misalignment of

components and the different RAS set configurations are considered, and a case for the use of off-normal incidence RAS is presented.

Chapter seven presents a summary and conclusions of the work contained in the thesis; potential further work is also discussed.

Appendix A covers the mathematical derivation of the 4×4 matrix methods for the optical response of anisotropic materials, which is used to produce the simulated results contained within chapter six.

Appendices B & C contain simulated results of complex angle fitting to off normal incidence spectra and signal to noise analysis, both of which are discussed in chapter six.

Appendix D contains references to the publication of work related to this thesis.

References to cited work can be found at the end of the relevant chapter.

1.4 References

[1.1] Oxford English Dictionary (Online) 2nd Edition (1989)

[1.2] M. Prutton; *Introduction to Surface Physics*, Oxford University Press, Oxford (1994)

[1.3] G. Attard and C. Barnes; *Surfaces*, Oxford University Press, New York (1998)

[1.4] A. Zangwill; *Physics at Surfaces*, Cambridge University Press, Cambridge (1996)

[1.5] A. Chambers, R.K. Finch, and B.S. Halliday; *Basic Vacuum Technology* 2nd Edition, Institute of Physics Publishing, Bristol and Philadelphia (1998)

[1.6] J.F. McGilp; J. Phys.: Condens. Matter **2**, 7985 (1990)

Chapter 2: Optics

2.1 Reflection and Transmission of Light [2.1-2.3]

The most fundamental rules of the reflection and transmission of light are governed by Snell's law:

$$N_1 \sin\theta_i = N_1 \sin\theta_r = N_2 \sin\theta_t \qquad \textit{Eqn. 2.1}$$

where N_1 and N_2 are the complex refractive indices (of the form given in *Eqn. 2.2*) of the incident medium and the transmitted medium respectively and where θ_i, θ_r and θ_t are the angles of the incidence, reflection and transmission respectively as shown in *Figure 2.1*.

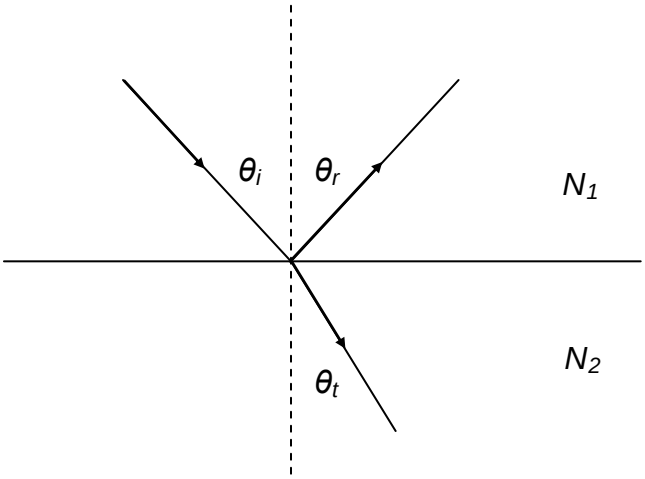

Figure 2.1: *The geometry of the reflection and transmission of light at an interface.*

$$N = n + ik \qquad \textit{Eqn. 2.2}$$

where n is the refractive index and k is the extinction coefficient. The complex refractive index is the ratio of the speed of light in the given medium to speed of light in a vacuum. These constants are related to the dielectric constants of these materials as shown below:

$$N = \sqrt{\varepsilon} = \sqrt{\varepsilon' - \varepsilon''} \qquad \textit{Eqn. 2.3}$$

where

$$\varepsilon' = n^2 - k^2 \qquad \textit{Eqn. 2.4}$$

$$\varepsilon'' = 2nk \qquad \textit{Eqn. 2.5}$$

Although Snell's law contains all the angular information required for reflection and refraction we need to use Fresnel coefficients to provide information regarding phase and amplitude of light which is reflected or refracted, to do this we must first consider the polarisation states of the light.

2.2 Polarisation

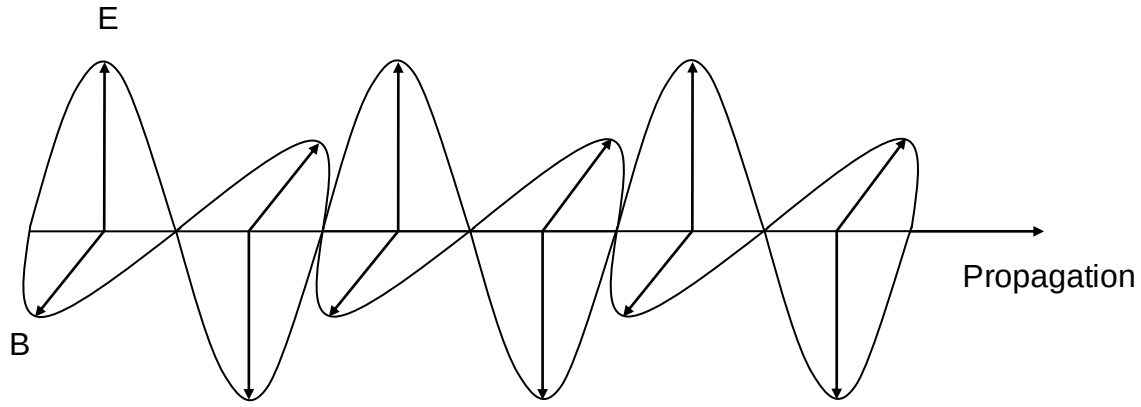

Figure 2.2: *The electric and magnetic field vectors of a light wave.*

Light waves have two oscillating components; an electric field vector and a magnetic field vector which are aligned perpendicular both to each other and to the direction of propagation, as shown in *Figure 2.2*. The direction of the oscillation of the electric

field is defined as the polarisation of the wave. The electric field vector of a plane wave can be arbitrarily divided into two perpendicular components E_x and E_y (for a wave propagating in the *z*-direction). For simple harmonic waves considered in this work the *x* and *y* components always have the same frequency, however they may differ in amplitude and phase.

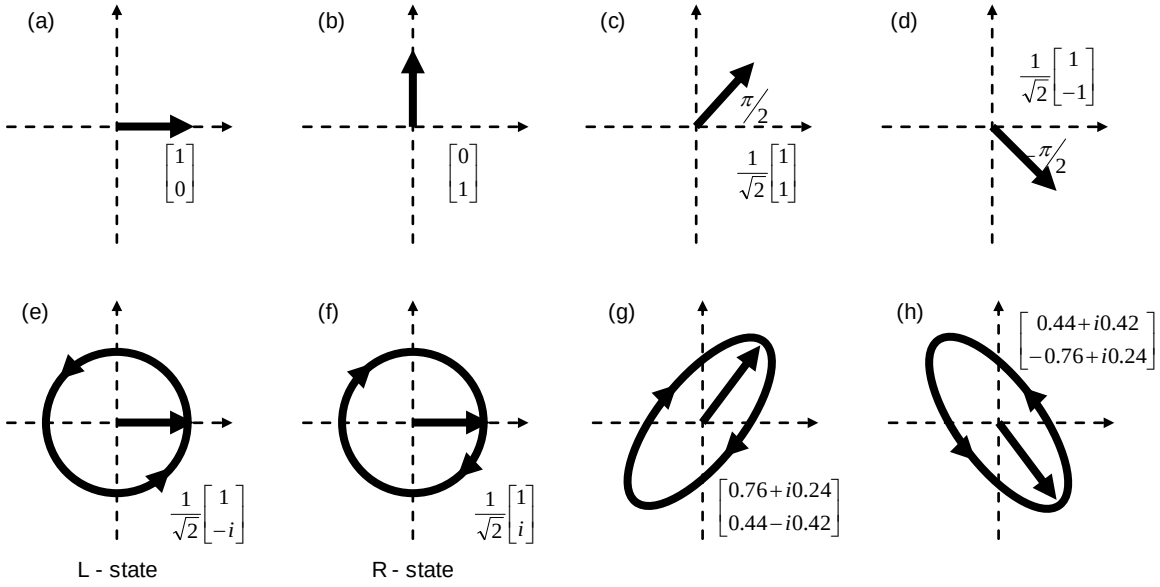

Figure 2.3: *Common polarisation states and their associated normalised Jones vectors, (a-d) linear states, (e-f) circular states and (g-h) elliptical states. Figure adapted from Ref [2.4].*

For linearly polarised light (*Figure 2.3(a-d)*) the E_x and E_y are in phase meaning that the electric field vector (a vector sum of E_x and E_y) is always pointing in the same direction, this direction is defined by the relative amplitudes of the two components.

For circularly polarised light (*Figure 2.3(e-f)*) E_x and E_y have exactly the same amplitude and are exactly $\pi/2$ out of phase, this results in the electric field vector's direction varying with time and tracing out a circle. There are two possible polarisation states for circularly polarised light, one sees E_x lead E_y by $\pi/2$, the other sees E_y lead E_x by $\pi/2$. These are called left handed circular polarisation and right handed circular polarisation, and are dependent on the direction in which the electric field vector rotates. In this work the observers convention is used (i.e. looking back

at the source), this means that if the electric field vector is rotating clockwise then the light is right handed circularly polarised.

For all cases of polarised light other than the two outlined above, the electric field vector will trace out an ellipse; these are hence known as elliptically polarised light (*Figure 2.3(g-h)*). The degree of ellipticity is determined by the relative amplitudes and phases of E_x and E_y.

2.2.1 Plane of Incidence

The plane of incidence as defined in *Figure 2.4* below distinguishes two different polarisation states: those with the their electric field vector parallel to the plane of incidence; *p*- polarised, and those with their electric field vector perpendicular to the plane of incidence; *s*- polarised.

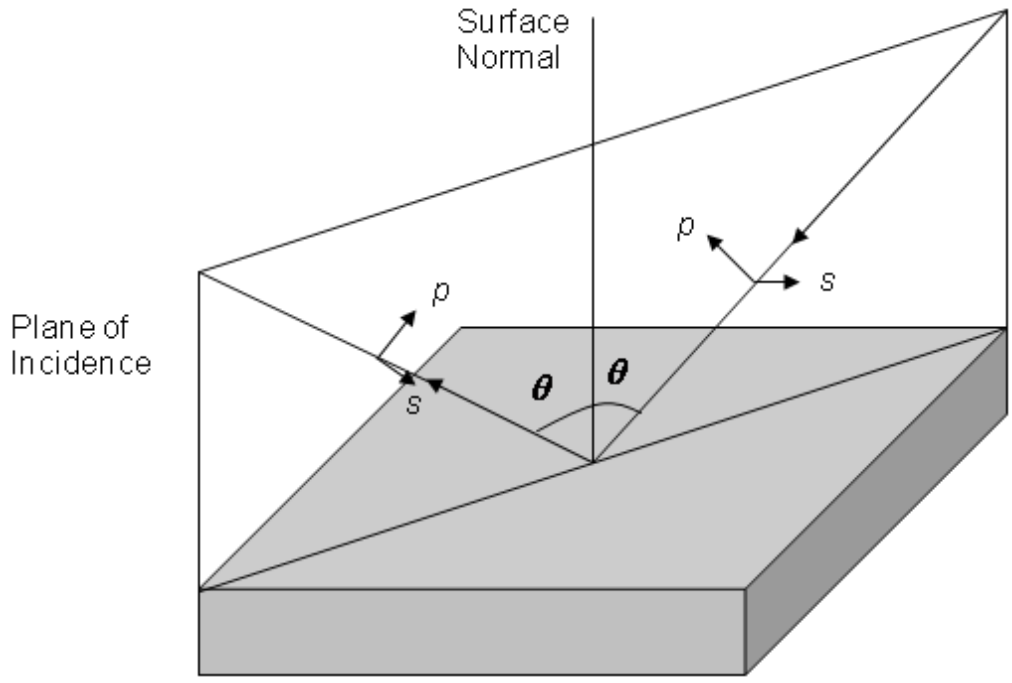

Figure 2.4: *The plane of incidence, and s- and p- polarisation directions.*

We need to consider separately the polarisation states of *s*- and *p*- polarised light as these behave differently when encountering an interface.

2.2.2 **Reflection of s- polarised light** [2.1-2.3]

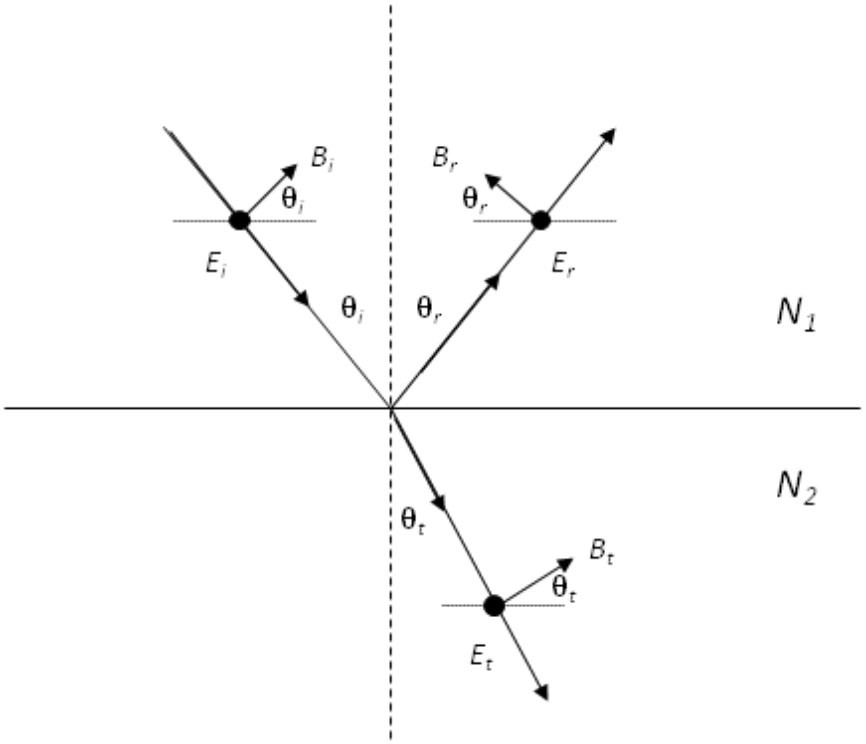

Figure 2.5: *Reflection of s- polarised light from an interface.*

From *Figure 2.5* we can see that the electric field has only a tangential component; by applying the continuity of this component we obtain:

$$E_{0i} = E_{0t} + E_{0r} \qquad \textit{Eqn. 2.6}$$

For the magnetic field:

$$\frac{B_i}{\mu_1}\cos\theta_i - \frac{B_r}{\mu_1}\cos\theta_r = \frac{B_t}{\mu_2}\cos\theta_t \qquad \textit{Eqn. 2.7}$$

where μ_1 and μ_2 are the permeability of media 1 and 2 respectively.

Noting that $\theta_i = \theta_r$ gives:

$$\left(\frac{B_i}{\mu_1} - \frac{B_r}{\mu_1}\right)\cos\theta_i = \frac{B_t}{\mu_2}\cos\theta_t \qquad \textit{Eqn. 2.8}$$

The magnitudes of the magnetic and electric fields are related by:

$$B = \frac{E}{v} \qquad \textit{Eqn. 2.9}$$

where v is the speed of light in the medium.

Substituting this into *Eqn. 2.8* and noting that $v_i = v_r$ gives:

$$\frac{1}{\mu_1 v_1}\left(E_{0i} - E_{0r}\right)\cos\theta_i = \frac{1}{\mu_2 v_2} E_{0t}\cos\theta_t \qquad \textit{Eqn. 2.10}$$

Noting that $v \propto \frac{1}{N}$:

$$\frac{N_1}{\mu_1}\left(E_{0i} - E_{0r}\right)\cos\theta_i = \frac{N_2}{\mu_2} E_{0t}\cos\theta_t \qquad \textit{Eqn. 2.11}$$

Combining this with *Eqn. 2.6* gives:

$$\frac{E_{0r}}{E_{0i}} = r_s = \frac{\frac{N_1}{\mu_1}\cos\theta_i - \frac{N_2}{\mu_2}\cos\theta_t}{\frac{N_1}{\mu_1}\cos\theta_i + \frac{N_2}{\mu_2}\cos\theta_t} \qquad \textit{Eqn. 2.12}$$

$$\frac{E_{0t}}{E_{0i}} = t_s = \frac{2\frac{N_1}{\mu_1}\cos\theta_i}{\frac{N_1}{\mu_1}\cos\theta_i + \frac{N_2}{\mu_2}\cos\theta_t} \qquad \textit{Eqn. 2.13}$$

For a non-magnetic medium *Eqns. 2.12 & 2.13* simplify to:

$$\frac{E_{0r}}{E_{0i}} = r_s = \frac{N_1\cos\theta_i - N_2\cos\theta_t}{N_1\cos\theta_i + N_2\cos\theta_t} \qquad \textit{Eqn. 2.14}$$

$$\frac{E_{0t}}{E_{0i}} = t_s = \frac{2N_1 \cos\theta_i}{N_1 \cos\theta_i + N_2 \cos\theta_t} \qquad \textit{Eqn. 2.15}$$

2.2.3 **Reflection of p- polarised light** [2.1-2.3]

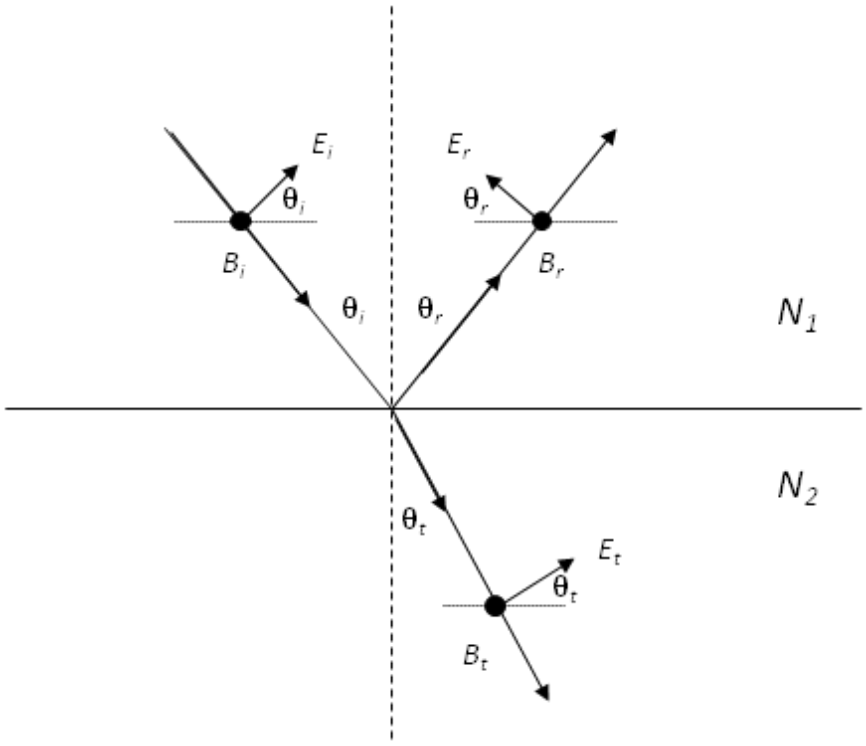

Figure 2.6: *Reflection of p- polarised light from an interface.*

Using *Figure 2.6* and a similar method to the *s*- polarisation case and using the continuity equations:

$$E_{0i}\cos\theta_i - E_{0r}\cos\theta_r = E_{0t}\cos\theta_t \qquad \textit{Eqn. 2.16}$$

$$\frac{1}{\mu_1 v_1}\left(E_{0i} + E_{0r}\right) = \frac{1}{\mu_2 v_2} E_{0t} \qquad \textit{Eqn. 2.17}$$

yields:

$$\frac{E_{0r}}{E_{0i}} = r_p = \frac{\frac{N_2}{\mu_2}\cos\theta_i - \frac{N_1}{\mu_1}\cos\theta_t}{\frac{N_2}{\mu_2}\cos\theta_i + \frac{N_1}{\mu_1}\cos\theta_t} \qquad \textit{Eqn. 2.18}$$

$$\frac{E_{0t}}{E_{0i}} = t_p = \frac{2\frac{N_1}{\mu_1}\cos\theta_i}{\frac{N_1}{\mu_1}\cos\theta_t + \frac{N_2}{\mu_2}\cos\theta_i} \qquad \textit{Eqn. 2.19}$$

For non-magnetic media:

$$\frac{E_{0r}}{E_{0i}} = r_p = \frac{N_2\cos\theta_i - N_1\cos\theta_t}{N_2\cos\theta_i + N_1\cos\theta_t} \qquad \textit{Eqn. 2.20}$$

$$\frac{E_{0t}}{E_{0i}} = t_p = \frac{2N_1\cos\theta_i}{N_1\cos\theta_t + N_2\cos\theta_i} \qquad \textit{Eqn. 2.21}$$

2.2.4 Reflectance and Transmittance

The reflectance and transmittance give the ratio of the intensities of light reflected and transmitted from an interface, and can be calculated by:

$$R = |r|^2 \qquad \textit{Eqn. 2.22}$$

$$T = |t|^2 \qquad \textit{Eqn. 2.23}$$

where *R*, *T*, *r* and *t* can be those of either *s*- or *p*- polarised light. *Figure 2.7* compares the reflectance of *s*- and *p*- polarised light from an interface between two non-absorbing media.

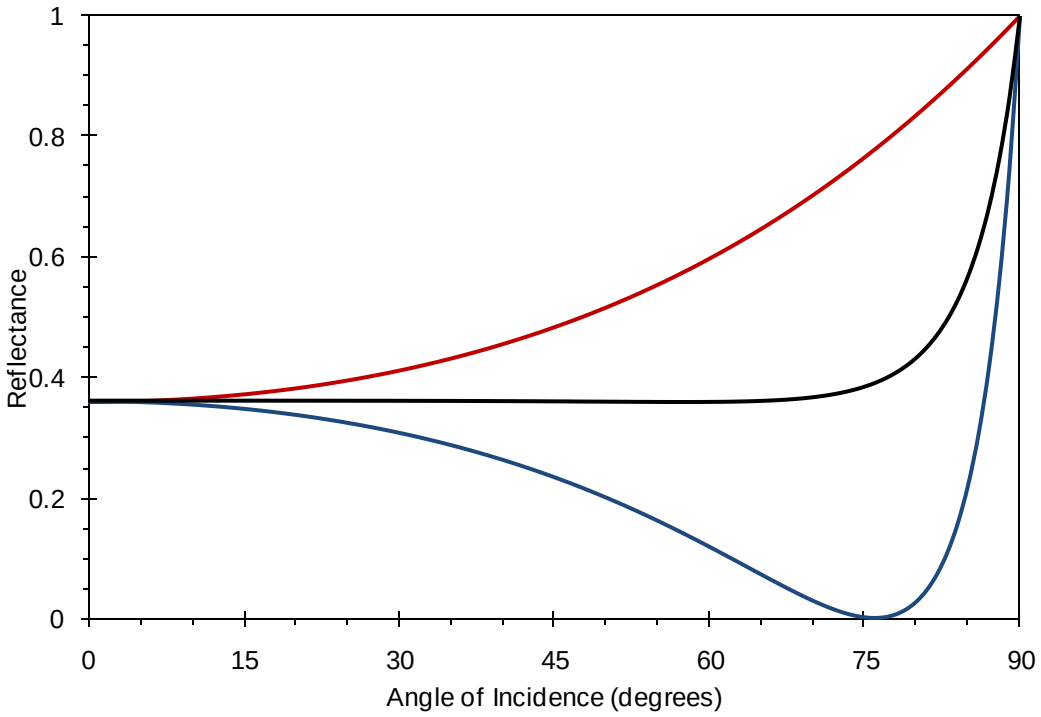

Figure 2.7: *The reflectance of s- polarised light (red) and p- polarised light (blue), and unpolarised light (black), from an interface where n_1=1, k_1=0, n_2=3, k_2=0.*

Figure 2.7 shows the reflectance of *s*- and *p*- polarised light as well as unpolarised light (a mixture of *s*- and *p*-), the two polarisation states behave differently as a function of angle of incidence. For a certain angle of incidence there is no reflection of *p*- polarised light; the angle is known as the Brewster angle θ_B and can be calculated from:

$$\tan\theta_B = \frac{n_2}{n_1} \qquad \textit{Eqn. 2.24}$$

where n_1 and n_2 are the refractive indices of media 1 and 2 respectively, where both media are non-absorbing. If unpolarised light is incident on an interface at the Brewster angle then the reflected light will be *s*- polarised hence Brewster's angle is also known as the polarisation angle. If absorbing media are used then a pseudo-Brewster effect is observed, where the shape of the curves are similar but R_p reaches a non-zero minimum.

2.3 The 3-Phase Model

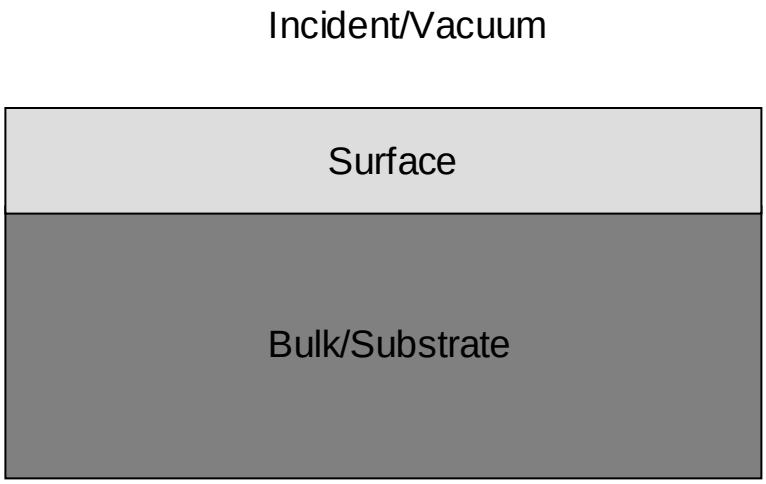

Figure 2.8: *The three-phase model.*

When studying surfaces and thin films our system is more complex than the simple reflections considered so far. The three phase model was first introduced by Heavens in 1955 [2.5] and additions were made by MacIntyre and Aspnes in 1971 [2.6]. The system as shown in *Figure 2.8* consists of 3 layers or phases, which are all homogeneous with abruptly terminating interfaces. The three phases are: a bulk (or substrate) phase, a surface layer and an incident (vacuum or ambient) phase. The bulk layer and incident phase are both considered to be semi-infinite whereas the surface layer has a finite thickness.

2.3.1 Reflection and Transmission in a 3-Phase system [2.5]

With all the Fresnel coefficients (r_s, r_p, t_s and t_p) for the reflection and transmission of light from an interface which have been derived earlier, it is fairly trivial to apply them to the three phase system, it is just a case of applying them to each boundary and keeping track of each medium, as is demonstrated in *Figure 2.9*.

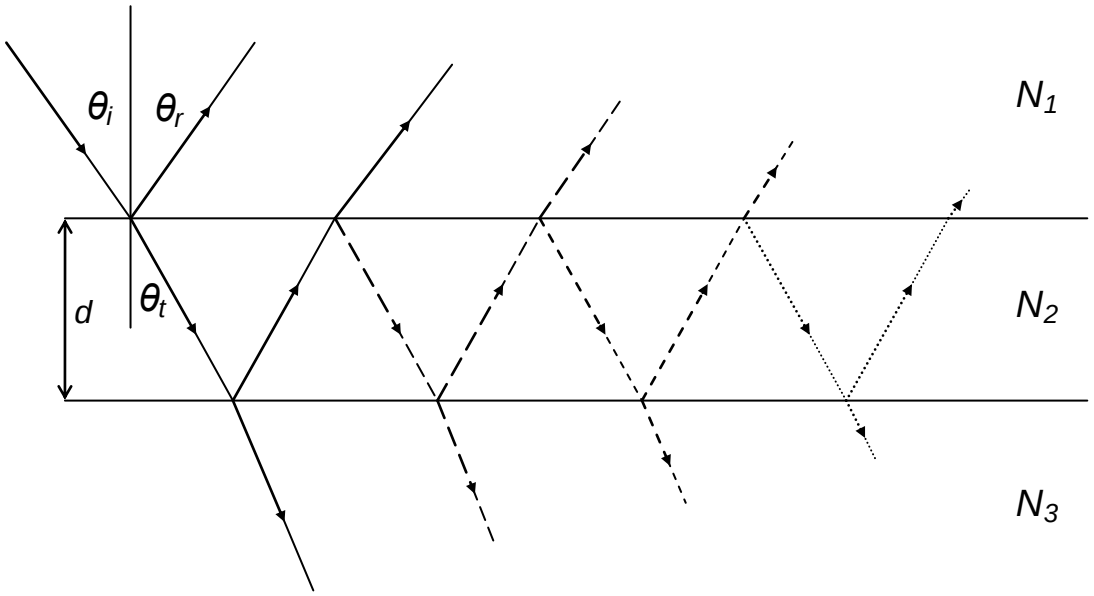

Figure 2.9: *Reflection and transmission in a three-phase system.*

The Fresnel coefficients from a three-phase system (r_{123} and t_{123}) are obtained by adding all the reflected and all of the transmitted components. The Fresnel coefficients for light incident at the boundary between N_1 and N_2 are denoted r_{12} and t_{12}, whereas at the interface between N_2 and N_1 are denoted r_{21} and t_{21}. The summation of all the reflected components gives:

$$r_{123} = r_{12} + t_{12}t_{21}r_{23} + t_{12}t_{21}r_{21}r_{23}^{\ 2} + t_{12}t_{21}r_{21}^{\ 2}r_{23}^{\ 3} + \ldots \qquad \textit{Eqn. 2.25}$$

As $r_{21} = -r_{12}$

$$r_{123} = r_{12} + t_{12}t_{21}r_{23} - t_{12}t_{21}r_{12}r_{23}^{\ 2} + t_{12}t_{21}r_{12}^{\ 2}r_{23}^{\ 3} + \ldots \qquad \textit{Eqn. 2.26}$$

Each time the wave passes through the surface region (medium 2) there is a phase change relative to the primary reflection this is given by:

$$\beta_2 = 2\pi N_2 \cos\theta_t \frac{d}{\lambda} \qquad \textit{Eqn. 2.27}$$

where d is the thickness of medium 2 and λ is the wavelength of light.

After considering the phase changes the resulting reflection coefficient is given by:

$$r_{123} = r_{12} + t_{12}t_{21}r_{23}e^{-2i\beta_2} - t_{12}t_{21}r_{12}r_{23}{}^2e^{-4i\beta_2} + t_{12}t_{21}r_{12}{}^2r_{23}{}^3e^{-6i\beta_2} + \ldots \qquad \textit{Eqn. 2.28}$$

$$r_{123} = r_{12} + \frac{t_{12}t_{21}r_{23}e^{-2i\beta_2}}{1 + r_{12}r_{23}e^{-2i\beta_2}} \qquad \textit{Eqn. 2.29}$$

Using $t_{12}t_{21} = 1 - r_{12}{}^2$ gives the more common form:

$$r_{123} = \frac{r_{12} + r_{23}e^{-2i\beta_2}}{1 + r_{12}r_{23}e^{-2i\beta_2}} \qquad \textit{Eqn. 2.30}$$

Applying the thin film approximation $d << \lambda$ means *Eqn. 2.30* can be approximated to:

$$r_{123} = \frac{r_{12} + r_{23}(1 - 2i\beta_2)}{1 + r_{12}r_{23}(1 - 2i\beta_2)} \qquad \textit{Eqn. 2.31}$$

Following the method of MacIntyre and Aspnes [2.6]:

$$r_{13} = \frac{r_{12} + r_{23}}{1 + r_{12}r_{23}} \qquad \textit{Eqn. 2.32}$$

combining *Eqn. 2.31* and *Eqn. 2.32* gives:

$$\frac{r_{123}}{r_{13}} = \frac{1 - 2i\beta_2\left[r_{23}/(r_{12} + r_{23})\right]}{1 - 2i\beta_2\left[r_{12}r_{23}/(1 + r_{12}r_{23})\right]} \qquad \textit{Eqn. 2.33}$$

Expanding the denominator and considering only 1st order terms in β yields:

$$\frac{r_{123}}{r_{13}} = 1 + 2i\beta_2\left[\frac{r_{23}\left(r_{12}^{\ 2} - 1\right)}{\left(r_{12} + r_{23}\right)\left(1 + r_{12}r_{23}\right)}\right] \qquad \textit{Eqn. 2.34}$$

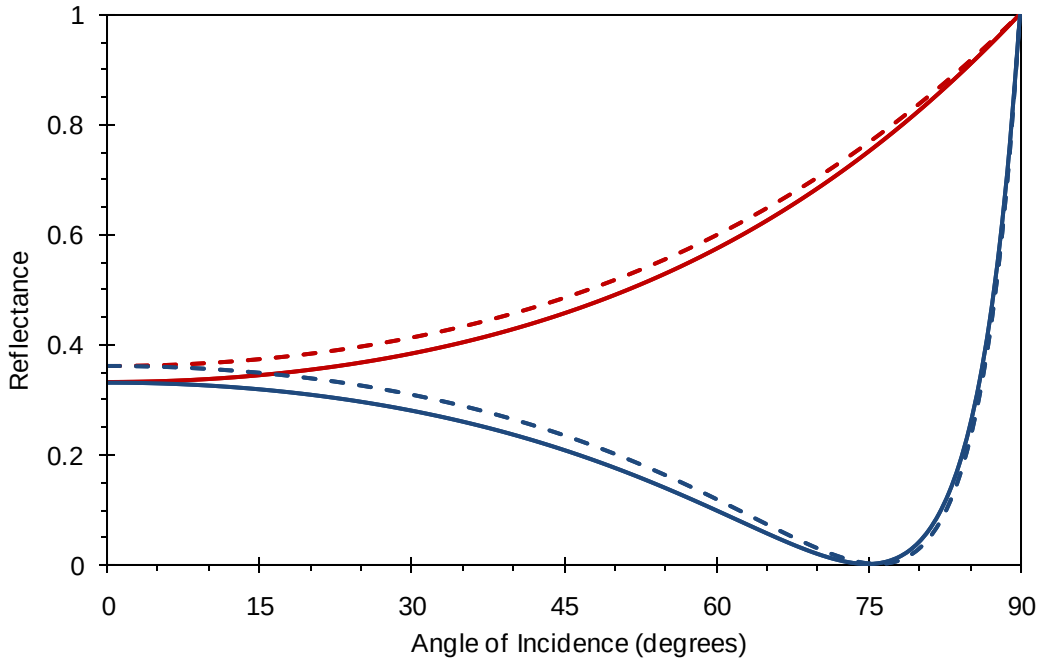

Figure 2.10: *The reflectance of an absorbing thin film for d/λ =0.005, n_1=1, k_1=0, n_2=3, k_2=1.5, n_3=4, k_3=0. Solid lines show R_{123}, dashed lines show R_{13} for s- (red) and p- (blue) polarisations.*

Figure 2.10 shows how the presence of a thin film ~1-2nm in thickness can affect the optical response of an interface, epioptic probes [2.7] can be used to measure these effects.

2.4 Epioptic Probes

The Fresnel equations and the three-phase model provide the fundamental knowledge on which epioptic probes work. Ellipsometry [2.7-2.8] for example is a surface sensitive probe which can be used to determine the complex refractive index and thickness of thin films by measuring the ratio ρ.

$$\rho = \frac{r_s}{r_p} \qquad \textit{Eqn. 2.35}$$

While Ellipsometry may have surface sensitivity and can be used on both isotropic and anisotropic surfaces, it is not surface specific. There are bulk contributions in the information it provides us with. If we are interested in the anisotropic nature of a surface or thin film, simply probing the two directions independently and comparing them using a surface sensitive technique which contains a significant amount of bulk information is not very effective or efficient. What is required is a surface specific technique which contains no bulk information and can measure the two anisotropic directions simultaneously.

One technique that can do this is Reflection Anisotropy Spectroscopy (RAS). It measures the difference between the Fresnel reflection coefficients of two perpendicular directions, normalised to their average.

$$\frac{\Delta r}{r} = \frac{2\left(r_x - r_y\right)}{\left(r_x + r_y\right)} \qquad \textit{Eqn. 2.36}$$

As RAS operates at normal incidence the bulk contribution of cubic crystals will cancel by symmetry making the technique surface specific. Normal incidence also simplifies some of the algebra expressed above; also the concepts of r_s and r_p are negated as there is no longer a plane of incidence for them to be parallel or perpendicular to, so the Fresnel coefficients are expressed in an *x*-*y* lab frame.

2.4.1 The Anisotropic 3-Phase Model and RAS

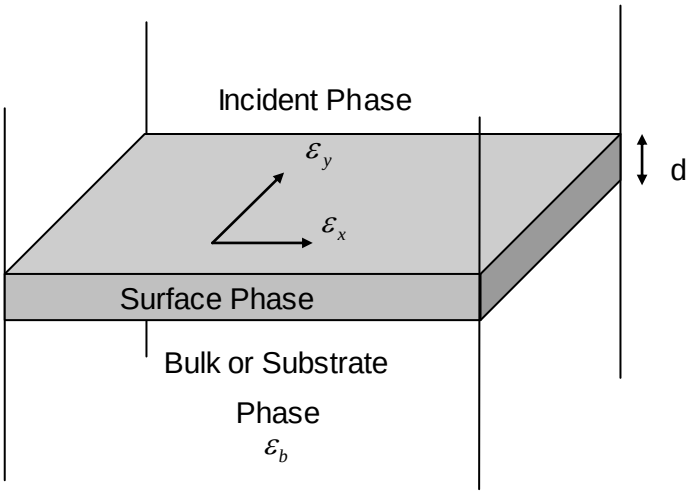

Figure 2.11: *The three-phase model for an anisotropic surface.*

Figure 2.11 shows a simple anisotropic three phase system. Generally the treatment of anisotropic systems requires 4×4 matrix algebra, but for normal incidence the earlier expressions for the 3-phase system and thin film approximation work if applied separately for the *x* and *y* directions. The Fresnel coefficients at normal incidence can be written:

$$r_{ij} = \frac{N_j - N_i}{N_j + N_i} \qquad \textit{Eqn. 2.37}$$

Substituting this into *Eqn 2.34* and using *Eqn. 2.3* to give $\varepsilon = N^2$ and assuming medium 1 is vacuum ($\varepsilon_1 = 1$) then:

$$\frac{r_{123}}{r_{13}} = 1 - \frac{2i\omega d}{c}\left[\frac{\varepsilon_2 - \varepsilon_3}{1 - \varepsilon_3}\right] \qquad \textit{Eqn. 2.38}$$

For anisotropic surface layers of cubic crystals the Fresnel reflection coefficients are different along the two principal crystallographic directions *x* and *y*, meaning *Eqn. 2.38* can be split into *x* and *y* components:

$$\frac{r_x}{r} = 1 - \frac{2i\omega d}{c}\left[\frac{\varepsilon_{2(x)} - \varepsilon_3}{1-\varepsilon_3}\right] \qquad \textit{Eqn. 2.39}$$

$$\frac{r_y}{r} = 1 - \frac{2i\omega d}{c}\left[\frac{\varepsilon_{2(y)} - \varepsilon_3}{1-\varepsilon_3}\right] \qquad \textit{Eqn. 2.40}$$

Subtracting *Eqn. 2.39* from *Eqn. 2.40*, defining $\Delta r = r_x - r_y$ and considering that $\omega = 2\pi f$ and that $\lambda = c/f$ then the reflection anisotropy can be written:

$$\frac{\Delta r}{r} = -\frac{4i\pi d}{\lambda}\left[\frac{\varepsilon_{2(x)} - \varepsilon_{2(y)}}{1-\varepsilon_3}\right] \qquad \textit{Eqn. 2.41}$$

As this work is only concerned with the real part of $\Delta r/r$:

$$\mathrm{Re}\left(\frac{\Delta r}{r}\right) = -\frac{4\pi d}{\lambda}\,\mathrm{Im}\left[\frac{\Delta\varepsilon_2}{1-\varepsilon_3}\right] \qquad \textit{Eqn. 2.42}$$

2.5 The History of RAS

The idea of reflection anisotropy measurements pre-dates the use of RAS. Cardona [2.9] studied Si (110) using a technique called "Rotoreflectance" in 1968 while McIntyre and Aspnes showed normalised reflectivity can be used to gain information of the physical properties of a surface in 1971 [2.6].

The RAS technique was initially developed by Aspnes and his co-workers [2.10-2.14] in the mid 1980's under the name reflectance difference spectroscopy (RDS) as a method of studying properties of semiconductors and monitoring their growth in real time. These experiments were mainly carried out under atmospheres of noble gases and since electron microscopy and spectroscopy techniques could not operate

as the electrons were scattered by the atmosphere, the development of a technique using an optical source became important.

The surface sensitivity of the technique had been demonstrated with observations of surface reconstruction [2.13, 2.15], dimer orientations [2.15-2.16] and atomic steps [2.17-2.18].

RAS was not just limited to work on semiconductors; the first studies of single crystal metals were reported in 1993 when Borensztein et al. studied Ag (110) [2.19] followed by Hofmann et al who studied Cu (110) [2.20].

RAS is sensitive to the electronic structure of the surface around the Fermi level and has been able to identify transitions between surface states in both semiconductors and metals enabling it to become a probe of surface state behaviour [2.21]. Surface electronic structure has traditionally been probed by techniques such as photoemission and inverse photoemission which obtain surface sensitivity by the short penetration depth of electrons into materials. The use of electrons in this manner limits such probes to ultra high vacuum conditions; RAS being an optical probe has no such restrictions and can therefore operate in any optically transparent medium [2.21] and has been applied to studies in UHV, ambient conditions [2.19] and at the solid/liquid interface [2.22].

More recently there have been studies of material stress [2.23], liquid crystal device fabrication [2.24-2.27], catalysts [2.28], Langmuir –Blodgett films [2.29-2.30] and molecular adsorbates [2.31-2.33].

2.6 The Spectrometer

The reflection anisotropy spectrometer currently in use was built by Brian MacDonald as part of his PhD Thesis [2.34] and is of the form of the later Aspnes design [2.14] using a photoelastic modulator (PEM) rather than the rotating sample of [2.10]. The advantages of this are an increased signal to noise ratio and because

the PEM uses phase modulation rather than intensity modulation it is possible to measure both the real and imaginary parts of $\Delta r/r$ [2.22]. A schematic diagram of the system is shown in *Figure 2.12*.

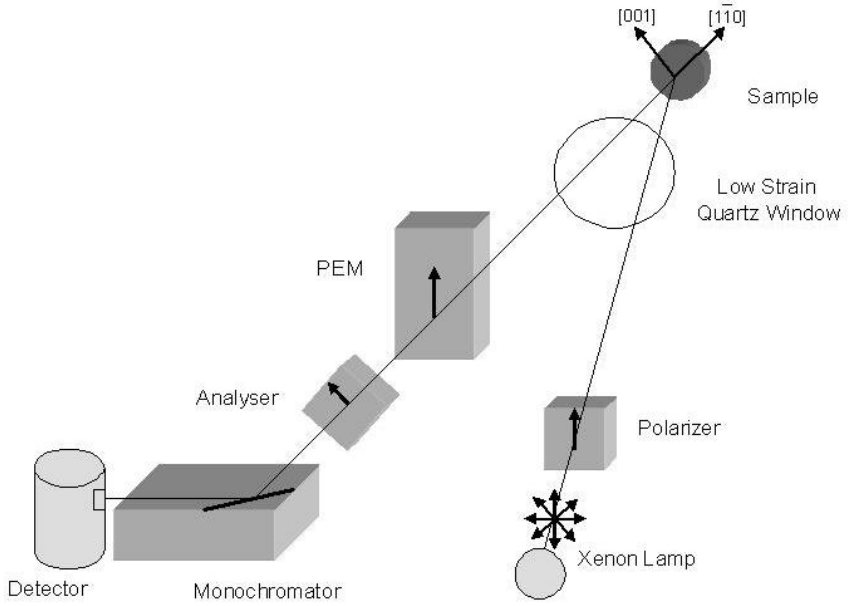

Figure 2.12: *Schematic diagram showing the setup of a Reflection Anisotropy Spectrometer.*

2.6.1 Xenon Lamp

The light source is a Hamamatsu 75W Xenon arc lamp, with a continuous output in the wavelength range of ~180nm (~6.9eV) to ~1µm (~1.25eV) which is from infra-red though to low energy ultra violet, meaning that it is ideal for RAS studies in the 1.5eV to 6eV energy range.

The lamp operates as a point light source when a voltage is applied across an anode and a cathode separated by a volume of high pressure Xe gas. The aperture of the lamp is very small ~1mm in diameter and the light passing through is intense.

For optimum performance of the lamp it is best to allow a period of time (approximately 20 minutes) for the gas to reach a state of thermal equilibrium, in this period no measurements are taken.

2.6.2 Focusing Mirrors

Incident light from the lamp is focused onto the sample and reflected light from the sample is focused into the monochromator using focusing mirrors. These mirrors are aluminium coated spherical concave mirrors with an average reflectivity of greater than 87% over the wavelength range of 400-800nm.

2.6.3 Polariser

As the input light required by the spectrometer must be linearly polarised, a Rochon polariser is used to turn the unpolarised light from the lamp into polarised light, as shown in *Figure 2.13*. This is made of two quartz wedge shaped prisms which are cemented together with their optical axes perpendicular. The light is polarised by a double refraction (birefringent) process which splits the incident beam into its ordinary and extraordinary components. The first prism allows both the ordinary and extraordinary component of the beam to pass through it undeviated. As the light enters the second prism the ordinary beam is again allowed to pass through undeviated as the refractive index has remained the same, while the lower refractive index causes the extraordinary beam to be deviated, the same happens when the light leaves the second prism meaning the light is polarised. The ordinary beam stays in the system and is used for recording spectra while the extraordinary beam is removed from the system.

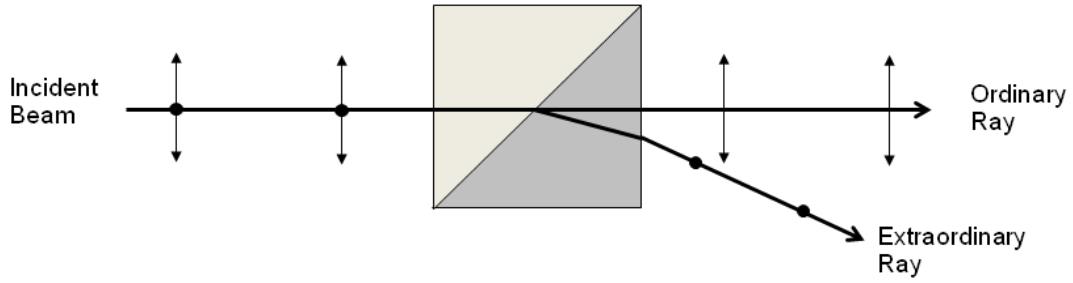

Figure 2.13: *Separation of ordinary and extraordinary beams by a Rochon polariser.*

2.6.4 Low Strain Quartz Window

For experiments conducted inside the ultra high vacuum chamber the light from the spectrometer must enter and exit the chamber through a window. The window used

for this purpose is made of low strain quartz because the birefringent effects of quartz are less much less than those of glass, also glass absorbs ultra violet light.

Even though the effect of the window is minimized by the use of a low strain quartz window, it is still detectable with RAS and hence all measurements carried out in the chamber are subject to a window correction. This correction is outlined later in *Section 2.9.1*.

2.6.5 Sample

In the standard RAS configuration the crystallographic directions of the sample are aligned with the *x* and *y* axes of the analyser at ±45° to the vertical. For a (110) crystal as used for experiments in some of the later chapters RAS is measuring the difference between the [001] and the $[1\bar{1}0]$ directions, hence *Eqn. 2.35* can be rewritten as:

$$\frac{\Delta r}{r} = \frac{2(r_{[1\bar{1}0]} - r_{[001]})}{r_{[1\bar{1}0]} + r_{[001]}} \qquad \textit{Eqn. 2.41}$$

Although RAS is a powerful surface specific probe there are limitations of its use. It is capable of monitoring the surface on the nanoscale but because the size of the beam is of the order of a few millimetres it requires the surface to have long range order over this range; which is why single crystals are commonly used: crystals with grain boundaries would not be suitable for characterisation studies of clean surfaces. The second condition has already briefly been mentioned earlier and that is that the sample have an isotropic bulk structure. In order to be able to obtain surface sensitivity the contributions from the bulk must cancel. This is why cubic structures are commonly studied. Also the sample must be anisotropic in nature or undergo processes which will create anisotropy; as isotropic structures give a zero RAS signal.

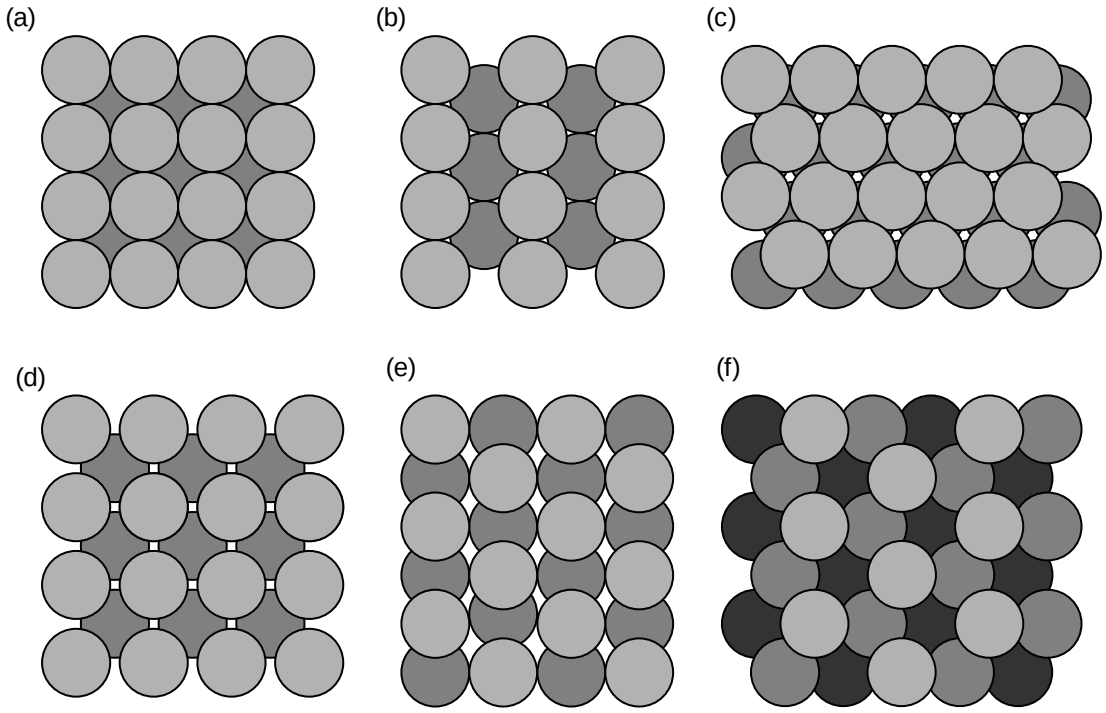

Figure 2.14: *Atomic surface structure of cubic materials fcc: (a) (100), (b) (110), (c) (111); bcc: (d) (100), (e) (110), and (f) (111).*

Figure 2.14 shows the ideal bulk terminated (100), (110) and (111) surfaces of both face centre cubic (fcc) and body centre cubic (bcc) crystal structures. For both the fcc and bcc the (100) and (111) surfaces are optically isotropic to RAS, while for both the fcc and bcc the (110) surface is anisotropic. This is why the (110) surfaces have become the primary focus of RAS studies.

2.6.6 Photoelastic Modulator

The photoelastic modulator (PEM) is a wave retarder; it alters the polarisation states of the elliptically polarised light reflected from the sample. As the light passes through the PEM its phase is modulated at f = 50 kHz. This is done by applying an electric field to a piezoelectric crystal coupled to fused silica. This is orientated with the modulation axis in a vertical orientation meaning that the vertical component of the light travelling along the modulation axis will undergo retardation, while the horizontal component travelling in the direction perpendicular to the modulation axis will be unaffected. This means that the vertical component will lag the horizontal

component by a phase difference of π resulting in an oscillation between two elliptically polarised states.

2.6.7 Analyser

This is another Rochon prism identical to that of the polariser in its construction. Its role is to convert the phase modulated beam from the PEM into an amplitude modulated beam. In the standard RAS set-up the optical axis of the analyser is parallel to the *x* crystallographic axis and at 45 degrees to the PEM; this means the light transmitted by the analyser will be only the long or short axis of the elliptically polarised incident upon it (*Figure 2.15*), as it modulates between the two states. The maximum amplitudes are a measure of the reflectivity in the *x* and *y* directions; meaning the difference between these two amplitudes is a measure of the anisotropy of the sample. The average amplitude of the two states gives the average reflectivity of the sample.

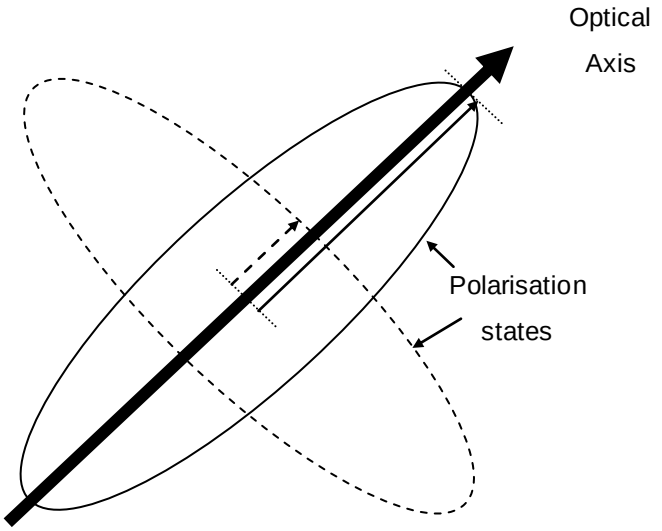

Figure 2.15: *The effect of the analyser on the two polarisation states of light.*

2.6.8 Monochromator

To record the RA signal in spectrum form the incoming light must be separated into individual wavelengths; this is done using a monochromator. The monochromator (as shown in *Figure 2.16*) consists of a diffraction grating with 1200 grooves per mm and has a spectral range of 200-750nm. By changing the angle of the diffraction grating it is possible to select the frequency of light that is to be transmitted through

the monochromator. Once the wavelength has been selected the light is transmitted through the monochromator into the detector.

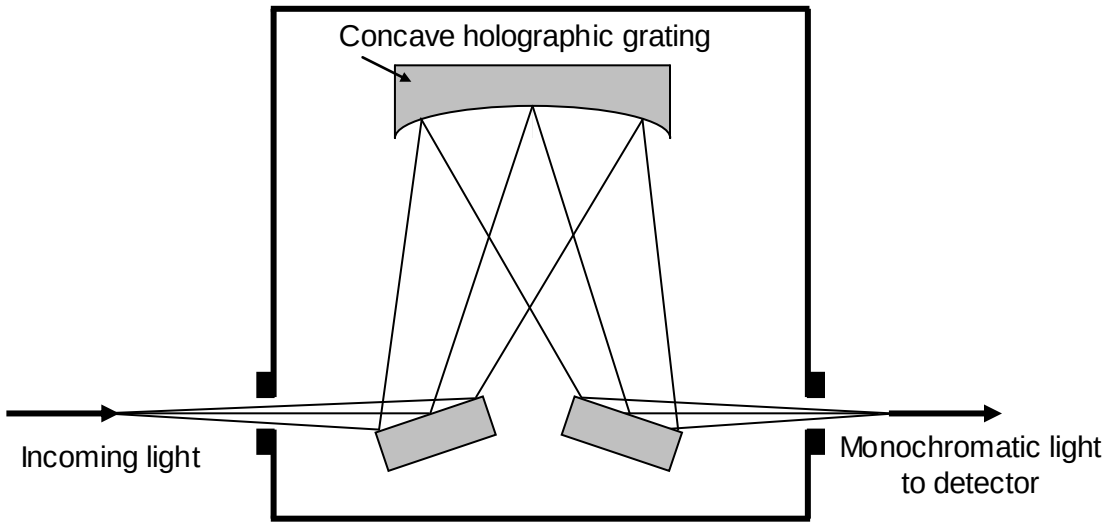

***Figure 2.16**: The monochromator.*

2.6.9 Detector

The detector used to convert the light from the monochromator into an electric current is a photomultiplier tube (PMT) which operates in the wavelength range of 185-900nm. The photomultiplier tube gives very high sensitivity, nanosecond response time and low noise. The power is supplied by a 15V dual power supply.

The output signal from the PMT is a current of typical amplitude of a few micro-amps. The signal consists of an AC component on top of a DC offset. The AC signal is related to the anisotropy and the DC to the reflectivity. The AC and DC currents are then converted into AC and DC voltages which are then amplified.

2.6.10 Lock-in Amplifier

A lock-in amplifier is used to isolate and measure the AC and DC signals. The DC component of the signal is sent to the analogue to digital converter of the lock-in amplifier. The AC component is phase sensitively measured by the lock-in using the modulation frequency of the PEM as a reference signal. The output is then sent to the computer and software calculates the RA signal from this information.

The two important settings of the lock-in amplifier are the sensitivity and the integration time. The sensitivity will depend on the amplitude of the signal measured and when recording data the sensitivity should be set to the highest possible value. The integration time is mostly concerned with signal to noise. The signal is less noisy when the integration time is longer; this is because the recorded signal is averaged over a longer timescale. The noise on the signal for different integration times is shown in *Figure 2.17*.

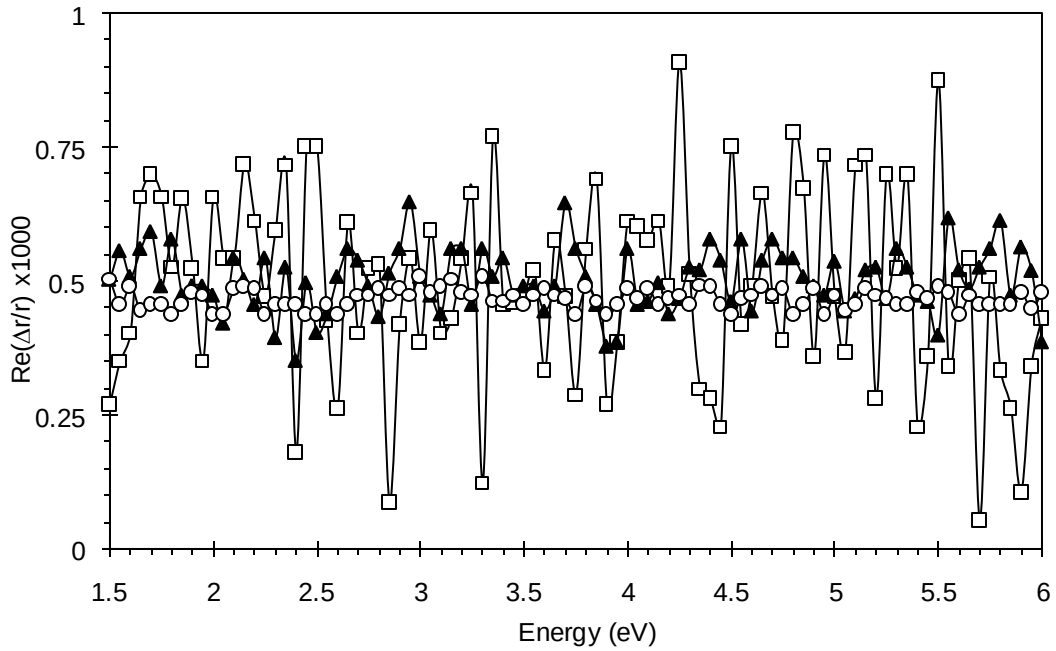

Figure 2.17: *No light spectra recorded at a sensitivity of 10mV for integration times of 3ms (open squares), 30ms (filled triangles) and 300ms (open circles).*

2.6.11 Computer Control

The set up is controlled by computer, which communicates with the monochromator, lock-in amplifier and PEM independently via RS232 serial cables. *Figure 2.18* shows the communication channels between the individual components of the spectrometer. The software controlling the system records AC and DC values as well as the real and imaginary parts of $\Delta r/r$.

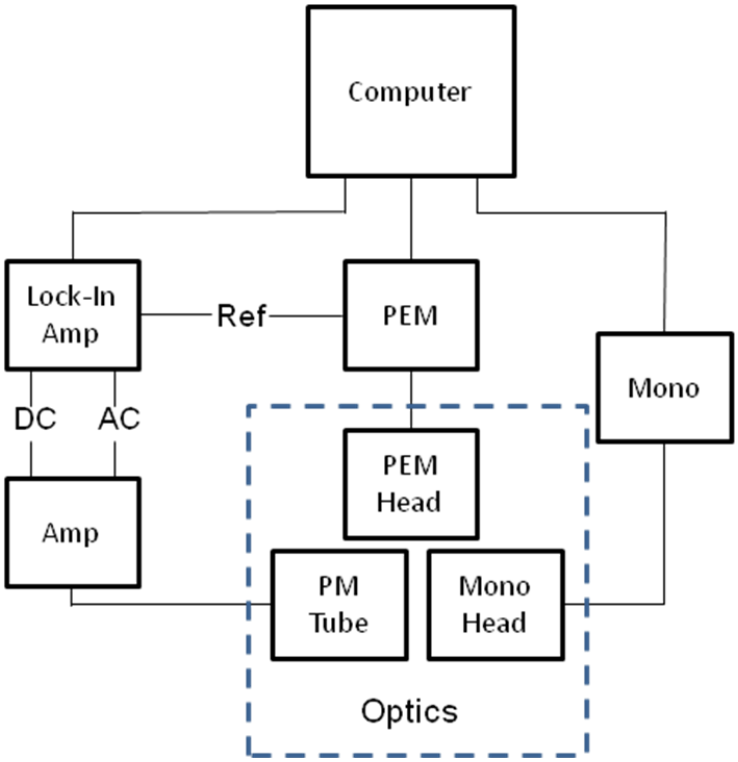

Figure 2.18: *Systems communications diagram.*

2.6.12 Modes of Operation

The spectrometer can operate in two modes. The most common mode is the spectroscopic mode where the RA signal is recorded for a period of time set by the integration time, at a particular energy before moving on to the next energy and repeating the process. The data is then plotted as $\Delta r/r$ against photon energy. The second mode of operation is constant energy mode where the RA signal is measured at a particular energy as a function of time; this is useful when the evolution of a feature is being observed during a controlled process such as molecular deposition or ion bombarding etc. In this mode of operation the RA signal can be measured with accuracy on small time scales. The system is capable of recording data every few milliseconds. The AC signal is measured on very small time scales while the DC signal is averaged over a few data points.

2.7 Jones Vectors and Jones Calculus

In order to consider the polarisation state of the light travelling through the various components of the spectrometer Jones calculus will be employed. This method was devised by R.C. Jones [2.35]; each polarisation state is represented by a 1×2 matrix vector consisting of a horizontal and a vertical component.

$$E = \begin{bmatrix} E_x \exp(i\varphi_x) \\ E_y \exp(i\varphi_y) \end{bmatrix} \qquad \textit{Eqn. 2.43}$$

where E_x, E_y and φ_x, φ_y are the amplitudes and phases in x and y directions, hence horizontal, vertical and 45° polarisation states are described by:

$$E_h = \begin{bmatrix} E_x \exp(i\varphi_x) \\ 0 \end{bmatrix} \qquad \textit{Eqn. 2.44}$$

$$E_v = \begin{bmatrix} 0 \\ E_y \exp(i\varphi_y) \end{bmatrix} \qquad \textit{Eqn. 2.45}$$

$$E_{45} = \begin{bmatrix} E_x \exp(i\varphi_x) \\ E_y \exp(i\varphi_y) \end{bmatrix} \qquad \textit{Eqn. 2.46}$$

For the E_{45} case the phases and amplitudes are equal meaning *Eqn. 2.46* can be written as:

$$E_{45} = \begin{bmatrix} E_x \exp(i\varphi_x) \\ E_x \exp(i\varphi_x) \end{bmatrix} \qquad \textit{Eqn. 2.47}$$

After factorising *Eqn. 2.44*, *2.45* & *2.47* become:

$$E_h = E_x \exp(i\varphi_x) \begin{bmatrix} 1 \\ 0 \end{bmatrix} \qquad \textit{Eqn. 2.48}$$

$$E_v = E_y \exp(i\varphi_y)\begin{bmatrix}0\\1\end{bmatrix} \qquad \textit{Eqn. 2.49}$$

$$E_{45} = E_x \exp(i\varphi_x)\begin{bmatrix}1\\1\end{bmatrix} \qquad \textit{Eqn. 2.50}$$

And in many applications the exact amplitudes and phases are not required and in such cases it is easier to use normalised values in which case *Eqns. 2.48-2.50* become:

$$E_h = \begin{bmatrix}1\\0\end{bmatrix} \qquad \textit{Eqn. 2.51}$$

$$E_v = \begin{bmatrix}0\\1\end{bmatrix} \qquad \textit{Eqn. 2.52}$$

$$E_{45} = \frac{1}{\sqrt{2}}\begin{bmatrix}1\\1\end{bmatrix} \qquad \textit{Eqn. 2.53}$$

Now the polarisation state of the light has been described using Jones vectors, we need to consider the effects that each individual component that the light interacts with has on its polarisation state. This effect can be described by a 2×2 Jones matrix; as each component affects the behaviour differently a different matrix is needed for each component. The orientation of the vector as it travels between the different reference frames of the various components must be considered also. A rotation matrix can then be used to switch between reference frames; this is of the form:

$$\begin{bmatrix}\cos\theta & \sin\theta\\ -\sin\theta & \cos\theta\end{bmatrix} \qquad \textit{Eqn. 2.54}$$

where θ is the angle of rotation of the component about its surface normal, with respect to a defined co-ordinate system. The polarisation state of a beam emerging from a component (or a series of components) can be described in terms of the beam entering the system by:

$$E_f = ME_i \qquad \textit{Eqn. 2.55}$$

where M is the matrix representation of the component, or series of components. For a series of components the system matrix is obtained by multiplying together the series of non-commutative matrices describing the effect of the individual components in the system.

For the RAS kit the E_f is described by *Eqn. 2.56*:

$$E_f = \begin{bmatrix} 1 & 0 \\ 0 & 0 \end{bmatrix} \begin{bmatrix} \cos\theta_{M-A} & \sin\theta_{M-A} \\ -\sin\theta_{M-A} & \cos\theta_{M-A} \end{bmatrix} \begin{bmatrix} \exp(i\delta_M) & 0 \\ 0 & 1 \end{bmatrix} \begin{bmatrix} \cos\theta_M & -\sin\theta_M \\ \sin\theta_M & \cos\theta_M \end{bmatrix} \begin{bmatrix} 1 & 0 \\ 0 & \exp(i\delta w_2) \end{bmatrix} \times \begin{bmatrix} r_x & 0 \\ 0 & r_y \end{bmatrix} \begin{bmatrix} 1 & 0 \\ 0 & \exp(i\delta w_1) \end{bmatrix} \begin{bmatrix} \cos\theta_P & \sin\theta_P \\ -\sin\theta_P & \cos\theta_P \end{bmatrix} \begin{bmatrix} 1 \\ 0 \end{bmatrix} \qquad \textit{Eqn. 2.56}$$

where the matrices (from top left) are those of: the analyser, rotation, PEM, window, sample, window, rotations, polarised light. Note that the window is there twice because the incident light passes through the window before hitting the sample, then the reflected beam passes through the window after hitting the sample.

Taking the frame of reference of the sample - where the eigenaxes of the sample are usually at ±45° to the vertical, and θ_S is the rotation of the sample from this position. The standard RAS configuration (as shown in *Figure 2.12*) requires that: $\theta_S = 0°$, $\theta_A = 0°$, $\theta_M = 45°$ and $\theta_P = 45°$

Evaluating E_f results in a vector of the form:

$$E_f = \begin{bmatrix} A \\ 0 \end{bmatrix} \qquad \textit{Eqn. 2.57}$$

where A is a non-zero element which can be evaluated:

$$A = \frac{1}{\sqrt{2}} r_x \left(0.5 + 0.5e^{i\delta m}\right) + \frac{1}{\sqrt{2}} r_y \left(0.5e^{i\delta m} - 0.5\right)\left(e^{i\delta w_1} e^{i\delta w_2}\right) \qquad \textit{Eqn. 2.58}$$

The window retardation for a low strain window is small and can be evaluated thus [2.36]:

$$e^{i\delta w_1} e^{i\delta w_2} = e^{i\delta w} = \cos\delta w + i\sin\delta w \approx 1 + i\delta w \qquad \textit{Eqn. 2.59}$$

This simplifies A to:

$$A = \frac{1}{2\sqrt{2}} \left[\left(r_x - r_y\right) + e^{i\delta m}\left(r_x - r_y\right) - i\delta w r_y \left(1 - e^{i\delta m}\right)\right] \qquad \textit{Eqn. 2.60}$$

The Fresnel coefficients can be separated into their real and imaginary parts:

$$r_x = a + ib \qquad \textit{Eqn. 2.61}$$

$$r_y = c + id \qquad \textit{Eqn. 2.62}$$

Once the light has passed through the analyser the polarisation state is no longer altered as the monochromator and detector are independent of polarisation; only the time dependent intensity is measured (for each wavelength). The measured time dependent intensity I is proportional to $E_f{}^2$ which in turn depends on A:

$$I = |A|^2 = \{\mathrm{Re}(A)\}^2 + \{\mathrm{Im}(A)\}^2 \qquad \textit{Eqn. 2.63}$$

Following a little algebra *Eqn. 2.63* becomes:

$$I \propto \tfrac{1}{4}\left[\left(a^2 + b^2\right) + \left(c^2 + d^2\right) + \left(c^2 + d^2\right)\delta w^2\right] + \tfrac{1}{4}\left[\left(a^2 + b^2\right) - \left(c^2 + d^2\right) - \left(c^2 + d^2\right)\delta w^2\right]\cos\delta m + \tfrac{1}{2}\left[(ad - bc) - (ac + bd)\delta w\right]\sin\delta m \qquad \textit{Eqn. 2.64}$$

It then follows that the light intensity reaching the detector is of the form:

$$I = I_0 + I_\omega \sin\delta m + I_{2\omega} \cos\delta m \qquad \textit{Eqn. 2.65}$$

The PEM retardation varies sinusoidally according to:

$$\delta m = \alpha(\lambda)\sin\omega t \qquad \textit{Eqn. 2.66}$$

where ω is the angular frequency and $\alpha(\lambda)$ is the amplitude of the modulation. The frequency components of the signal are determined by Fourier expansions [2.37] of the cosδm and sinδm terms which introduce the Bessel functions [2.37] $J(\alpha)$ of order n as described by *Eqns. 2.67-2.68* and shown in *Figure 2.19*.

$$\cos(\alpha\sin\omega t) = J_0(\alpha) + 2\sum_{n=1}^{\infty} J_{2n}(\alpha)\cos(2n\omega t) \qquad \textit{Eqn. 2.67}$$

$$\sin(\alpha\sin\omega t) = 2\sum_{n=0}^{\infty} J_{2n+1}(\alpha)\sin[(2n+1)\omega t] \qquad \textit{Eqn. 2.68}$$

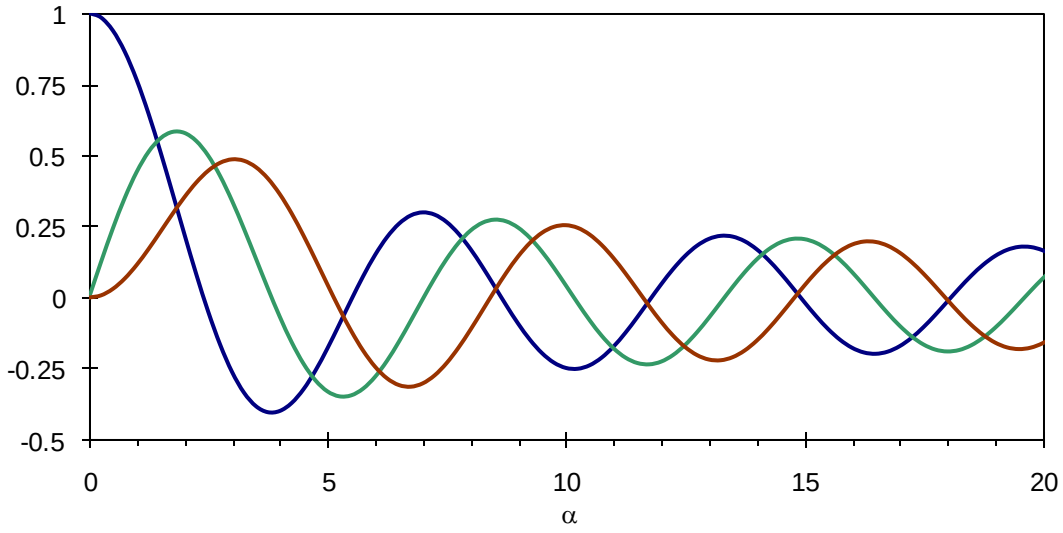

Figure 2.19: *Bessel functions $J_n(\alpha)$ with n=0 (blue), n=1 (red) and n=2 (green).*

By adjusting the voltage supplied to the photoelastic modulator $J_0(\alpha)=0$ can be achieved:

$$I = I_0 + I_\omega 2J_1(\alpha)\sin\omega t + I_{2\omega} 2J_2(\alpha)\cos 2\omega t \qquad \textit{Eqn. 2.69}$$

Comparing *Eqn. 2.69* and *Eqn. 2.64* the intensity coefficients can be determined. Considering only first order terms of the window strain; the normalized frequency terms are:

$$I_0 \sim \frac{\left(|r_x|^2 + |r_y|^2\right)}{2} = R \qquad \textit{Eqn. 2.70}$$

$$\frac{I_\omega}{I_0} \sim \mathrm{Im}\left(\frac{\Delta r}{r}\right) - \delta w \qquad \textit{Eqn. 2.71}$$

$$\frac{I_{2\omega}}{I_0} \sim \mathrm{Re}\left(\frac{\Delta r}{r}\right) \qquad \textit{Eqn. 2.72}$$

These parts can all be separated by their different frequencies; I_0 (the DC) is related to the reflectivity of the sample (note this is not the absolute reflectivity as the components of the spectrometer affect this; a correction for this effect is outlined later in this chapter). At frequency ω the imaginary part of $\Delta r/r$ is measured and its intensity is found to be dependent on the first order window term. At frequency 2ω the signal is that or the real part of $\Delta r/r$ and because this term is only sensitive to second order window strain (much less significant) most studies of RAS only report the real part of $\Delta r/r$ [2.36].

2.8 Azimuth Dependent RAS (ADRAS)

The RA spectra obtained from a sample also have a dependence on the azimuthal orientation (rotation about the surface normal) of the sample. Studies where the spectrum is recorded as a function of azimuthal angle (φ) as well as wavelength have been termed 'azimuth dependent RAS' [2.38-2.39]. In experiments such as these the optical eigenaxes are no longer along the *x* and *y* axes of the spectrometer; this means that the Jones matrix for the sample expressed in *Eqn. 2.56* becomes:

$$\begin{bmatrix} r_{xx} & r_{xy} \\ r_{yx} & r_{yy} \end{bmatrix} \qquad \textit{Eqn. 2.73}$$

The terms r_{ab} are the complex Fresnel amplitudes for converting a to b polarisations for normal incidence. The fact that this matrix now has 4 non-zero elements to it rather than the previous two means that we are no longer measuring $\Delta r/r$ in the form of *Eqn. 2.35*, we are measuring the 'generalised anisotropy' which is expressed as [2.39]:

$$S(\phi,\lambda) = \frac{\Delta s}{s} = 2\frac{r_{xx} - r_{yy} + r_{xy} - r_{yx}}{r_{xx} + r_{yy} + r_{xy} + r_{yx}} \qquad \textit{Eqn. 2.74}$$

Rotation of the sample about the azimuth leads to a shift of θ from its original value $\theta(\phi,\lambda) = \theta_0(\lambda) + \phi$ therefore it follows that [2.21]:

$$S(\varphi,\lambda) = F(\lambda)\frac{\cos\left[2\varphi + 2\theta_0(\lambda)\right]}{1 + F(\lambda)\sin\left[2\varphi + 2\theta_0(\lambda)\right]/2} \approx F(\lambda)\cos\left[2\varphi + 2\theta_0(\lambda)\right]$$

Eqn. 2.75

where θ_0 is the angle between one of the eigenaxes and the *x* axis and where $F(\lambda)$ is the anisotropy when $\theta_0 = 0$.

In most cases reported in the literature θ_0 is independent of λ and in these cases the azimuth dependence is just a multiplicative cosine factor [2.21] and in these cases

the only information to be obtained is the orientation of the optical eigenaxes. However in general this is not the case: θ_0 varies as a function of λ, meaning that the RA spectra not only change in amplitude but in shape when rotated [2.38]. This means that ADRAS is able to separate competing anisotropies in more complicated systems such as those of adsorbates and substrates and allows them to be separated into their individual components [2.38] and analysed separately.

2.9 Errors and Corrections

2.9.1 Window Effect Correction

Measurements taken inside the vacuum chamber are subject to additional errors; as the light passes though the window to the chamber it is modified. The birefringence and optical absorption effects are minimised by the use of a low strain quartz window; however there is still some effect from the window which needs correcting for. The signal obtained can be considered to consist of two parts, a part from the sample and a part from the window. The window effect can be found by taking two spectra at perpendicular azimuthal angles.

$$RAS_0 = RAS_{window} + RAS_{sample} \qquad \textit{Eqn. 2.76}$$

$$RAS_{90} = RAS_{window} - RAS_{sample} \qquad \textit{Eqn. 2.77}$$

The effect of the window can then be found by taking the average of these two spectra. The RA spectra of the sample can then be found by subtracting the window effect from the data.

$$RAS_{window} = \frac{RAS_0 + RAS_{90}}{2} \qquad \textit{Eqn. 2.78}$$

The size of the window effect is (usually) small compared to that of the sample but its effect is to create a zero line for the sample that varies with energy; as a result

there is a superposition effect of the sample anisotropy and the window anisotropy, which must be removed to compare results with those taken in different chambers.

2.9.2 Offset Correction

It has been observed while recording data that the AC and DC signals do not converge to zero when no light is incident upon the detector. The values which the AC and DC signals converge to have been found to vary with the lock-in sensitivity setting. This sensitivity effect is the same for every spectrum taken at a given sensitivity, but switching between sensitivities creates a shift in intensity across the spectral range (independent of photon energy). As the measured RA signal is a ratio of AC to DC signals, at low light levels the RA signal converges to an offset value which is dependent on the sensitivity setting; an example of this effect is shown in *Figure 2.20*.

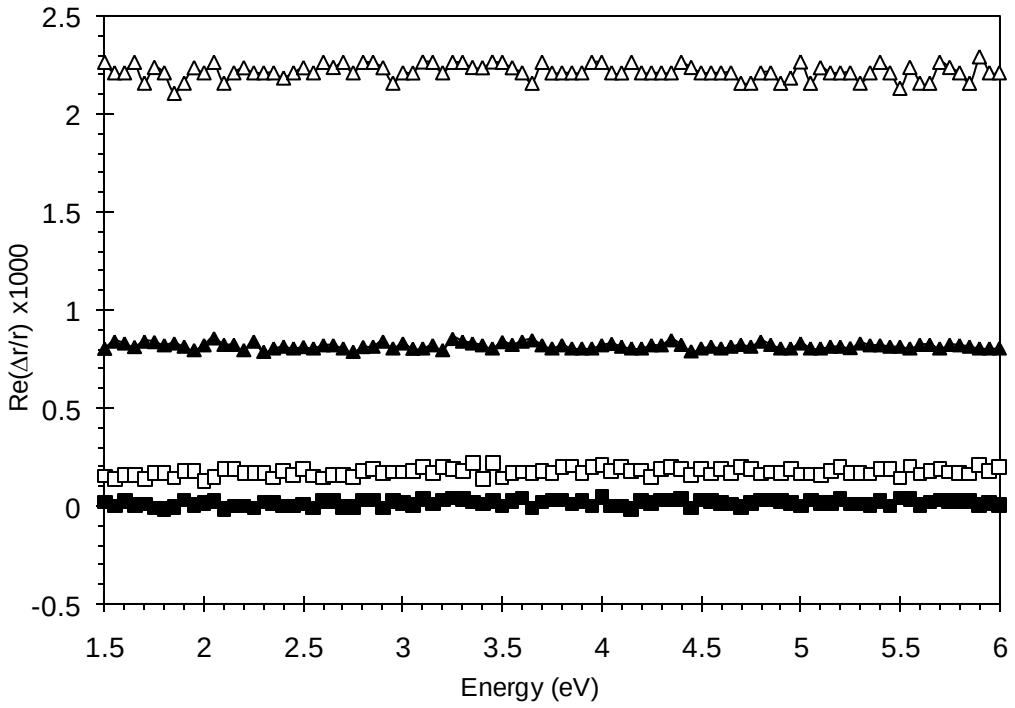

Figure 2.20: *No light spectra recorded at an integration time of 300ms for sensitivities of 1mV (filled squares), 3mV (open squares), 10mV (filled triangles) and 30mV (open triangles).*

This correction is made by recording a "no light spectra" (a spectrum recorded with the aperture to the monochromator blocked) at each sensitivity, which isolates the offsets in both the AC and DC signals, these can then be subtracted from measured data and allow the true spectra to be found.

$$AC_{True} = AC_{Measured} - AC_{Offset} \qquad \textit{Eqn. 2.79}$$

$$DC_{True} = DC_{Measured} - DC_{Offset} \qquad \textit{Eqn. 2.80}$$

The true RAS signal can then be found from:

$$RAS_{True} = const \times \frac{AC_{True}}{DC_{True}} \qquad \textit{Eqn. 2.81}$$

2.9.3 Normalisation of Reflectivity

The DC signal is proportional to the reflectivity of the sample; however the proportionality functions depend on a number of parameters. Firstly none of the components making up the spectrometer are ideal reflectors or transmitters and the amount of light they reflect or transmit varies for different wavelengths of light. Secondly the number of photons emitted from the lamp, and the sensitivity of the detector are arbitrary values (the detector sensitivity can be varied by adjusting the amplification settings). The true reflectivity (*R*) can be found using *Eqn. 2.82*:

$$R(\lambda) = DC(\lambda) \times g(\lambda) \qquad \textit{Eqn. 2.82}$$

where $g(\lambda)$ can be found using a calibration sample of known reflectivity $R(\lambda)$; calculated using *Eqns. 2.2, 2.14, 2.20* & *2.22* and *n* and *k* values obtained from Palik [2.40].

$$g(\lambda) = \frac{R(\lambda)_{cal}}{DC(\lambda)_{cal}} \qquad \textit{Eqn 2.83}$$

$g(\lambda)$ is shown for two different calibration samples in *Figure 2.21*:

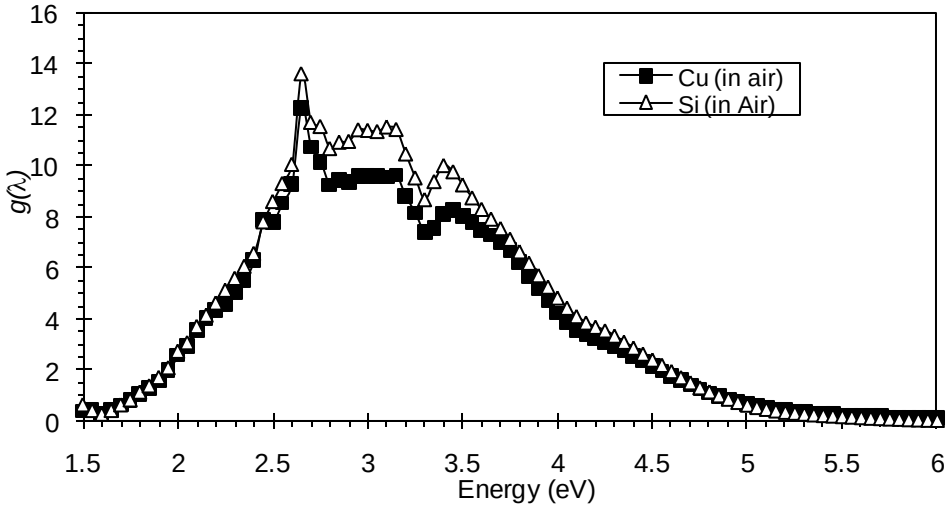

Figure 2.21: *The error in the reflectivity; g(λ) calculated using Eqn. 2.82 (Note these two spectra were taken at different detector amplification settings hence the difference in signal amplitudes).*

2.10 References

[2.1] E. Hecht; *Optics*, 4th Edition. Addison-Wesley, Harlow, England (2002)

[2.2] D. Goldstein; *Polarized Light*, 2nd Edition. Marcel Dekker, Inc, New York (2003)

[2.3] M. Born and E. Wolf, *Principles of Optics*, 5th Edition, Pergamon Press Oxford (1975)

[2.4] R.M.A. Azzam and N.M. Bashara; *Ellipsometry and Polarised Light*, North Holland, Amsterdam (1987)

[2.5] O.S. Heavens; *Optical Properties of Thin Solid Films*. Butterworths, London (1955)

[2.6] J.D.E. McIntyre and D.E. Aspnes; Surf. Sci. **24**, 417 (1971)

[2.7] J.F. McGilp; Prog. Surf. Sci. **49**, 1 (1995)

[2.8] T.E. Jenkins; J. Phys. D: Appl. Phys. **32**, R45 (1999)

[2.9] M. Cardona, F.H. Pollak, and K.L. Shaklee; J. Phys. Soc. Jap. **21**, 89 (1968)

[2.10] D.E. Aspnes and A.A. Studna; Phys Rev Lett. **54**, 1956 (1985)

[2.11] D.E. Aspnes; J. Vac. Sci. Technol. B **3**, 1498 (1985)

[2.12] D.E. Aspnes and A.A. Studna; J. Vac. Sci. Technol. A **5**, 546 (1987)

[2.13] D.E. Aspnes, J.P. Harbison, A.A. Studna and L.T. Florez; J. Vac. Sci. Technol. A **6**, 1327 (1988)

[2.14] J.P. Harbison, D.E. Aspnes, A.A. Studna, L.T. Florez and M.K. Kelly; Appl. Phys. Lett. **52**, 2046 (1988)

[2.15] M. Wassermeier, I. Kamiya, D.E. Aspnes, , L.T. Florez and J.P. Harbison; J. Vac. Sci. Technol. B **9**, 2263 (1991)

[2.16] J.R. Power, P Weightman, S. Bose, A.I. Shkrebtii and R. Del Sole; Phys. Rev. Lett. **80**, 3133 (1998)

[2.17] S.G. Jaloviar, J.L. Lin, F. Liu, V. Zielasek, L. McCaughan and M.G. Lagally; Phys. Rev. Lett. **82**, 791 (1999)

[2.18] J.R. Power, T. Farrell, P. Gerber, S. Chandola, P. Weightman and J.F. McGlip; Surf. Sci. **372**, 83 (1997)

[2.19] Y. Borensztein, W.L. Mochan, J. Tarriba, R.G. Barrera and A. Tadjeddine; Phys. Rev. Lett. **71**, 2334 (1993)

[2.20] Ph. Hoffman, K.C. Rose, V. Fernandez, A.M. Bradshaw and W. Richter; Phys. Rev. Lett. **75**, 2039 (1995)

[2.21] P. Weightman, D.S. Martin, R.J. Cole and T. Farrell; Rep.Prog. Phys. **68**, 1251 (2005)

[2.22] B. Sheridan, D.S. Martin, J.R. Power, S.D. Barrett, C.I. Smith, C.A. Lucas, R.J. Nichols and P. Weightman; Phys. Rev. Lett. **85**, 4618 (2000)

[2.23] R.J. Cole, S. Kheradmand, D.D. Higgins, F. Madani, B.F. MacDonald, V. Koutsos and J.R. Blackford; J. Phys. D: Appl. Phys. **36**, L115 (2003)

[2.24] B.F. MacDonald, R.J. Cole, W. Zheng and C. Miremont; Phys. Stat. Sol (a) **188**, 1577 (2001)

[2.25] B.F. MacDonald, W. Zheng, R.J. Cole and I. Underwood; J. Phys. D: Appl. Phys. **35**, L41 (2002)

[2.26] B.F. MacDonald and R.J. Cole; Surf. Sci. **532**, 1098 (2003)

[2.27] B.F. MacDonald, W Zheng and R.J. Cole; J. Appl. Phys. **93**, 4442 (2003)

[2.28] S.M. Scholz, F. Mertens, K. Jacobi, R. Imbihl and W. Richter; Surf. Sci. **340**, L945 (1995)

[2.29] C. Di Natale, C. Goletti, R. Paolesse, F. Della Sala, M. Drago, P. Chiaradia, P. Lugli and A. D'Amico; Appl. Phys. Lett. **77**, 3164 (2000)

[2.30] C. Goletti, R. Paolesse, C. Di Natale, G. Bussetti, P. Chiaradia, A. Froiio, L. Valli and A. D'Amico; Surf. Sci. **501**, 31 (2002)

[2.31] B.G. Frederick, J.R. Power, R.J. Cole, C.C. Perry, Q. Chen, S. Haq, Th. Bertrams, N.V. Richardson and P. Weightman; Phys. Rev. Lett. **80**, 4490 (1998)

[2.32] R.J. Cole, B.G. Frederick, J.R. Power, C.C. Perry, Q. Chen, C. Verdozzi, N.V. Richardson and P. Weightman; Phys. Stat. Sol. (a) **170**, 235 (1998)

[2.33] C.C. Perry, B.G. Frederick, J.R. Power, R.J. Cole, S. Haq, Q. Chen, N.V. Richardson and P. Weightman; Surf. Sci **427**, 446 (1999)

[2.34] B.F. MacDonald; *Reflection Anisotropy Spectroscopy and Scanning Probe Microscopy Studies with Applications to Liquid Crystal Alignment Layers*, PhD Thesis, The University of Edinburgh (2002)

[2.35] R.C. Jones; J. Opt. Soc. Am. **31**, 488 (1941)

[2.36] D.S. Martin and P. Weightman; Surf. Interface Anal. **31**, 915 (2001)

[2.37] M. Abramowitz and I.A. Stegun (Editors), *Handbook of Mathematical Functions*. Dover Publications, New York (1970)

[2.38] B.F. MacDonald and R.J. Cole; Appl. Phys. Lett. **80**, 3527 (2002)

[2.39] B.F. MacDonald, J.S. Law and R.J. Cole; J. Appl. Phys. **93**, 3320 (2003)

[2.40] E.D. Palik (Editor); *Handbook of Optical Constants of Solids*, Academic Press, Orlando/London (1985).

Chapter 3: Equipment & Complementary Techniques

3.1 Introduction to Ultra High Vacuum (UHV)

Ultra high vacuum (UHV) is the term used to define a system whose pressure is in the range of 10^{-8} to 10^{-12}mbar [3.1]. A UHV system is used to keep the sample clean. The mean free path of a molecule, λ, (defined as the average distance travelled by a molecule between collisions [3.2]) is given by:

$$\lambda = \frac{1}{\sqrt{2}\pi d^2 n} \qquad \textit{Eqn. 3.1}$$

where πd^2 is the collision cross section and n is the number of molecules. As the number of molecules is dependent on the pressure of the system, the mean free path is also dependent on the pressure. At room temperature and a pressure of 10^{-3}mbar the mean free path of a N_2 molecule is ~7cm. The mean free path of the same molecule at a pressure of 10^{-10}mbar is ~700km [3.1].

Given this type of information it is possible to calculate the impingement rate of molecules onto our sample's surface per second [3.1, 3.3]:

$$J = \frac{P}{\sqrt{2\pi mkT}} \qquad \textit{Eqn. 3.2}$$

where P is pressure (in mbar), m is mass of gas (kg), k is Boltzman's constant (JK^{-1}) and T is temperature (K), or

$$J = \frac{PN_A}{\sqrt{2\pi MRT}} \qquad \textit{Eqn. 3.3}$$

where N_A is Avogadro's number, M is molecular mass of gas (kg), and R is the gas constant ($JK^{-1}mol^{-1}$).

Again using the example of Nitrogen, assuming that a surface monolayer consists of 10^{15}atoms/cm^2, and assuming a sticking coefficient of 1 (every molecule incident on the surface sticks) then the monolayer formation time τ (in seconds) is given by:

$$\tau = \frac{10^{15}}{J} \qquad \textit{Eqn. 3.4}$$

For this example at room temperature the monolayer formation time at 10^{-6}mbar is approximately 3.5 seconds, while at 10^{-10}mbar it is approximately 3.5×10^4seconds (nearly 10 hours). This time scale demonstrates why UHV systems are so important in studies of surfaces.

3.2 The Vacuum Chamber

The chamber (*Figure 3.1*) has been used for approximately 8 years and was constructed by Brian MacDonald as part of his PhD [3.4]. It was initially designed for the in-situ monitoring by RAS of processes such as ion bombardment and molecular sublimation without any movement of the sample, and changes could be monitored in real time. As a result the majority of the ports on the chamber point towards the centre where the sample is housed on the manipulator.

The vacuum chamber can be considered in three sections; the main chamber, the pumping chamber and the transfer chamber. All these chambers can achieve UHV pressures and can be isolated from each other using a series of valves. The main chamber is where all the measurements are carried out and houses all the experimental equipment. Connected to the base of the main chamber is the pumping chamber; this houses a liquid nitrogen trap and connects the diffusion pump to the main chamber. The transfer chamber performs a number of operations; mainly it allows rapid changes of samples into the main chamber without exposing the whole

chamber to ambient conditions. It also can be used to pump out materials that are no longer required by the evaporator or the ion gun.

To optimise the performance of the RAS kit light enters and exits the chamber through a low-strain quartz window, which allows higher levels of UV light to be transmitted through the window, and also reduces birefringence effects.

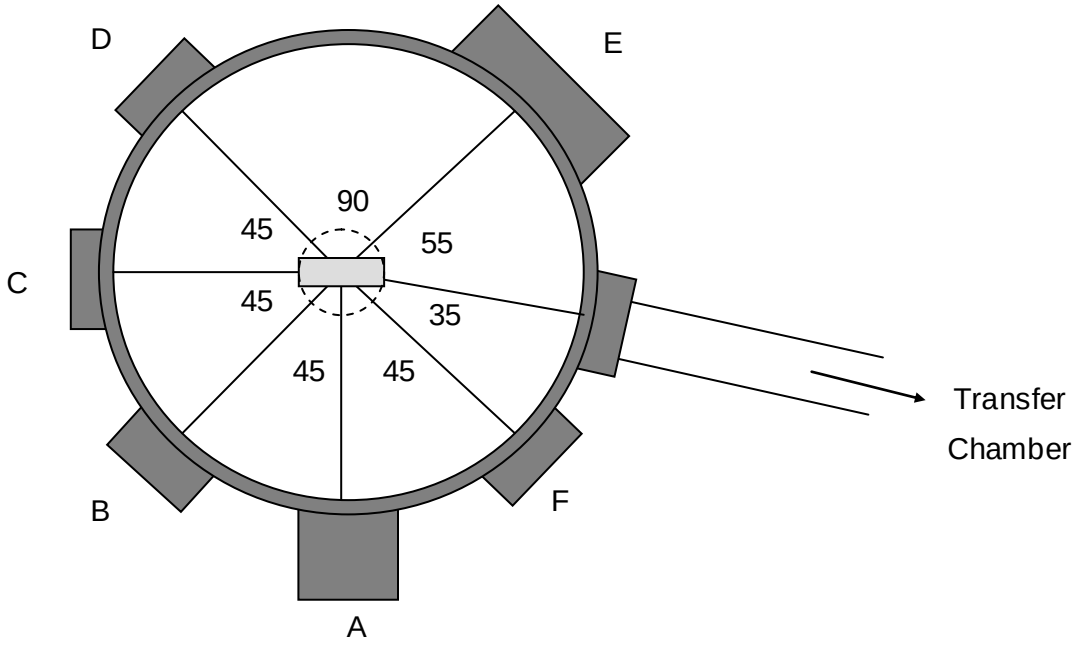

Figure 3.1: *Vacuum chamber layout plan (as seen from above). Numbers denote angles between ports.*

Position	Top	Middle	Bottom
A	Ion Gun	RAS Window	View Port
B	-	Molecular Evaporator	Mass Spectrometer
C	View Port	View Port	-
D	-	View Port	-
E	-	LEED	-
F	-	View Port	-

Table 3.1: *Positions of analysis equipment (Position letters correspond to positons shown on Figure 3.1).*

3.2.1 The Sample Manipulator

The manipulator on which the sample (*Figure 3.2*) is mounted allows translation of the sample in the *x*, *y* and *z* directions as well 360° rotation so that the sample can face any direction/port in the chamber. There is also the ability to rotate the sample 120° about the surface normal and a tilt mechanism which corrects any slight offsets which may occur. As the sample manipulator also houses a sample heater and a copper braid for heating and cooling there are feed throughs for these.

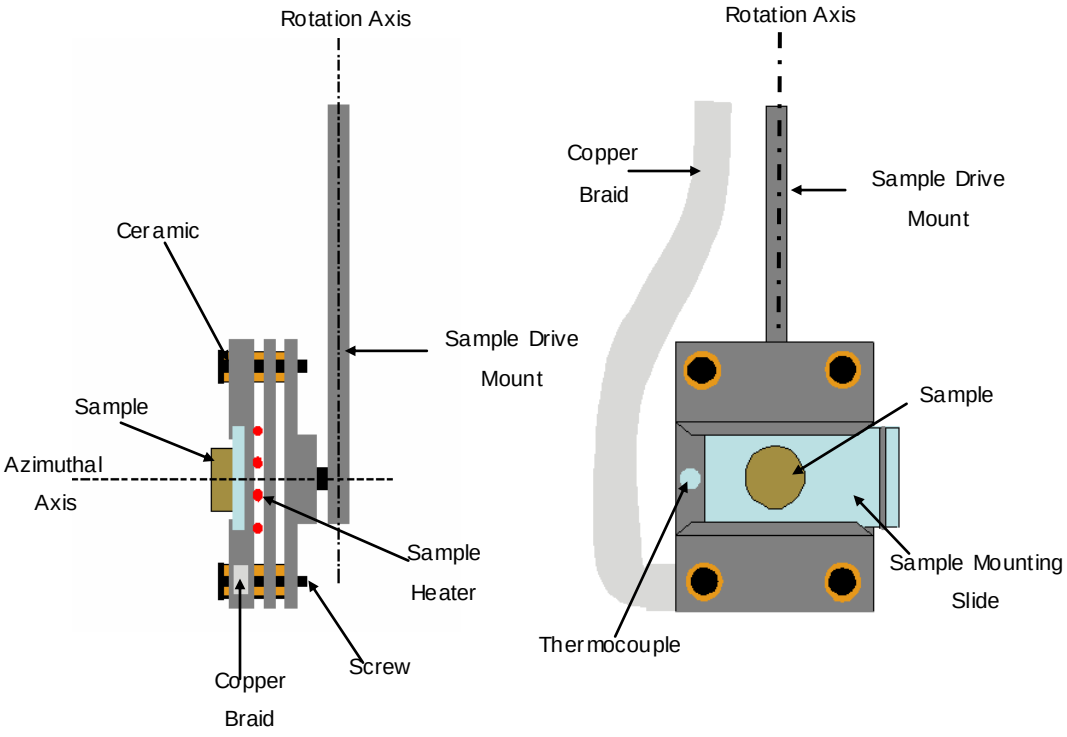

Figure 3.2: *Sample manipulator, left: side view, right: front view.*

The base of the sample manipulator is stainless steel although the front facing plates are made from copper. There are a number of ceramic parts through which the screws holding the body of the manipulator together pass through this is so that each metal plate is electrically isolated from the rest meaning that it is possible to measure the drain current between the sample and earth; this also means that this is not affected by the current to the sample heater.

The copper braid is connected to its feed through via a sapphire contact which is a thermal conductor but an electrical insulator. This allows the sample to be cooled and prevents the sample from being earthed, making it possible to monitor the current through the sample due to the flow of charged ions during ion bombardment.

The copper braid method allows cooling to ~180K which is a much higher temperature that that of liquid nitrogen (77K) and this is due to the inefficiency of this method; however the other alternative having a flow of liquid nitrogen through capillary tubes to the sample is impractical due to the necessity of rotating the sample, both around the chamber and though azimuthal rotations.

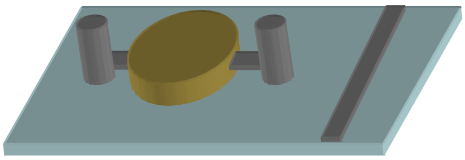

Figure 3.3: *Sample slide.*

The sample itself is a single crystal (MaTecK, Germany) 1cm in diameter and oriented to ~0.1°. The sample was mounted on a 2cm by 3cm slide (as shown in *Figure 3.3*) and is held in position by two clips screwed into the back of the slide. These clips hold the sample into position by slotting into groves on the side of the sample. The slide also has a groove in it which is where it slots into the transfer arm allowing samples to be moved in and out of the main chamber. The slide is simply pushed into the manipulator where it can then be held firmly by the jaws of the manipulator. To remove the slide from the manipulator the groove in the slide is lowered into the transfer arm and then simply pulled out.

3.2.2 Pumping and Pressure Monitoring

There are two pumping systems in the chamber. The first is a diffusion pump in the pumping chamber backed by a rotary pump and this is used to pump the main chamber most of the time. This system in combination with the liquid nitrogen trap and a titanium sublimation pump positioned just below the main chamber means the base pressure of the main chamber is 10^{-11}mbar. The second system, a turbomolecular pump backed by another rotary pump, pumps the transfer chamber and is capable of quickly pumping down from atmospheric to a base pressure of 10^{-7} mbar, useful when changing samples.

Pirani gauges are used to measure the pressure in the backing lines of the chambers which is usually of the order 10^{-1}mbar, confirming the correct performance of the backing pumps. The pressures inside all chambers are measured by ionization gauges, two positioned on the main chamber, one in the pumping chamber and one in the transfer chamber. The system is safeguarded by a pressure trip switch which cuts power to all the electronic equipment except the pumps when the pressure falls below a set level, preventing damage to filaments and other components sensitive to pressure. In the event of a pump failure an electronic circuit is used to isolate the diffusion pump and deactivate all the other pumps to prevent the chamber being flooded with oil.

3.3 Experimental and Analysis Equipment

3.3.1 LEED

Low Energy Electron Diffraction is a technique used to give information on the structure, periodicity and orientation of the sample. The main use of this technique is to verify the orientation of the sample. A detailed description of the technique is given later in this chapter.

3.3.2 Ion Gun

The Ion gun is used to clean the sample and in ion bombarding experiments. The gun operates by firing Argon ions of fixed energy (in the range of 100-3000eV) at the surface, giving a typical beam current of 10-12μA. The ions are created by leaking Argon gas into the gun discharge chamber and focusing them on the sample. The energetic ions then impact on the surface causing the surface materials to be removed. The ion gun operates at a typical pressure of 2×10^{-5}mbar.

3.3.3 Sample Heater

The sample heater is a tungsten wire which acts as a filament, mounted on the sample holder behind the sample. Pulses of current are sent through the wire causing the filament to undergo Joule heating, from which the sample receives radiant heat. The temperature is controlled by a thermocouple mounted on the sample holder and fed back into the controller so that the current can be varied to increase or maintain the temperature as necessary. The heater is capable of temperatures as high as 750°C, while the thermocouple can be used to monitor the temperature in the range of -200°C to 1370°C.

3.3.4 Mass Spectrometer

The mass spectrometer is used to measure partial pressures of materials in the chamber and is used to check for leaks, to assess the purity of substances admitted into the chamber (e.g. Argon) and also to monitor materials coming off the sample in experiments.

3.3.5 Molecular Evaporator

The molecular evaporator, although unused for the work in this thesis, works by using the sample heater controller to heat a filament and sublimate a molecule so that it can pass into the chamber and be deposited onto the surface of the sample.

3.3.6 Bake Out System

The bake out system for the chamber consists of four 1kW heaters mounted at the base of the chamber, an insulating hood which covers the whole chamber and the bake out controller which monitors the temperature via a thermocouple. Using this system the bake can reach a maximum temperature of 200°C for a period of up to 30 hours.

3.4 Low Energy Electron Diffraction (LEED) [3.3, 3.5-3.6]

LEED is one of the complementary techniques used alongside RAS which gives additional information or backs up the observations seen by RAS and is mainly used to check the periodicity, cleanliness and orientation of the sample.

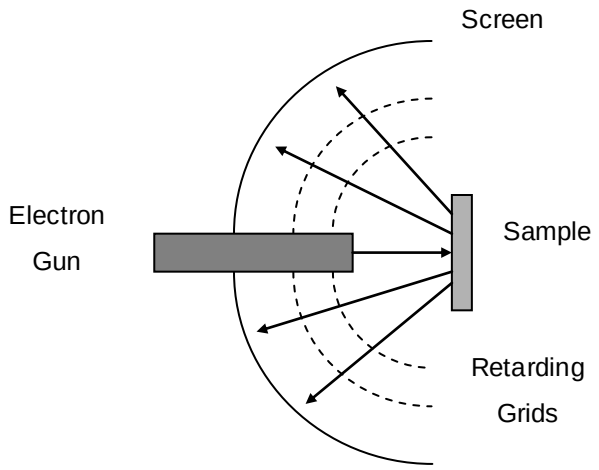

Figure 3.4: *Schematic diagram of the LEED equipment.*

LEED obtains surface sensitivity by firing low energy (up to 1keV) electrons at the sample; because of their low energy these electrons are only able to penetrate the first few atomic layers of the surface. These electrons are then elastically scattered from the surface to form a diffraction pattern on the screen. There are retarding grids between the sample and the screen which filter out electrons which have lost more than 3% of their initial energy. The layout of the LEED apparatus is shown in *Figure 3.4*.

From the diffraction pattern obtained in reciprocal space information about the size, symmetry and orientation of the unit cell in real space can be obtained, and from the intensity of the spots it is possible to obtain information about atomic positioning, as illustrated in *Figure 3.5*.

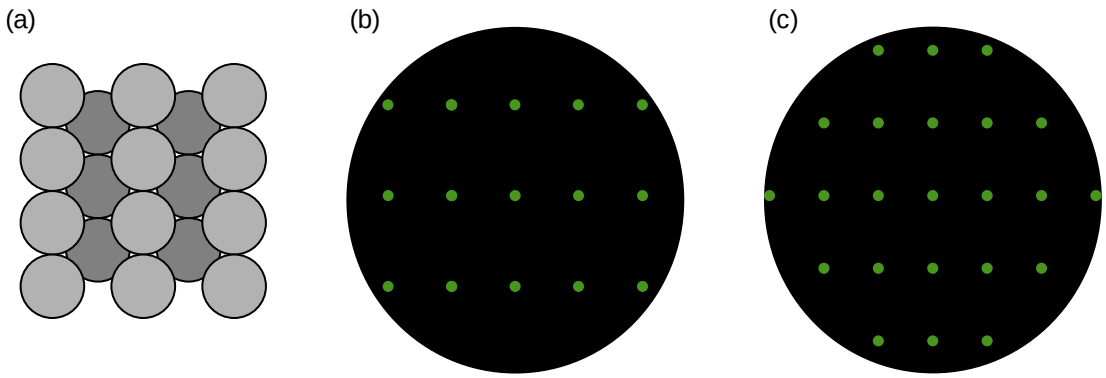

Figure 3.5: *(a): A schematic diagram of the fcc (110) crystal plane. Representations of the LEED pattern expected from an fcc (110) crystal plane at (b) low energy and (c) high energy.*

The De Broglie relationship:

$$E = \frac{h^2}{2m_e\lambda^2} \qquad \textit{Eqn. 3.5}$$

where E is the energy, h is Planck's constant, m_e the mass of an electron and λ the wavelength, can be used to show that within the energy region in which LEED typically operates (10-300eV) the electrons have wavelengths in the order of atomic dimensions, which is necessary for atomic diffraction to occur.

The surface sensitivity of the technique can be demonstrated by considering the universal curve of electron escape depths from the surface of a material as a function of their energy. This is illustrated in *Figure 3.6* and shows that in the energy range used in LEED the electrons detected can only have interacted with the first few atomic layers.

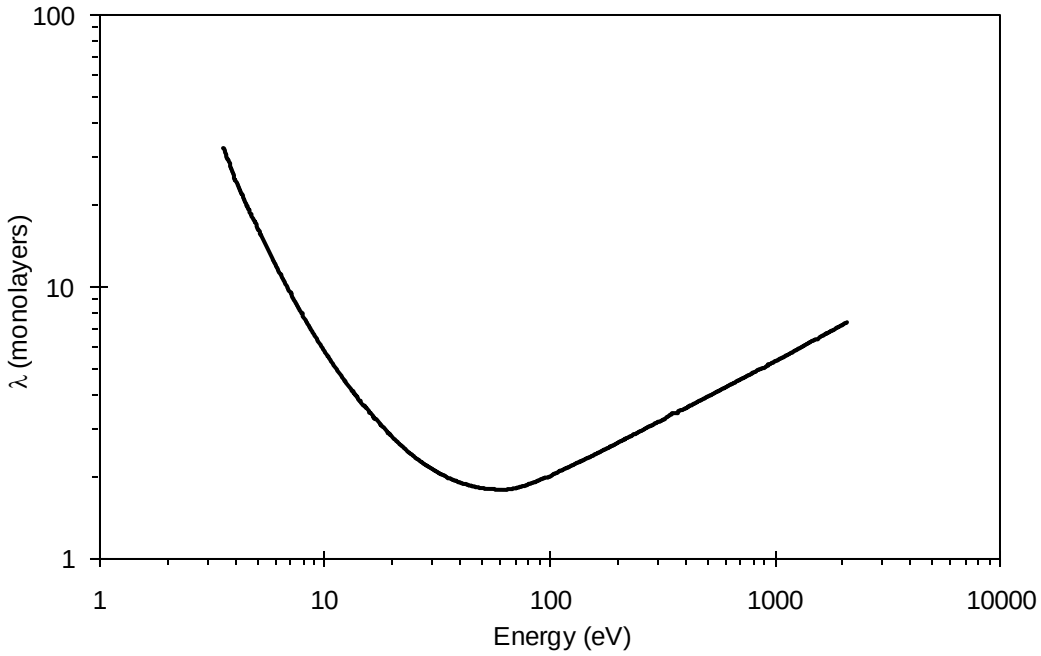

Figure 3.6: *The universal curve of electron mean free path against energy (reproduced from reference 3.3).*

3.4.1 Interpreting LEED patterns

Take the (110) surface in real space; the unit cell is defined by the vectors A_s and B_s in *Figure 3.7*.

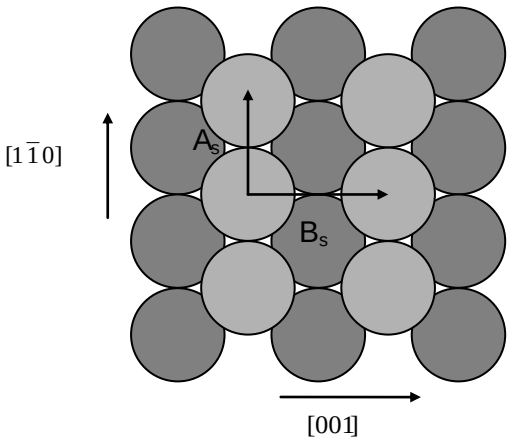

Figure 3.7: *The positions of atoms on a (110) surface in real space.*

The unit cell of the LEED pattern for the substrate is defined in reciprocal space by the vectors a_s and b_s and similarly the unit cell of the overlayer is defined by the vectors a_o and b_o, as shown in *Figure 3.8*.

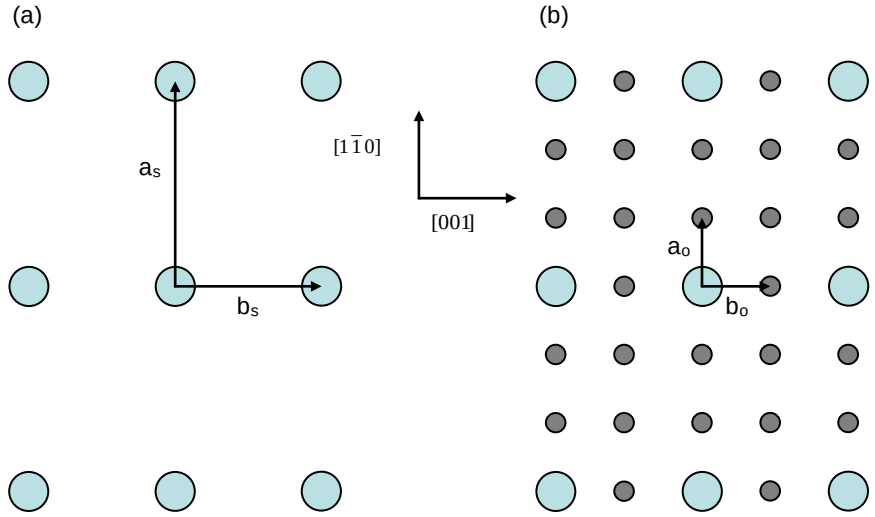

Figure 3.8: *LEED patterns from (a) a (110) surface (b) a (110) surface with a deposited overlayer.*

The vectors in real space and reciprocal space are related by the scalar products:

$$a \cdot A = 2\pi \qquad \textit{Eqn. 3.6}$$

$$a \cdot B = 0 \qquad \textit{Eqn. 3.7}$$

$$b \cdot A = 2\pi \qquad \textit{Eqn. 3.8}$$

$$b \cdot B = 0 \qquad \textit{Eqn. 3.9}$$

To find the positions of the overlayer atoms in real space it is necessary to rewrite their defining vectors in terms of those of the substrate.

$$\begin{pmatrix} a_o \\ b_o \end{pmatrix} = M \begin{pmatrix} a_s \\ b_s \end{pmatrix} \qquad \textit{Eqn. 3.10}$$

$$a_o = m_{11} a_s + m_{12} b_s \qquad \textit{Eqn. 3.11}$$

$$b_o = m_{21}a_s + m_{22}b_s \qquad \textit{Eqn. 3.12}$$

where

$$M = \begin{bmatrix} m_{11} & m_{12} \\ m_{21} & m_{22} \end{bmatrix} \qquad \textit{Eqn. 3.13}$$

In this case

$$a_o = 1/3(a_s) + 0(b_s)$$
$$b_o = 0(a_s) + 1/2(b_s)$$

giving

$$M = \begin{bmatrix} 1/3 & 0 \\ 0 & 1/2 \end{bmatrix}$$

To convert from reciprocal space into real we need to take the "inverse transpose" of the matrix *M*.

$$N = \frac{1}{\det M}\begin{bmatrix} m_{22} & -m_{21} \\ -m_{12} & m_{11} \end{bmatrix}$$

$$\det M = (m_{22}m_{11}) - (m_{21}m_{12})$$
$$\det M = (1/2)(1/3) - (0)(0) = 1/6$$

$$N = \frac{1}{1/6}\begin{bmatrix} 1/2 & -0 \\ -0 & 1/3 \end{bmatrix} = \begin{bmatrix} 3 & 0 \\ 0 & 2 \end{bmatrix}$$

Hence this LEED pattern would be described as $\begin{bmatrix} 3 & 0 \\ 0 & 2 \end{bmatrix}$ in matrix form or as a p(3×2) in more standard Wood notation [3.3, 3.5-3.6]. In this thesis the LEED patterns will be expressed in the Wood notation, but for simplicity were calculated

initially in matrix form. The Wood notation indicates a real space unit cell with dimensions $3a \times 2b$ with a and b often chosen to be orthogonal. The p and c prefixes are used to distinguish 'primitive' and 'centred' unit cells (a centred unit cell being one with an additional lattice site at the centre of the cell).

3.5 Scanning Tunnelling Microscopy (STM) [3.3, 3.5, 3.7-3.9]

Scanning tunnelling microscopy (STM) is a surface topographical imaging technique, capable of operating in a range of environments and obtaining atomic scale resolution. This combination of attributes has made the technique one of the most commonly used surface characterisation techniques. STM was developed in 1981 by Binnig et al. [3.10-3.11] and earned its inventors a Nobel Prize for Physics in 1986.

STM uses the principle of quantum tunnelling to probe the density of states near the Fermi energy (E_F) of a metallic (or semi-conducting) material, using an atomically sharp conducting tip at a distance of within a few nanometres from the surface. A small potential difference is applied, usually such that the tip is positively charged with respect to the sample, thus encouraging a flow of electrons between the sample and the tip where their potential energy will be lowered.

Classically electrons are confined within solids, and electron flow across free space is forbidden, if the activation energy (work function) is greater than the kinetic energy of the electron. The quantum tunnelling process allows electron wave functions to permeate through a potential barrier, meaning there is a finite probability that an electron will exist in a classically forbidden region. The magnitude of this probability has an exponential dependence on the barrier width, in the case of STM the distance between the sample and the tip. The larger the distance between the sample and the tip the smaller the current measured; an image is obtained by measuring the magnitude of the tunnelling current as the tip is moved across the surface. The tunnelling current (I) through a potential barrier of width W is given by *Eqn. 3.14*:

$$I(W) = C\exp\left(-W\sqrt{\varphi}\right) \qquad \textit{Eqn. 3.14}$$

where φ is the work function, and C is a constant.

The scanning of the tip across and its approach towards the surface are controlled by piezoelectric scanners on which the tip is mounted. Piezoelectrics expand/contract upon application of a voltage across them, typically by ~1Å per mV meaning the tip placement with respect to the sample can be determined to an extremely high level of accuracy.

STM can be operated in two modes: constant height mode and constant current mode. In constant height mode the tip is scanned across the *x*-*y* plane of the surface whilst maintaining a constant position in the *z*-direction. As the tip is scanned across the surface the surface protrusions cause changes in the sample-tip separation (W) and hence the tunnelling current (I), and an image is then constructed by plotting tunnelling current against surface position. In constant current mode the surface-tip separation (and hence tunnelling current) is fixed and the position of the tip is varied to maintain this value. An image is then constructed by plotting *z*-piezo position against surface position. For atomically flat surfaces constant height mode is preferred as scanning is quicker, for rough surfaces constant current mode is preferred as it avoids surface-tip collisions which would damage the tip.

As the technique is highly sensitive to the sample-tip separation distance, in order to obtain high quality images the STM must be isolated from external vibrations. This means that careful thought must go into the design and location of such systems. Common methods used to keep STM systems vibration free include spring systems, magnetic levitation, anti-vibration stacks and mechanisms for eddy current damping.

3.6 References

[3.1] A. Chambers, R.K. Fitch and B.S. Halliday; *Basic Vacuum Technology* 2nd Edition, Institute of Physics Publishing, Bristol and Philadelphia (1998)

[3.2] *Oxford Dictionary of Physics* 4th Edition, A. Isaacs (Editor), Oxford University Press, Oxford/New York (1999)

[3.3] M. Prutton; *Introduction to Surface Physics*, Oxford University Press, Oxford (1994)

[3.4] B.F. MacDonald; *Reflection Anisotropy Spectroscopy and Scanning Probe Microscopy Studies with Applications to Liquid Crystal Alignment Layers*, PhD Thesis, The University of Edinburgh (2002)

[3.5] G. Attard and C. Barnes; *Surfaces*; Oxford University Press, New York (1998)

[3.6] A. Zangwill; *Physics at Surfaces*; Cambridge University Press, Cambridge (1996)

[3.7] C. Bai; *Scanning Tunneling Microscopy and its Application*, Springer (Berlin) (1995)

[3.8] E. Meyer, H.J. Hug and R. Bennewitz; *Scanning Probe Microscopy The Lab on a Tip*, Springer (Berlin) (2004)

[3.9] T. Sakurai and Y. Watanabe (Editors); *Advances in Scanning Probe Microscopy*, Springer (Berlin) (2000)

[3.10] G. Binnig, H. Rohrer, Ch. Gerber and E. Weibel; Appl, Phys. Lett. **40**, 178 (1982)

[3.11] G. Binnig, H. Rohrer, Ch. Gerber and E. Weibel; Phys. Rev. Lett. **49**, 57 (1982)

Chapter 4: Ion Bombarding Copper

4.1 Copper (110)

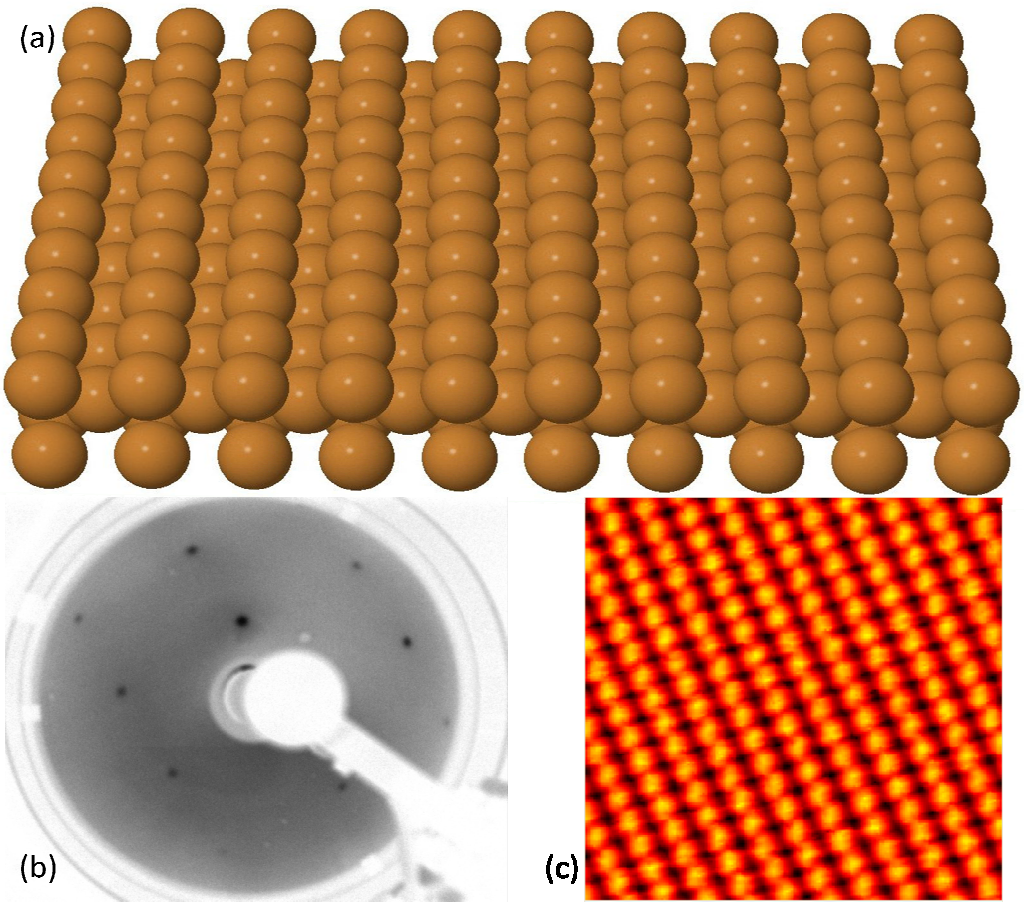

Figure 4.1: *(a): The atomic positions of atoms on the Cu(110) surface. (b): The LEED pattern recorded from the clean Cu(110) surface used in this work. (c): A 4×4nm STM image of the clean Cu(110) surface recorded in constant current mode at 78K, 2.1nA and +0.051V.*

The Cu(110) surface is one of the most studied metal surfaces by RAS and as a result is probably one of the best understood, which makes it an ideal surface to study the effects of nanoscale modification. It possesses a (1×1) surface atomic order when free from contaminants as evident from LEED patterns (Figure 4.1 (b)). The RAS of Cu(110) was first reported in 1995 by Hoffman et al. [4.1] along with the spectra were possible explanations of some of the main features observed at 2.1eV and

around 4eV. *Figure 4.2* shows the RA response of the Cu(110) sample used for the work in this chapter, recorded at room temperature.

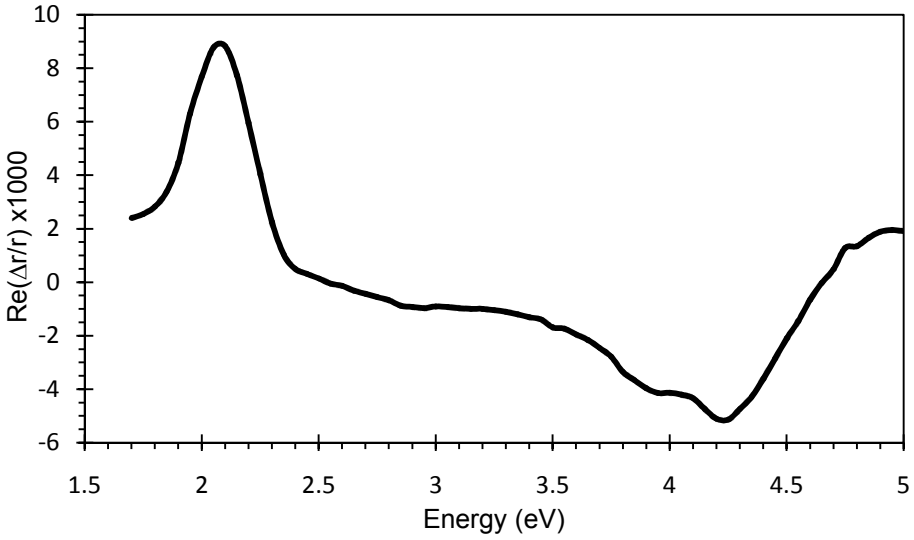

Figure 4.2: *The RA response of the clean Cu (110) surface at room temperature.*

4.2 The 2.1eV Region

Hoffman et al.[4.1] understood the 2.1eV peak to be due to transitions at the $\bar{Y}$ symmetry point of the Brillouin zone between the occupied and unoccupied states at 0.4eV below the Fermi level and at approximately 1.8eV above the Fermi level. These were based on the predications of Jiang et al. [4.2] who described the dipole selection rules which allow a transition between the two surface states when induced by [001] polarised light. Hansen et al. also assigned a second smaller contribution assigned to local field effects at the surface [4.3-4.4] which can be observed when the sample is exposed to air, as the surface state peak is sensitive to contamination. When exposed to air an adlayer of oxygen forms on the surface causing a reduction in the number of unoccupied states. This causes a reduction in the number of surface state transitions causing the surface state peak at 2.1eV to reduce in intensity [4.5-4.6]. Similarly adsorption of other molecules [4.7-4.11] has seen the reduction in intensity of the peak.

More recently Sun et al. [4.12] have reported that the anisotropy of the 2.1eV feature can be described as the superposition of three different contributions: transitions between the surface states as described above, interband transitions involving modified Cu bulk states and a Drude contribution due to surface intraband transitions.

4.2.1 Surface State Transitions

The termination of the bulk crystal at the surface results in surface atoms having lower co-ordination numbers than their bulk counterparts. This produces electronic states which are localised in the plane of the surface, called surface states [4.13]. These states have energies which lie in forbidden energy gaps of the projected bulk continuum states.

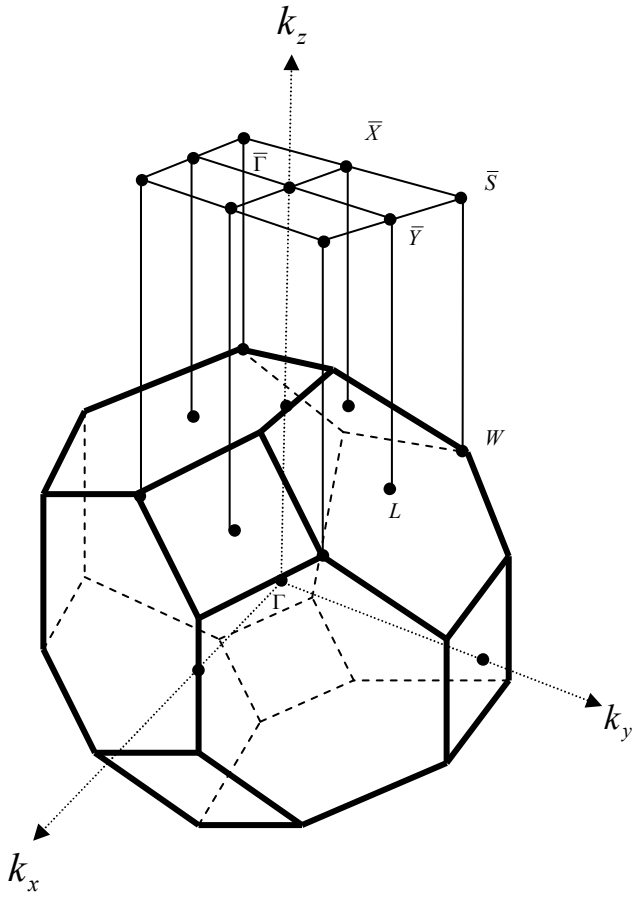

Figure 4.3: *Surface Brillouin zone of the (110) surface projected from the bulk Brillouin zone [4.13].*

When discussing the surface electronic structure of a material it is necessary to define a surface Brillouin zone (SBZ), which is characterised by a two dimensional wave vector *k*. For each value of *k* in the SBZ a rod extends back into the three dimensional Brillouin zone and the energy bands along these rods can then be projected onto the SBZ. The example of this for the (110) surface is shown in *Figure 4.3*.

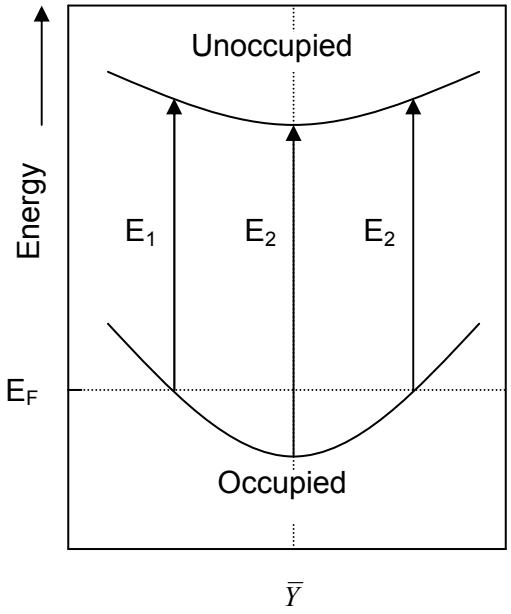

Figure 4.4: *The band structure of Copper at the* $\bar{Y}$ *symmetry point.*

Electronic structure studies of the surfaces of noble metals have revealed the existence of both occupied and unoccupied surface bands within gaps around the Fermi energy at different points on the SBZ [4.2]. *Figure 4.4* shows the location of the surface states for Cu(110); it possesses two surface bands that lie in the *p-s* band gap at the $\bar{Y}$ point of the SBZ, one occupied the other unoccupied. Photoemission results indicate that the occupied state lies ~0.4eV below E_F [4.14-4.16], and Inverse Photoemission indicate that the unoccupied state exists ~1.8eV above E_F [4.17-4.19]. The occupied state has been described as being p_y in nature whilst the unoccupied state is (s + p_z) in nature [4.20-4.21]. The application of dipole selection rules indicate that transitions between these states can only be induced by [001] polarised light [4.2]. A transition between these two states is at the correct energy for a peak to

be observed at ~2.1eV in the RA spectrum. Cu(110) also possesses two other bands within the p-s band gap at the $\overline{X}$ point [4.2]; their energies are ~2.0eV above and ~1.0 eV below the Fermi level. However these were thought not to contribute to the RA spectrum observed [4.1].

4.2.2 Surface Local Field Effect

The surface local field effect has been used in a number of studies to model the response of noble metal surfaces in particular copper [4.3-4.4, 4.22] and also silver [4.22-4.24]. Although not considered in detail in the work outlined in this thesis previous work using this model is referred to, so a basic understanding is required. The interaction of an electric field with a dielectric medium causes the polarisation of atoms within the material creating atomic dipoles. These atomic dipoles then exhibit an electric field that in turn can influence other local atomic dipoles; as a result the electric field experienced by any atom has a contribution from the external electric field and the local field produced by the materials response.

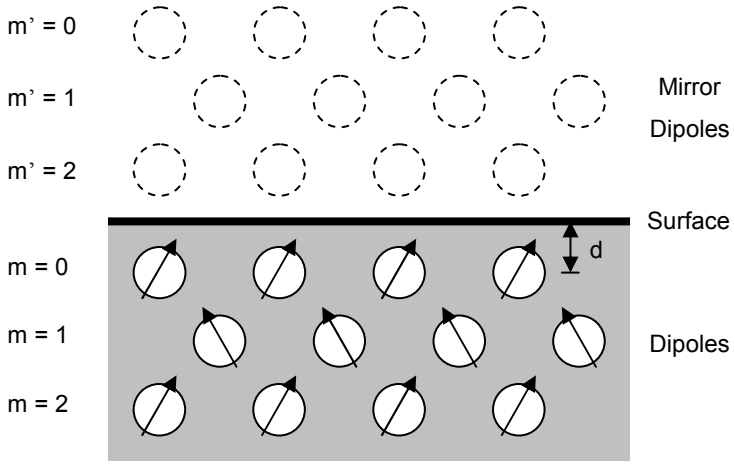

Figure 4.5: *The Swiss cheese model.*

The surface local field effect theory was developed by Mochan et al. [4.25-4.26] to calculate the RA response of various materials. Copper atoms have a shell structure of $1s^2 2s^2 2p^6 3s^2 3p^6 3d^{10} 4s^1$; for the case of copper the model is based on the assumption that the 3*d* electrons are localised at lattice sites, while the 4*s* electrons

are delocalised. The anisotropy can then be modelled using the "*Swiss cheese model*" shown in *Figure 4.5*.

The full 3*d* shells are represented as ionic cores, shown here as circles, with their associated dipoles. The space between circles is occupied by the delocalised 4*s* electrons which act as a Drude-like electron free gas. Close to the surface the electron distribution is ordered such that the electric field would be the same as if the lattice sites were mirrored. The dipole moment of each ionic core can be found from adding all the dipoles and mirror dipoles together. Then the system can be broken down into *x* and *y* components from which the surface conductivity in *x* and *y* directions can be found and the RA response is given by:

$$\frac{\Delta r}{r} = \frac{2\left(\sigma_x - \sigma_y\right)}{c\varepsilon_0\left(\varepsilon - 1\right)} \qquad \textit{Eqn. 4.1}$$

where σ_x and σ_y are the surface conductivity in the *x* and *y* directions and all other symbols have their usual meanings. A non-zero RAS response is therefore obtained when the surface inter-band contributions are not equal. For a more in depth discussion of the surface local field effect see Reference [4.22].

4.2.3 Derivative Model

In order to continue further into the understanding of the reported mechanisms of the 2.1eV region, it is necessary to outline details of the derivative model.

RA spectra often exhibit distinct features at the same photon energies as peaks in the bulk dielectric function, ε_b [4.27]. The features in ε_b are as a result of transitions between bands at critical points in the Brillouin zone; the surface creates perturbations in these transition energies ΔE_g and linewidths $\Delta\Gamma$. Noticing that the link between the RA spectra and ε_b was $d\varepsilon_b/dE$ derivative-like, Rossow et al. [4.28] devised the model and applied it to Si. This model has since been applied to the clean Cu(110) surface by Sun et al. [4.29] and the ion bombarded Cu(110) by Martin et al. [4.30], both for the regions above photon energies of 3eV. For a biaxial surface

such as Cu(110) different energy shifts and linewidths changes for the $[1\,\bar{1}\,0]$ and [001] directions arise giving different values of surface dielectric functions ε_x and ε_y. The difference between these two is given by:

$$\Delta\varepsilon_s \approx \left(\Delta E_g - i\Delta\Gamma\right)\frac{d\varepsilon_b}{dE} \qquad \textit{Eqn. 4.2}$$

Substituting this into the 3-phase model (as outlined in *Chapter 2*) yields:

$$\frac{\Delta r}{r} = \frac{4\pi i d}{\lambda}\frac{\left(\Delta E_g - i\Delta\Gamma\right)}{\varepsilon_b - 1}\frac{d\varepsilon_b}{dE} \qquad \textit{Eqn. 4.3}$$

As we are interested in the real part of $\Delta r/r$ we can obtain [4.30]:

$$\mathrm{Re}\left(\frac{\Delta r}{r}\right) = X(E)\Delta E_g + Y(E)\Delta\Gamma \qquad \textit{Eqn. 4.4}$$

where if $\varepsilon_b = \varepsilon' + i\varepsilon''$:

$$X(E) = \frac{4\pi d}{\lambda}\frac{1}{(\varepsilon'-1)^2 + \varepsilon''^2}\left(\varepsilon''\frac{\partial\varepsilon'}{\partial E} + (\varepsilon'-1)\frac{\partial\varepsilon''}{\partial E}\right) \qquad \textit{Eqn. 4.5}$$

$$Y(E) = \frac{4\pi d}{\lambda}\frac{1}{(\varepsilon'-1)^2 + \varepsilon''^2}\left(\varepsilon''\frac{\partial\varepsilon''}{\partial E} + (\varepsilon'-1)\frac{\partial\varepsilon'}{\partial E}\right) \qquad \textit{Eqn. 4.6}$$

4.2.4 $\Delta_5 \rightarrow \Delta_1$ Interband Transitions

Stahrenberg et al. [4.5] have first attempted to use the derivative model to rationalise the modified bulk contribution of the RA signal around 2.1eV. In their study they isolated the modified bulk contribution from the surface state by quenching the surface state contribution by exposing the Cu(110) surface to air. However it is believed that this method also affects the bulk related transitions and hence the surface anisotropy [4.12].

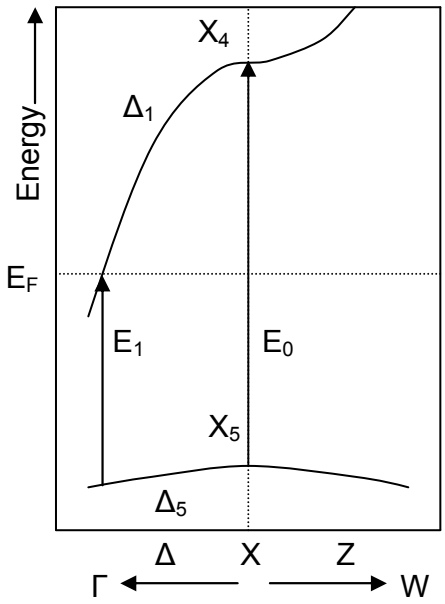

Figure 4.6: *The Copper bulk band structure around the X symmetry point.*

Sun et al. [4.12] used the derivative model as a difference model in which the surface anisotropy $\Delta\varepsilon_s$ is the difference between two rigidly shifted functions $\varepsilon_x(E,\Gamma)$ and $\varepsilon_y(E,\Gamma) = \varepsilon_x(E - \Delta E_{xy}, \Gamma - \Delta\Gamma_{xy})$. This difference model relates the shift in surface d- bands to the different atomic densities in the two crystallographic directions. *Figure 4.6* shows the band structure of copper E_1 = 2.1eV [4.31-4.32] and E_0 = 3.95eV [4.31-4.33] is the energy gap at the critical point *X*. The transitions between Δ_5 and Δ_1 dominates the imaginary part of the dielectric function, ε''. The band structure in the near surface region is shifted from that of the bulk, also a small relative energy shift in the *x* and *y* directions lead to shifts in ε'', which the derivative model equations show will produce a contribution in the RA signal. By considering these differences a large positive peak at ~2.1eV was observed as well as a small negative peak at ~4eV [4.12]. The peak was found to scale with $\Delta E_{xy} d$ so for a typical thickness *d* of 1nm an energy shift ΔE_{xy} of ~50meV was obtained.

4.2.5 Intraband Contributions

To model the intraband contributions Sun et al. [4.12] used a free electron type description as proposed by Hansen et al. [4.3] to mimic the dielectric function of

copper below the plasmon frequency $\omega_p = \sqrt{ne^2/\varepsilon_0 m_e}$. Using an effective electron mass $m_e = 1.49 m_0$ as quoted by [4.34] and an atomic density $n = 1/v_{at} = 4/a^3$ (where v_{at} is the volume of an atom and a is the lattice constant) we obtain a plasmon energy $E_p = \hbar\omega_p = 8.9\,\text{eV}$, which means the intraband contribution to the dielectric function is given by:

$$\varepsilon_D(E) = 1 - \frac{{E_p}^2}{E(E + i\hbar/\tau)} \qquad \textit{Eqn. 4.7}$$

Using $E_p = 8.9\,\text{eV}$ and a relaxation time $\tau = 6.9\times10^{-15}\,\text{s}$ as obtained from [4.34] gives a good account of the dielectric function. In the near surface region E_p and τ will be different for electrons moving in the $[1\bar{1}0]$ and [001] directions. Using $\Delta\varepsilon_D(E)$ as the anisotropic dielectric function the Drude contribution to the RA spectrum can be obtained by writing the 3-phase model in the form:

$$\left(\frac{\Delta r}{r}\right)_D = -\frac{4\pi i d}{\lambda(\varepsilon_b - 1)}\left[\frac{{E_{px}}^2}{E(E + i\hbar/\tau_x)} - \frac{{E_{py}}^2}{E(E + i\hbar/\tau_y)}\right] \qquad \textit{Eqn. 4.8}$$

The shape of the curve was found to depend on the two parameters $\Delta E_p = E_{px} - E_{py}$ and $\Delta\tau = \tau_x - \tau_y$. Sun et al.'s results were obtained by using parameters of $d = 1$ nm, $\tau_x = \tau = 6.9\times10^{-15}$, $\tau_y = 2.7\times10^{-15}$ and an increase of E_{py} by ~0.2eV with respect to E_{px}.

4.2.6 Combination of Effects

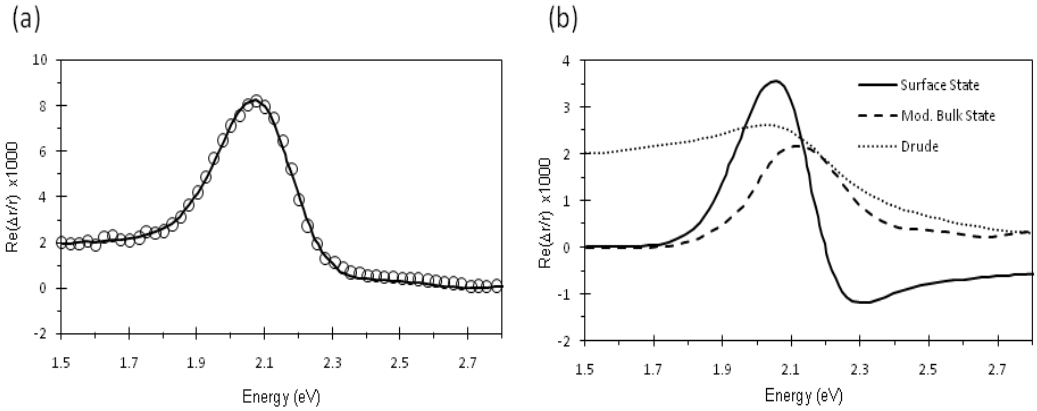

Figure 4.7: *(a): Individual contributions of the surface state(solid line), interband (dashed line) and intraband (dotted line) terms at 300K, (b): Open circles: experimental data, solid line: summation of the 3 contributions shown in (a). Reproduced from data in ref [4.12].*

This section looks at the contribution of the above effects as outlined by Sun et al. [4.12]. *Figure 4.7 (a)* shows the individual contributions of the effects as calculated by Sun and *Figure 4.7 (b)* shows the summation of these effects compared to the experimental results obtained. The absolute values of the individual values should be treated with caution as the parameters used to obtain them cannot be assessed within the model itself and certain simplifications have been made [4.12]. It is also recognised that experimental data for the electronic and optical properties is required to further back up the model theories. The surface state remains the biggest contributor to the peak and is still the best understood.

4.3 The 4eV Region

The feature at around 4eV region consists of a double peak; one main feature centred around ~4.2eV and a secondary feature at ~3.9eV. The main feature has been attributed to transitions from $E_F \rightarrow L_1^u$ in the bulk state (*Figure 4.8*); this assignment was backed up by the temperature dependence of the energy position of the feature which agrees with thermovariation optical spectroscopy data assigned to this transition [4.35]. Further support for this comes from density field theory local

density approximation (DFT-LDA) calculations of the RA spectra which find the RA signal in this region comes from bulk-state to bulk-state transitions [4.36].

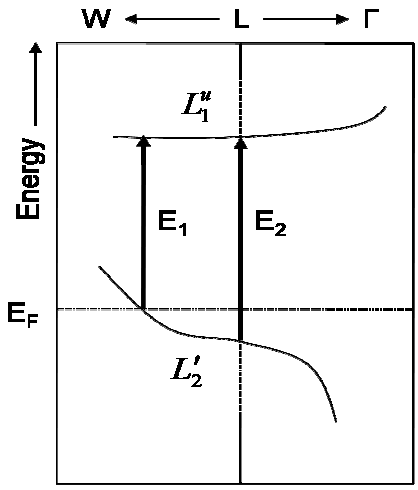

Figure 4.8: *Transitions in 4eV region: E_1 transition responsible for 4.2eV peak, E_2 transition responsible for 4.9eV peak.*

The secondary peak is only observed under certain conditions, as the feature seems sensitive to contamination and because of this was suggested to have surface state origins [4.12, 4.40].

The high energy peak at ~4.9eV has also been attributed to bulk state transitions $L_2' \rightarrow L_1^u$ [4.29] (*Figure 4.8*). This assignment has also been backed up by the thermovariation optical spectroscopy data for this transition [4.35].

This region of the RA spectrum has been found to be sensitive to numerous surface effects, steps [4.37], thermal effects [4.29, 4.37], adsorption and reconstruction [4.4] and ion bombardment [4.27, 4.29, 4.37-4.40] which is discussed in more detail later in this chapter. The sign of a peak in this region on vicinal surfaces has also been found to be influenced by step density and co-ordination of corner atoms at step edges [4.41].

4.4 The Process of Obtaining a Clean Sample

Once the sample is mounted inside the vacuum chamber it is necessary to clean it. A clean sample is obtained by repeated cleaning cycles consisting of two stages firstly ion bombardment, where the sample is bombarded with 0.5keV Ar^+ ions for a time of typically 30 minutes, and secondly annealing the sample at a temperature of 840K. This process removes any contaminants from the surface and allows the clean surface to be studied.

The layout of the chamber used in these experiments enables in situ monitoring of the cleaning process in real-time, as the ion source is mounted above the RAS window. Many chambers are not designed like this; they would require the sample to be transferred from a separate chamber or at least re-orientated. The incident ion beam is at an angle of incidence (defined from the surface normal) of 30° and the beam direction with respect to the crystallographic directions is at 45° to both the $[1\,\bar{1}\,0]$ and [001] directions unless otherwise specified.

At least one cleaning cycle consisting of ~30 minutes ion bombardment at room temperature and ~20-30 minutes annealing at 840K and subsequent cooling back to room temperature, were carried out prior to the recording of any results.

4.5 Temperature Dependence of Cu (110)

RA Spectra of the clean Cu(110) sample at temperatures of 183-773K are shown in *Figure 4.9* these results are consistent with the Cu (110) published spectra [4.12, 4.27, 4.37, 4.40, 4.42]. The 2.1eV peak can clearly be seen to decrease in intensity and shift to lower energy with increasing temperature; also the 4.2eV peak can be seen to reduce in intensity with increasing temperature and seems to shift to lower energy. The secondary feature at around ~3.9eV becomes less pronounced with increasing temperature until ~473K at which point the peak is no longer observed.

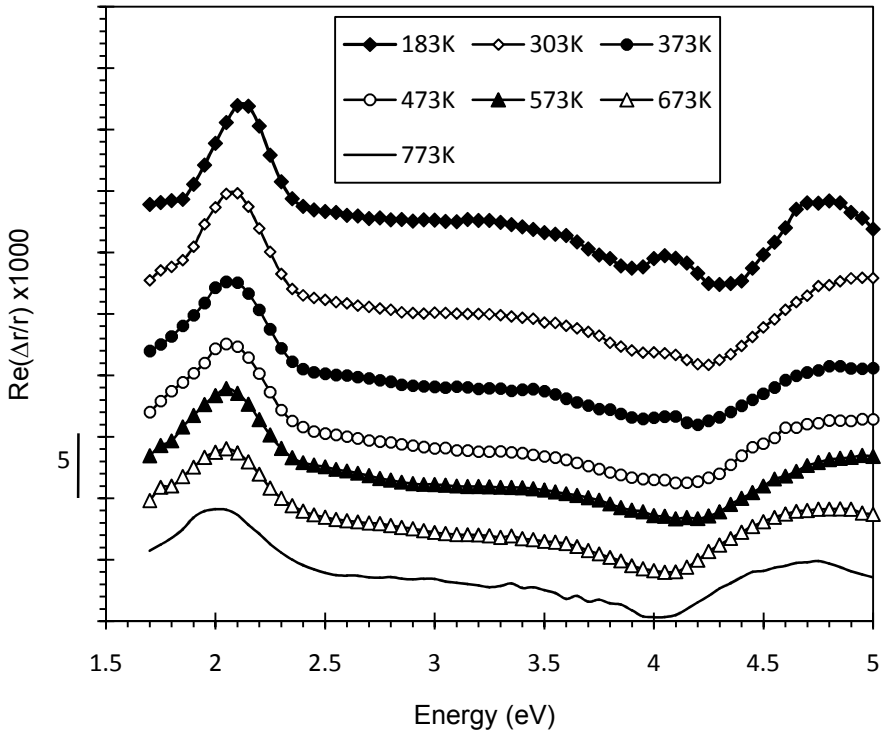

Figure 4.9: *RAS of clean Cu (110) as a function of temperature (Spectra shifted vertically for clarity).*

The temperature dependence of the binding energies of the electrons at the $\overline{Y}$ point for the occupied and unoccupied states have been found using angle resolved ultraviolet photoelectron spectroscopy (ARUPS) [4.16] and inverse photoemission spectroscopy (IPES) [4.43]. The bottom of the parabola-like occupied state was found to shift upwards with temperature according to:

$$E_0(T) = -(0.51 \pm 0.015)eV + (2.6 \pm 0.2) \times 10^{-4} eV/K \times T \qquad \textit{Eqn. 4.9}$$

while the position of the unoccupied state has a negligible shift. From these observations we infer that the surface state contribution of the peak should shift by a similar amount to that of the occupied state. Indeed the shift in position of the RA signal was found by Sun et al. [4.12] to be:

$$E_0(T) = -(2.15 \pm 0.1)eV + (2.25 \pm 0.2) \times 10^{-4} eV/K \times T \qquad \textit{Eqn. 4.10}$$

This temperature dependence is indeed very similar to that of the occupied state although there are other contributions to consider; including the thermal behaviour of the bulk band related electrons, Straube et al. [4.16] suggested that these two contributions (thermal effects of the surface state and the bulk) should separate out at higher temperatures due to the shifting of the surface state contribution, which could explain the broadening effect with increasing temperature seen in *Figure 4.9*.

The reduction of intensity of the 2.1eV peak can be explained by the movement of the occupied state upwards with temperature. It is becoming depopulated as it approaches the Fermi level; this results in fewer transitions between the states, and hence a reduction in surface state intensity.

The behaviour of the 4eV region has not been as fully investigated as that of the 2.1eV region but can be explained by the shifts of bulk bands as reported by Winsemius et al. [4.35].

As the temperature of the sample is increased above ~900K the creation of adatom-vacancy pairs becomes the dominant process in surface disordering [4.44-4.45] and at ~1000K [4.46-4.47] the surface undergoes a roughening transition whereby steps are formed on the surface and this seemingly contributes to the absence of a 2.1eV peak above these temperatures [4.27] as observed in the results of Martin et al. [4.37].

4.6 Ion Bombarding Cu(110)

Ion bombarding (also known as sputtering or etching) allows a degree of controlled modification of the surface on the nanoscale; it is known that the ion bombarding of Cu(110) at non grazing angles of incidence induces ripples on the surface [4.48].

The ion bombarding process carried out in these experiments was done by firing 0.5keV Ar^+ ions at the sample from an incidence angle of 30° off normal and monitoring the current obtained between the sample and earth. The current obtained

was 10μA over an area of approximately 5cm^2 yielding a flux of 1.25×10^{13} ions cm^{-2}s^{-1}. Room temperature for the purpose of these experiments is taken to be 303K.

The results taken in this section are consistent with those reported previously elsewhere [4.37-4.40].

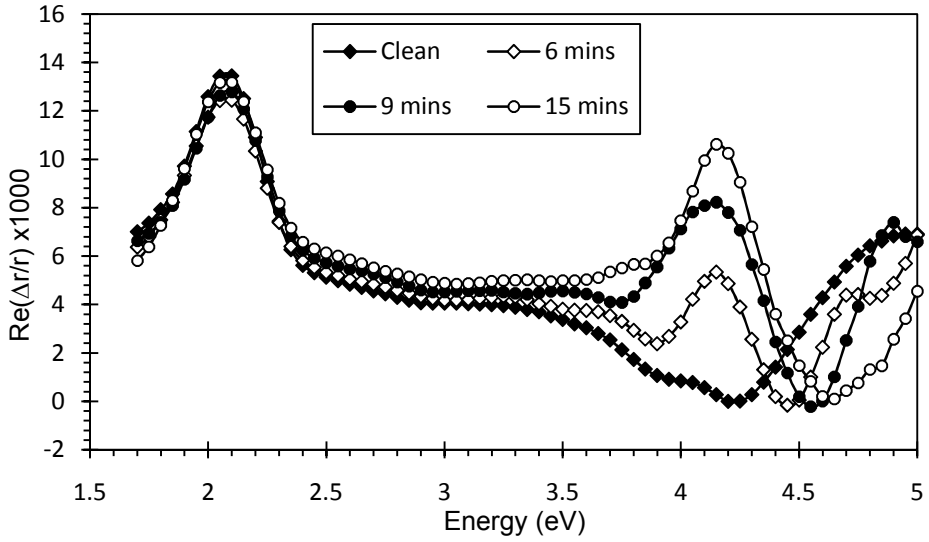

Figure 4.10: *RA Spectra of Cu (110) ion bombarded at 303K as a function of bombardment time.*

The 2.1eV peak remains unchanged throughout this bombardment process whereas the region at around 4eV is changed significantly as can be seen from *Figure 4.10*. This region goes from having two negative peaks to having one positive peak over a period of 30 minutes continuous bombardment. This feature is thought by Bremer et al. [4.38] to be as a result of an increased number of steps and vacancies on the surface. The growth of this feature is approximately linear initially until it reaches a saturation point after approximately 15 minutes. It has been suggested [4.40] that the intensity of this feature could give a measure of the number of defects on the surface. It is not known how many defects are created on the surface by one impinging ion but it has been suggested a yield of up to 5 vacancies per ion [4.49], although a value of 1-2 seems more commonly reported [4.50] for systems similar to the one used in this work. This would mean that the number of vacancies on the surface is proportional to the number of ions incident on the surface. Adatoms are also created

by the ions impacting on the surface, but as etching is primarily an erosive technique their numbers should be less than the number of vacancies. The process of ion bombarding leads to ion induced diffusion [4.51], where the mobility of defects is governed by Arrheneus like behaviour [4.52]:

$$D = D_0 \exp\left(\frac{E}{k_B T}\right) \qquad \textit{Eqn. 4.11}$$

where D is the diffusion co-efficient, D_0 is a constant, known as the diffusivity (or often referred to as the pre-exponential factor), E is the energy barrier for the process occurring whilst k_B is Boltzmann's constant and T is temperature. The energy barrier will differ for diffusion of different particles (adatoms or vacancies) and in different environments such as motion in different crystallographic directions or motion over/around step edges.

4.6.1 Annealing

Once the cycle of ion bombardment is complete the surface is 'damaged' and it is necessary to anneal the surface to repair it and restore surface order and periodicity. The heat provided by the annealing process gives energy to the atoms on the surface enabling them to move around and fill the vacancies. It should be pointed out that the diffusion process occurs via a random walk [4.53]. Atoms have no knowledge of which direction to go to repair a defect; motion is considered to be a series of independent hops, with the previous hop having no effect on the next. For the simplest (1-dimensional) case, there is an equal probability of an atom jumping to an identical spot to the left or to the right; this probability is determined by the energy barrier of the process. In the more complex cases of real surfaces there are a number of different energy barriers corresponding to movement in different directions, meaning some hopping processes will be more likely to occur than others. The RA Spectra measured during this annealing process are shown in *Figure 4.11*.

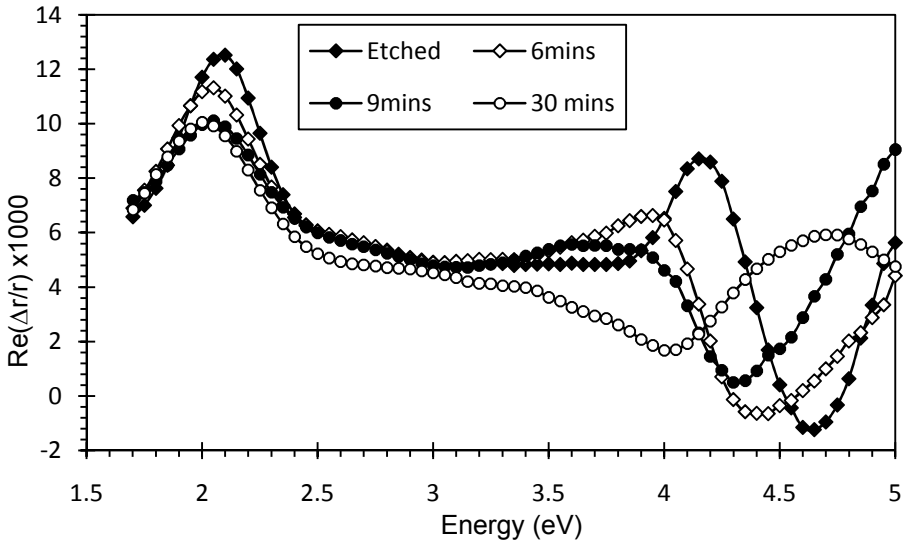

Figure 4.11: *RA spectra of the Cu (110) surface being heated from room temperature to 773K as a function of time. Spectra of sample etched for 30mins at 303K is shown for comparison.*

Comparison of the etched and annealed spectra in *Figure 4.11* shows that the 2.1eV peak has been reduced in intensity and shifted to lower energy. This is due to the temperature dependence of this feature as described previously. The peak intensity is initially higher than would be expected for Cu(110) at 773K because it was not possible to take these measurements under steady state conditions. The positive peak at 4.2eV of the etched spectrum also appears to shift to a lower energy and decreases in intensity before eventually resembling that of a clean spectrum at this temperature, a process which is rapid at first but slows down later on. A likely explanation for this is that initially there are a lot of defects on the surface so it is easy for an adatom to find vacancies to recombine with. As more vacancies are repaired the probability of an adatom finding a vacancy is reduced an hence less adatom-vacancy interactions occur in a given time.

4.7 Ion Bombarding at Various Temperatures

The effects of ion bombarding and subsequent annealing seem to have opposing effects on the spectrum; the ion bombarding causes the creation of a positive peak in

this region while the effect of the annealing causes this peak to be destroyed. If the two effects are combined these processes would seemingly compete.

4.7.1 High Temperature Ion Bombarding

In these experiments the clean sample was heated to the appropriate temperature and left for 30mins to allow the sample to reach steady state conditions so that no further thermally induced changes would be observed in the experimental results. The sample was then ion bombarded constantly for 30 minutes with spectra recorded every 3 minutes during this time. The results are shown below in *Figure 4.12*.

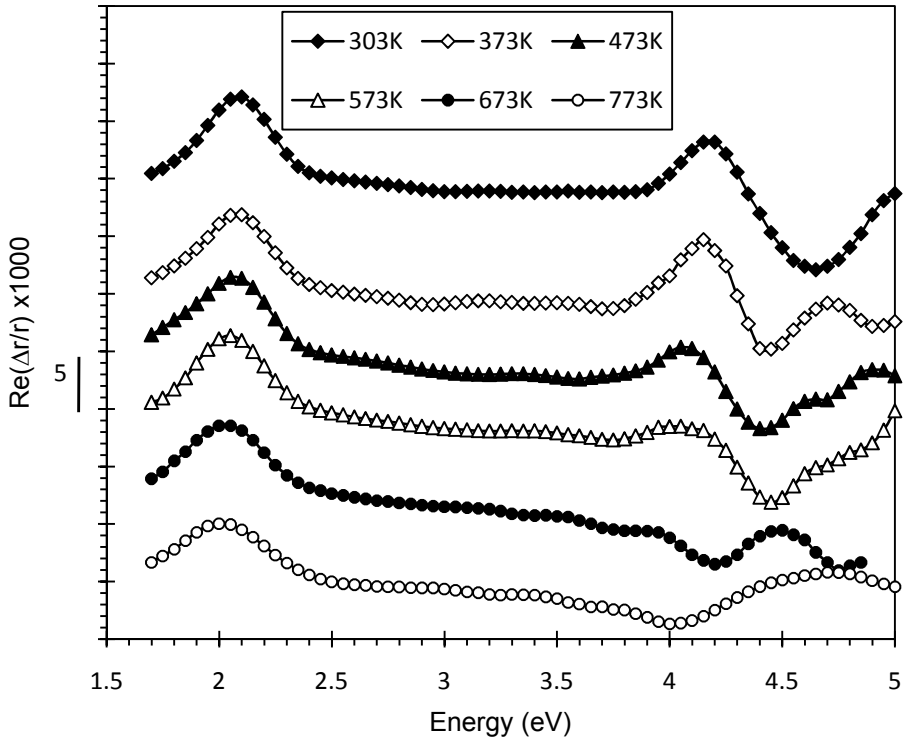

Figure 4.12: *The RA response of Cu(110) after 30mins ion bombarding at elevated temperatures.*

The effects of ion bombarding decrease with temperature; for temperatures up to 473K there is a clear positive peak in the 4eV region of the spectrum as a result of the bombarding. For higher temperatures 573K and 673K there are still some changes in this region of the spectrum from that of the clean surface; there is no large

positive peak, but the negative features of the spectrum have decreased in intensity and are now more flat. The spectrum recorded at 773K shows no difference from the clean spectrum at the corresponding temperature, so at this temperature the thermal effects dominate the effects of the ions. This would seemingly imply that the mobile particles on the surface have sufficient energy and are present in sufficient numbers to repair any damage caused by the ions instantaneously.

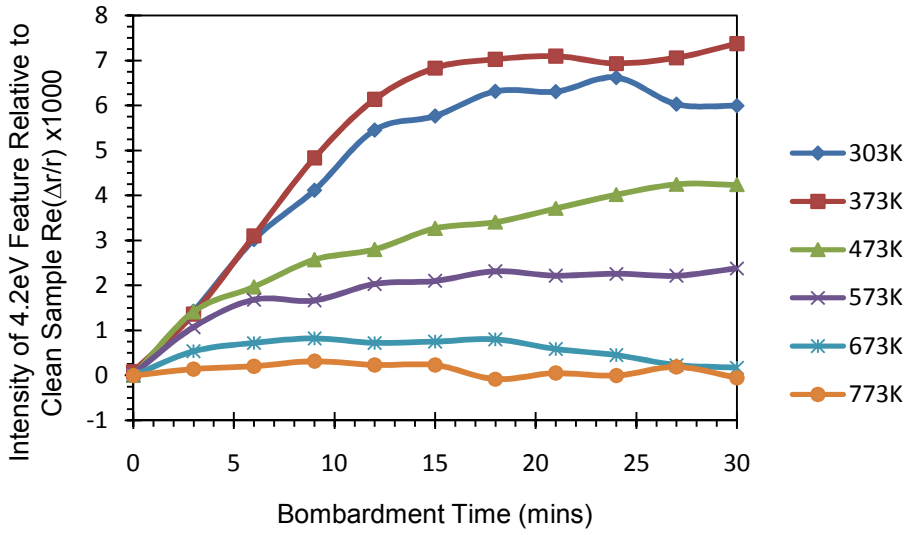

Figure 4.13: *The change in the RA response of Cu(110) at 4.2eV as a function of bombardment time.*

Figure 4.13 shows the change in intensity of the 4.2eV feature as a function of bombardment time. The greatest change in intensity is observed at 373K where the peak intensity reaches a saturation point after ~15mins whilst none of the other temperatures above this reach a saturation point during the time scale shown (except that of the surface at 773K which is unchanged by the bombardment process). This result is consistent with those taken by MacDonald [4.40] on a similar surface. The smaller changes in intensity at higher temperatures are expected due to the increased numbers and mobility of adatoms on the surface as the temperature increases; more diffusion increases the probability of adatom-vacancy recombination hence reducing the effects of ion damage.

The fact that the peak reaches a higher intensity at 373K than at 303K is however not consistent with this argument, which suggests a different mechanism or other restrictions are placed on the system below 373K. MacDonald [4.40] cited work on Ag(100) by Costantini et al. [4.54] as a possible explanation. Costantini et al. [4.54] reported that surface roughness due to ion bombarding Ag(100) was maximised at ~400K because for temperatures below 440K the adatoms created on the surface cannot balance out the effects of ion bombarding because they are not present in sufficient numbers; the ion bombarding being an erosive process means many atoms ejected from the surface by the ions are "lost" and not available to repair the surface. The higher energy barrier for the removal of an adatom from a step edge site as opposed to a kink site, means adatoms contribute to the formation of straight step edges. For the lower temperatures a low rate of diffusion means that adatoms and vacancies are localised around the impact site, resulting in layer by layer errosion. The erosion to a layer below will not begin until almost all the layer above has been eroded; as a result there is little surface roughness. An increase in energy means more diffusion and adatoms and vacancies are no longer localised to the impact site meaning the etching can produce deeper features and surface roughness will increase. For temperatures above ~440K more adatoms can evaporate off step edges leading to an increased density of adatoms on the surface which with increasing temperature will eventually out number the vacancies.

4.7.2 Low Temperature Ion Bombarding

The response of the system upon ion bombardment varies with temperature; it would seem likely that studies at lower temperatures may give extra information as to the behaviour of the surface.

The RA response of the 4eV region during ion bombardment at 183K is similar to the changes observed at room temperature in that again the negative peak becomes positive as bombardment time increases (*Figure 4.14*). The major difference between ion bombarding at low temperature is the erosion of the 2.1eV peak. Throughout all the other bombarding experiments this peak has remained at the same intensity as the clean spectrum for the corresponding temperature. The peak on the clean spectrum at

183K is more intense than at any other temperature reported in this work. Also the rate at which it disappears is vastly different to the other changes observed in the 4eV region of the spectrum.

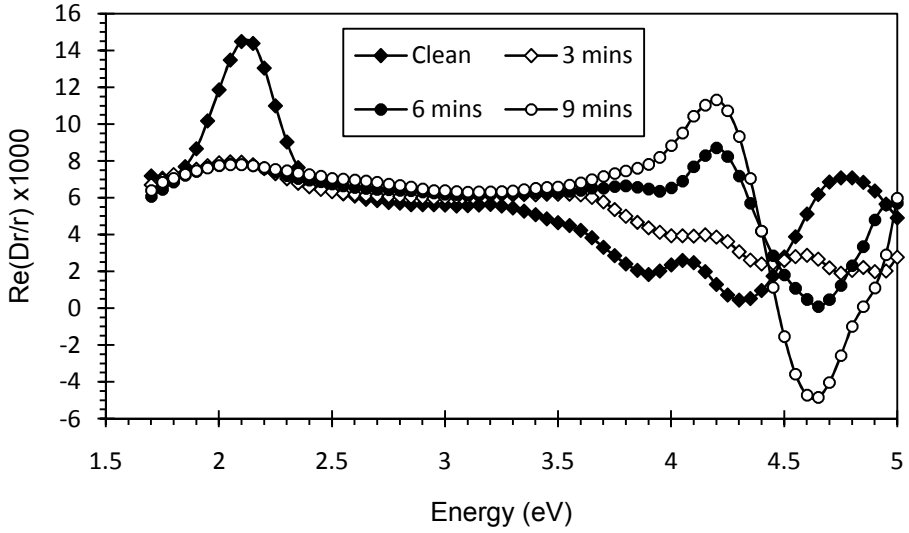

Figure 4.14: *The RA response of Cu(110) during ion bombarding at 183K.*

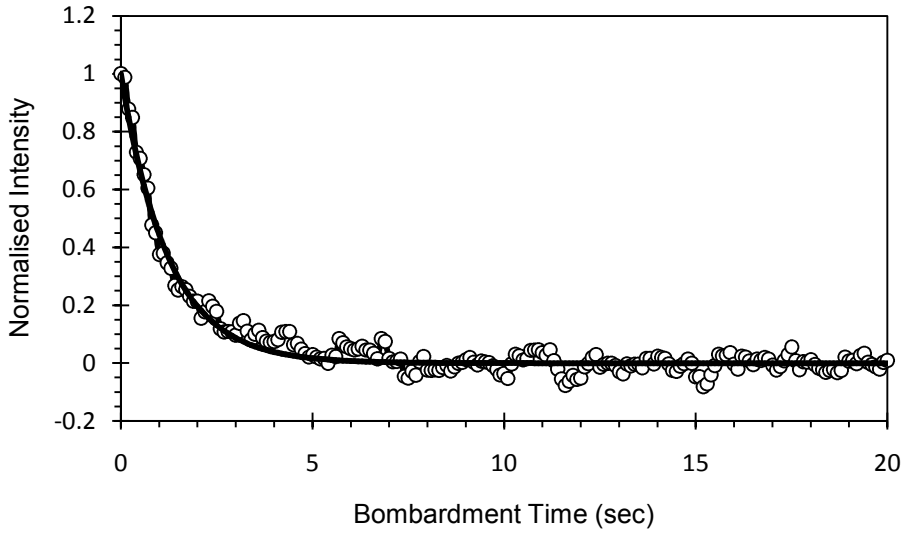

Figure 4.15: *The RA response of the 2.1eV peak as a function of ion bombardment time. Open circles denote recorded data, solid line denotes an exponential fit to the data (for simplicity the fit will be used in data analysis).*

Figure 4.15 shows the reduction in intensity of the peak as a function of time. The peak also decays in a non-linear fashion implying the cause of the reduction in

intensity of this peak is not due to defect coverage. In fact given the ion flux used and assuming two defects are created per ion the defect coverage would be ~0.12ML.

4.7.3 Patch Sizes

Inverse photoemission spectroscopy (IPES) results of Heskett et al. [4.55] studying the unoccupied state involved in the surface state transition on copper, show that the state is destroyed by ion bombardment at temperatures ~170K. The time taken for the peak to be destroyed in Heskett et al.'s experiments is ~120 sec which is around 12 times longer than observed in these RAS experiments. This difference can be attributed to the difference in flux; our flux is 15 times that of the one used by Heskett et al., so in this work the defects on the surface are created at a rate 15 times faster. Heskett et al. observed that the peak was destroyed at a faster than linear rate, and predicted a defect coverage of ~0.12ML was sufficient to completely destroy the peak, by making the assumption an atom could not contribute to the electronic state unless it was on a clean $N \times N$ patch, thus resulting in a faster than linear decay of the unoccupied state. Heskett et al. ran Monte Carlo simulations to find the patch size which matched best the experimental data; a 12×12 patch was found to be best. The consistency of these results with those of Heskett et al. [4.55] confirm that the Cu(110) 2.1eV peak has a large contribution from optical transitions between surface states, which is destroyed in the ion bombarding process at low temperature due to the destruction of the unoccupied state participating in the transition. The fact that the peak is destroyed and there remains little or no trace of any feature at 2.1eV once the surface has been bombarded means that this feature is either solely due to surface state transitions or the other two contributions to this feature (the interband and intraband contributions) outlined by Sun et al. [4.12] are also destroyed at a similar rate. This would seem unlikely as the feature at ~4.2eV also has bulk origins [4.36] and this changes on a timescale of the order of 10 minutes not 10 seconds as can be seen from *Figure 4.14*.

A non-linear reduction in the surface state peak intensity with coverage was also observed by Sun et al. [4.11] in experiments documenting the adsorption of CO onto

the Cu(110). Sun et al. attribute this behaviour to the depolarisation of the associated surface states in the vicinity of the adsorbed CO molecules which occurs due to the isotropic scattering of surface state electrons from these adsorbates. This effect causes the anisotropy of the *p*-like surface state in the region surrounding the CO molecule to be lost, resulting in the decrease of the surface state contribution to the RAS peak in this surface region. Sun calculated that a single CO molecule could quench the local contribution to the RAS peak over an area of ~1000Å^2.

Although these two effects are different in their origins their effects are similar in RAS terms, and the defects on the surface (adatoms or vacancies) cause the quenching of surface state transitions at a similar rate, - converting between the two notations (using the area of a unit cell) the effect observed by Sun et al. [4.11] would correspond to a patch of ~10.5×10.5 atoms.

In this work the basic Heskett approach is followed; the application of patch sizes to the destruction of the peak in an attempt to explain the non-linear decay behaviour. However some alterations are made to the model used by Heskett et al. [4.55]. Most notably the model used in this work assumes that sites cannot contribute to the RAS peak if there is a defect in any of the sites in the $N\times N$ sites around which the patch is centred. (This is a minor variation of the model used by Sun et al. [4.11] in that the patches are square rather than circular.) If a defect site is present then all the sites within a patch area $N\times N$ around it cannot contribute to the peak (as the defect site will be in their patch). The Heskett model considered the clean sites by fitting patches of clean atoms around the defect sites; this meant for very low coverages a single defect may not quench any adjacent sites. Hence the reduction in peak intensity is initially very slow with this model. A comparison of the two models is given in *Figure 4.16*.

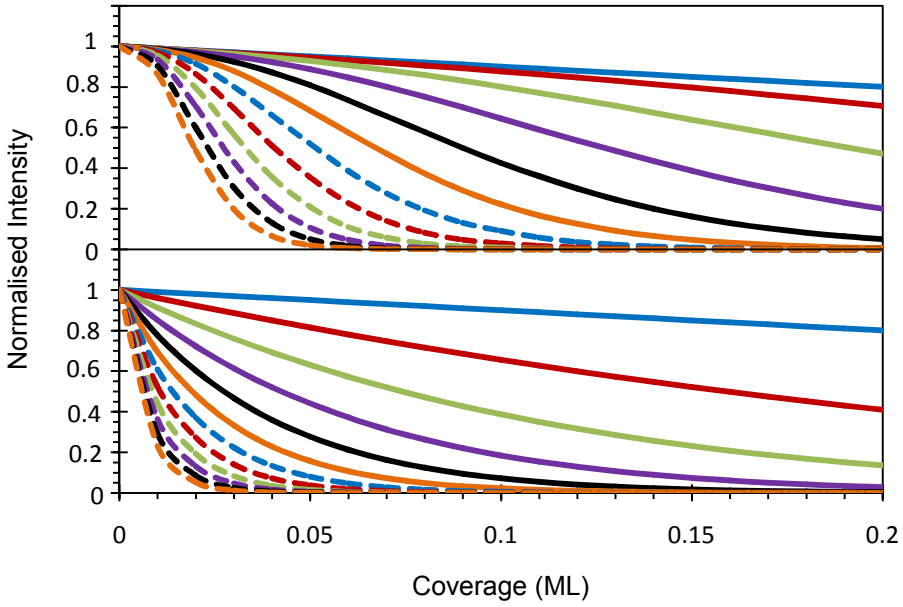

Figure 4.16: *Comparison of the model used by Heskett et al. [4.55] for 1 defect per ion (upper panel) and the model used in this work (lower panel); for patch sizes of 1 (solid blue line), 2 (solid red line), 3 (solid green line), 4 (solid purple line), 5 (solid black line), 6 (solid orange line), 7 (dashed blue line), 8 (dashed red line), 9 (dashed green line), 10 (dashed purple line), 11 (dashed black line) and 12 (dashed orange line).*

Taking *Figure 4.16* into account, Heskett's 12×12 patch size corresponds to a patch size of between N=4 and N=9 with the method used here matching N=4 at low coverages and N=9 at high coverages. In the new model it would be best represented by a patch size of N=7. Physically, the reason a particular Heskett patch size corresponds to a smaller Sun patch size can be attributed to the fact that the Heskett model assumes there is a RAS intensity from sites *anywhere* on an $N \times N$ patch, whereas RAS-active sites in the Sun model must also be $N/2$ spacings away from the edges of these clean patches.

It is recognised that the area destroyed by a defect is not necessarily square (if fact it is fairly unlikely): what is important is the area contained within that patch. A square is simplest to work with computationally; other shapes e.g. a circle with the same area would yield similar results. *Figure 4.17* shows the area quenched by a defect for a patch size of N=5.

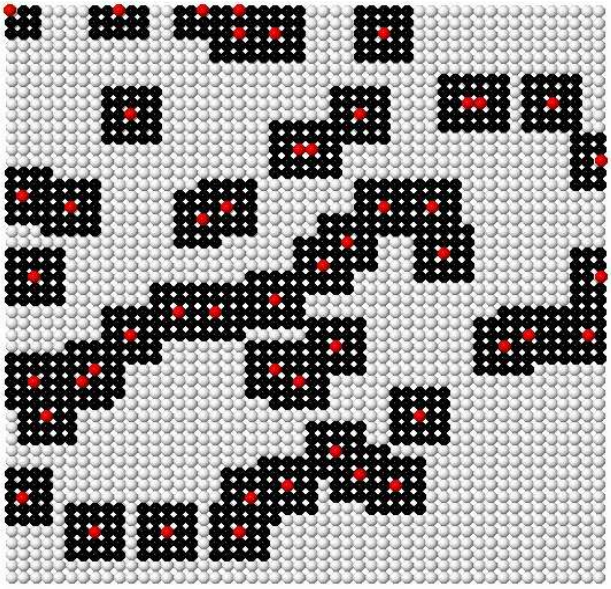

Figure 4.17: *A visual representation of the area quenched by defects on a 50 × 50 atom terrace for a defect coverage of 0.02ML. Red dots denote defect sites, black dots denote sites whose contribution has been quenched by a defect for a patch size of N=5.*

Heskett et al.[4.55] creates defects randomly upon the surface using an average sputtering yield of 2 atoms per ion and defects created by the same ion are in adjacent atomic sites on the surface. This condition causes an average of 2 defects per patch and suggests the minimum defect coverage to completely destroy the peak is ~0.12ML whereas if the condition of defects created by the same ion being adjacent were removed (or a sputtering yield of 1 defect per ion was used) then the minimum defect coverage to destroy the peak would be approximately half that of Heskett's reported value, around 0.06ML. Such conditions have a dependence on the molecular mass of the bombardment ions; heavy ions such as Xenon or Krypton cause vacancies to be localised to the impact site while lighter ions produce a less localised distribution of defects [4.50]. As this work uses Argon ions it is therefore assumed that defects are not localised to the impact site but are distributed randomly with respect to one another.

In a manner similar to that of Heskett [4.55] the defect coverage (c) at a given time can be obtained using:

$$c = \frac{N_I Y t}{10^{15}} \qquad \text{Eqn. 4.12}$$

where N_I is the number of ions per second: 1.25×10^{13}, Y is the sputter yield (the number of defects created per ion) and t is bombardment time. Therefore for different sputter yields patch sizes can be fitted.

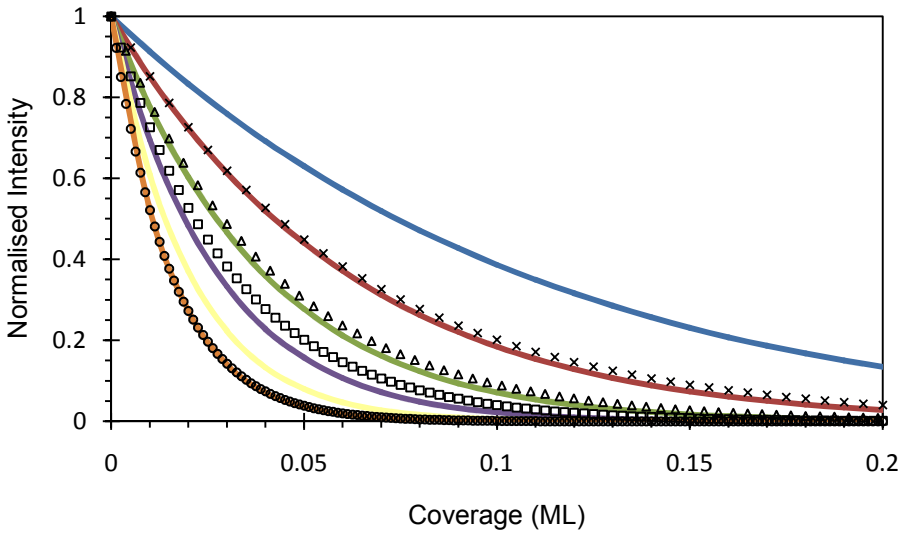

Figure 4.18: *2.1eV data at 183K converted into defect coverage for Y=1 (circles), Y=2 (squares), Y=3 (triangles) and Y=4 (crosses). Compared with patch sizes of N=3 (blue), N=4 (red), N=5 (green), N=6 (purple), N=7 (yellow) and N=8 (orange).*

Figure 4.18 shows that to destroy the 2.1eV peak requires either a lot of defects or a large patch size; the larger the patch size the less damage is required. As both adatoms and vacancies can quench the surface state both must be considered. Previous studies [4.50] indicate that the number of vacancies produced is ~2 per ion. In order to create a single atomic vacancy an adatom must be ejected which suggests a sputter yield of 4 (2 adatoms and 2 vacancies). However we must remember that sputtering is an erosive technique, meaning the number of vacancies must out number the number of adatoms; hence some of the adatoms created are 'lost'. A sputter yield of 3 (2 vacancies and 1 adatom) is more realistic, from *Figure 4.15* this would correspond to a patch size of N=5.

Ion bombarding at room temperature and then cooling the sample to 183K does not see the 2.1eV peak destroyed. The spectrum behaves in a similar manner to that of the clean sample when cooled; the 2.1eV feature increases slightly in intensity while the rest of the spectrum remains unchanged. The comparison of this behaviour with the behaviour seen after ion bombarding at 183K, demonstrates that it is not simply the case of combining low temperature and ion bombardment which leads to these effects but the whole mechanics of the system depend on the temperature at which the ion bombardment occurs.

Perhaps significantly the analysis above ignores any diffusion or repair effects occurring on the surface. Any such effects would mean *Figure 4.18* is overestimating the defect coverage and hence underestimating the patch size. It is not known if the level of diffusion occurring on the surface at 183K is significant or not. In order to gauge some indication of the extent to which diffusion-induced repair occurs, results for the same experiment carried out at different temperatures are shown in *Figure 4.19*.

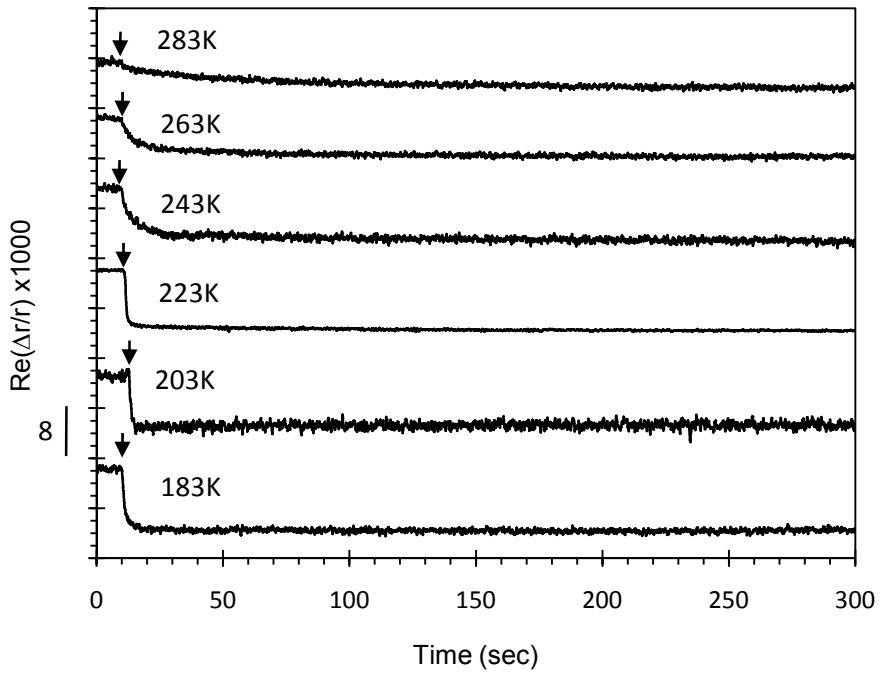

Figure 4.19: *The RA response of the 2.1eV peak as a function of ion bombardment time for different temperatures. Arrows denote time at the ion gun was switched on.*

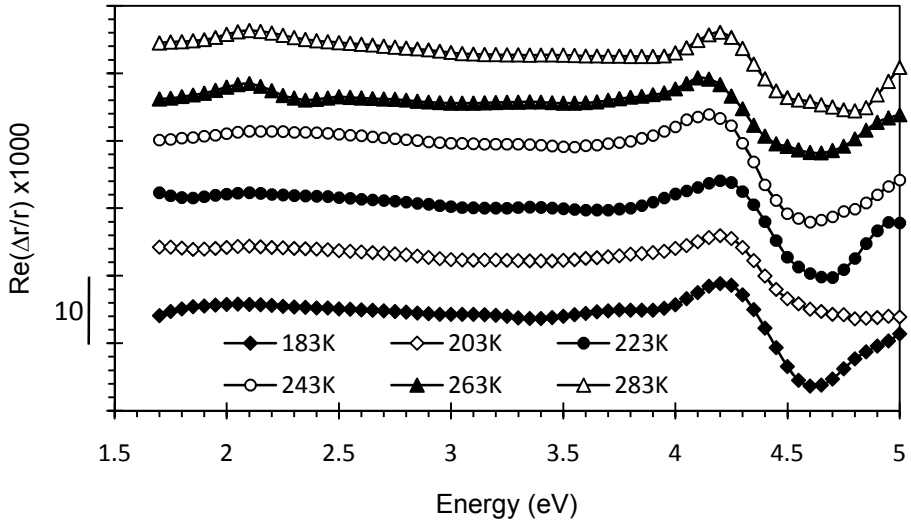

Figure 4.20: *The RA response of Cu(110) after ion bombarding for 30mins at low temperatures.*

The destruction of the 2.1eV peak at 183K takes approximately 10 seconds and for temperatures up to 243K there is little change in this time. At 263K this time has increased to approximately 15 seconds. By a temperature of 283K the peak can no longer be fully destroyed on this time scale; its intensity has been significantly reduced, but a peak is still visible (*Figure 4.20*). As the ion bombard conditions are identical in each case, the difference must be due to the effects of temperature. These effects oppose the destruction on the peak and put up significant resistance against the effects of the ions. By 303K the opposition to the ions is enough to prevent any destruction of the peak on this timescale.

4.7.4 Diffusion

In order to investigate any diffusion effects, consideration must be given to the different types of diffusion that could be occurring on the surface. A survey of the literature allows us to find values of the energy barriers for diffusion processes on the surface of Cu(110); perhaps the most comprehensive lists are the simulated values of Stoltze [4.56]. Stoltze [4.56] gives a good overview of the energy barriers of various diffusion processes on the surface a summary of which is shown in *Figure 4.21*.

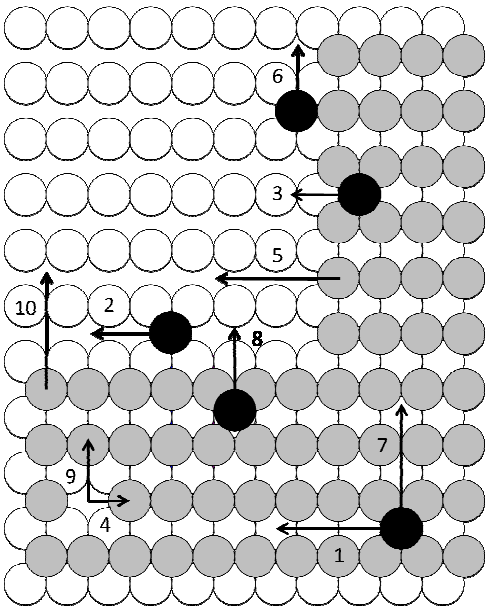

Process	Description	Barrier (eV)
1	110 Terrace diffusion	0.29
2	Along 110 step	0.31
3	Over 001 step	0.48
4	110 vacancy diffusion	0.51
5	Atom out of 001 step	0.53
6	Along 001 step	0.74
7	001 terrace diffusion	0.83
8	Over 110 step	0.84
9	001 vacancy diffusion	0.92
10	Atom out of 110 step	1.17

Figure 4.21: *Diffusion energy barriers for hopping processes on Cu(110) obtained from Ref. [4.56]*

The values in *Figure 4.21* while not taken as absolute (as values in the literature vary); give an indication of the diffusion processes occurring on the surface and which of these will dominate. Two important pieces of information can be gathered from this data; firstly the lower energy barriers of adatom processes compared with vacancy processes mean that adatom diffusion is the most prevalent, secondly diffusion along the open channels (110 direction) dominates the diffusion processes occurring on the surface. This being the case, for the work in this thesis when considering diffusion, only diffusion of adatoms along the open channels (process 1) is considered. A further survey of the literature finds other values for process 1 as being 0.23eV [4.57-4.59], 0.24eV [4.60] and 0.25eV [4.61]. At this point it is worth drawing the reader's attention to the fact that these values (except for processes 5 & 10 in *Figure 4.21*) are for the diffusion of an already created defect on the surface. Their origins are generally unimportant; however for this section we will consider that they have been created by the ion bombardment process (The coverage of thermal adatoms will be negligible at 183K, and most likely also at room temperature). In the case of processes 5 & 10 in *Figure 4.21* these atoms are not adatoms; in order to diffuse they must first break away from the surface, hence the

values for these processes contain both the formation and diffusion energy barriers which must be overcome in order for atom to become mobile[4.62].

The effects of adatom diffusion on the surface were considered, using *Eqn. 4.11* and using typical values of D_0 and E which were 0.0625cm^{2}s^{-1} and 0.23eV respectively. The energy barrier of 0.23eV relates to diffusion of adatoms in the open channels, other processes (such as vacancy diffusion) have sufficiently high energy barriers that their influence is deemed irrelevant. For a given temperature T *Eqn. 4.11* can calculate the diffusion rate, and *Eqns. 4.13 & 4.14* [4.63] can then be used to determine the number of hops per second, a method outlined in Reference [4.64].

$$x = Dt \qquad \text{Eqn. 4.13}$$

$$\langle x \rangle = \sqrt{Dt} \qquad \text{Eqn. 4.14}$$

where x is the total distance (cm), D is the diffusion coefficient (cm^{2}s^{-1}), t is time (s) and $\langle x \rangle$ is the average displacement (cm) in time t. From this the number of hops per second from one site to the next (atomic spacing 2.55Å), at a temperature of 183K is 6709, with the average displacement 81 hops per second.

In order to simulate the effects of low temperature ion bombardment, a sputter yield of 3 defects per ion (2 vacancies and 1 adatom) is applied as a function of time. All the defect sites are created randomly and the positions of vacancies are fixed. Adatoms are allowed to diffuse at the rate outlined above; when an adatom and vacancy coincide they recombine thus reducing the total number of surface defects. In order for an adatom to repair a vacancy it must be able to hop to a defect site; however this is made easier by the fact that the number of vacancy sites increases with time (thus making the average separation distance of vacancies smaller). The results are shown in *Figure 4.22*.

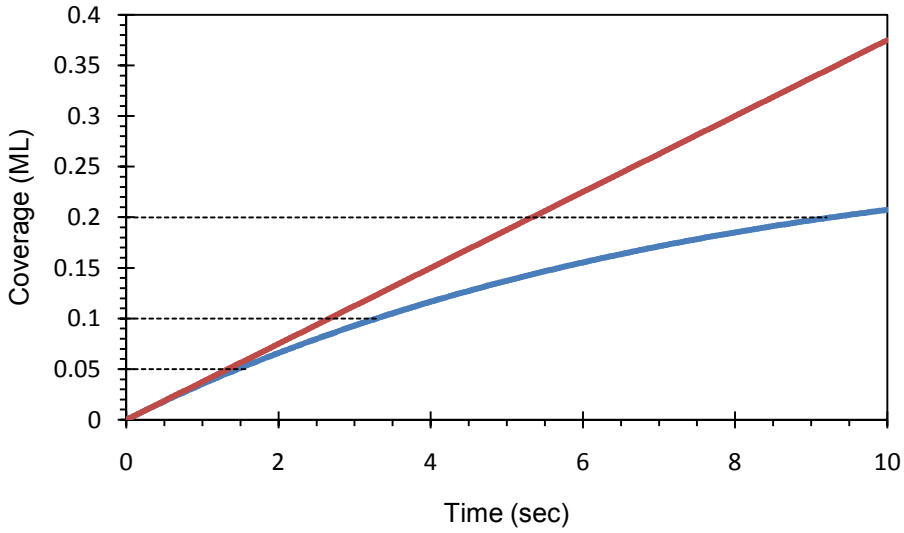

Figure 4.22: *Damage rates for ion bombardment at 183K using 3 defects per ion (2 vacancies and 1 adatom) taking into account diffusion (blue line), ignoring diffusion (red line).*

Figure 4.22 shows the comparison of the damage rates of ion bombarding at 183K for taking diffusion into account and ignoring it. Ignoring diffusion and hence repair effects means that the defect coverage is significantly overestimated for times longer than ~2 seconds. The difference between the two graphs at any given time is the repair rate. For short times <2 seconds there is little difference between the two; this is because the low defect coverage makes it unlikely that an adatom can find a vacancy to repair. As time goes on more and more defects are created making it easier for an adatom to find a vacancy. As time goes on further the damage rate tends toward a value which is approximately one third of its original value. At this stage almost every adatom can repair a vacancy in a short time, as vacancies are so plentiful and only the excess of vacancies can damage the surface (i.e. those which outnumber the adatoms available to repair them). This analysis is only valid in the low coverage regime, so in this work it is limited to 183K. However it can be used to see how diffusion impacts on the patch sizes deduced earlier, as the conversion between time and coverage is done using the number of defects at a given time. The results are shown in *Figure 4.23*.

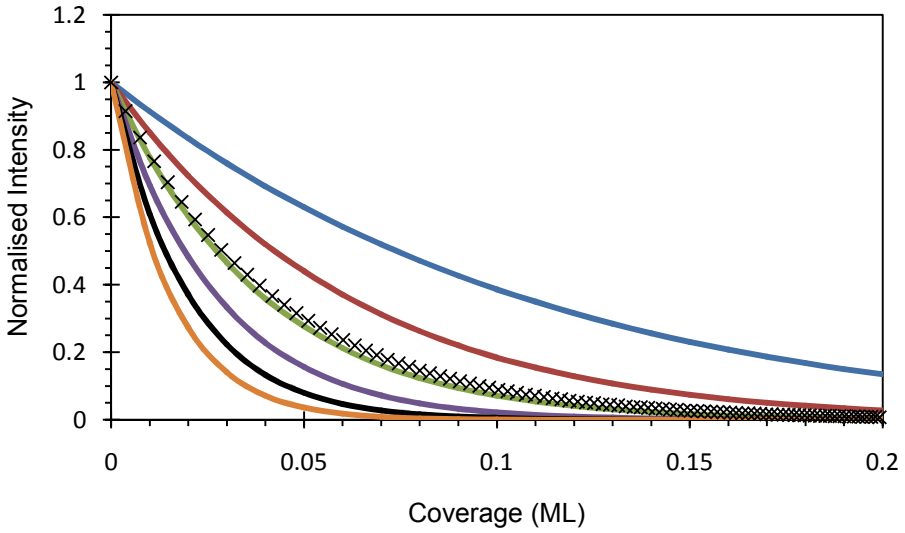

Figure 4.23: *Cu(110) 2.1eV RAS data converted into coverage taking into account diffusion from a sputter yield of 2 vacancies and 1 adatom per ion (crosses). Compared with patch sizes of N=3, (blue), N=4, (red), N=5 (green), N=6 (purple), N=7 (black) and N=8 (orange).*

Once again the data give a good match to a patch size of 5. Given the difference between two graphs in *Figure 4.22*, this seems quite surprising. A further look at *Figure 4.22* shows that up until a coverage of ~0.05ML the two graphs are approximately the same (i.e. there is little damage repaired). A coverage of 0.05ML and a patch size of 5 sees the intensity of the 2.1eV peak drop by ~72%. By the time a coverage of 0.1ML has been reached there is only a small difference between the two graphs; however by the time this coverage has been reached the peak has lost ~93% of its original intensity. By the time the repair effects occur in significant numbers at 183K the 2.1eV peak has already been almost completely destroyed so they have little impact on the results or analysis outlined earlier in this work.

4.8 Surface State Transitions as a Function of Temperature

If it is assumed at this point that the 2.1eV peak is due solely to surface states (or at least that they are the dominant contribution) then it is possible to simulate the effects of temperature on the binding energy of electrons in the occupied bands responsible for this surface state transition and hence determine the RAS response of the 2.1eV peak. In order to achieve this, an approach similar to than of Sun et al.

[4.12] is used to calculate the transitions between the occupied and unoccupied states. The shape of both bands around the $\overline{Y}$ point can be described by:

$$E(k) = E_0 + \frac{\hbar^2}{2m}|k - k_0|^2 \qquad \textit{Eqn. 4.15}$$

where k is an electron wave vector, k_0 (0,0.87) Å^{-1} [4.12] is the position in reciprocal space of the $\overline{Y}$ point, E_0 is the surface state energy at $\overline{Y}$ and m is the effective mass of the surface state electrons. The experimental values of E_0 and m for the occupied state have been found by Angle Resolved Ultraviolet Photoemission Spectroscopy (ARUPS) [4.65] to be -0.39eV and $0.26m_0$ respectively, where m_0 is the free electron mass. Similarly experimental values of E_0 and m for the unoccupied state have been found by Inverse Photoemission Spectroscopy (IPES) [4.66] to be 1.8eV and $0.8m_0$ respectively. Whilst the position of the unoccupied state remains independent of temperature, the occupied state moves towards the Fermi level at a rate of 2.6×10^{-4}eV/K.

The model used allows transitions to be induced from any position on the occupied state that is below the Fermi energy. Performing a 2-dimensional integral over the Brillouin zone around k_0 gives the imaginary part of the surface dielectric function ε_s'' as described by *Eqn. 4.16*. The model includes a Gaussian L with a temperature dependent line width $\sigma(T) = 50\text{meV} + [0.1\text{meV/K}]T$ to account for lifetime broadening [4.67-4.68]. A Fermi-Dirac distribution term F is included to account correctly for the occupation of states around the Fermi energy. At high temperatures F can allow transitions from electrons at some points above the Fermi energy. Although for Cu this Fermi-Dirac term has little effect, it plays a significant role in other materials such as Ag [4.69] but is included here for completeness. The relationship between these transitions and the imaginary part of the dielectric function is given by:

$$\varepsilon_s''(E,T) \propto \frac{1}{E^2}\int_{-\infty}^{\infty} L[E - E_f + E_i(k), \sigma(T)] \cdot F[E_i(k), T]kdk \qquad \textit{Eqn. 4.16}$$

where E_i and E_f are the initial and final energies of an electronic transition as given by *Eqn. 4.15* and all other terms are as described above.

The real part of the dielectric function ε_s' can be obtained from ε_s'' using Kramers-Kronig relations [4.70]. For comparison with experiment a complete polarisation asymmetry is assumed where $\Delta\varepsilon_s = \varepsilon_{sx} - \varepsilon_{sy} = -\varepsilon_s$. The RA response can then be calculated using the equation described by Cole et al. [4.71]:

$$\mathrm{Re}\left(\frac{\Delta r}{r}(\omega)\right) = -\frac{2\omega d}{c}\left[A(\omega)\varepsilon_s'' + B(\omega)\varepsilon_s'\right] \qquad \textit{Eqn. 4.17}$$

where d is the thickness of the surface layer; it cannot be determined because *Eqn. 4.16* contains an unknown proportionality constant. To eradicate this problem and allow comparison of simulated and experimental data, a constant scaling value was determined by comparison of the simulated and experimental data at the lowest temperature where the thermal defect coverage was negligible (see *Figure 4.24*). $A(\omega)$ and $B(\omega)$ are given by [4.71]:

$$A(\omega) = \frac{1-\varepsilon'}{(1-\varepsilon')^2 + \varepsilon''^2} \qquad \textit{Eqn. 4.18}$$

$$B(\omega) = \frac{\varepsilon''}{(1-\varepsilon')^2 + \varepsilon''^2} \qquad \textit{Eqn. 4.19}$$

where ε' and ε'' are the real and imaginary parts of the bulk dielectric function obtained from Reference [4.72].

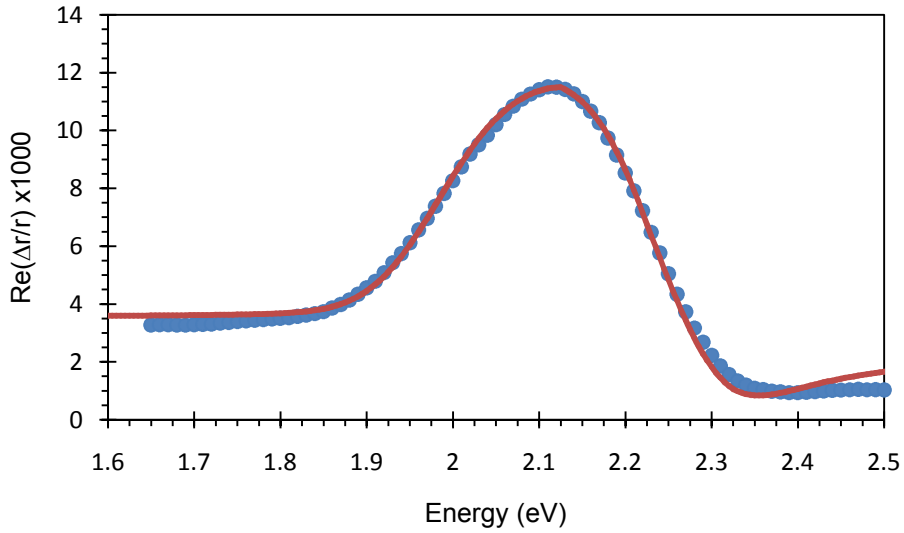

Figure 4.24: *Comparison of experimental data of Sun et al. [4.12] (blue circles) and simulated surface state response (red line) for Cu(110) at 100K.*

The simulated RAS peaks for selected temperatures are shown in *Figure 4.25*:

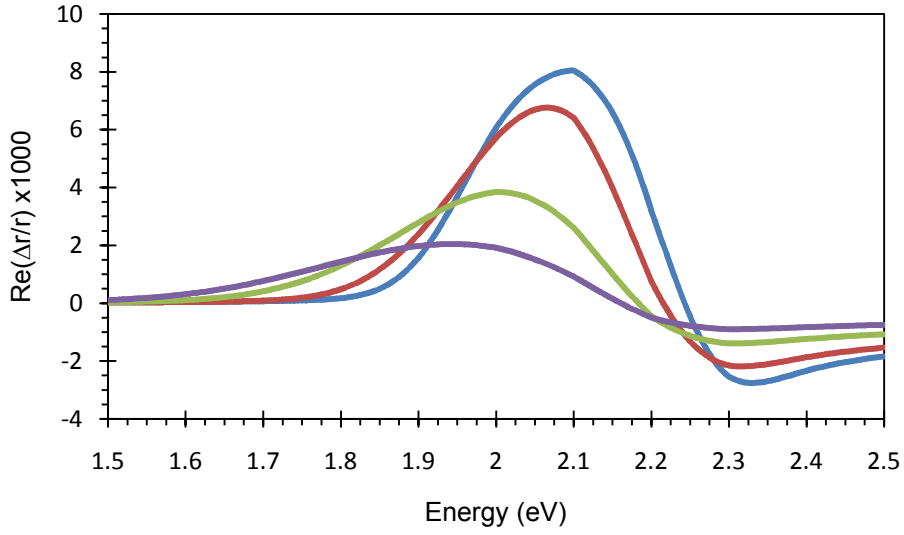

Figure 4.25: *The simulated RAS response for Cu(110) surface state contribution at 100K (blue), 303K (red), 673K (green) and 1000K (purple).*

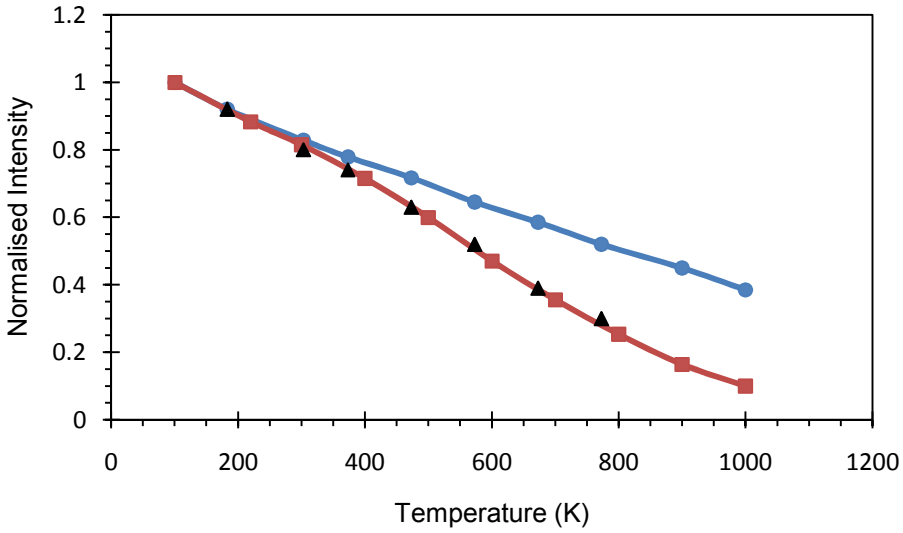

Figure 4.26: *Comparison of the experimental results from this thesis (black triangles) and of Sun et al. [4.12] (red squares) with those obtained by the model using Eqn. 4.16 and Eqn. 4.17 (blue circles).*

By normalising the experimental intensity (the area under the peak) at 100K to the theoretical results obtained from *Eqn. 4.16* and *Eqn. 4.17* as shown in *Figure 4.26*, it is apparent that this method so far (i.e. the accepted theory for the temperature dependence of the RAS surface state peak) is not sufficient to explain quantitatively the experimental measurements. Thermally created defects on the surface also need to be considered as these are known to reduce the intensity of the surface state by reducing the number of unoccupied states, just as adsorbates and ion induced defects do.

4.8.1 Thermal Defect Simulation

To take this analysis further the role of thermal defects is considered. For a given temperature T, the defect coverage c is given by the Arrhenius expression [4.73] given below:

$$c = \exp\left(\frac{-E_d}{KT}\right) \qquad \textit{Eqn. 4.20}$$

where E_d is the defect formation energy and K is Boltzmann's constant. These defects are adatoms which "boil off" step edges – most likely at kink sites (as these have the lowest energy barriers), and onto the terraces where their influence can disrupt the surface state.

The surface used to model this system consists of 10^6 atomic sites; these defects are distributed randomly with each site having an equal probability of being the site at which a thermal defect occurs. Note that although the Cu(110) unit cell is rectangular, for computational simplicity a square unit cell was used; this has no impact on the results produced. Now all these defects have been simulated the patch argument described in *Section 4.7.3* is applied. The effect of patch size on the RAS intensity for various temperatures is shown in *Figure 4.27*.

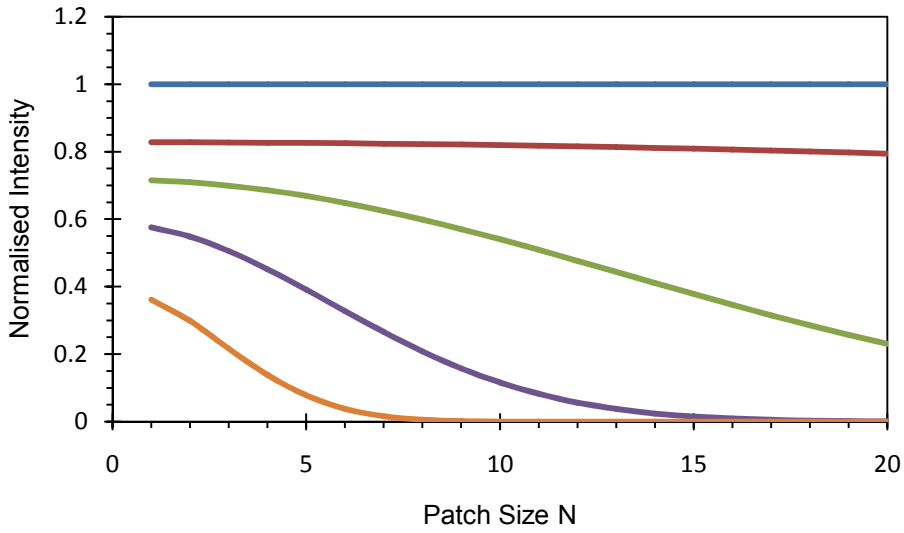

Figure 4.27: *The effect of patch size on the intensity of the 2.1eV peak for 100K (blue), 303K (red), 473K (green), 673K (purple) and 1000K (orange) for an adatom formation energy barrier of 0.24eV.*

Multiplying the two effects (the thermal shift in states and the effect of the patch) gives a new normalised peak intensity for the surface state feature, which takes into account both the reduction in the number of transitions due to the temperature dependence of the occupied state, and the reduction due to thermally induced defects on the surface. Using this it has been possible to extract values for N and E_d

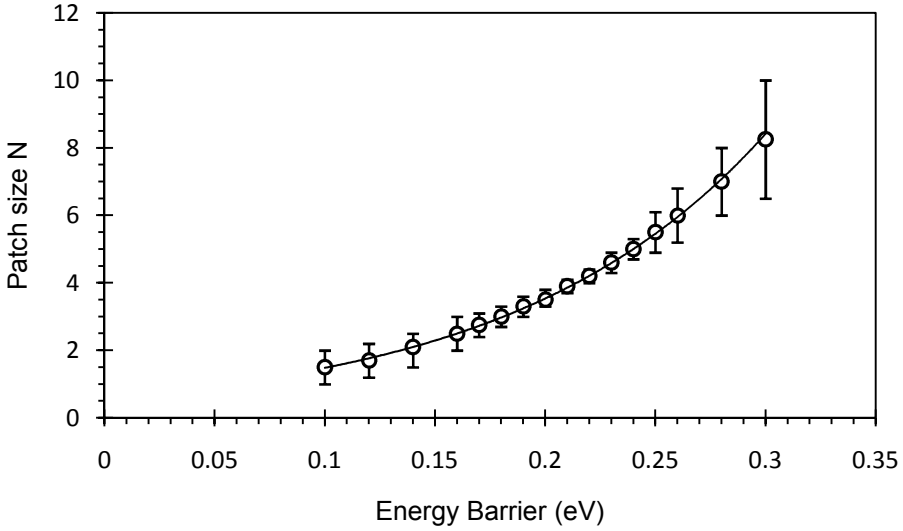

Figure 4.28: *Adatom formation energy barrier against patch size.*

Figure 4.28 shows the adatom formation energy barrier against patch size; error bars denote the range of patches the experiment curve would bisect, open circles denote average patch size values. While the separation of successive curves is smaller for high patch sizes than for lower ones making the data bisect more patches (and hence the error bars bigger) it is still true to say that the best fits are those in the middle of the graph. From this figure the range of energy barriers which provide the best fit to experimental data would be ~0.2 to ~ 0.28, which correspond to a range of patch sizes of ~3.5 to ~7. Selected fits of the data in this range are shown in *Figures 4.29 & 4.30*.

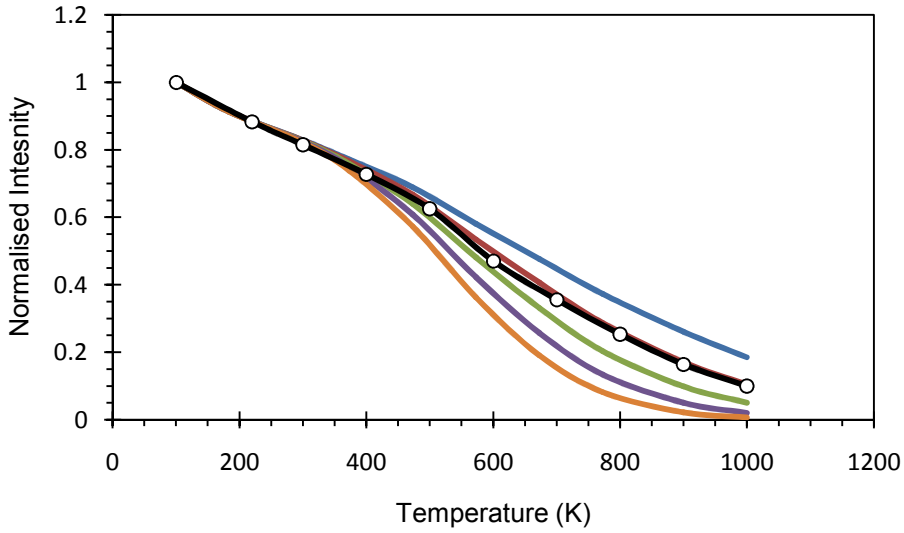

Figure 4.29: *Normalised intensity of 2.1eV peak for patch sizes of 3 (blue), 4 (red), 5 (green), 6 (purple), 7 (orange) for an energy barrier Ed = 0.22eV. Experimental data of Sun et al. [4.12] (black).*

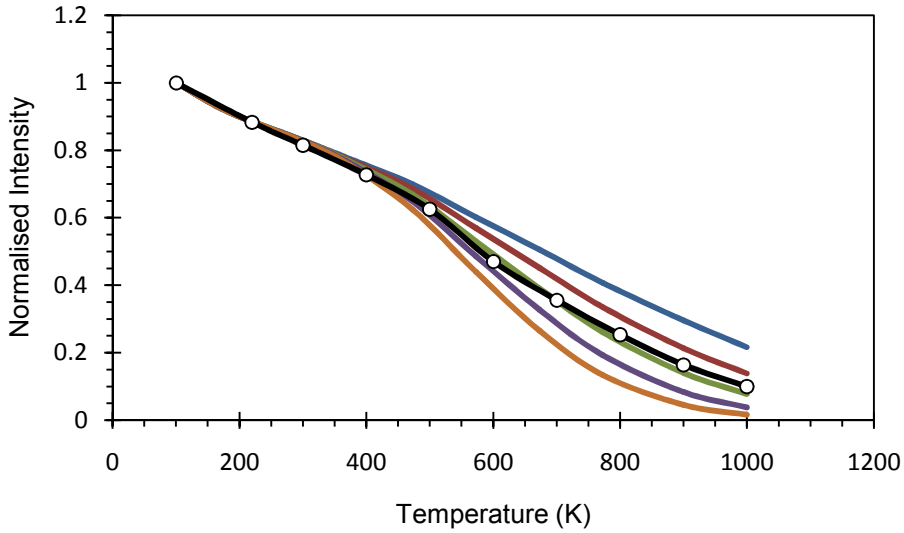

Figure 4.30: *Normalised intensity of 2.1eV peak for patch sizes of 3 (blue), 4 (red), 5 (green), 6 (purple), 7 (orange) for an energy barrier Ed = 0.24eV. Experimental data of Sun et al. [4.12] (black).*

The range of energy barrier values obtained from this work seems to be consistent with adatom formation energy barriers obtained in the literature for the creation of adatoms detaching from step edges - the most likely source of adatoms.

Stoltze [4.56] shows that the creation of defects on a stepped surface is easier than on a flat surface. The processes at step and terrace sites are different: a flat surface yields adatom-vacancy pairs whereas the stepped surface yields only adatoms (the site left behind is technically a vacancy but not considered so in this context). Stoltze shows that the energy barrier for the creation of an adatom from a surface with 001 steps is 0.268eV (from 110 steps is 0.455eV) and from a kink site is 0.239eV. This is compared to a value of 0.466eV for an adatom vacancy pair.

One would imagine from the model outlined above that an atom on a step edge would not contribute to the surface state, as a patch of atoms around it would not be complete.

4.9 Vicinal Copper

To take this work further, the next step is to add an additional level of complexity by moving to vicinal surfaces. The vast majority of work in surface science is carried out on low index surfaces such as (100), (110) and (111) but there have been a few studies using RAS on vicinal surfaces. Schmidt and Bernholc studied Si(112) [4.74]and stepped Si(100) surfaces [4.75] whilst studies on metals have been carried out Baumberger et al. on Cu(221) and Cu(112) [4.41] and on Cu(771) by MacDonald [4.40]. The surface used in this work is the Cu(13,13,1) surface which is a Cu(110) surface mis-cut by an angle of 3.1° resulting in a surface which has (111) step edge facets separated by (110) terraces 8 atoms long. The steps run parallel to the close packed rows in the $[1\bar{1}0]$ direction. A model of the surface is shown in *Figure 4.31* below.

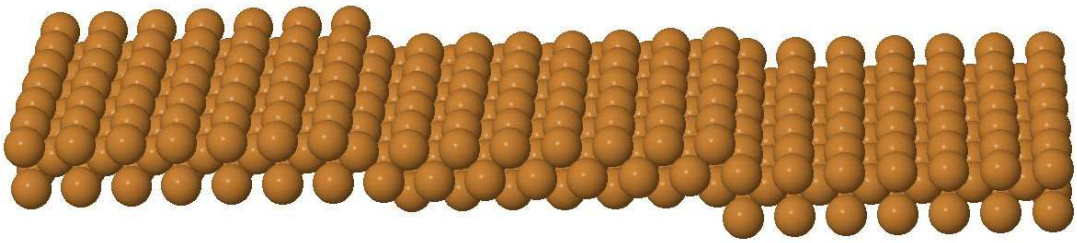

Figure 4.31: *A model of the Cu(13,13,1) surface.*

This surface is of interest because the (110) terraces naturally make it similar to the Cu(110) surface. The study of MacDonald [4.40] showed that RA response of the Cu(771) bore a resemblance to the Cu(110) surface in its shape but saw a much less intense peak at 2.1eV.

The sample was prepared in an identical way to the Cu(110) surface, and room temperature LEED experiments showed a pattern which would indicate a large unit cell 8 times that of Cu(110) with additional less intense spots in the [001] direction; indicating that the surface has the expected structure.

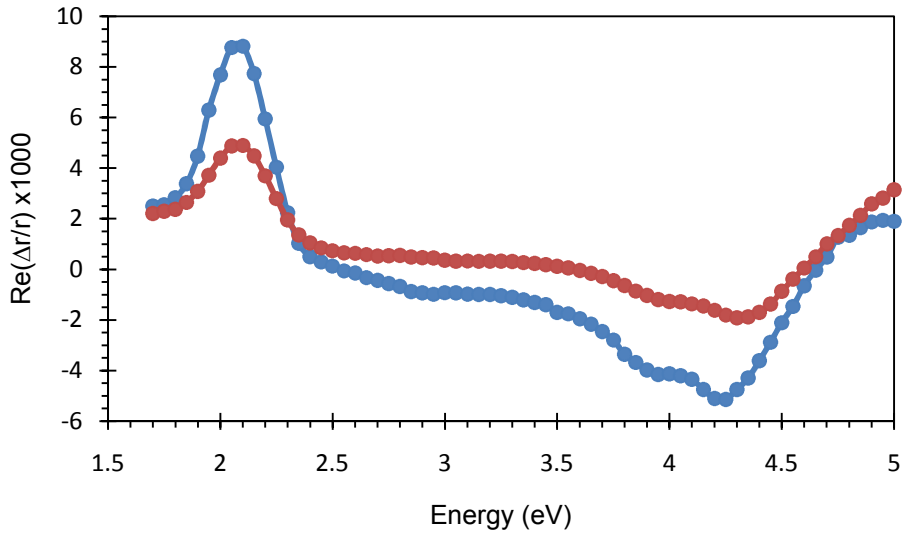

Figure 4.32: *A comparison of the RA response from the Cu(110) (blue circles) and Cu(13,13,1) (red circles) surfaces at room temperature.*

A comparison of the RA responses of Cu(110) and Cu(13,13,1) is shown in *Figure 4.32*. The integrated intensity under the 2.1eV peak on Cu(13,13,1) is almost exactly a half of the value of that of the Cu(110), this reduction is most likely due to the steps. If each terrace is considered individually, then in that terraces frame of reference the steps can be considered as defect sites; the step up would be a series of adatoms, and the step down vacancies. Applying the patch argument, only sites around which an $N \times N$ can fit without encountering a defect site can contribute to the 2.1eV RAS peak. The earlier work in this chapter found that the patch size which

best fit the data on Cu(110) was a value of *N*=5. Applying a patch size of *N*=5 to the Cu(13,13,1) terrace allows some sites to contribute and the steps prevent others from doing so; an overview of this is shown in *Figure 4.33*. (Again a square lattice is used for simplicity).

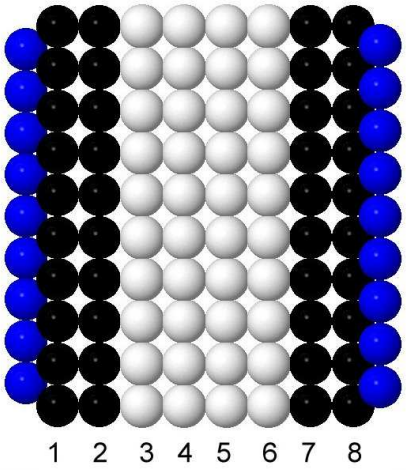

Figure 4.33: *A terrace of the (13,13,1) surface. Blue sites denote step sites, black sites denote those sites whose contribution would be quenched by a patch size of N=5, white sites denote sites which could contribute to the surface state for a patch size of N=5.*

Figure 4.33 shows that for a patch size of 5 only the atoms in columns 3 to 6 can contribute. The step sites prevent a patch fitting on the terrace around the atoms in columns 1&2 and 7&8. This means that only half the sites can contribute to the surface state, which is consistent with the experimental observations seen from the RAS at 2.1eV.

The RA response of the Cu(13,13,1) sample at room temperature is plotted in *Figure 4.32* along side that of Cu(110). The spectra are very similar and there is appears to be no contribution from the steps. This is not unexpected as MacDonald observed no anisotropic contribution from the steps on the Cu(771) surface [4.40] which should have twice the step density of the (13,13,1) surface.

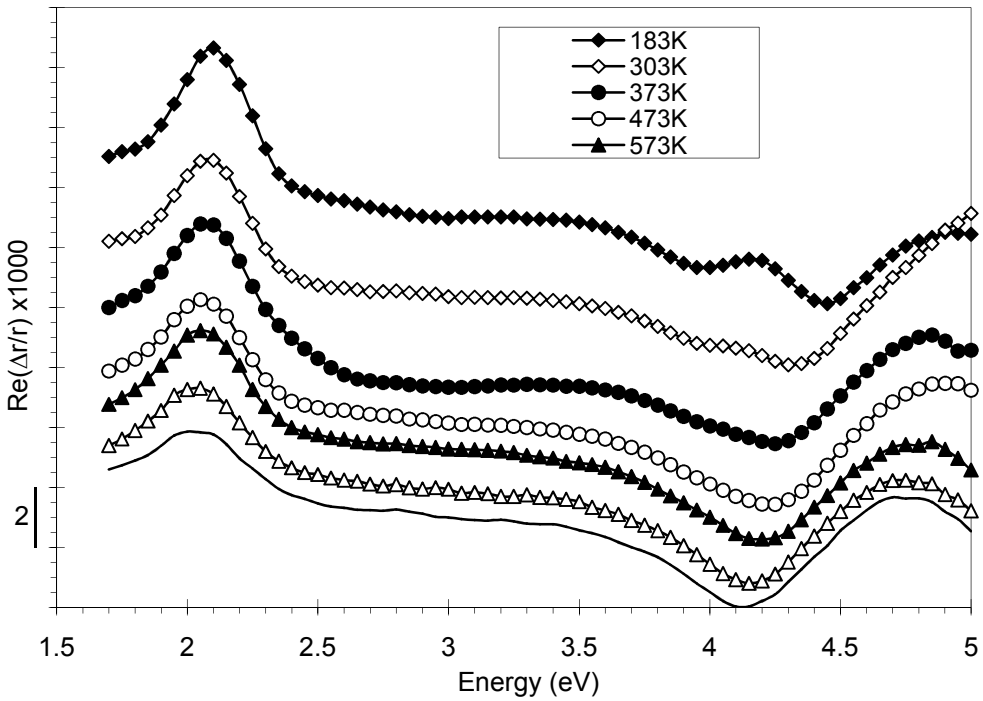

Figure 4.34: *The RA response of Cu(13,13,1) as a function of temperature.*

The thermal behaviour of the clean Cu(13,13,1) sample (*Figure 4.34*) is also similar to that of the Cu(110) surface indicating the features of the spectra have the same origins as on the (110) surface. What is of great interest is the intensity of the 2.1eV peak, the IPES measurements and Monte Carlo simulation of Heskett [4.55] suggested that in order to sustain a surface state peak clean patches of 12×12 atoms were required. It was established earlier that this would correspond to a patch size *N* of between 4 and 7 with the model used in this work. The (13,13,1) surface only has terraces 8 atoms in length; even allowing for the fact that the surface may not be perfect and that there may be some terraces of length 12 atoms or more, the intensity of the peak still seems curiously large. This offers more justification for the model used here, opposed to the model of Heskett [4.55]. The origins of the surface state contribution and the patch argument of Heskett et al.[4.55] could be looked at in more detail; Heskett et al. only apply the patch argument to the surface for ion induced defects but the surface state contribution should also be affected by the presence of thermally created defects.

4.9.1 Ion Bombarding Cu(13,13,1)

The ion bombarding of the Cu(13,13,1) sample was done under identical conditions to the Cu(110) and the results are shown in *Figures 4.35-4.37*:

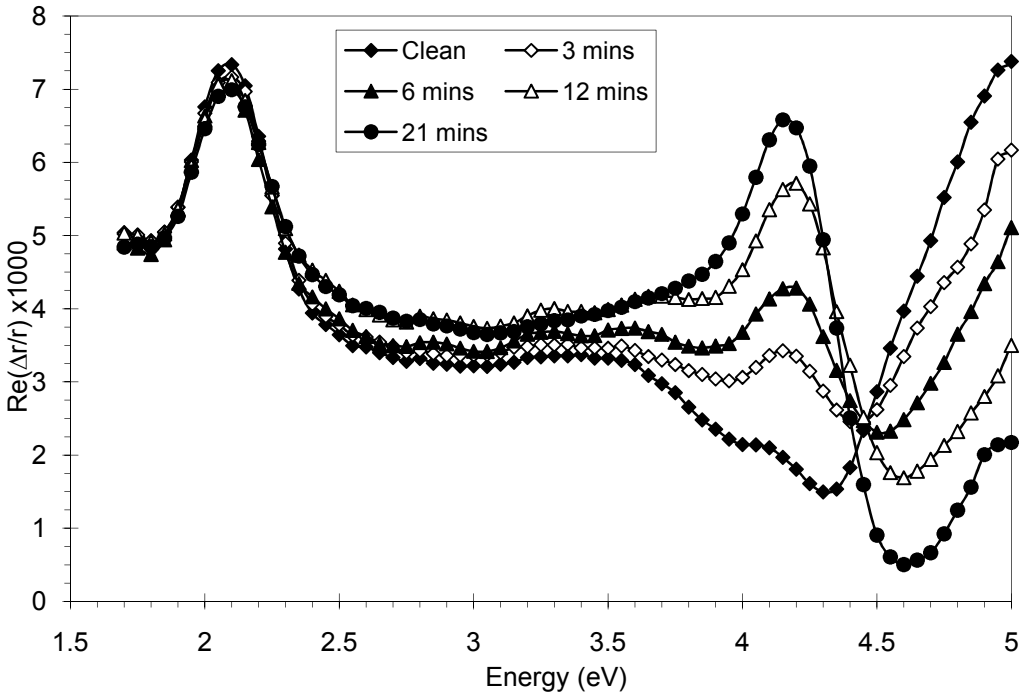

Figure 4.35: *RA Spectra of Cu (13,13,1) ion bombarded at 303K as a function of bombardment time.*

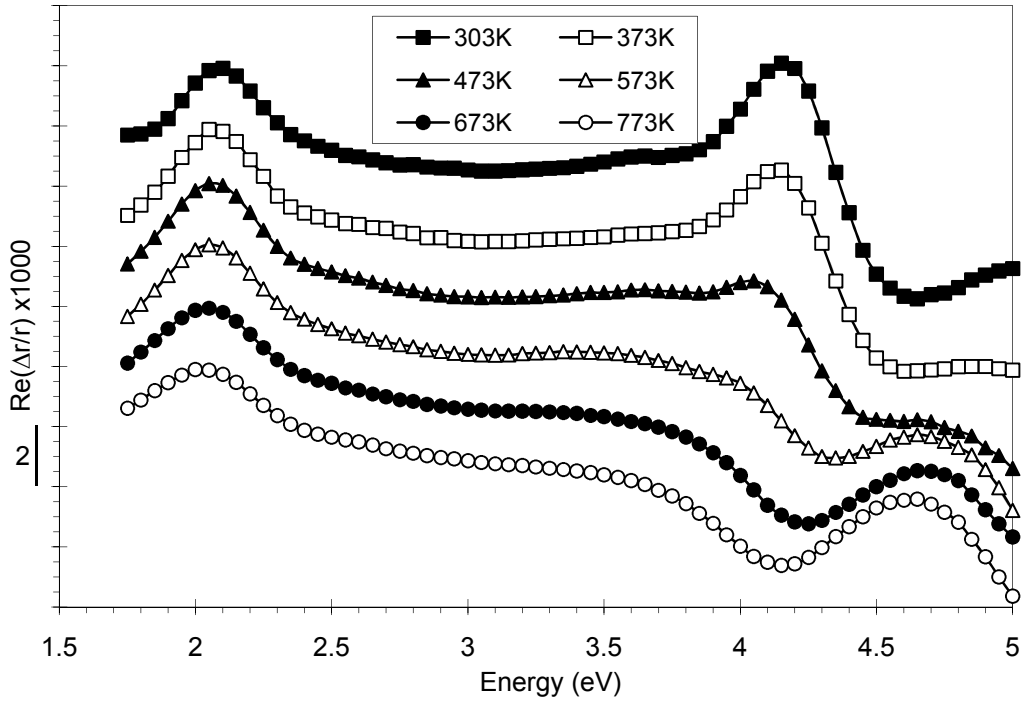

Figure 4.36: *The RA response of Cu(13,13,1) after 30mins ion bombarding at elevated temperatures.*

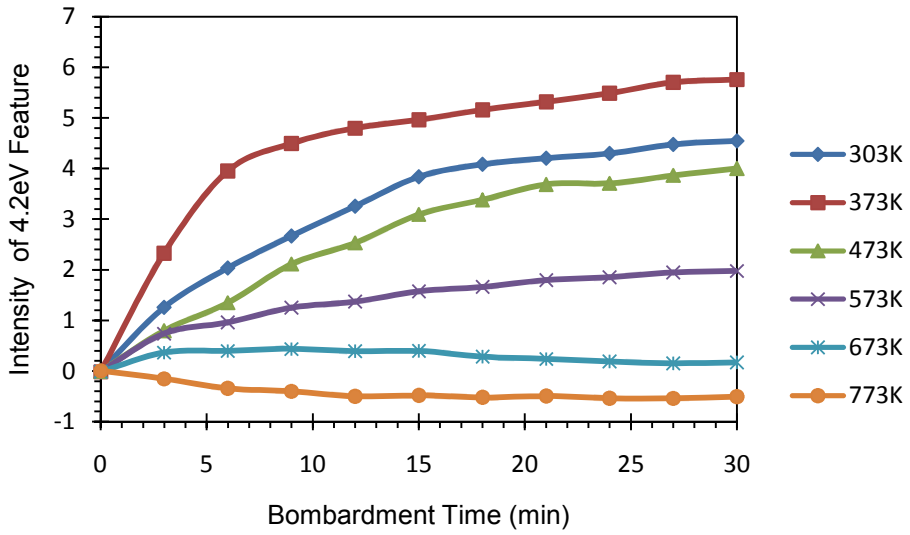

Figure 4.37: *The change in the RA response of Cu(13,13,1) at 4.2eV as a function of bombardment time.*

Results obtained during the ion bombarding at both room temperature and at high temperature show are very similar behaviour to the corresponding spectra on the Cu(110) surface. There is no change in intensity of the 2.1eV peak and the 4eV

region goes from a small negative peak on the clean surface to a large positive peak after bombarding for 30 minutes. The only difference is in the time taken for these changes to occur.

4.9.2 Low Temperature Ion Bombarding

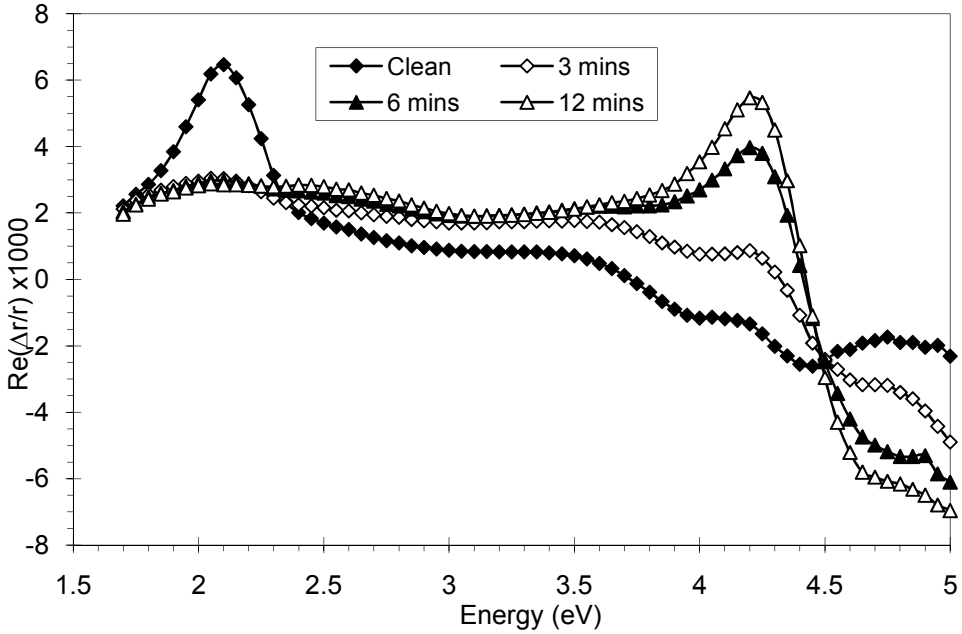

Figure 4.38: *The RA response of Cu(13,13,1) during ion bombarding at 183K.*

Looking at the spectra of the low temperature ion bombarding of Cu(13,13,1) in *Figure 4.38* and comparing them to corresponding spectra on the Cu(110) surface, the same change at 4.2eV occurs, again the low temperature ion bombarding destroys the 2.1eV peak.

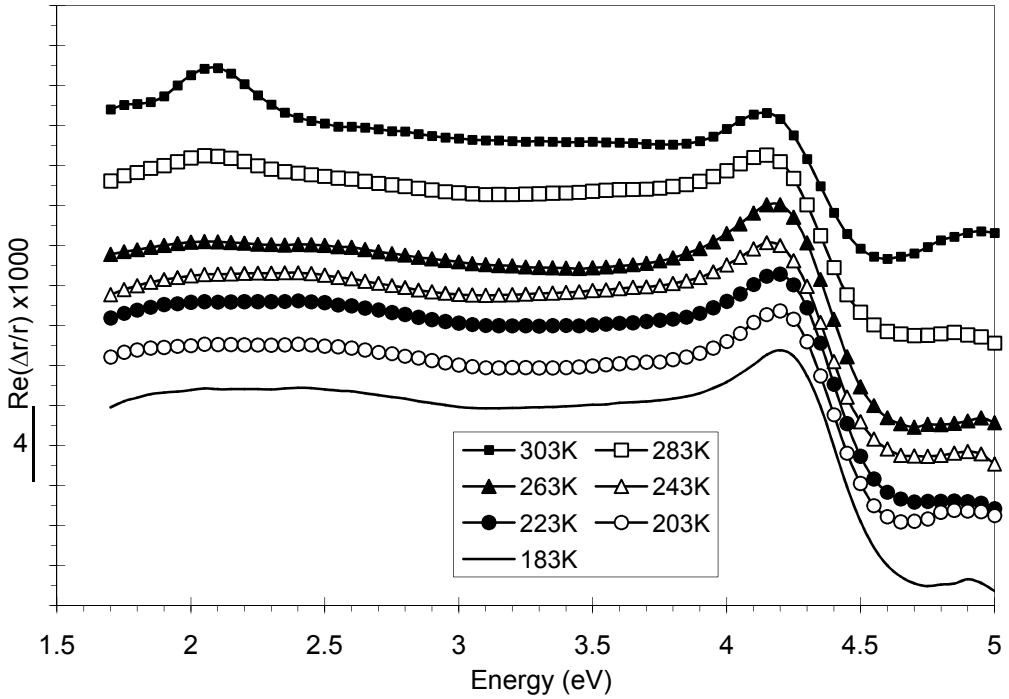

Figure 4.39: *The RA response of the Cu(13,13,1) surface after ion bombarding for 30 mins at different temperatures.*

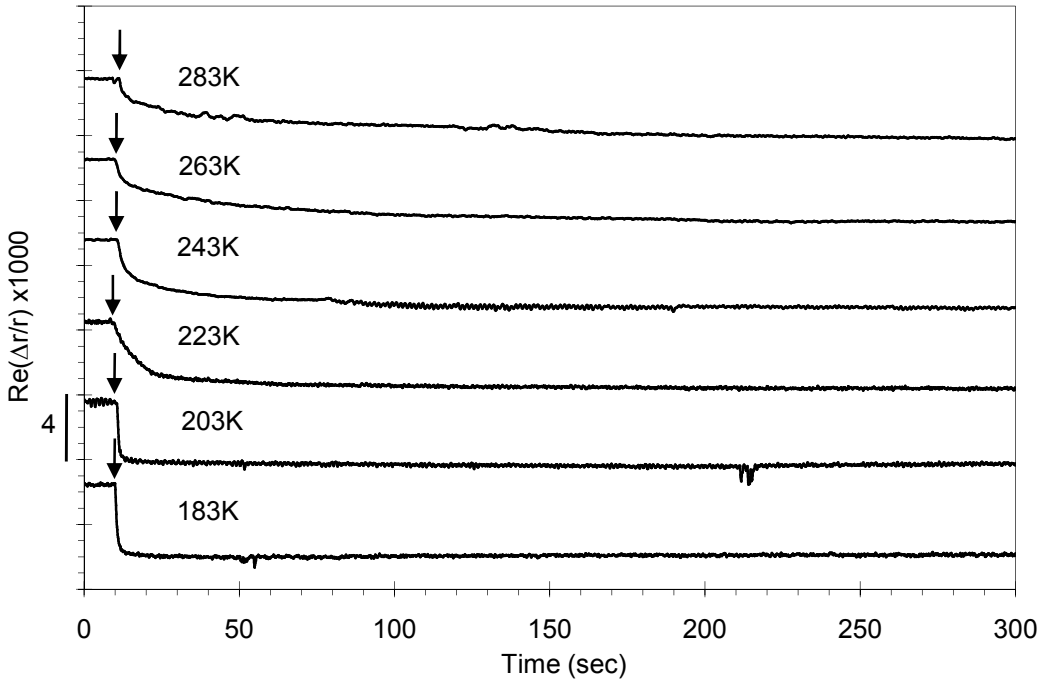

Figure 4.40: *The RA response of the Cu(13,13,1) 2.11eV peak as a function of ion bombardment time for different temperatures. Arrows denote time at which the ion gun was switched on.*

Figure 4.39 shows that the RA spectra response from the Cu(13,13,1) surface is almost identical to that of the Cu(110) surface. However *Figure 4.40* shows that the timescales on which the 2.1eV is destroyed are different for the two surfaces at many temperatures. At 183K the rate of destruction of the peak is the same; for the two peaks (despite their initial intensities being different). For temperatures above this the Cu(13,13,1) peak is destroyed at a slower rate, and for 283K the peak is not completely destroyed on this timescale. This behaviour could be explained by the higher step density and shorter terraces, meaning more repairs can be carried out as the defect separation distance is much less than for Cu(110). Also considering the patch argument and referring to *Figure 4.33* some sites do not contribute to the surface state due to the steps (those in columns 1,2,7&8). If a defect were created in one of these columns it would quench less of the surface state contribution than if it were formed in columns 3-6. A combination of these two effects could explain this behaviour.

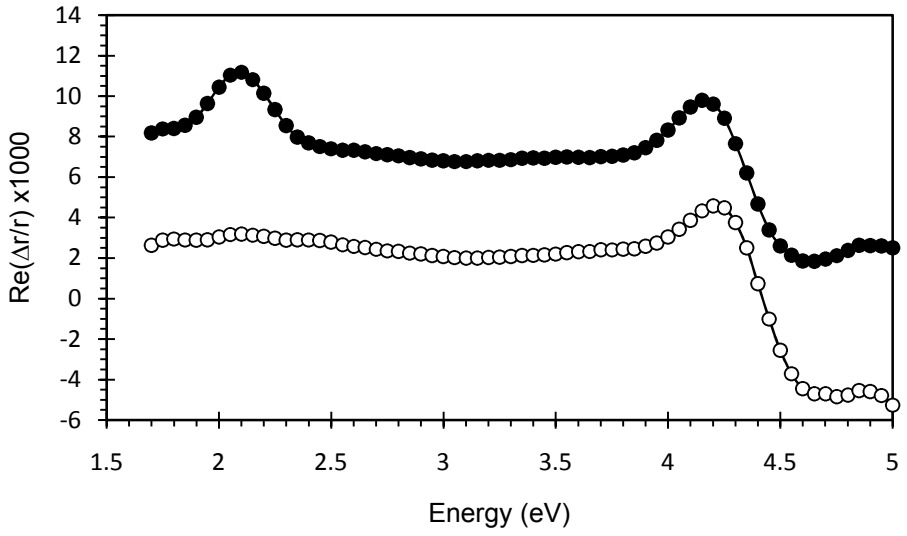

Figure 4.41: *The RA response of the Cu(13,13,1) after ion bombarding for 30 mins at 183K (open circles) and the same sample after allowing it to heat up to room temperature (filled circles).*

The repair rates of the two surfaces can be compared by observing the behaviour of the 2.1eV peaks after heating the bombarded surface. The samples were both ion bombarded for 30 minutes at 183K (hence their 2.1eV peaks were both destroyed),

the samples were then allowed to warm up to room temperature. The peak on the Cu(110) surface showed no increase in intensity, while the peak on the Cu(13,13,1) surface had almost recovered to its original value, as shown in *Figure 4.41*.

4.10 Discussion

The similarities between the RA responses of the Cu(110) and Cu(13,13,1) surfaces is clear from the spectra, the major difference being the intensity of the 2.1eV peak and the timescales on which the ion bombarding effects are observed. These differences are most likely due to the larger step density on the Cu(13,13,1) surface. The effect of this high step density is twofold: firstly on the clean surface, the step sites have a disruptive influence in that they cause reduction in the intensity of the spectral features. However on a damaged surface the high step density facilitates a mechanism by which the damage can be limited. These step sites because of their lower energy barriers are a source of adatoms which can repair damage, and it is for this reason that many of the processes occurring on the surface take longer on the Cu(13,13,1) surface than on the Cu(110) surface.

The ion bombarding at low temperature (183K) destroys the surface state peak by destroying the unoccupied state as shown by the IPES measurements of Heskett et al. [4.55]. Once this peak has been destroyed (after ~10 seconds ion bombarding) there is only a very small, almost insignificant feature remaining, not the large contributions proposed by Sun et al. [4.12]. As these additional features are bulk based it is unlikely they would be destroyed on a similar timescale to the surface state; the bulk features at 4.2eV change on a time scale of order 15 minutes. This suggests the surface state is by far the largest contribution to the 2.1eV peak. The thermal behaviour of the 2.1eV peak can be modelled using a combination of both surface state transitions and defects as described in *Section 4.8*.

The patch argument has successfully been applied to a number of different situations; thermal adatoms, ion bombardment and the effect of steps on the Cu(13,13,1) surface. All these methods produced similar results which suggest that

an atom can contribute to the surface state only if it sits at the centre of a patch with area equivalent to that of 5×5 atoms patch free of defects. A single defect can therefore quench an area up to this size (depending on the proximity of other defect sites).

The ion bombardment process creates both adatoms and vacancies, which providing the thermal conditions are appropriate, can diffuse and repair some of the defect sites. Thermal adatoms are also available and these can add to the numbers of defects created by the ions. The structures produced by ion bombardment in this work are considered only in the low coverage regime where there is no coagulation of defects (all defects are randomly distributed) and the patch and diffusion arguments can explain the behaviour at 2.1eV.

For larger damages it has been shown by Rusponi et al. [4.76] that ripples form on the surface Cu(110); it might seem unlikely that the 2.1eV peak can be maintained, however the results in this thesis show that it is. Even with a very large step density as in the case of Cu(13,13,1) a surface state peak can be maintained; however its intensity will be reduced. The similarities between steps and ripples can be drawn, and as long as the step density (or ripple density) is very low, the intensity of the 2.1eV peak will be large so long as defects in terraces (opposed to on step/ripple edges) are repaired. This could perhaps explain why the surface state peak is maintained when the 4.2eV region has a significant amount of damage.

4.11 Conclusions

This work has considered numerous sources of nanoscale defects on the copper surfaces, and is the first work to demonstrate that kinetic parameters can be deduced from quantitative analysis of RAS data. These nanoscale defects affect the RA response of the system in different ways but are mostly observed in the behaviour of the 2.1eV peak. Defects caused by ion bombarding, thermal excitation and by the presence of steps all cause a reduction in the intensity of the 2.1eV feature. By modelling the peak as arising from only surface state transitions, the behaviour of the

surface due to these different sources of defects can be explained well. This suggests that the 2.1eV peak arises predominantly due to surface state transitions. The rate at which the peak is reduced by these defects suggests that a single defect can quench a surface state contribution equivalent to the area occupied by a patch of 5×5 atoms.

The presence of steps on the surface whilst having a negative effect on the surface state contribution of the clean surface offers some benefit on a damaged surface. The presence of steps provides a low energy source of mobile adatoms which can facilitate repairs by recombining with vacancy sites. Hence many of the processes which damage the surface occur more slowly on surfaces with higher step densities.

4.12 References

[4.1] Ph. Hoffman, K.C. Rose, V. Fernandez, A.M. Bradshaw and W. Richter; Phys. Rev. Lett. **75**, 2039 (1995)

[4.2] M.Y. Jiang, G. Pajer and E. Burstein; Surf. Sci. **242**, 306 (1991)

[4.3] J.-K. Hansen, J. Bremer and O. Hunderi; Surf. Sci. Lett. **418**, L58 (1998)

[4.4] J.-K. Hansen, J. Bremer and O. Hunderi; Phys. Stat. Sol. (a) **170**, 271 (1998)

[4.5] K. Stahrenberg, Th. Herrmann, N. Esser and W. Richter; Phys. Rev. B **61**, 3043 (2000)

[4.6] G.E. Isted and D.S. Martin; Appl. Surf. Phys. **252**, 1883 (2005)

[4.7] N.P. Blanchard, D.S. Martin, A.M. Davarpanah, S.D. Barrett and P. Weightman; Phys. Stat. Sol. (a) **118**, 1505 (2001)

[4.8] D.S. Martin, A.M. Davarpanah, S.D. Barrett and P. Weightman; Phys. Rev. B **62**, 15417 (2000)

[4.9] D.S. Martin and P. Weightman; J. Phys.: Condens. Matter, **14**, 675 (2002)

[4.10] B.G. Frederick, J.R. Power, R.J. Cole, C.C. Perry, Q. Chen, S. Haq, Th. Bertrams, N.V. Richardson and P. Weightman; Phys. Rev. Lett. **80**, 4490 (1998)

[4.11] L.D. Sun, M. Hohage, P. Zeppenfeld, R.E. Balderas-Navarro, K. Hingeri, Phys. Rev. Lett. **90**, 106104 (2003)

[4.12] L.D. Sun, M. Hohage, P. Zeppenfeld and R.E. Balderas-Navarro; Surf. Sci. **589**, 153 (2005)

[4.13] H. Lüth; *Solid Surfaces, Interfaces and Thin Films*, 4th Edition, Springer-Verlag, Berlin (2001)

[4.14] P. Heimann, J. Hermanson, H. Miosga and H. Neddermeyer; Surf. Sci. **85**, 263 (1979)

[4.15] S. Kevan; Phys. Rev. B **28**, 4822 (1983)

[4.16] P. Straube, F. Pforte, T. Michalke, K. Berge, A. Gerlach and A. Goldmann; Phys. Rev. B **61**, 14072 (2000)

[4.17] R.A. Bartynski, T. Gustafsson and P. Soven; Phys. Rev. B **31**, 4745 (1985)

[4.18] B. Reihl and K.H. Frank; Phys. Rev. B **31**, 8282 (1985)

[4.19] R. Schneider, H. Durr, Th. Fauster and V. Dose; Phys. Rev. B **42**, 1638 (1990)

[4.20] D. Tang, C. Su and D. Heskett; Surf. Sci. **295**, 427 (1993)

[4.21] P. Sandl and E. Bertel; Surf. Sci. **302**, L325 (1994)

[4.22] J.-K. Hansen; *Electronic and Optical Surface Properties of Noble Metals Studied by Reflection Anisotropy Spectroscopy*, PhD Thesis, Norges teknisk-naturvitenskapelige universitet, Trodheim (2000)

[4.23] Y. Borensztein, W.L. Mochan, J. Tarriba, R.G. Barrera and A. Tadjeddine; Phys. Rev. Lett. **71**, 2334 (1993)

[4.24] J. Bremer, J.-K. Hansen, K. Stahrenberg and T. Worren; Surf. Sci. **459**, 39 (2000)

[4.25] W.L. Mochan and R.G. Barrera; Phys. Rev. Lett. **55**, 1192 (1985)

[4.26] W.L. Mochan, R.G. Barrera, Y. Borensztein and A. Trondheim; Physica A **207**, 334 (1994)

[4.27] P. Weightman, D.S. Martin, R.J. Cole and T. Farrell; Rep. Prog. Phys. **68**, 1251 (2005)

[4.28] U. Rossow, L. Mantese and D.E. Aspnes; J. Vac. Sci. Technol. B **14**, 3070 (1996)

[4.29] L.D. Sun, M. Hohage, P. Zeppenfeld, R.E. Balderas-Navarro and K. Hingerl; Surf. Sci. Lett. **527**, L184 (2003)

[4.30] D.S. Martin, R.J. Cole and P. Weightman; Phys. Rev. B **72**, 35408 (2005)

[4.31] J.F. Janak, A.R. Williams and V.L. Moruzzi; Phys. Rev. B. **11**, 1522 (1975)

[4.32] A.B. Chen and B. Segall; Phys. Rev. B. **12**, 600 (1975)

[4.33] U. Gerhardt; Phys. Rev. **172**, 651 (1968)

[4.34] P.B. Johnson and R.W. Christy; Phys. Rev. B **6**, 4370 (1972)

[4.35] P. Winsemius, F.F. van Kampen, H.P. Lengkeek and C.G. van Went; J. Phys. F: Met. Phys. **6**, 1583 (1976)

[4.36] P. Monachesi, M. Palummo, R. Del Sol, R. Ahuja and O. Eriksson; Phys. Rev. B **64**, 115421 (2001)

[4.37] D.S. Martin, A. Maunder and P. Weightman; Phys. Rev. B 63, 155403 (2001)

[4.38] J. Bremer, J.-K. Hansen and O. Hunderi; Surf. Sci. **436**, L735 (1999)

[4.39] B.F. MacDonald and R.J. Cole; Phys. Stat. Sol. (a) **188**, 1489 (2001)

[4.40] B.F. MacDonald; *Reflection Anisotropy Spectroscopy and Scanning Probe Microscopy Studies with Applications to Liquid Crystal Alignment Layers*, PhD Thesis, The University of Edinburgh (2002)

[4.41] F. Baumberger, Th. Herrmann, A. Kara, S. Stolbov, N. Esser, T.S. Rahman, J. Osterwalder, W. Richter and T. Greber; Phys. Rev. Lett. **90**, 177402 (2003)

[4.42] D.S. Martin and P. Weightman; Surf. Interface Anal. **31**, 915 (2001)

[4.43] W. Jacob, V. Dose, U. Kolac, Th. Fauster and A. Goldmann; Z. Phys. B: Condens. Matter **63**, 459 (1986)

[4.44] P. Zeppenfeld, K. Kern, R. David and G. Comsa; Phys. Rev. Lett. **62**, 63 (1989)

[4.45] P.D. Ditlevsen, P. Stoltze and J.K. Norskov. Phys. Rev. B **44**, 13002 (1991)

[4.46] H. Häkkinen, J. Merikoski, M. Manninen and J. Timonen; Phys. Rev. Lett. **70**, 2451 (1993)

[4.47] H. Dürr, H. Schneider and Th. Fauster; Phys. Rev. B **43**, 12187 (1991)

[4.48] U. Valbusa, C. Boragno and F. Buatier de Mongeot; J. Phys.: Condens. Matter **14**, 8153 (2002)

[4.49] R. Behrisch, H.H. Anderson and H.L. Bay; *Sputtering by Particle Bombardment 1*, Springer, Berlin (1991)

[4.50] V.S. Smentowski; Prog. Surf. Sci. **64**, 1 (2000)

[4.51] M.A. Makeev and A.L. Barabási; Appl. Phys. Lett. **71**, 2800 (1997)

[4.52] V.P. Zhdanov; Surf. Sci. Rep. **12**, 183 (1991)

[4.53] See for example: F. Schwabl; *Statistical Mechanics*, Springer-Verlag, Berlin (2002)

[4.54] G. Costantini, S. Rusponi, R. Gianotti, C. Boragno and U. Valbusa; Surf. Sci. **416**, 245 (1998)

[4.55] D. Heskett, D. DePietro, G. Sabatino and M. Tammaro; Surf. Sci. **513**, 405 (2002)

[4.56] P. Stoltze; J. Phys. Condens. Matter **6**, 9495 (1994)

[4.57] H. Yildirim, A. Kara, S. Durukanoglu and T.S. Rahman; Surf. Sci. **600**, 484 (2006)

[4.58] F. Montalenti and R. Ferrando; Phys. Rev. B **59**, 5881 (1999)

[4.59] C.L. Liu, J.M. Cohen, J.B. Adams, A.F. Voter; Surf. Sci. **253**, 334 (1991)

[4.60] M. Karimi, T. Tomkovski, G. Vidali and O. Biham; Phys. Rev. B **52**, 5364 (1995)

[4.61] U. Kurpick; Phys. Rev. B **64**, 075418 (2001)

[4.62] S.V. Eremeev, A.G. Lipnitskii, A.I. Potekaev and E.V. Chulkov; Russ. Phys. J. **40**, 584 (1997)

[4.63] G. Attard and C. Barnes; *Surfaces*, Oxford University Press, Oxford (1998)

[4.64] K. Oura, V.G. Lifshits, A.A. Saranin, A.V. Zotov and M. Katayama; *Surface Science: An Introduction*. Springer-Verlag, Berlin (2003)

[4.65] S.D. Kevan, N.G. Stoffel and N.V. Smith; Phys. Rev. B **31**, 3348 (1985)

[4.66] A. Goldmann, V. Dose, and G. Borstel; Phys. Rev. B **32**, 1971 (1985)

[4.67] A. Gerlach, G. Meister, R. Matzdorf, A. Goldmann; Surf. Sci. **443**, 221 (1999)

[4.68] R. Matzdorf; Chem. Phys. **251**, 151 (2000)

[4.69] G.E. Isted, P.D. Lane and R.J. Cole; Phys. Rev. B **79**, 205424 (2009)

[4.70] *See for example:* G.B. Arfken and H.J. Weber; *Mathematical Methods for Physicists*, 6th Edition, Elsevier, London (2005)

[4.71] R.J. Cole, B.G. Frederick and P. Weightman; J. Vac. Sci. Technol. A **16**, 3088 (1998)

[4.72] K. Stahrenberg, Th. Herrmann, K Wilmers, N. Esser, W. Richter, and M.J.G. Lee; Phys. Rev. B **64**, 115111 (2001)

[4.73] R.M. Tromp and M. Mankos; Phys. Rev. Lett. **81**, 5 (1998)

[4.74] W.G. Schmidt and J. Bernholc; Phys. Rev. B **61**, 7604 (2000)

[4.75] W.G. Schmidt and J. Bernholc; Phys. Rev. B **63**, 045322 (2001)

[4.76] S. Rusponi, G. Constantini and U. Valbusa; Phys. Rev. Lett. **81**, 2735 (1998)

Chapter 5: Methanethiol on Copper

5.1 Introduction

Recently there has been a significant interest in the adsorption of sulphur containing molecules on metal surfaces because of their importance in fields such as molecular electronics, wear protection, corrosion inhibition, chemical sensor fabrication, lubrication and biotechnology [5.1-5.10]. To enable the development and optimisation of such devices built using this interface it is first necessary to understand and characterise the interactions occurring at this interface both between the adsorbate material and the substrate, and between adsorbates themselves.

This work considers the adsorption of methanethiol (CH_3-SH), the simplest alkanethiol molecule, on the Cu(110) surface, and the subsequent removal of the alkane group to leave sulphur on copper. It is known that many of these thiol-containing molecules bond to the surface through the sulphur forming molecule-metal bonds [5.11-5.20]. This occurs through the deprotonation of the molecule at the surface to form a self-assembled monolayer (SAM). SAMs are interesting as conductive channels in molecular electronics, or as barrier films to prevent oxidation of the metal surface.

Although this system has been studied with other techniques [5.19-5.22], no previous studies with RAS have been undertaken. RAS has however been used numerous times to monitor/study adsorption of molecules on to metal surfaces; studies involving Cu(110) have seen 3-thiophene carboxlate [5.23], Terephthalic Acid [5.24], Oxalic Acid [5.25], Carbon Monoxide [5.26], Oxygen [5.27], and L-Cysteine [5.28-5.29] deposited on the surface. RAS has also been useful in determining the orientation of molecules on surfaces [5.23, 5.30-5.31] so has proved a useful tool in this kind of work, and a number of sulphur containing molecules on noble metals surfaces have also been studied [5.28-5.29, 5.32-5.34].

In *Section 5.3* a brief summary of previous relevant work is given. New experimental results for the methanethiol and sulphur on copper systems are presented in *Section 5.5* and discussed in *Section 5.6*. *Sections 5.7-5.8* present new methods of simulating these results.

5.2 Copper

The RA spectrum for a clean Cu(110) surface and explanations of the features contained within it is discussed in detail in *Chapter 4*.

5.3 Related work: Sulphur containing molecules

5.3.1 Hydrogen Sulphide

Atrei et al. [5.16] studied various coverages of hydrogen sulphide (H_2S) on Cu(110) using LEED and surface extended X-ray absorption fine structure (SEXAFS). For the lowest coverage, 0.3 monolayers a diffuse c(2×2) LEED pattern was observed. It was suggested that at this coverage islands of the adsorbate were forming leaving domains of clean copper in other regions of the sample. As the exposure was increased to 0.4 monolayers the LEED spots were observed to split firstly in the [001] direction, then in the $[1\bar{1}0]$ direction. The saturation coverage, 0.64 monolayers, yielded a different LEED pattern which is shown in *Figure 5.1 (d)*. It was suggested that this pattern could be reported as c(8×2) with missing spots. The same sequence of LEED patterns had also been reported by Boulliard [5.17] in a detailed LEED study of segregated sulphur on Cu(110). The SEXAFS results of Atrei et al. [5.16] indicated the favoured bonding site was the two fold hollow site on the Cu(110) and reported a bond length of 2.37 Angstroms for all the reported states.

Stensgaard et al. [5.18] reported a study of the same system using LEED and STM but observed a slightly different set of LEED patterns for increasing coverage; an additional p(5×2) state with missing spots was observed before a complete c(8×2) pattern at saturation.

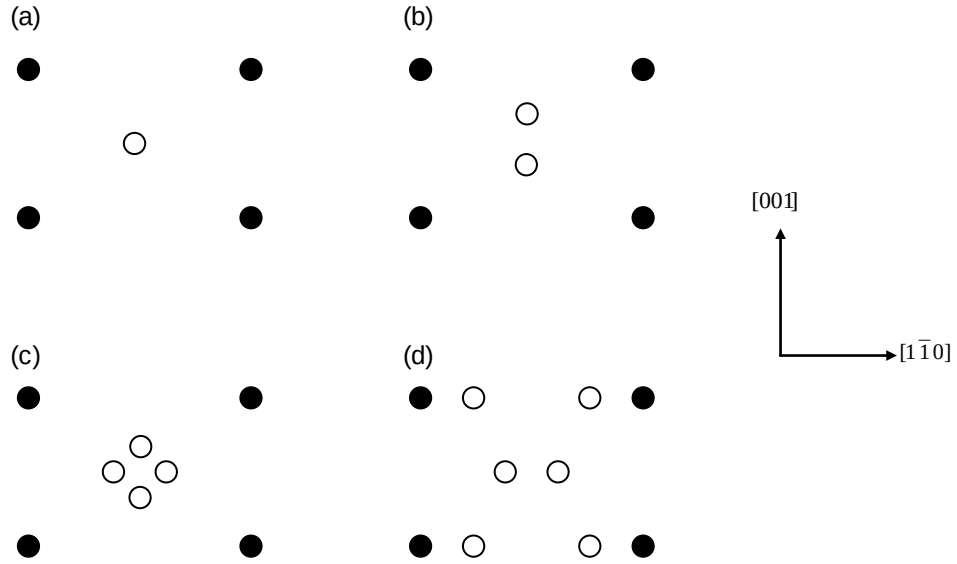

Figure 5.1: *Illustration of LEED patterns observed by Atrei et al.[5.16] for the adsorption of H_2S onto Cu(110). Exposure lowest to highest (a) to (d). Filled circles denote substrate spots, and open circles denote additional spots due to adsorbate.*

5.3.2 Methanethiol

The adsorption of methanthiol onto Cu(110) has been studied by Carley et al. [5.19-5.20] using LEED, STM and X-ray photoemission spectroscopy (XPS). Saturation coverage was found to be 0.66ML (where 1ML is equivalent to a molecular density equal to the atomic density of Cu atoms) and at this coverage a p(3×2) LEED pattern was observed. XPS results indicate that upon adsorption the S-H bond is broken and mercaptide (CH_3S-) is adsorbed at the surface [5.11]. For a coverage of ~0.3ML the STM studies showed the existence of small islands of c(2×2) structure on narrow terraces and adsorbate-decorated step edges. Further methanethiol exposure causes these islands to grow to cover the surface giving a coverage of ~0.45ML. XPS results confirm that there is no decomposition of the methanethiol molecule at room temperature [5.20]; decomposition starts to occur at 325K for low coverages and for high coverages does not begin until between 400-450K.

After thermal decomposition of the molecule (after heating to 450K for 60 mins) XPS data [5.20] shows that all carbon has been removed, leaving a chemisorbed

sulphur adlayer on the surface; this adlayer is found to be identical to that produced via exposure of the surface to hydrogen sulphide. The structure of the sulphur adlayer depends on the coverage before heating. For a coverage of ~0.45ML a p(5×2) structure was observed. For saturation coverage a p(3×2) structure was observed. This p(3×2) structure was also reported by Domange et al. [5.13] upon hydrogen sulphide deposition. In order to account for the adsorption site and bond length proposed by Atrei et al. [5.16] Carley et al. propose a surface buckling is responsible for the p(5×2) and p(3×2) structures caused by the compression of the Cu/S layer by varying amounts; the authors also suggest that the c(8×2) reported by Stensgaard et al. [5.18] is a metastable state which exists between the p(5×2) and p(3×2) phases.

A theoretical study using ab initio DFT calculations gives insight into the structural and electronic properties of the Cu/CH_3S surface, D'Agostino et al. [5.22] show that for the c(2×2) structure the most stable configuration is for the sulphur atom to occupy the short bridge site with the C-S bond at 56° to the surface normal, which is close to the 45° from the surface normal reported by Lee et al. [5.21] parallel to the <001> plane.

5.3.3 L-Cysteine

The more complicated L-cysteine molecule ($HS-CH_2-CH(NH_2)-COOH$) was studied by Isted [5.29] using RAS. This molecule contains both a thiolate group and a carboxylic group, which is also known to bond to copper [5.23, 5.35-5.36]. Results for increasing coverage of L-cysteine showed a reduction in the 2.1eV peak intensity, an increase in the RA response between ~2.3eV and ~4.5eV with the development of shoulders at ~2.3eV and ~3.5eV, and a shift of the 4.2eV feature to higher energies. At saturation a c(2×2) LEED pattern was observed. Isted made comparisons with the work of Frederick et al. [5.23], who observed similar changes in the RA response of a flat lying 3-thiophene carboxylate (3TC). As the 3TC coverage was increased the molecule re-orientated itself such that it was standing upright and interacting with the surface only through the carboxylic group; a reduction in the RA response between 2eV and 5eV was observed. The response

from the L-cysteine/Cu did not exhibit similar behaviour suggesting that the L-cysteine interacted with the copper surface differently from the 3TC, but via which group(s) the L-cysteine interacted with the surface was not conclusively established.

Upon heating to 580K the L-cysteine molecule dissociated and left only sulphur on the surface; this was confirmed by XPS results. After allowing the sample to cool to room temperature, significant changes in the RA response were reported; the negative peak at ~4.3eV was no longer observed and instead a negative peak centred at ~3.3eV and a broader positive peak centred at ~4eV were reported along with LEED results showing a p(3×2) diffraction pattern with missing spots at positions (+1/3, ±1/2) corresponding to real space directions (<$1\bar{1}0$>, <001>) [5.29]. After further heating of the system up to 930K, the negative peak centred at ~3.3eV became less intense and shifted to ~3eV, while the positive feature became more intense and also shifted to lower photon energy, centring at ~3.7eV, at this point a complete c(8×2) LEED pattern was reported. It was suggested that the initial change in coverage upon heating from a c(2×2) to a p(3×2) diffraction pattern was due to additional sulphur atoms being available for bonding to the surface after the L-cysteine molecule had dissociated, the subsequent reduction in coverage observed from a change from a p(3×2) to a c(8×2) diffraction pattern was attributed to a reduction in surface buckling. The negative RAS peak at 3.3eV (580K) was attributed to the surface buckling of the p(3×2) structure, while the other peaks at ~3.7eV (930K) or 4eV (580K) were attributed surface morphological changes induced by the sulphur adlayer.

5.4 Experimental Method

The experiments were carried out under UHV conditions with a base pressure ~ 10^{-10} mbar, at the University of Liverpool in a chamber of similar layout to that described in *Chapter 3*. The Cu(110) surface was prepared by repeated cycles of ion bombardment (15min, ~6μA, 0.5kV, 300K) and annealing to 840K. Surface order was monitored by LEED. The Cu(110) surface was exposed to methanethiol gas (99.5% Aldrich) which was admitted into the chamber via a fine leak valve, for a short period at a recorded pressure to dose the sample. The exposure (in Langmuirs)

could then be calculated. After each dose a RA spectrum and LEED pattern were recorded at room temperature (300K).

5.5 Results

The RA response of the clean Cu(110) surface was consistent with previous work in *Chapter 4* and other studies of the surface [5.37-5.47]. This indicates a clean well ordered surface; the LEED pattern obtained was a sharp (1×1) pattern again indicating a clean well ordered atomic surface structure.

5.5.1 Methanethiol Exposure

The RA response was recorded after the sample was exposed to a dose of the methanethiol gas and significant changes in the spectra were observed; these results are shown in *Figure 5.2 (a-g)* for low to high coverage. *Figure 5.2 (g)* corresponds to the saturation coverage of methanethiol on the Cu(110) surface; exposing the sample to further doses results in no changes in the RA spectra.

Note all the RA spectra in this chapter have been vertically displaced to aid comparison. The solid lines at the higher energies denote reference positions which show the amount each spectrum has been displaced.

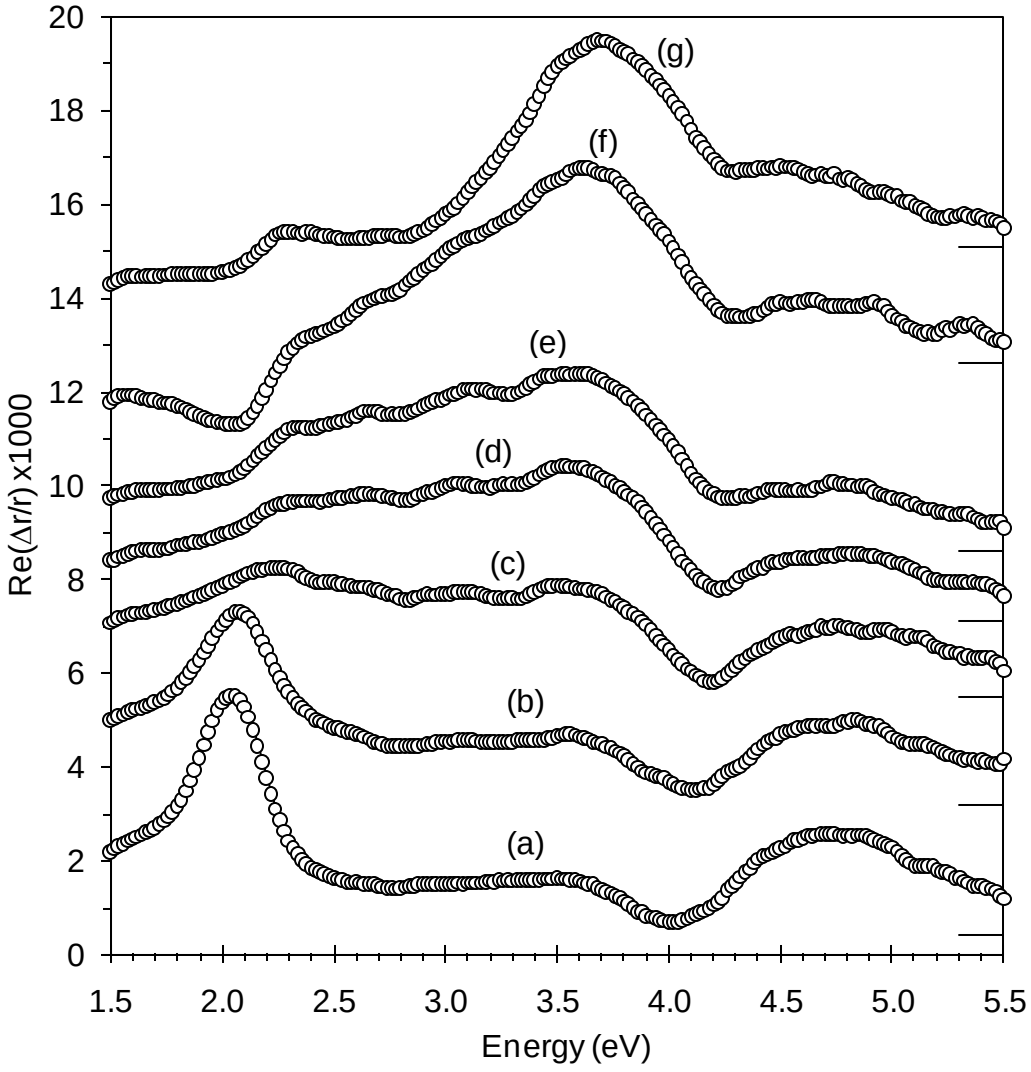

Figure 5.2: *(a): RA spectra of clean Cu(110). (b) – (f): Methanethiol on Cu(110) low to high coverage. (g): Methanethiol saturated surface.*

Exposure of the methanethiol to the surface sees the RA response of the surface change in a number of ways. Firstly there is reduction in the intensity of the peak at 2.1eV, even small exposures see a significant reduction in this feature. Secondly the feature at ~4eV on the clean sample initially narrows and is shifted to higher energy before appearing to flatten out. Thirdly there is the development of a large broad feature developing in the range of 2.8 to 4eV in the transition between *Figure 5.2 (c)* and *5.2 (f)*, between *Figure 5.2 (f)* and saturation (*Figure 5.2 (g)*) the feature becomes more peak-like in shape and shifts its position so that it is centred at ~3.7eV at saturation coverage. The response of the spectra above 4.5eV shows little change.

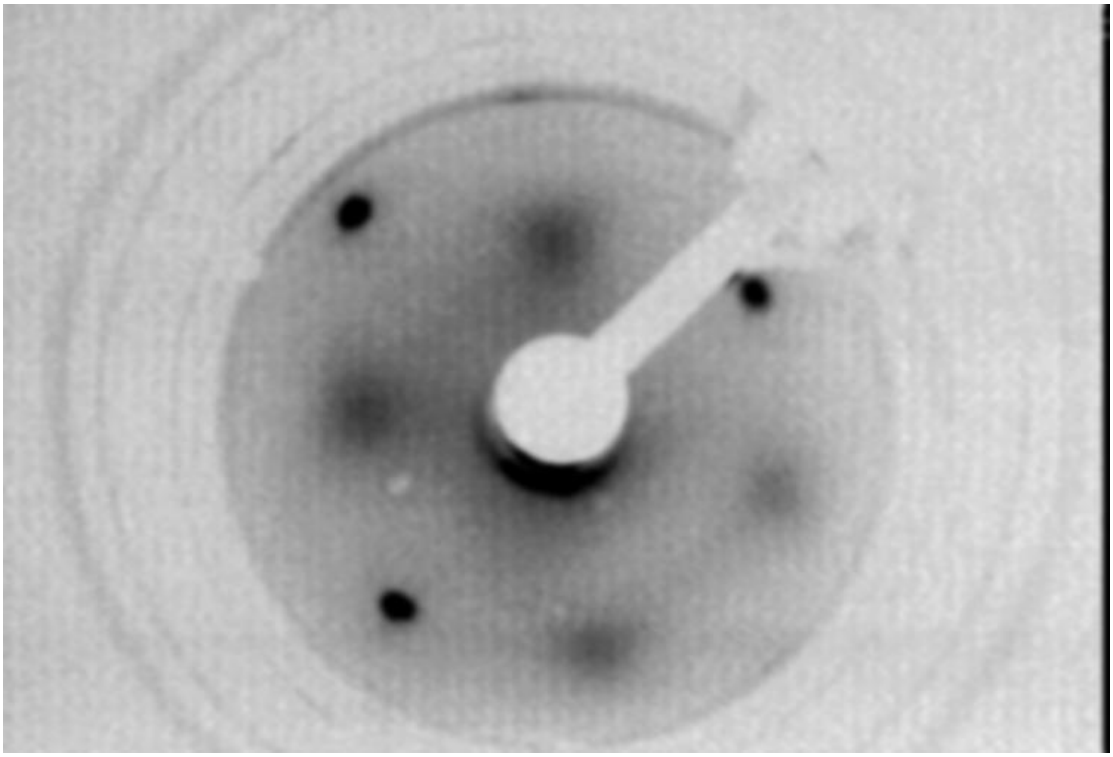

Figure 5.3: *LEED pattern corresponding to 0.09L Exposure (RAS Figure 5.2(e)) taken at 74eV.*

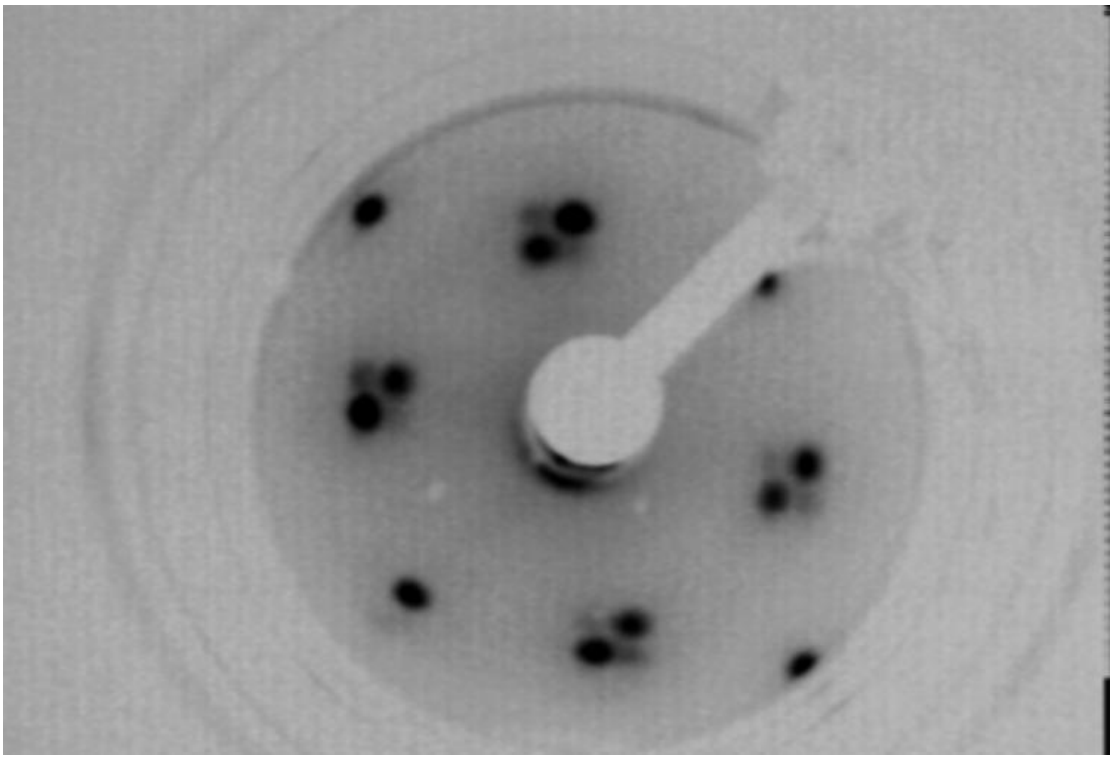

Figure 5.4: *LEED pattern corresponding to 0.4L Exposure (RAS Figure 5.2(f)) taken at 76eV.*

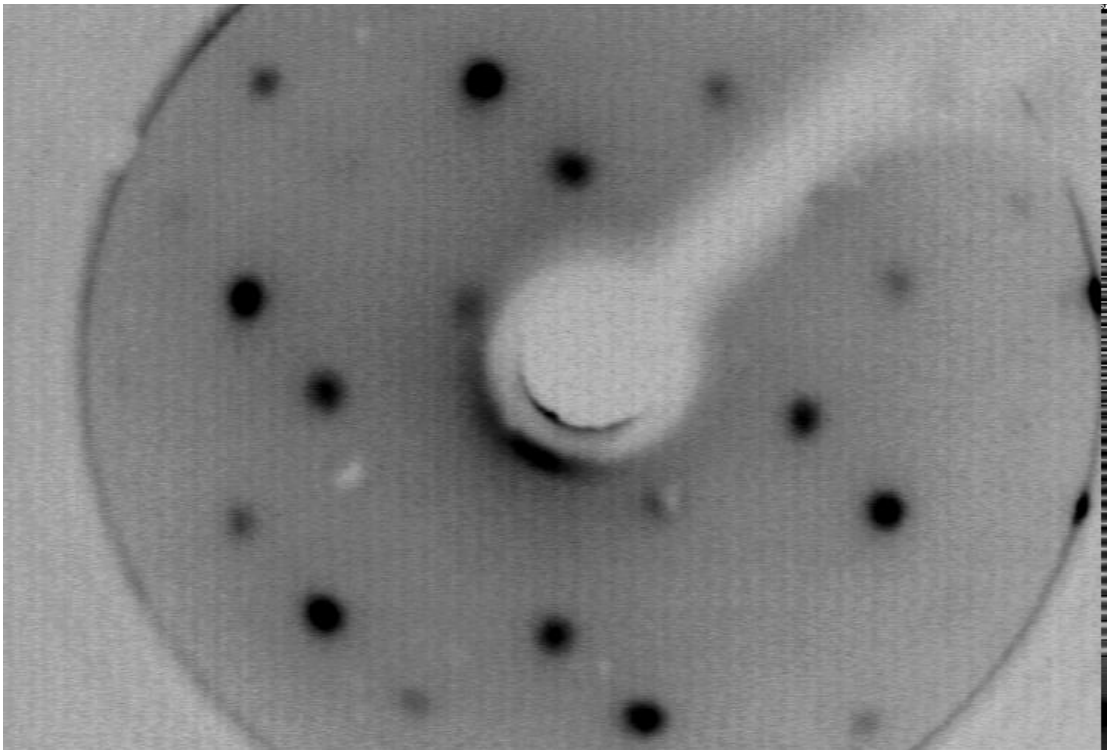

Figure 5.5: *LEED pattern corresponding to saturation coverage (RAS Figure 5.2(g)) taken at 74eV.*

The LEED pattern shown in *Figure 5.3* corresponding to the RAS results shown in *Figure 5.2 (e)* shows a broad and diffuse c(2×2) structure. As coverage increases the broad and diffuse spots split firstly in the [001] direction then in the $[1\bar{1}0]$ direction, *Figure 5.4* shows the splitting in the [001] direction clearly with sharp spots whilst the splitting in the $[1\bar{1}0]$ direction has more diffuse spots, but is still visible. The saturation LEED pattern (*Figure 5.5*) shows a c(8×2) structure with missing spots. This sequence of LEED patterns is the same as those observed by Atrei et al. [5.16] for Hydrogen Sulphide as shown in *Figure 5.1* and the saturation coverage pattern is the same as that observed by Domange and Oudar [5.13].

Given the consistency of LEED results with previous work [5.16-5.17] the coverage at various stages can be estimated from the LEED results and assigned to the corresponding RAS signal. The diffuse c(2×2) structure shown in *Figure 5.3* would correspond to a coverage of ~0.3ML, the split c(2×2) (*Figure 5.4*) would correspond to a coverage of ~0.4ML, whilst the saturation coverage (*Figure 5.5*) would correspond to ~0.64ML coverage.

5.5.2 Heating the Adlayer

Heating the surface (at various exposures) to 580K for 20mins and allowing to cool back to room temperature induced further changes in the LEED and RA responses of the system. These effects are shown for selected methanethiol coverages.

~0.3ML Coverage of Methanethiol

Figure 5.6 shows the effects of heating the surface with a coverage of ~0.3ML of methanethiol for various temperatures. The start point (*Figure 5.6(a)*) corresponds to *Figure 5.2(e)* and the LEED pattern shown in *Figure 5.3*.

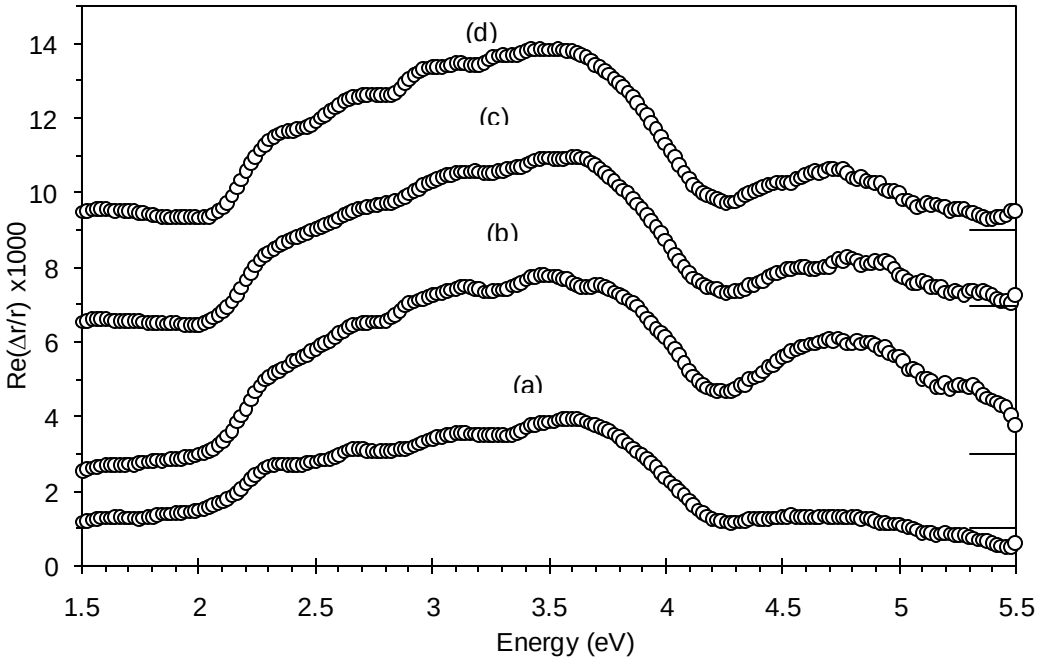

Figure 5.6: *RA response from (a) exposure to 0.09L methanethiol; the same surface at room temperature following heating to (b) 580K; (c) 690K and (d) 780K.*

The heating of the sample up from room temperature to 580K sees an increase in the overall RA response of the system between 2.2eV and 4.2eV, and the development of a positive feature centred at ~4.7eV. The LEED response of the system also changes from the broad and diffuse c(2×2) structure observed in *Figure 5.3* to a c(2×2) with spot splitting in the [001] direction as shown in *Figure 5.7*.

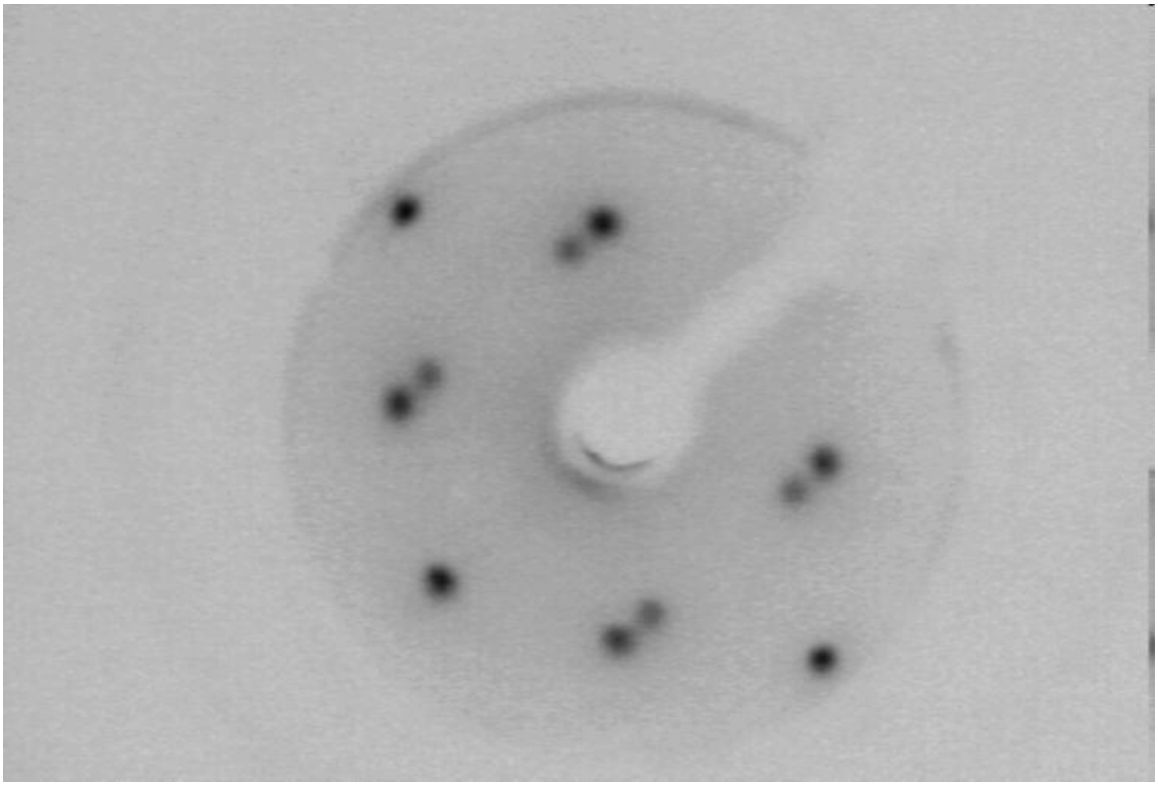

Figure 5.7: *LEED pattern corresponding to 0.09L exposure of methanethiol after heating to 580K (RAS Figure 5.6(b)), taken at 74eV.*

Subsequent heating of the system to 690K (*Figure 5.6(c)*), sees no major changes in either the LEED pattern or the RA response of the system. The peak in the RAS at ~4.7eV has become reduced in intensity whilst the rest of the spectrum remains unchanged. The LEED pattern observed was similar to that shown in *Figure 5.7* after heating to 580K.

Further heating to 780K (*Figure 5.6(d)*) again saw no changes in the LEED or RA response from that of the sample after heating to 690K.

~0.4ML Coverage of Methanethiol

Figure 5.8 shows the effects of heating the surface with a coverage of ~0.4ML of methanethiol for various temperatures. The start point (*Figure 5.8(a)*) corresponds to *Figure 5.2(f)* and the LEED pattern shown in *Figure 5.4*.

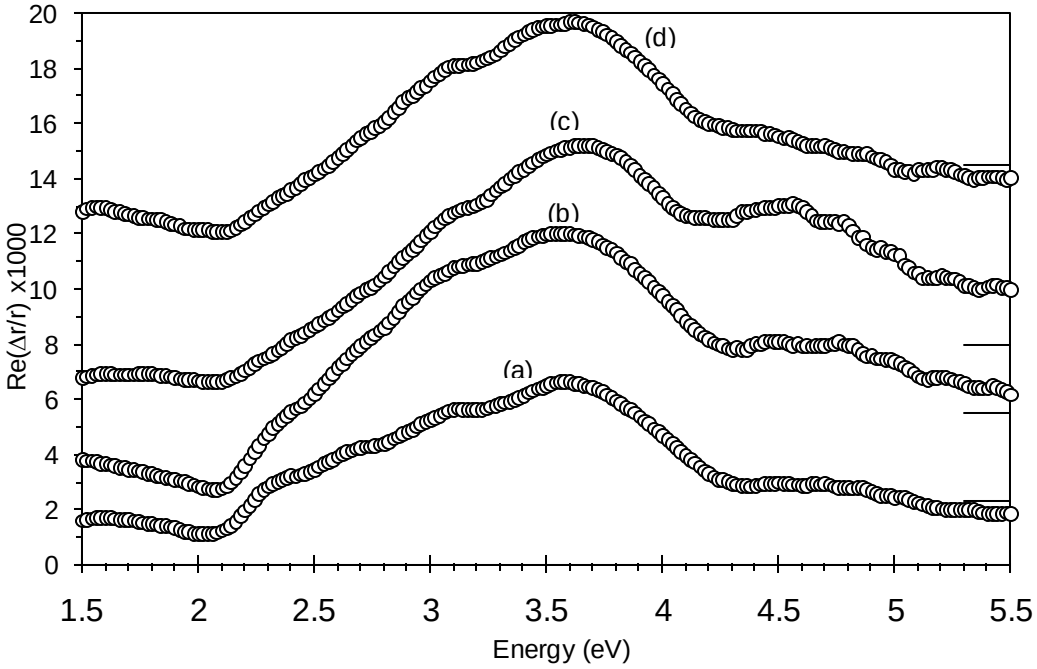

Figure 5.8: *RA response from (a) exposure to 0.4L methanethiol; the same surface at room temperature following heating to (b) 580K; (c) 690K and (d) 780K.*

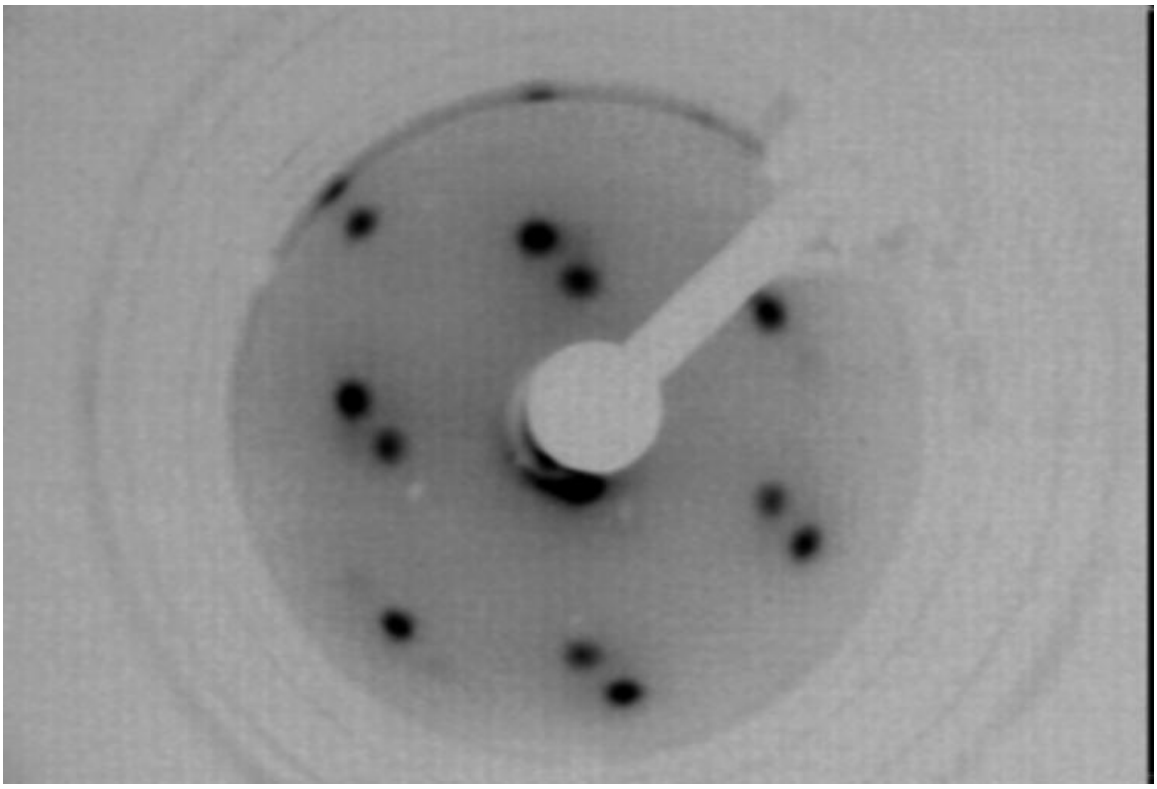

Figure 5.9: *LEED pattern corresponding to 0.4L exposure of methanethiol after heating to 580K (RAS Figure 5.8(b)), taken at 76eV.*

Again heating to 580K sees a large increase in the RA response between 2.2eV and 4.2eV. Again there is the development of a peak centred at ~4.7eV; however this feature is less pronounced than for the lower coverage (~0.3ML). The LEED response of the sample changes from a c(2×2) with spot splitting in both the [001] and $[1\bar{1}0]$ directions, to a c(2×2) with spot splitting in the $[1\bar{1}0]$ direction only.

Further heating of the sample to 690K (*Figure 5.8(c)*) sees the peak at ~4.7eV increase in intensity, thus causing the peak at ~3.7eV to look less pronounced than previously; however close examination of the spectrum shows that the region from 2.2-4.2eV has not changed in intensity. The LEED pattern observed was similar to the one taken after heating to 580K as shown in *Figure 5.9*.

Heating the sample to 780K (*Figure 5.8(d)*) sees the peak at ~4.7eV disappear and this region of the spectrum again becomes featureless. There is also a slight reduction in the intensity in the 2.2-4.2eV region of the RA spectrum. The LEED pattern observed at this point was similar to the patterns obtained after heating to 580K and 690K.

~0.64ML Methanethiol Saturation Coverage

Figure 5.10 shows the effects of heating the methanethiol saturated surface for various temperatures. The start point (*Figure 5.10(a)*) corresponds to *Figure 5.2(g)* and the LEED pattern shown in *Figure 5.5*.

Upon heating the methanethiol saturated surface to 580K there are no significant changes in the LEED pattern, the same c(8×2) pattern with missing spots is observed (*Figure 5.11*). The changes in the RA response are fairly minor, the spectrum appears to decrease in intensity. However this is not the case, it appears so because of the offsetting of the spectra. In fact the centres of the peaks at ~3.7eV match in intensity (before shifting); it is the increase in RA intensity at the lower energy of the spectrum (1.5-3.0eV) which is responsible for the discrepancy.

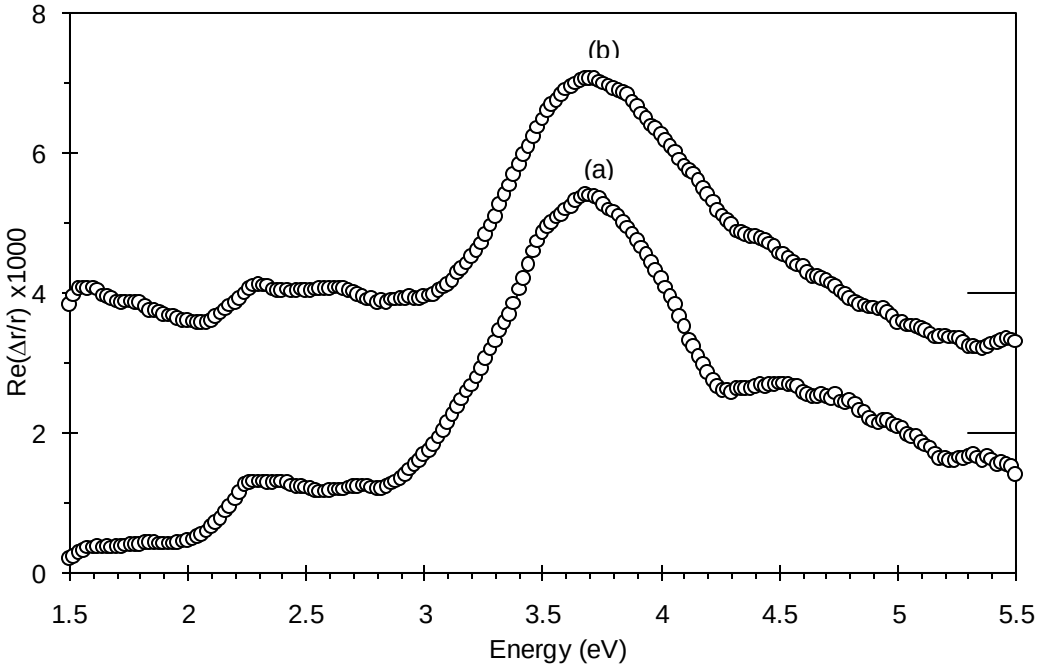

Figure 5.10: *RA response from (a) methanethiol saturated surface; (b) the same surface at room temperature following heating to 580K.*

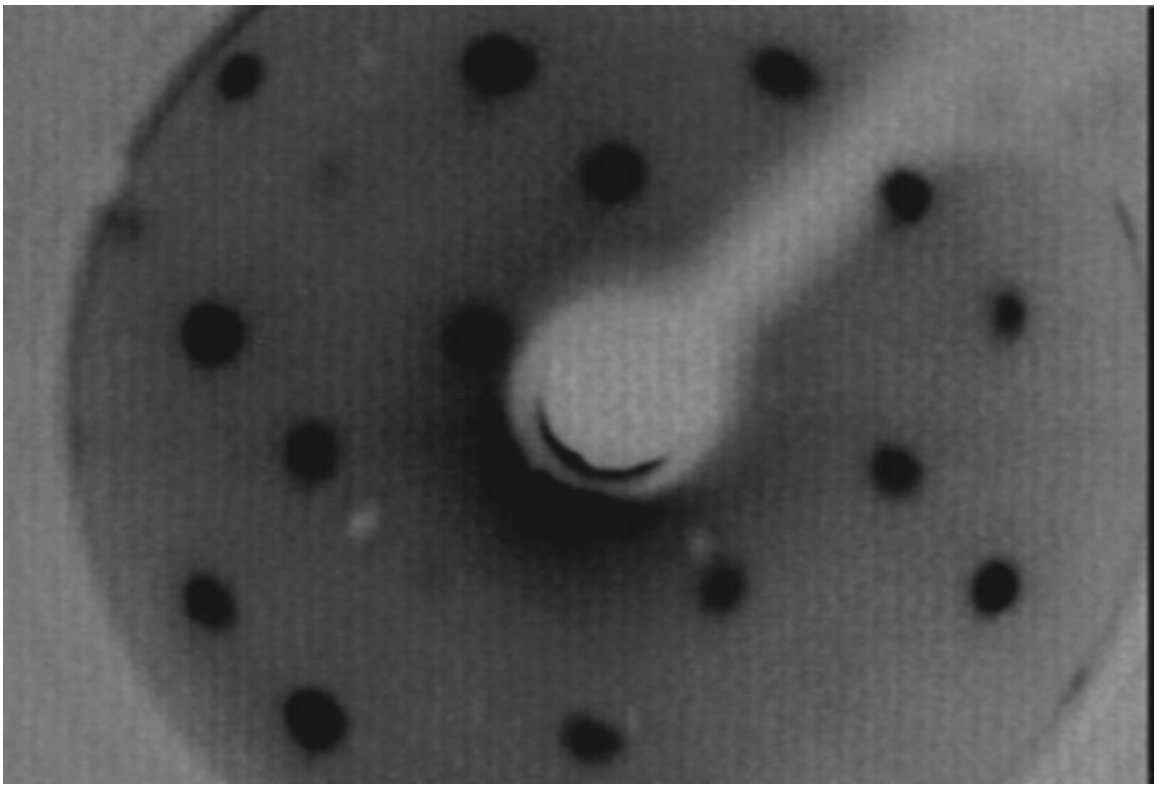

Figure 5.11: *LEED pattern corresponding methanethiol saturated surface after heating to580K (RAS Figure 5.8(b)), taken at 71eV.*

5.6 Discussion

5.6.1 Methanethiol Exposed Surface

Low Methanethiol Coverage < 0.3ML

Observing the results of *Figure 5.2(a-e)*, the most obvious change in the RA response of the signal is the reduction in anisotropy in the 2.1eV region of the spectrum. As discussed in *Chapter 4* this feature contains a large surface state contribution and the reduction in intensity of this feature with exposure to the methanethiol is consistent with a quenching of the surface state transitions, due to unoccupied states which exist on the clean surface becoming occupied due to the presence of the adsorbate. Deposition of various other molecules onto the Cu(110) surface has seen a similar effect [5.29, 5.41-5.47]; again as observed in the ion bombarding work carried out in *Chapter 4* the peak intensity is reduced at a faster than linear rate. A similar observation was made by Sun et al. with the adsorption of CO [5.47].

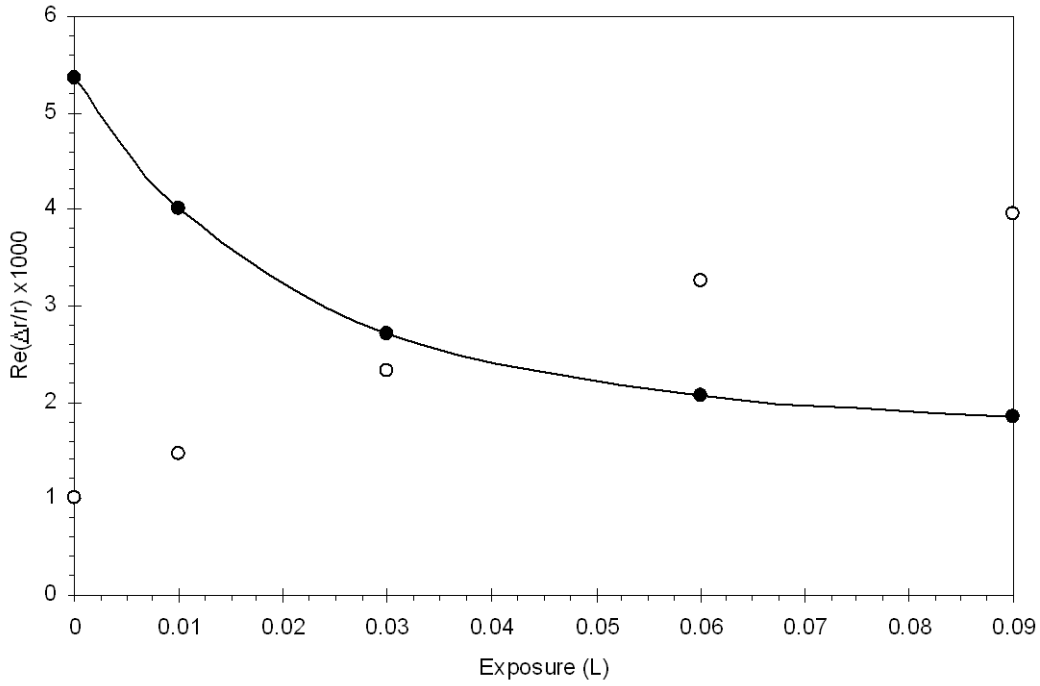

Figure 5.12: *Comparison of RA intensities at 2.1eV (filled circles) and 3.6eV (open circles) as a function of methanethiol exposure.*

Assuming coverage scales linearly with exposure (a valid approximation for low coverages) and knowing that the coverage at an exposure of 0.09L is 0.3ML; the rate at which the 2.1eV feature is quenched (*Figure 5.12*)can be fitted to a patch size of *N*=4 using the methods outlined in *Chapter 4*.

The other change in the spectrum sees an increase in anisotropy 2.3-3.8eV as this region which is initially flat on the clean surface starts to develop a positive feature which is linear with exposure of the molecule. This effect continues with further exposure of methanethiol.

The region above ~4eV exhibits a negative feature centred at ~4.2eV and a positive feature at ~4.7eV both of which reduce in intensity with exposure. Peaks are visible in the clean Cu(110) spectrum at similar energies and for the clean spectrum have been attributed to bulk to bulk transitions (these are discussed in more detail in *Chapter 4*). It is likely that for low coverages of methanethiol these features could still be observed, but as coverage increases their intensities are reduced.

The broad and diffuse c(2×2) LEED pattern suggests the structure is not perfectly ordered all across the surface as would be indicated by sharp LEED spots. At such low coverages it is likely that the structure is growing in islands, and hence there are regions with high concentrations and regions with low concentrations of the adsorbate such an explanation was proposed by Carley et al. [5.19-5.20] in STM studies of the system.

High Methanethiol Coverage > 0.3ML

Further exposure of the sample to methanethiol from *Figure 5.2 (e)* to *Figure 5.2 (f)* sees the continued increase in the RA signal in the region 2.3-4.8eV with a peak centred at ~3.7eV, with a shoulder like feature at ~3.2eV. The c(2×2) LEED pattern in *Figure 5.3* corresponding to RA spectra in *Figure 5.2 (e)* has now undergone spot splitting and where there was initially only a single diffuse spot was present, *Figure 5.4* clearly shows four sharper spots indicating a more ordered structure.

The observation from LEED that there is now a more ordered structure means that it is not surprising that there is a significant increase in the RA response.

Again further exposure of the sample to methanethiol from *Figure 5.2 (f)* to *Figure 5.2 (g)* sees a further increase in the RA signal around the peak centred on ~3.7eV; however there is a flattening out of the region between 2.3 and 3.0eV, which results in the 3.7eV feature looking like a more clearly defined peak than at lower coverages, as the feature continually grows with exposure to the molecule up until saturation it seems apparent that this feature indicates a measure of the molecule's coverage of the surface.

5.6.2 After Heating

As mentioned previously the XPS results of Carley et al. [5.20] show that dissociation of the mercaptide molecule begins for low coverages at 325K and for higher coverages at 400-450K. This dissociation sees the breaking of the sulphur-carbon bond and leaves a sulphur adlayer on the surface.

0.3ML Coverage Methanethiol

For the coverage of ~0.3ML of methanethiol the temperature of 580K is significantly higher than the temperatures at which Carley et al. saw the dissociation of the molecule. The changes in the LEED pattern after heating; from broad and diffuse spots to sharper more well defined spots, indicate an increase in surface order. The increase in the RA response across the spectrum would be consistent with this. Another possible explanation would be an increase in coverage of the molecule on the surface, as the methanethiol exposure experiments in this work and the work of Boulliard et al. [5.17] see the appropriate changes in the LEED pattern when coverage is increased. However due to measures taken in the experimental method it is unlikely that there is any methanethiol remaining in the system; so this explanation can be discounted.

An increase in surface order is likely to come about due to the removal of the CH_3 group. As the mercaptide molecule bonds to the surface through only one anchoring

point (the sulphur atom) there is little to determine the orientation of the sulphur-carbon bond on initial adsorption onto the surface. Once island growth has begun it is possible that each island will impose a preferential orientation on its growth, but the orientation imposed by different islands is unlikely to be consistent across the surface, leading to a cancellation of the RAS signal.

As the LEED patterns obtained are the same as Boulliard et al. [5.17] observe from hydrogen sulphide it seems that that the LEED response is obtained from the sulphur atoms rather than from the CH_3 group. The presence of this CH_3 group is therefore likely to have a "masking" effect on the LEED pattern obtained. The removal of this group could explain the change from a diffuse LEED pattern to a sharper, more well defined pattern.

As further heating sees no further changes to the spectrum it can be assumed that no subsequent re-ordering of the surface takes place, and as all the CH_3 has been removed the RA response is due to the sulphur on the surface.

~0.4ML Coverage Methanethiol

Upon heating of the sample with ~0.4ML coverage of methanethiol to 580K there is again an increase in intensity of the RA response of the system across the spectral range with no significant change in spectral lineshape except for the development of the feature at ~4.7eV. Again the change in RA response is accompanied by a change in the LEED pattern. Where the initial pattern (*Figure 5.4*) was a c(2×2) pattern with splitting of the ½ order spots in both the $[1\bar{1}0]$ and [001] directions, the pattern observed after heating was a c(2×2) with splitting of the ½ order spots in the $[1\bar{1}0]$ direction only. This pattern was reported by Boulliard et al. [5.17] for the deposition of hydrogen sulphide at a coverage of 0.45ML after observing splitting in both directions for lower coverages (0.37-0.44ML). This would indicate an increase in coverage of the molecule on the surface. However as there was no more methanethiol present in the system this cannot be the explanation. A more likely explanation is that the heating of the surface allows some re-ordering of surface

structure but no change in the coverage occurs; this would explain both the changes in the LEED and RA response of the system.

~0.64ML Coverage Methanethiol

The heating of the methanethiol saturated surface has little effect on either the RA response or the LEED pattern, which suggests that no re-ordering occurs (a saturated surface is more difficult to restructure) and that the signal is due to the sulphur on the surface and that the presence or absence of the CH_3 group makes little difference to the response obtained from the surface. It is now useful to compare the RA response of this system with the RA study of another sulphur containing molecule L-Cysteine [5.29].

Comparison with L-Cysteine

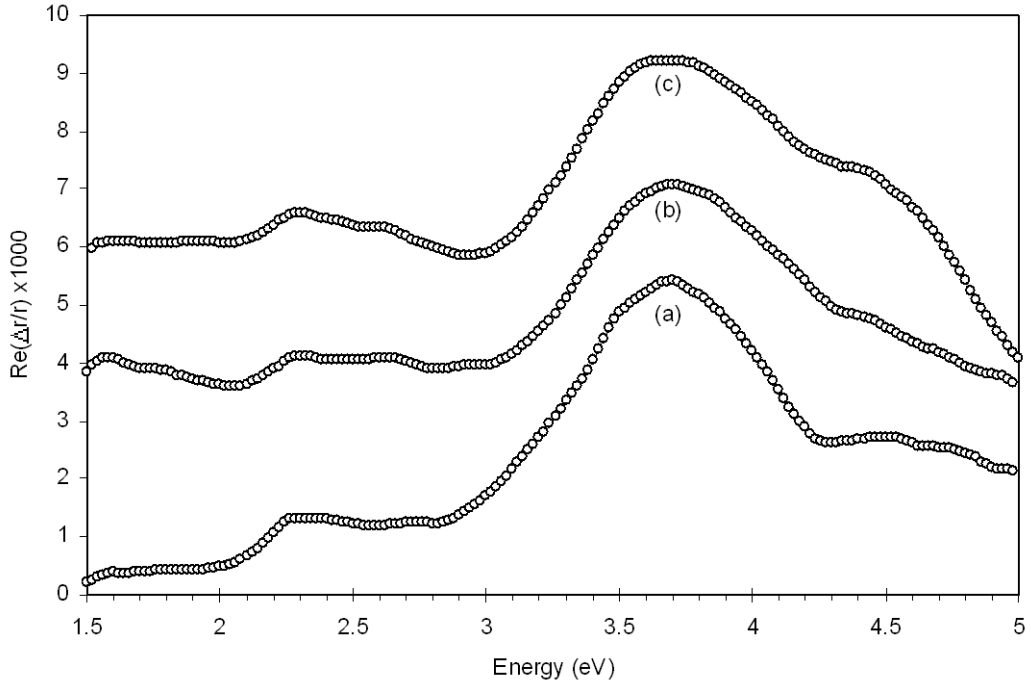

Figure 5.13: *Comparison of RA spectra of S/Cu(110) c(8×2) obtained via different methods: (a) methanethiol at room temperature, (b) after heating methanethiol, (c) after heating L-Cysteine (Results from Ref 5.29).*

Figure 5.13 shows a comparison of three sulphur containing species adsorbed on the surface of Cu(110) in a c(8×2) arrangement; those obtained from methanethiol at room temperature and those after heating methanethiol are compared with the results of Isted et al. [5.28-5.29] for a sulphur layer formed after the heating (and dissociation of) L-Cysteine. All three systems show a very similar RA line shape in the region of 1.5-4.0eV with a large positive feature centred at ~3.7eV which indicates that this is a RAS fingerprint of a high sulphur coverage on the Cu(110) surface.

5.7 Simulations

It is possible to simulate RA spectra using a number of methods, the principles of some of which have been discussed earlier in this thesis (e.g. the three phase model and the derivative model). In order to calculate the RA spectra of Sulphur on Cu(110) it is necessary to use a more complex system than the 3-phase model [5.48-5.49]. As the initial copper surface is anisotropic and the experimental results show a change in the RA response the system once the adsorbate material is deposited the system can then be considered to consist of 4 layers: (i) an incident or vacuum medium, (ii) an anisotropic sulphur layer, (iii) an anisotropic copper layer and (iv) a bulk copper substrate.

5.7.1 A 4-Phase Model

Heavens [5.49] defines the Fresnel reflection coefficient for a 4-phase system as:

$$r_{1234} = \frac{r_{12} + r_{23}e^{-2i\beta_1} + r_{34}e^{-2i(\beta_1+\beta_2)} + r_{12}r_{23}r_{34}e^{-2i\beta_2}}{1 + r_{12}r_{23}e^{-2i\beta_1} + r_{12}r_{34}e^{-2i(\beta_1+\beta_2)} + r_{23}r_{34}e^{-2i\beta_2}} \qquad \textit{Eqn. 5.1}$$

By applying the method of MacIntyre and Aspnes [5.48] for the 3-phase system it is possible to derive an equivalent expression for the 4 layer system:

$$r_{14} = \frac{r_{12} + r_{23} + r_{34} + r_{12}r_{23}r_{34}}{1 + r_{12}r_{23} + r_{12}r_{34} + r_{23}r_{34}} \qquad \textit{Eqn. 5.2}$$

Combining *Eqns 5.1* and *5.2* we obtain:

$$\frac{r_{1234}}{r_{14}} = \frac{1 - 2i\left[\left(\beta_1 r_{12}r_{23} + (\beta_1 + \beta_2)r_{12}r_{34} + \beta_2 r_{12}r_{23}r_{34}\right)/\left(r_{12} + r_{23} + r_{34} + r_{12}r_{23}r_{34}\right)\right]}{1 - 2i\left[\left(\beta_1 r_{12}r_{23} + (\beta_1 + \beta_2)r_{12}r_{34} + \beta_2 r_{23}r_{34}\right)/\left(1 + r_{12}r_{23} + r_{12}r_{34} + r_{23}r_{34}\right)\right]}$$

Eqn. 5.3

Expanding the denominator as a binomial series and neglecting terms higher than first order in β:

$$\frac{r_{1234}}{r_{14}} = 1 + 2i\left[\frac{A - C}{\left(1 + r_{12}r_{23} + r_{12}r_{34} + r_{23}r_{34}\right)\left(r_{12} + r_{23} + r_{34} + r_{12}r_{23}r_{34}\right)}\right] \qquad \textit{Eqn. 5.4}$$

where:

$$A = \beta_1 r_{12}{}^2 r_{23} + (\beta_1 + \beta_2)r_{12}{}^2 r_{34} + \beta_2 r_{23}{}^2 r_{34} + \beta_2 r_{23} r_{34}{}^2 + \beta_1 r_{12}{}^2 r_{23}{}^2 r_{34} + (\beta_1 + \beta_2)r_{12}{}^2 r_{23} r_{34}{}^2 + \beta_2 r_{12} r_{23}{}^2 r_{34}{}^2 \qquad \textit{Eqn. 5.5}$$

$$C = \beta_1 r_{23} + (\beta_1 + \beta_2)r_{34} + \beta_2 r_{12}{}^2 r_{23}{}^2 r_{34} + \beta_2 r_{12}{}^2 r_{23} r_{34}{}^2 + \beta_1 r_{23}{}^2 r_{34} + (\beta_1 + \beta_2)r_{23} r_{34}{}^2 + \beta_2 r_{12} r_{23}{}^2 r_{34}{}^2 \qquad \textit{Eqn. 5.6}$$

For normal incidence the Fresnel coefficients at an interface can be written:

$$r_{ij} = \frac{N_j - N_i}{N_j + N_i} \qquad \textit{Eqn. 5.7}$$

the values of β are given by:

$$\beta_1 = \frac{\omega}{c} N_2 d_1 \qquad \beta_2 = \frac{\omega}{c} N_3 d_2 \qquad \textit{Eqn. 5.8}$$

where d_1 and d_2 are the thicknesses of the first and second surface layers respectively, and the two surface layers must still meet the criteria of the thin film approximation i.e. $\lambda >> d_1+d_2$.

using $N^2 = \varepsilon$, and if the incident medium is vacuum $\varepsilon_1 = 1$, *Eqn 5.4* then becomes:

$$\frac{r_{1234}}{r_{14}} = 1 - 2i\frac{\omega}{c}\left[\frac{d_1(\varepsilon_2 - \varepsilon_4) + d_2(\varepsilon_3 - \varepsilon_4)}{(1 - \varepsilon_4)}\right] \qquad \textit{Eqn. 5.9}$$

The 3-phase model can be obtained from this expression by making either the first surface layer an extension of the incident (vacuum) medium or second surface layer a extension of the bulk; this is done by setting $r_{12} = 0$ and $\beta_1 = 0$ or $r_{23} = 0$ and $\beta_2 = 0$. (The values of β can be set to zero as the layer has become an extension of either the incident medium or the bulk medium, both of which are semi-infinite in thickness meaning the value of β is negligible in comparison.)

For anisotropic surface layers the Fresnel reflection coefficients are different along the two principal crystallographic directions *x* and *y*, meaning *Eqn 5.9* can be split into *x* and *y* components:

$$\frac{r_x}{r} = 1 - 2i\frac{\omega}{c}\left[\frac{d_1(\varepsilon_{2(x)} - \varepsilon_4) + d_2(\varepsilon_{3(x)} - \varepsilon_4)}{(1 - \varepsilon_4)}\right] \qquad \textit{Eqn. 5.10}$$

$$\frac{r_y}{r} = 1 - 2i\frac{\omega}{c}\left[\frac{d_1(\varepsilon_{2(y)} - \varepsilon_4) + d_2(\varepsilon_{3(y)} - \varepsilon_4)}{(1 - \varepsilon_4)}\right] \qquad \textit{Eqn. 5.11}$$

It is worth pointing out at this point that the two surface layers in the model will have the same optical axes; this will not necessarily be the case for the experiment. The relative orientations of the two films can be determined experimentally using ADRAS [5.50-5.51] (a brief discussion of which is given in *Chapter 2*).

By subtracting *Eqn. 5.11*, from *Eqn. 5.10*, defining $\Delta r = r_x - r_y$ and considering $\omega = 2\pi f$ and $\lambda = c/f$ the reflection anisotropy is given by:

$$\frac{\Delta r}{r} = -\frac{4i\pi}{\lambda}\left[\frac{d_1\left(\varepsilon_{2(x)} - \varepsilon_{2(y)}\right) + d_2\left(\varepsilon_{3(x)} - \varepsilon_{3(y)}\right)}{1-\varepsilon_4}\right] \qquad \textit{Eqn. 5.12}$$

The real part of $\Delta r/r$ can then be written as:

$$\mathrm{Re}\left(\frac{\Delta r}{r}\right) = -\frac{4\pi}{\lambda}\left\{d_1\,\mathrm{Im}\left[\frac{\Delta\varepsilon_2}{1-\varepsilon_4}\right] + d_2\,\mathrm{Im}\left[\frac{\Delta\varepsilon_3}{1-\varepsilon_4}\right]\right\} \qquad \textit{Eqn. 5.13}$$

This result allows the simulation of adsorbate materials on anisotropic surfaces; previously it would only have been possible to simulate a layer of an adsorbate material on a bulk substrate.

5.7.2 Multilayer Systems

Extension of the method to enable its application to multilayered systems is possible providing the Fresnel reflection coefficients of the multilayered system is known, These can be found for transparent layers using the methods of Crook [5.52], Rouard [5.53], and Vašíček [5.54] as cited by Heavens [5.49], for adsorbing layers at normal incidence as outlined by Heavens [5.49]. For details for off normal incidence (a case not considered here) the reader is referred to the work of Abelés [5.55].

For *n* isotropic phases where layers 1 and *n* are the semi-infinite incident and substrate phases respectively the Fresnel formula for an *n* layered system can be written as:

$$\frac{r_{123..n}}{r_{1n}} \approx 1 + \sum_{j=2}^{n-1} \frac{4\pi i\sqrt{\varepsilon_j}\,d_j}{\lambda} \frac{r_{jn}\left(r_{1j}{}^2 - 1\right)}{\left(r_{1j} + r_{jn}\right)\left(1 + r_{1j}r_{jn}\right)} \qquad \textit{Eqn. 5.14}$$

For normal incidence it follows:

$$\frac{r_{123..n}}{r_{1n}} = 1 - \frac{2\pi i\sqrt{\varepsilon_1}}{\lambda(\varepsilon_1 - \varepsilon_4)}\sum_{j=2}^{n-1} d_j(\varepsilon_j - \varepsilon_b) \qquad \textit{Eqn. 5.15}$$

Hence when the surface layers are anisotropic the RA response has the form:

$$\frac{\Delta r}{r} = \sum_{j=2}^{n-1} \frac{4\pi i d_j}{\lambda} \frac{\Delta\varepsilon_j}{\varepsilon_b - 1} \qquad \textit{Eqn. 5.16}$$

Hence the RAS signal from a sample of multiple thin films is additive. This approximation is valid providing the sum of the thicknesses d_j is much less than the wavelength of light i.e.:

$$\sum_{j=2}^{n-1} d_j << \lambda \qquad \textit{Eqn. 5.17}$$

5.8 Simulating Sulphur on Copper

Now a method has been established to simulate the RA response from a 4 layer system the specific details of the sulphur on copper system must be considered. As discussed previously the system must consist of an isotropic infinite incident (vacuum) medium, a semi-infinite substrate and anisotropic copper and sulphur layers.

5.8.1 The Derivative Model – Copper

The copper layer can be simulated by using the derivative model [5.56], as was demonstrated by Sun et al. [5.57] for the clean copper surface.

The Derivative model was introduced earlier in *Chapter 4* and the RAS expression can be written in terms of bulk dielectric properties as:

$$\frac{\Delta r}{r} = \frac{4\pi i d}{\lambda} \frac{\Delta E_g - i\Delta\Gamma}{\varepsilon_b - 1} \frac{d\varepsilon_b}{dE} \qquad \textit{Eqn. 5.18}$$

where $\Delta E_g = \Delta E_g^x - \Delta E_g^y$ and $\Delta\Gamma = \Delta\Gamma^x - \Delta\Gamma^y$ are the differences in gap energies and linewidths in the *x* and *y* directions.

The real part of *Eqn. 5.18* can then be written as:

$$\Re\left(\frac{\Delta r}{r}\right) = X(E)\Delta E_g + Y(E)\Delta\Gamma \qquad \textit{Eqn. 5.19}$$

where if $\varepsilon_b = \varepsilon' + i\varepsilon''$ *X(E)* and *Y(E)* can be written:

$$X(E) = \frac{4\pi d}{\lambda} \frac{1}{(\varepsilon' - 1)^2 + \varepsilon''^2} \left(\varepsilon'' \frac{d\varepsilon'}{dE} + (\varepsilon' - 1)\frac{d\varepsilon''}{dE} \right) \qquad \textit{Eqn. 5.20}$$

$$Y(E) = \frac{4\pi d}{\lambda} \frac{1}{(\varepsilon' - 1)^2 + \varepsilon''^2} \left(\varepsilon' \frac{d\varepsilon''}{dE} + (\varepsilon' - 1)\frac{d\varepsilon'}{dE} \right) \qquad \textit{Eqn. 5.21}$$

When simulating clean Cu(110) the 2.1eV peak is not reproduced by the model due to the surface state transitions not contributing to the bulk dielectric function. As has been shown numerous times [5.29, 5.41-5.47] the adsorption of molecules on the surface causes a reduction in the number of unoccupied surface states meaning that the transitions no longer occur, therefore the absence of this peak in the derivative model simulation is appropriate. The dielectric function of copper was obtained from measurements by Stahrenberg et al. [5.58] and Palik [5.59]. The simulated RA response of the copper layer is shown in *Figure 5.14*.

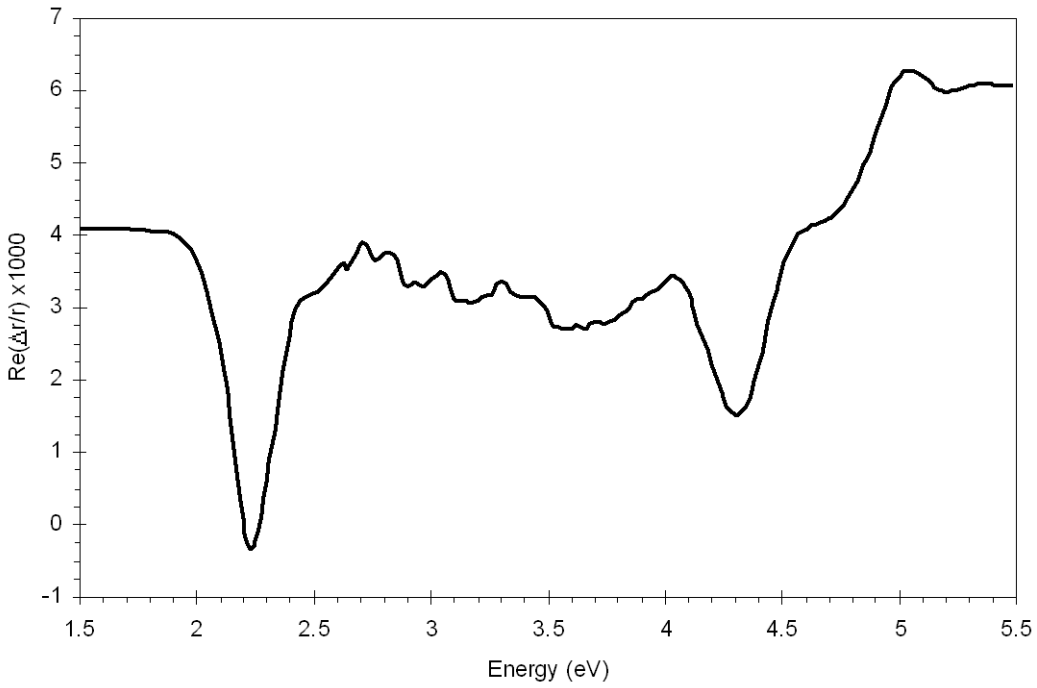

Figure 5.14: *Simulation of the RA of clean Cu(110) using the 3-phase and derivative model; d = 1nm, ΔE_g = 0.1, $\Delta\Gamma$ = 0.*

5.8.2 The Sulphur Layer

The sulphur layer is of more cause for concern. In order to simulate optical spectra homogeneous stratified layers are required; the sulphur layer on the surface is well ordered but incomplete – the saturation coverage is less than a monolayer hence there are gaps in the sulphur layer. In order to simulate this layer this effect must be accounted for.

Effective Medium Theory / Form Birefringence [5.60]

Birefringent effects can be observed to arise from an ordered system of particles of the form shown *Figure 5.15*:

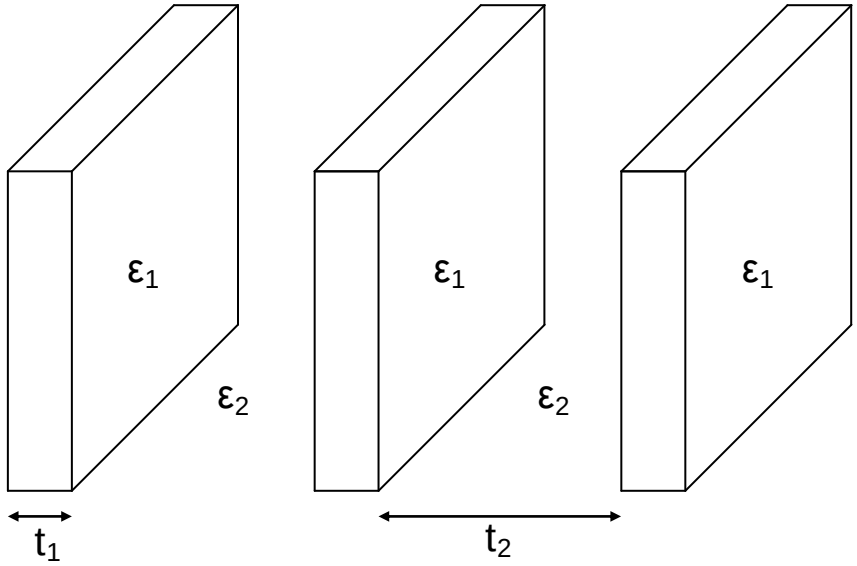

Figure 5.15: *An assembly of parallel plates which can give rise to form birefringence.*

If a monochromatic wave is incident on the system with its electric vector perpendicular to the direction of the plates, and the linear dimensions of the plates are large and the thicknesses small compared to the wavelength of light then the spaces may be considered uniform. Also the normal component of the electric displacement must be continuous across a surface at which the properties of the medium change abruptly; as a result the electric displacement must be the same inside the plates and the spaces.

If E_1 and E_2 are the electric fields:

$$E_1 = \frac{D}{\varepsilon_1} \qquad E_2 = \frac{D}{\varepsilon_2} \qquad \textit{Eqn. 5.22}$$

The mean E field averaged over the total volume is:

$$E = \frac{t_1 \frac{D}{\varepsilon_1} + t_2 \frac{D}{\varepsilon_2}}{t_1 + t_2} \qquad \textit{Eqn. 5.23}$$

The effective dielectric constant $\varepsilon_{\perp}$ is therefore:

$$\varepsilon_{\perp} = \frac{D}{E} = \frac{(t_1 + t_2)\varepsilon_1\varepsilon_2}{t_1\varepsilon_2 + t_2\varepsilon_1} = \frac{\varepsilon_1\varepsilon_2}{f_1\varepsilon_2 + f_2\varepsilon_1} \qquad \textit{Eqn. 5.24}$$

where:

$$f_1 = \frac{t_1}{(t_1 + t_2)} \quad f_2 = \frac{t_2}{(t_1 + t_2)} = 1 - f_1 \qquad \textit{Eqn. 5.25}$$

are fractions of the total volume occupied by the plates and the spaces respectively.

If the electric field has its wavevector parallel to the direction of the plates then the tangential component of the electric vector is continuous across the surface, hence the electric field will be the same inside the plates and the spaces.

$$D_1 = \varepsilon_1 E \qquad D_2 = \varepsilon_2 E \qquad \textit{Eqn. 5.26}$$

The mean electric displacement *D* is:

$$D = \frac{t_1\varepsilon_1 E + t_2\varepsilon_2 E}{t_1 + t_2} \qquad \textit{Eqn. 5.27}$$

Hence the effective dielectric constant is:

$$\varepsilon_{//} = \frac{D}{E} = \frac{t_1\varepsilon_1 + t_2\varepsilon_2}{t_1 + t_2} = f_1\varepsilon_1 + f_2\varepsilon_2 \qquad \textit{Eqn. 5.28}$$

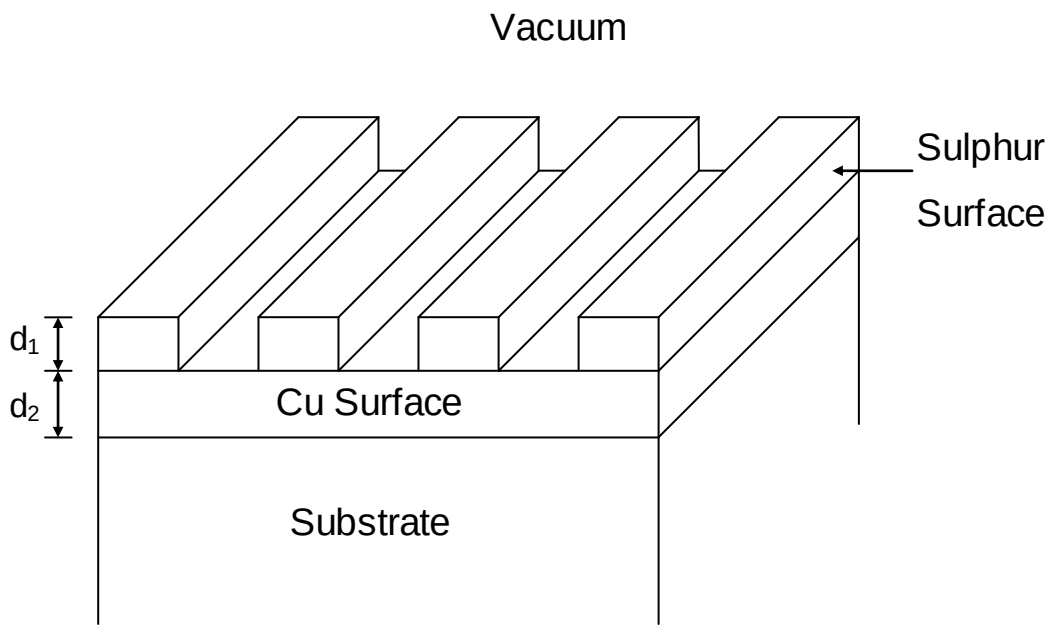

Figure 5.16: *A schematic diagram of how the physical system is modelled.*

By assuming the sulphur structure on the surface consists of "striped regions" i.e. there are regions where there are lines of sulphur atoms adjacent to regions where there are no sulphur atoms. Then *Eqns. 5.3 & 5.7* can be used to create an effective medium layer which is stratified in nature but has the properties of the striped surface, where ε_1 and ε_2 are the dielectric properties of sulphur and vacuum respectively. This can now be inserted into the model as the sulphur layer of the system. This technique has been used previously to model the effects of surface roughness in the simulation of optical spectra [5.61-5.64]. The dielectric function of sulphur was obtained from [5.65]. A schematic diagram of how the system is modelled is shown in *Figure 5.16*.

5.8.3 Results

The fitting parameters for the simulations were d_1 = 0.18nm, $f_1 = f_2$ = 0.5 and d_2 = 0.02nm. These thicknesses appear rather small; it is worth pointing out that the thickness of the effective medium layer is the thickness of a stratified layer with the same dielectric properties as the striped layer it represents. Hence both thicknesses are fitting parameters and have no real physical significance, other than to scale the relative anisotropic intensities of the two films.

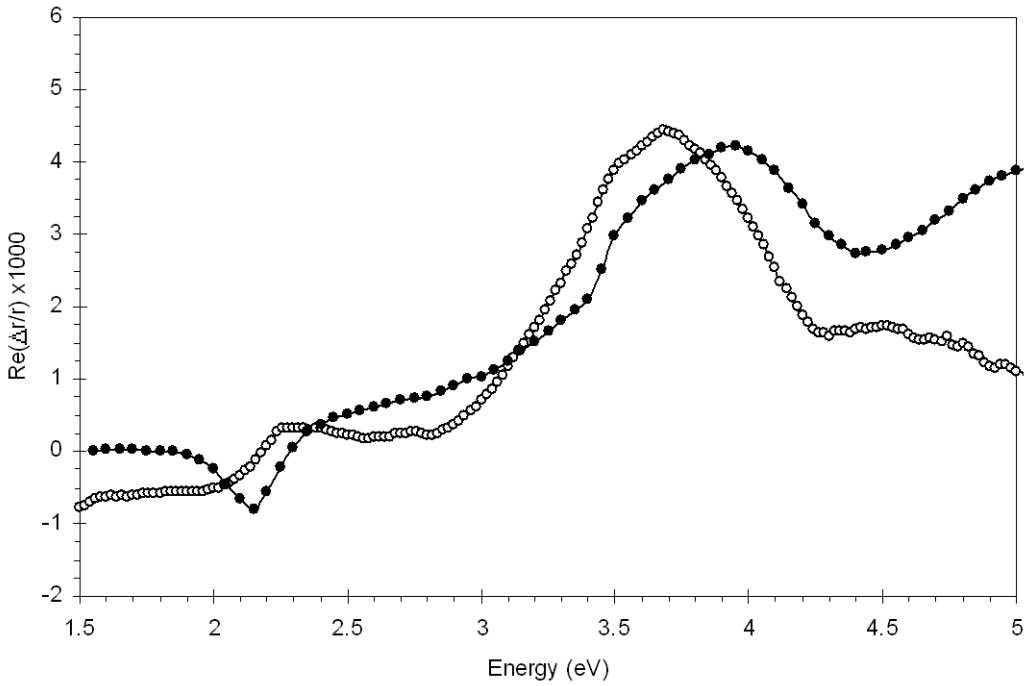

Figure 5.17: *Comparison of simulation (open circles) with experiment (filled circles) for saturated coverage of sulphur on copper*

5.8.4 Discussion

The simulation gives a good match to the experimental spectrum (*Figure 5.17*) reproducing its main results rather well and given the simplicity of the model this is as good as could be expected. The effective medium layer produces the feature in the 3-4eV region of the spectrum, whilst the derivative copper layer produces the negative feature at ~2eV. This feature can be attributed to anisotropic perturbation of the bulk electron bands in the vicinity of the *X* point of the Brillouin zone.

5.9 Conclusions

Depositing methanethiol on the Cu(110) surface results in a sequence of LEED patterns (coverage dependent) which are similar to those obtained in other studies of

sulphur containing molecules and are indicative of the thiolate linkage of the molecule to the surface. The RA response corresponding to this surface sees changes across the spectral range from that of the clean Cu(110) surface. Heating of the surface sees the decomposition of the molecule leaving a sulphur adlayer on the surface. Below saturation coverage sees re-ordering of the surface for which changes in both the RAS and LEED responses are observed. The saturation responses of the surface are very similar before and after heating. Comparison with an alternative method of obtaining a sulphur adlayer shows very similar results indicating that the method by which the adlayer is obtained is not so important as the structure and the thiolate linkage itself. A simple model also used to simulate the RA response of sulphur on copper and was able to reproduce the main features rather well.

5.10 References

[5.1] A. Ulman; Chem. Rev. **96**, 1533 (1996)

[5.2] A. Ulman, *An Introduction to Ultrathin Organic Films: Langmuir Blodgett to Self Assembly*, Academic, Boston (1991)

[5.3] A.W. Adamson; *Physical Chemistry of Surfaces* 3rd Edition, Wiley, New York (1976)

[5.4] G.M. Whitesides, J.P. Manthias and C.T. Seto; Science **254**, 1312 (1991)

[5.5] L.H. Dubois and R.G. Nuzzo, Annu. Rev. Phys. Chem. **43**, 437 (1992)

[5.6] Q. Chi, J. Zhang, J.U. Nielson, E. Friis, L. Chorkendorff, G.W. Canters, J.E.T. Anderson and J. Ulstrup; J. Am. Chem. Soc. **122**, 4047 (2000)

[5.7] C. Joachim, J.K. Gimzewski and A. Aviram; Nature **408**, 541 (2000)

[5.8] D.G. Castner and B.D. Ratner; Surf. Sci. **500**, 28 (2002)

[5.9] W.G. Schmidt and K. Seino; Surf. Rev. Lett. **10**, 221 (2003)

[5.10] V. Perebeinos and M. Newton; Chem. Phys. **319**, 159 (2005)

[5.11] A.F. Carley, P.R. Davies, R.V. Jones, K.R. Harikumar, M.W. Roberts and C.J. Welsby; Topics in Catalysis **22**, 161 (2003)

[5.12] A.F. Carley, P.R. Davies, R.V. Jones, K.R. Harikumar, G.U. Kulkarni and M.W. Roberts; Topics in Catalysis **11-12**, 299 (2000)

[5.13] J.L. Domange, J. Oudar; Surf. Sci. **11**, 124 (1968)

[5.14] A.R. Alemozafar, X.-C. Guo and R.J. Madix; Surf. Sci. **524**, L84 (2003)

[5.15] A.R. Alemozafar, X.-C. Guo and R.J. Madix; J. Chem. Phys. **116**, 4698 (2002)

[5.16] A. Atrei, A.L. Johnson and D.A. King; Surf. Sci. **254**, 65 (1991)

[5.17] J.C. Boulliard, M.P. Sotto, Surf. Sci. **217**, 38 (1989)

[5.18] I. Stensgaard, L. Ruan, F. Besenbacher, F. Jensen, and E. Laegsgaard; Surf. Sci. **269-270**, 81 (1992)

[5.19] A.F. Carley, P.R. Davies, R.V. Jones, K.R. Harikumar, G.U. Kulkarni and M.W. Roberts; Surf. Sci. **447**, 39 (2000)

[5.20] A.F. Carley, P.R. Davies, R.V. Jones, K.R. Harikumar and M.W. Roberts; Surf. Sci. **490**, L585 (2001)

[5.21] J.-G. Lee, J. Lee, and J.T. Yates Jr.; J. Phys. Chem. B **108**, 1686 (2004)

[5.22] S. D'Agostino, L. Chiodo, F. Della Sala, R. Cingolani and R. Rinaldi; Phys. Rev. B **75**, 195444 (2007)

[5.23] B.G. Frederick, R.J. Cole, J.R. Power, C.C. Perry, Q. Chen, N.V. Richardson, P. Weighman C. Verdozzi, D.R. Jennison, P.A. Schultz and M.P. Sears; Phys. Rev. B **58**, 10883 (1998)

[5.24] D.S. Martin, R.J. Cole and S. Haq; Phys. Rev. B **66**, 155427 (2002)

[5.25] D.S. Martin, R.J. Cole and S. Haq; Surf. Sci **539**, 171 (2003)

[5.26] L.D. Sun, M. Hohage, P. Zeppenfeld and R.E. Balderas-Navarro; Phys. Stat. Sol. (c) **8**, 3022 (2003)

[5.27] L.D. Sun, M. Hohage and P. Zeppenfeld; Phys. Rev. B **69**, 45407 (2004)

[5.28] G.E. Isted, D.S. Martin and R.J. Cole; (In Preperation)

[5.29] G.E. Isted; *Studies of the L-Cystine/noble metal interface and the preparation of noble metal surfaces for biomolecular adsorption*, PhD Thesis, The University of Liverpool (2006)

[5.30] R.J. Cole, B.G. Frederick, J.R. Power, C.C. Perry, Q. Chen, C. Verdozzi, N.V. Richardson and P. Weightman; Phys. Stat. Sol. (a) **170**, 235 (1998)

[5.31] B.G. Frederick, J.R. Power, R.J. Cole, C.C. Perry, Q. Chen, S. Haq, Th. Bertrams, N.V. Richardson and P. Weightman; Phys. Rev. Lett. **80**, 4490 (1998)

[5.32] G.E. Isted, D.S. Martin, C.I. Smith, R. LeParc, R.J. Cole and P. Weightman; Phys. Stat. Sol (c) **12**, 4012 (2005)

[5.33] D.S. Martin, G.E. Isted, R.J. Cole and P. Weightman; Phys. Stat. Sol (c) **12**, 4043 (2005)

[5.34] R. LeParc, C.I. Smith, M.C. Cuquerella, R.L. Williams, D.G. Fernig, C. Edwards, D.S. Martin and P. Weightman; Langmuir **22**, 3413 (2006)

[5.35] B.G. Frederick and N.V. Richardson; J. Electron Spectrosc. Relat. Phenom. **73**, 149 (1995)

[5.36] B.G. Frederick, C. Chen, S.M. Barlow, N.G. Condon, F.M. Leibsle and N.V. Richardson; Surf. Sci. **352**, 238 (1996)

[5.37] Ph. Hoffman, K.C. Rose, V. Fernandez, A.M. Bradshaw and W. Richter; Phys. Rev. Lett. **75,** 2039 (1995)

[5.38] B.F. MacDonald and R.J.Cole; Phys. Stat. Sol. (a) **188**, 1489 (2001)

[5.39] B.F. MacDonald; *Reflection Anisotropy Spectroscopy and Scanning Probe Microscopy Studies with Applications to Liquid Crystal Alignment Layers,* PhD Thesis, The University of Edinburgh (2002)

[5.40] D.S. Martin, R.J. Cole and P. Weightman; Phys. Rev. B **72**, 35408 (2005)

[5.41] K. Stahrenberg, Th. Herrmann, N. Esser and W. Richter; Phys. Rev. B **61**, 3043 (2000)

[5.42] G.E. Isted and D.S. Martin; Appl. Surf. Phys. **252,** 1883 (2005)

[5.43] N.P. Blanchard, D.S. Martin, A.M. Davarpanah, S.D. Barrett and P. Weightman; Phys. Stat. Sol. (a) **118**, 1505 (2001)

[5.44] D.S. Martin, A.M. Davarpanah, S.D. Barrett and P. Weightman; Phys. Rev. B **62**, 15417 (2000)

[5.45] D.S. Martin and P. Weightman; J. Phys.: Condens. Matter, **14**, 675 (2002)

[5.46] B.G. Frederick, J.R. Power, R.J. Cole, C.C. Perry, Q. Chen, S. Haq, Th. Bertrams, N.V. Richardson and P. Weightman; Phys. Rev. Lett. **80,** 4490 (1998)

[5.47] L.D. Sun, M. Hohage, P. Zeppenfeld, R.E. Balderas-Navarro, K. Hingeri, Phys. Rev. Lett. **90**, 106104 (2003)

[5.48] J.D.E. McIntyre and D.E. Aspnes; Surf. Sci. **24**, 417 (1971)

[5.49] O.S. Heavens; *Optical Properties of Thin Solid Films*, Butterworths, London (1955)

[5.50] B.F. MacDonald and R.J. Cole; Appl. Phys. Lett. **80**, 3527 (2002)

[5.51] B.F. MacDonald, J.S. Law and R.J. Cole; J. Appl. Phys. **93**, 3320 (2003)

[5.52] A.W. Crook; J. Opt. Soc. Am. **38**, 954 (1948)

[5.53] P. Rouard; Ann. d. Physique **7**, 291 (1937)

[5.54] A. Vašíček; J. d. Phys. **11**, 342 (1950)

[5.55] F. Abelés; Ann. d. Physique **3**, 504 (1948)

[5.56] U. Rossow, L. Mantese and D.E. Aspnes; J. Vac. Sci. Technol. B **14**, 3070 (1996)

[5.57] L.D. Sun, M.Hohage, P. Zeppenfeld, R.E. Balderas-Navarro and K. Hingerl; Surf. Sci. **527**, L184 (2003)

[5.58] K. Stahrenberg, Th. Herrmann, K Wilmers, N. Esser, W. Richter, and M.J.G. Lee, Phys. Rev. B **64**, 115111 (2001)

[5.59] D.W. Lynch and W.R. Hunter, in *Handbook of Optical Constants of Solids*, E.D. Palik (Ed.) Academic Press, Orlando/London (1985)

[5.60] M. Born and E. Wolf, *Principles of Optics* 7th Edition, Cambridge University Press, Cambridge (1999)

[5.61] D.E. Aspnes, J.B. Theeten and F. Hottier; Phys. Rev. B **20**, 3292 (1979)

[5.62] D.E. Aspnes; Phys. Rev. B **41**, 10334 (1990)

[5.63] O. Acher, S.M. Koch, F. Omnes, M. Defour and M. Razeghi; J. Appl. Phys. **68**, 3564 (1990)

[5.64] N. Blayo, R.A. Cirelli, F.P. Klemens and J.T.C. Lee; J. Opt. Soc. Am. A **12**, 591 (1995)

[5.65] K.A. Fuller, H.D. Downing and M.R. Querry, in *Handbook of Optical Constants of Solids III*, E.D. Palik (Ed.) Academic Press, San Diego (1998)

Chapter 6: Angular Effects in RAS

6.1 Introduction

So far in this work only the standard set up of the RAS kit (as defined in *Chapter 2*) has been considered for taking measurements; the idea of ADRAS [6.1-6.2] was discussed briefly and this can be useful particularly in determining the RA response from multilayer systems and determining orientations of different overlayers. Besides the ADRAS rotation of the sample there are a number of angular effects which affect the observed RA response. This chapter considers the effect some of these angles have on the system. These effects can be split into two parts: the first part uses the Jones formalism to simulate the effects of rotating spectrometer components; the second part simulates the effects of tilt and off normal incidence. All the results in this chapter are simulated using the 4×4 matrix formalism for anisotropic stratified media described in *Appendix A*.

6.2 Defining the system

The RA response of the system can be considered in two parts: firstly as the response of the sample itself, which has been the main focus of the earlier work in this thesis, secondly the effect the spectrometer has on the signal. The spectrometer consists of a number of polarisation sensitive elements which affect either the light incident on the sample (polariser) or on the light reflected from the surface (PEM and analyser). The relationship between the spectrometer and the sample also need to be considered (the plane of incidence).

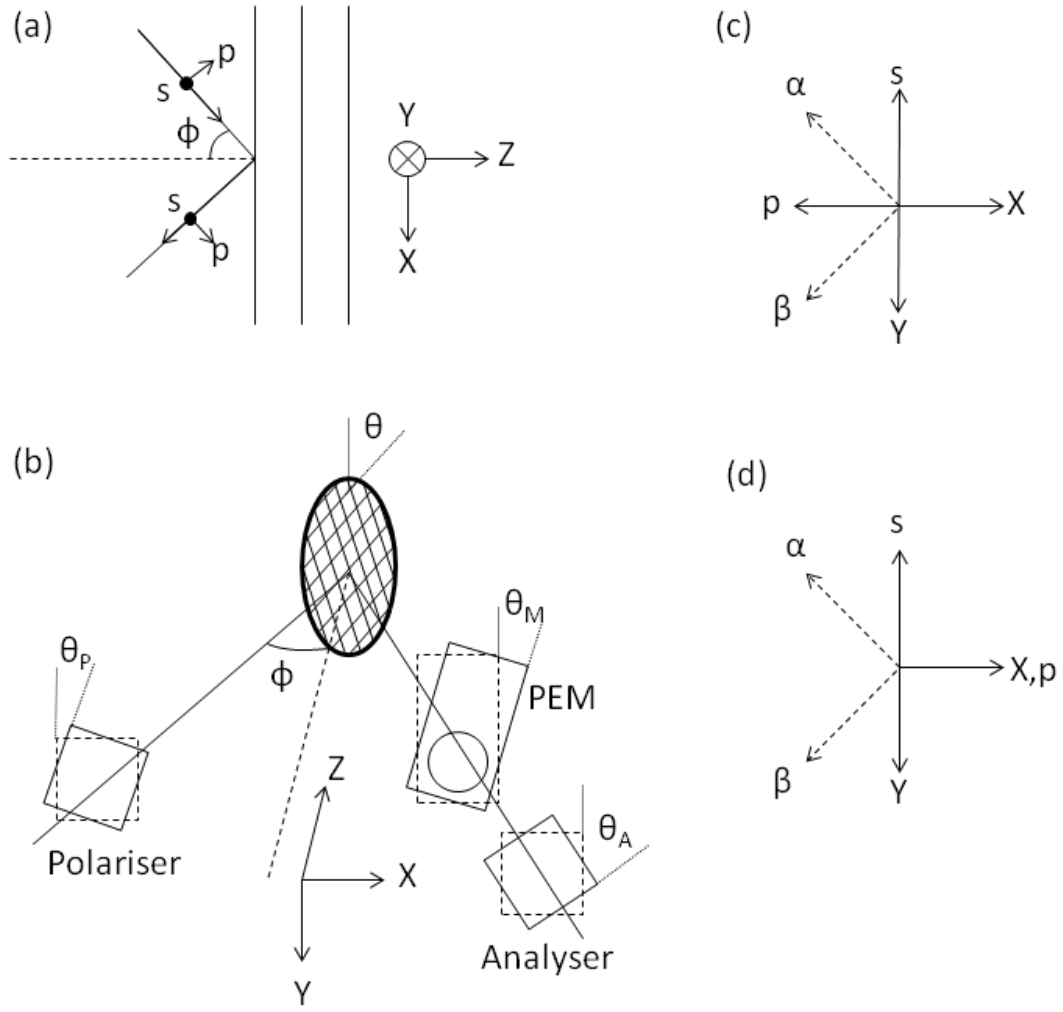

Figure 6.1: *(a): Schematic representation of a reflection from a stratified sample with lab co-ordinates and s- and p- directions indicated for incident and reflected beams. (b): The RAS spectrometer component orientation angles defined. (c) & (d): The relationship between the sp and αβ basis vectors for (c) incident and (d) reflected beams. (x and y axes for normal incidence are also shown).*

The system considered will be defined with respect to the lab frame, denoted by capital *X*, *Y* & *Z* (lower case *x*, *y* & *z* denote dielectric directions); the sample surface normal is the *Z*-direction with light incident upon the surface considered to be moving in the positive *Z*-direction. The plane of incidence is the *X*-*Z* plane; all spectrometer component angles are defined by clockwise rotations of the primary axis from the vertical (the negative *Y*-direction) as seen by an observer facing the sample.

The sample is considered to be a layered non-gyroscopic material consisting of interfaces parallel to the *X-Y* direction. Each layer has its own distinct set of orthogonal dielectric properties and is of defined thickness, while the sample bulk is considered to be semi-infinite. Rotation of the sample azimuthal angle considers the rotation of the whole sample (bulk and all surface layers) through the defined angle, θ about the surface normal (*Figure 6.1 (b)*).

As non-normal incidence angles are being considered it is no longer appropriate to consider the Fresnel coefficients of the sample in terms of *X* and *Y*; *s*- and *p*-polarisations must now be considered. The Jones Matrix *R* using an *sp* vector basis set can hence be defined as:

$$\begin{bmatrix} s^{out} \\ p^{out} \end{bmatrix} = R^{sp} \begin{bmatrix} s^{in} \\ p^{in} \end{bmatrix} = \begin{bmatrix} r_{ss} & r_{ps} \\ r_{sp} & r_{pp} \end{bmatrix} \begin{bmatrix} s^{in} \\ p^{in} \end{bmatrix} \qquad \textit{Eqn. 6.1}$$

In general it is necessary to cope with both the material anisotropy and the inequivalence of *s*- and *p*- polarisations (which may be referred to as ellipsometric anisotropy). It is now convenient to define the probed directions α and β in 3-dimensional space as:

$$\alpha^{in} = \frac{1}{\sqrt{2}}\left(s^{in} + p^{in}\right) = \frac{1}{\sqrt{2}}\left(-\cos\phi, -1, \sin\phi\right) \qquad \textit{Eqn. 6.2}$$

$$\beta^{in} = \frac{1}{\sqrt{2}}\left(-s^{in} + p^{in}\right) = \frac{1}{\sqrt{2}}\left(-\cos\phi, 1, \sin\phi\right) \qquad \textit{Eqn. 6.3}$$

$$\alpha^{out} = \frac{1}{\sqrt{2}}\left(s^{out} - p^{out}\right) = \frac{1}{\sqrt{2}}\left(-\cos\phi, -1, -\sin\phi\right) \qquad \textit{Eqn. 6.4}$$

$$\beta^{in} = \frac{1}{\sqrt{2}}\left(-s^{out} - p^{out}\right) = \frac{1}{\sqrt{2}}\left(-\cos\phi, 1, -\sin\phi\right) \qquad \textit{Eqn. 6.5}$$

where φ is the angle of incidence. Corresponding "in" and "out" vectors have identical projections into the surface plane, however the normal components are opposite in direction due to the reflection. The α and β vectors both contain equal

mixtures of *s*- and *p*- polarisations, which means that any anisotropy signal is due to the sample rather than the spectrometer set-up producing an ellipsometric anisotropy.

$$R^{\alpha\beta} = \frac{1}{2}\begin{bmatrix} r_{ss} + r_{ps} - r_{sp} - r_{pp} & -r_{ss} + r_{ps} + r_{sp} - r_{pp} \\ -r_{ss} - r_{ps} - r_{sp} - r_{pp} & r_{ss} - r_{ps} + r_{sp} - r_{pp} \end{bmatrix} \qquad \textit{Eqn. 6.6}$$

In terms of α and β matrix elements R^{sp} is given by:

$$R^{sp} = \frac{1}{2}\begin{bmatrix} r_{\alpha\alpha} - r_{\beta\alpha} - r_{\alpha\beta} + r_{\beta\beta} & r_{\alpha\alpha} + r_{\beta\alpha} - r_{\alpha\beta} - r_{\beta\beta} \\ -r_{\alpha\alpha} + r_{\beta\alpha} - r_{\alpha\beta} + r_{\beta\beta} & -r_{\alpha\alpha} - r_{\beta\alpha} - r_{\alpha\beta} - r_{\beta\beta} \end{bmatrix} \qquad \textit{Eqn. 6.7}$$

For the work contained in this chapter only the real part of the RA response is considered and hence the optical retardation effects due to the window are not considered. All other components are assumed to have ideal polarisation properties and are aligned perpendicular to the ray direction, hence the amplitude of the light *A* reaching the detector is given by:

$$A = \begin{bmatrix} 1 & 0 \\ 0 & 0 \end{bmatrix} T(\theta_A) T^{-1}(\theta_M) \begin{bmatrix} 1 & 0 \\ 0 & e^{i\delta} \end{bmatrix} T(\theta_M) \begin{bmatrix} r_{ss} & r_{ps} \\ r_{sp} & r_{pp} \end{bmatrix} T^{-1}(\theta_p) \begin{bmatrix} 1 \\ 0 \end{bmatrix} \qquad \textit{Eqn. 6.8}$$

where *T* is the rotation matrix:

$$T = \begin{bmatrix} \cos\theta & \sin\theta \\ -\sin\theta & \cos\theta \end{bmatrix} \qquad \textit{Eqn. 6.9}$$

A has the general form:

$$A = \begin{bmatrix} a & be^{i\delta} \\ 0 & 0 \end{bmatrix} \begin{bmatrix} c \\ d \end{bmatrix} = ac + bde^{i\delta} \qquad \textit{Eqn. 6.10}$$

where *a* and *b* are real, and *c* and *d* are complex, and their values are determined by the orientation of the polarisation sensitive elements of the spectrometer and the

Jones matrix of the sample. The measured intensity of the signal is $I = |A|^2$, a superposition of harmonics of the modulation frequency. The first three terms are given by:

$$I_0 = a^2|c|^2 + b^2|d|^2 \qquad \text{Eqn. 6.11}$$

$$I_\omega = 4abJ_1(\delta_0)\mathrm{Im}(cd^*) \qquad \text{Eqn. 6.12}$$

$$I_{2\omega} = 4abJ_2(\delta_0)\mathrm{Re}(c^*d) \qquad \text{Eqn. 6.13}$$

where again J_n is a Bessel function of order n and where δ_0 is chosen such that $J_0(\delta_0) = 0$.

The Fresnel coefficients are calculated using 4×4 matrix algebra reported by Teitler and Henvis [6.3], Berreman [6.4-6.5], Schubert [6.6] and Roseburgh [6.7], the principles of which are outlined in *Appendix A*.

6.3 The Standard Configuration

The standard configuration is the system used experimentally in the earlier chapters of this thesis (as defined in *Chapter 2*), this system requires that $\theta_M = 0°$, $\theta_A = 45°$ and $\theta_P = 0°$ (for *s*- polarised input) and 90° (for *p*- polarised input). It then follows that for *s*- polarised input:

$$\frac{I_{2\omega}}{I_0} = -2J_2\frac{\Re\left[r_{ss}{}^* r_{sp}\right]}{|r_{ss}|^2 + |r_{sp}|^2/4} \approx -2J_2\Re\left[\frac{r_{sp}}{r_{ss}}\right] \qquad \text{Eqn. 6.15}$$

and for *p*- polarised input:

$$\frac{I_{2\omega}}{I_0} = -2J_2\frac{\Re\left[r_{ps}{}^* r_{pp}\right]}{|r_{pp}|^2 + |r_{ps}|^2/4} \approx -2J_2\Re\left[\frac{r_{ps}}{r_{pp}}\right] \qquad \text{Eqn. 6.16}$$

where the approximations are valid for conditions where there is little *s*- *p*- mixing. For the near normal incidence case where *s*- and *p*- are essentially equivalent the *s*- case is assumed. When the sample is orientated such that the mirror planes are aligned with the α and β directions (crystallographic directions are at ±45° to the vertical) $R^{\alpha\beta}$ is diagonal and R^{sp} takes the simplified form:

$$R^{sp} = \begin{bmatrix} r & \Delta/2 \\ -\Delta/2 & -r \end{bmatrix} \qquad \textit{Eqn. 6.17}$$

where $r = (r_\alpha + r_\beta)/2$ and $\Delta = r_\alpha - r_\beta$; finally we obtain:

$$\frac{I_{2\omega}}{I_0} = -2J_2 \frac{\Re[r^*\Delta]}{|r|^2 + |\Delta|^2/4} \approx -2J_2 \Re\left[\frac{\Delta}{r}\right] \qquad \textit{Eqn. 6.18}$$

6.4 Spectrometer Component Rotation

As the RAS response from a system is dependent on the orientation of the polarisation sensitive elements of the spectrometer, the effects of misaligning (or even rotating) these components could provide additional information which may be of help or hindrance in obtaining and interpreting data. Some such situations are now considered.

6.4.1 Analyser Rotations

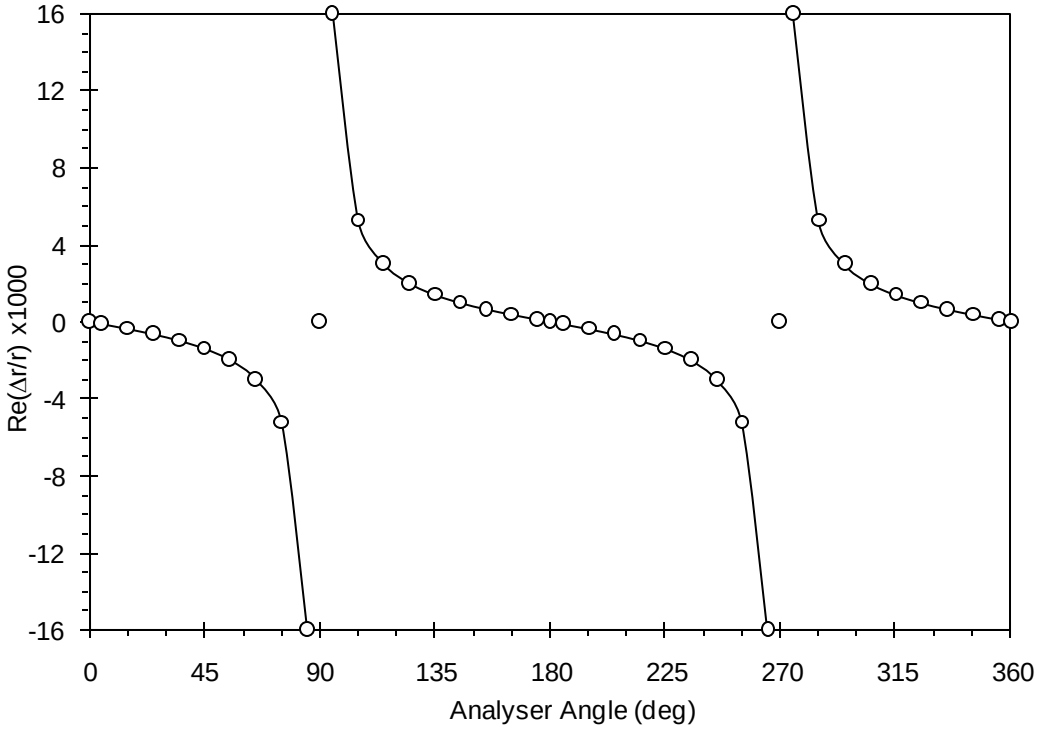

Figure 6.2: *The effect on the RAS signal upon rotation of the analyser.*

The $I_{2\omega}$ and I_0 terms are affected differently by the rotation of the analyser:

$$I_{2\omega} = |r|^2 J_2 \sin 2\theta_A \Re\left(\frac{\Delta}{r}\right) \qquad \textit{Eqn. 6.19}$$

$$I_0 = |r|^2 \left(\cos^2\theta_A + \left|\frac{\Delta}{2r}\right|^2 \sin^2\theta_A\right) \qquad \textit{Eqn. 6.20}$$

Hence:

$$\frac{I_{2\omega}}{I_0} = \frac{J_2 \sin 2\theta_A \Re\left(\frac{\Delta}{r}\right)}{\cos^2\theta_A + \left|\frac{\Delta}{2r}\right|^2 \sin^2\theta_A} \qquad \textit{Eqn. 6.21}$$

As $|\Delta| << |r|$ considering only terms to first order in Δ gives:

$$\frac{I_{2\omega}}{I_0} = \frac{J_2 \sin 2\theta_A \Re\left(\frac{\Delta}{r}\right)}{\cos^2 \theta_A} = 2J_2 \tan\theta_A \Re\left(\frac{\Delta}{r}\right) \qquad \textit{Eqn. 6.22}$$

Eqn. 6.22 and *Figure 6.2* demonstrate that the analyser has a scaling effect on the signal, and a rotation of the analyser by 90° can be used to flip the orientation of the signal. This also demonstrates that the perfect alignment of the analyser is not critical and small misalignments can be easily tolerated.

Koopmans et al. [6.8] demonstrated that "misaligning" the analyser by almost 45° i.e. approaching a condition where the analyser is crossed with the polariser and PEM allows a greater signal to noise ratio to be obtained. The $I_{2\omega}$ term scales with $\sin 2\theta_A$ whereas the I_0 term scales with $\cos^2\theta_A$. Hence as the crossed condition is approached the DC signal falls quadratically while the AC signal falls linearly. It then follows that the modulated components of the signal are buried in a proportionally smaller DC background. This would suggest a gain in signal proportional to $1/d\theta$ as the crossed condition is approached, however the noise on the system scales with $\sqrt{DC}$ and hence $d\theta$, resulting in no gain in the signal to noise. An analysis of the signal to noise ratio for different analyser angles is given in *Appendix B*.

6.4.2 Polariser Rotations

Using similar methods as for rotating the analyser:

$$\frac{I_{2\omega}}{I_0} = \frac{-2J_2\left[\Re\left(\frac{\Delta}{r}\right) + \sin 2\theta_P\left(1 + \left|\frac{\Delta}{2r}\right|^2\right)\right]}{1 + \frac{\Delta}{r}\sin 2\theta_P + \left|\frac{\Delta}{2r}\right|^2} \qquad \textit{Eqn. 6.23}$$

As $|\Delta/r| << 1$:

$$\frac{I_{2\omega}}{I_0} = -2J_2\left[\Re\left(\frac{\Delta}{r}\right) + \sin 2\theta_P\right] \qquad \textit{Eqn. 6.24}$$

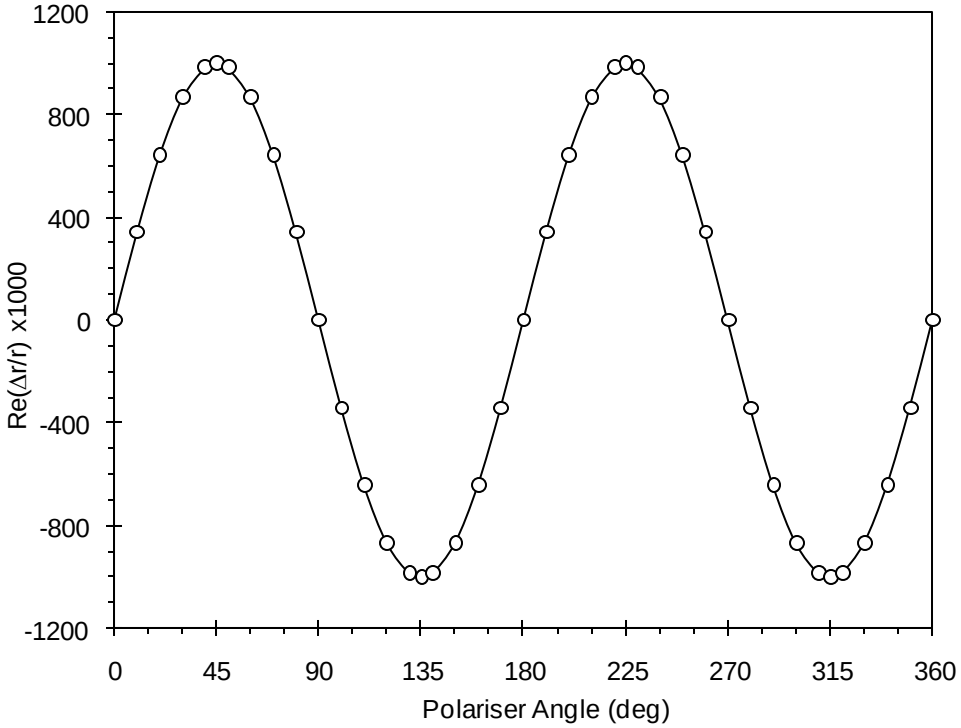

Figure 6.3: *The effect on the RAS signal upon rotation of the polariser.*

Eqn. 6.24 and *Figure 6.3* demonstrate that the misalignment of the polariser leads to an offset in the signal, which for small misalignments (to a first order approximation) do not affect the spectral shape or amplitude of the modulated signal as the offset is flat across the spectral range. However the offset is large for even small misalignments and modifies the quantity of interest significantly. Rumberg [6.9] suggested a polariser alignment accuracy of better than 30" was required to achieve optimum results; it is for this reason most groups use precision polariser mounts.

6.4.3 PEM Rotations

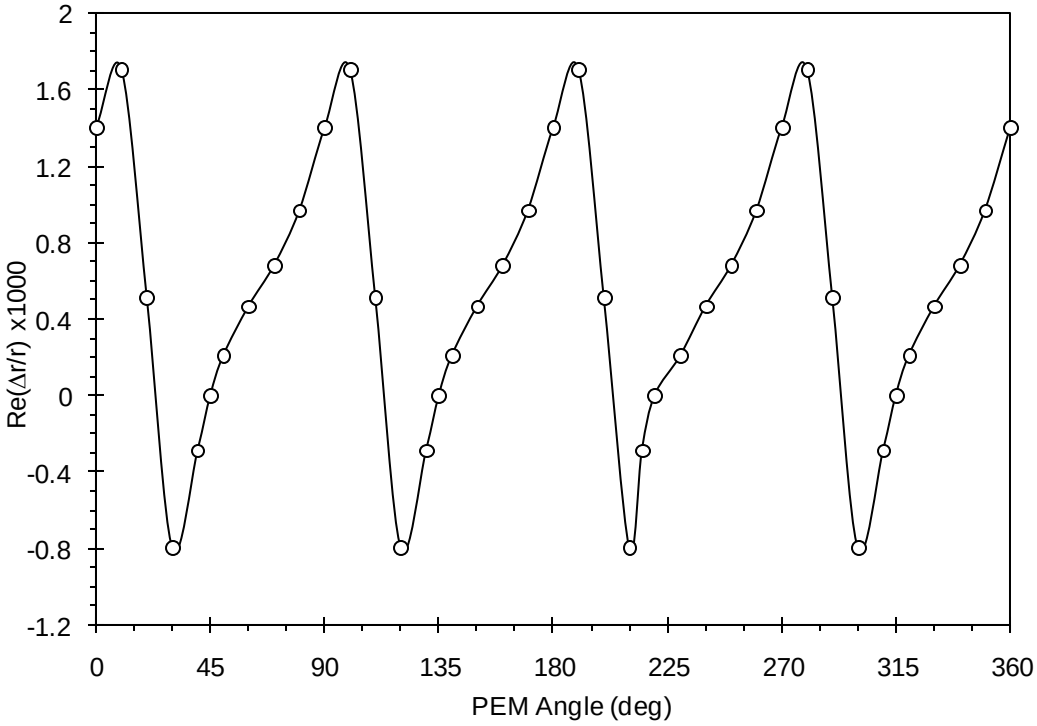

Figure 6.4: *The effect on the RAS signal upon rotation of the PEM.*

For misalignments of the PEM the effect observed in *Figure 6.4* is described by:

$$\frac{I_{2\omega}}{I_0} \approx 2J_2 \tan(45+\theta_M)\left[\Re\left(\frac{\Delta}{r}\right)\cos 2\theta_M + \sin 2\theta_M\right] \qquad \textit{Eqn. 6.25}$$

For the experimental set up of most spectrometers the PEM is mounted rigidly and hence does not have the rotational freedom of the other components, hence it is convenient to consider the PEM correctly aligned and adjust the other components to compensate. This can be done by rotation the polariser and sample by $\delta\theta_M$ and rotation of the analyser by - $\delta\theta_M$.

6.5 Rotation of the sample

The general case where the dielectric axes of the surface layer are randomly orientated was considered by MacDonald et al. [6.2]. In such a case the eigen-polarisations (those incident polarisations for which the sample acts as a perfect mirror) are elliptical; *Eqn. 6.18* remains valid provided $\Delta r/r$ is replaced by the "generalised anisotropy" $\Delta s/s$ [6.2]:

$$\frac{\Delta s}{s} = F\frac{\cos 2\theta - i\sin 2\varepsilon \sin 2\theta}{\cos 2\varepsilon + F\left[\sin 2\theta + i\cos 2\theta \sin 2\varepsilon\right]/2} \qquad \textit{Eqn. 6.26}$$

where ε is the ellipticity of the eigen-polarisations, F is the anisotropy in the diagonal (elliptical) basis and θ is the misalignment of the axes of the ellipses from the standard sample orientation (Note that the convention for sample alignment used in Ref. [6.2] and hence *Eqns. 6.26-6.29* differ from the one defined in *Figure 6.1* by 45°, meaning the sample rotation in this work varies as a sine rather than a cosine function). When one of the overlayers dielectric axes is aligned with the surface normal ε vanishes and *Eqn. 6.26* yields:

$$\frac{\Delta s}{s} = \frac{\left(\Re + i\Im\right)\cos 2\theta}{1+\left(\Re + i\Im\right)\sin 2\theta} \qquad \textit{Eqn. 6.27}$$

where $\Re$ and $\Im$ are the real and imaginary parts of Δ/r respectively.

Hence:

$$\frac{I_{2\omega}}{I_0} = J_2\frac{\Re\cos 2\theta + \sin 4\theta\left(\Re^2+\Im^2\right)/4}{1+\left(\Re^2+\Im^2\right)/4 - \Re\sin 4\theta} \qquad \textit{Eqn. 6.28}$$

$$\frac{I_{2\omega}}{I_0} \approx J_2\left[\Re\cos 2\theta + \frac{\Im^2-\Re^2}{4}\sin 4\theta\right] \qquad \textit{Eqn. 6.29}$$

To first order anisotropies *Eqns. 6.28 & 6.29* suggest that RA spectra undergo a $\cos 2\theta$ scaling in azimuthal rotation. This has been observed numerous times experimentally [6.10-6.12] and allows unknown dielectric axes to be identified, and is used by RAS practitioners for sample alignment. It should be pointed out that this is in fact non-trivial for samples lacking 2mm symmetry; as MacDonald et al. [6.1-6.2] emphasized the dielectric axes for such samples can vary with photon energy.

In recent work Farrell et al. [6.12] discussed the variation of the RAS signal of Ag(110) with azimuthal rotation. A $\sin 4\theta$ dependence was observed for one particular photon energy, with a $\cos 2\theta$ dependence observed elsewhere in the spectrum. Farrell et al. [6.12] explained that the 2θ and 4θ terms were first and second order in the optical anisotropy respectively and that the later term can dominate when $|r_x|^2 = |r_y|^2$. From *Eqn. 6.29* it is clear this condition can also be stated as $\Re = 0$. Hence a $\sin 4\theta$ dependence of $I_{2\omega}/I_0$ can be observed at all spectral nodes of $\Re$, at which point $I_{2\omega}/I_0 \propto \Im^2 \sin 4\theta$ would be observed.

Is the $\Re = 0$ condition common? In general $\Delta r/r$ can be expressed as a superposition of Cauchy functions:

$$\frac{\Delta r}{r}(\omega) = e^{i\gamma}\left[f(\omega) - ig(\omega)\right] \qquad \textit{Eqn. 6.30}$$

where f and g are of the form of the peak and wiggle functions shown schematically in *Figure 6.5* and γ is some phase angle. Thus $\Re$ has nodes except for the special case when $\gamma = 0$, so the $\sin 4\theta$ behaviour should be quite general. As f and g have similar amplitudes the relative amplitudes of the 2θ and 4θ ADRAS curves (measured at their respective optimal ω values) should scale linearly and quadratically respectively with the magnitude of the optical anisotropy. Aside from the nodes of $\Re$ a dominant 4θ term requires $|\Delta| >> |r|$.

While the 4θ effect discussed above is expected only at the nodes of $\Re$, other systems exhibit this behaviour across the spectrum [6.1-6.2, 6.13]. This behaviour has been attributed to an incoherence between the two probe polarisations which are

reflected from the lower interface of a material with a large bulk anisotropy [6.1-6.2, 6.13].

6.6 Simulations Set up

The simulations carried out from this section onwards until *Section 6.9* assume the case of strict normal incidence. The labels *x*, *y* & *z* denote the internal dielectric co-ordinates of the molecular overlayer.

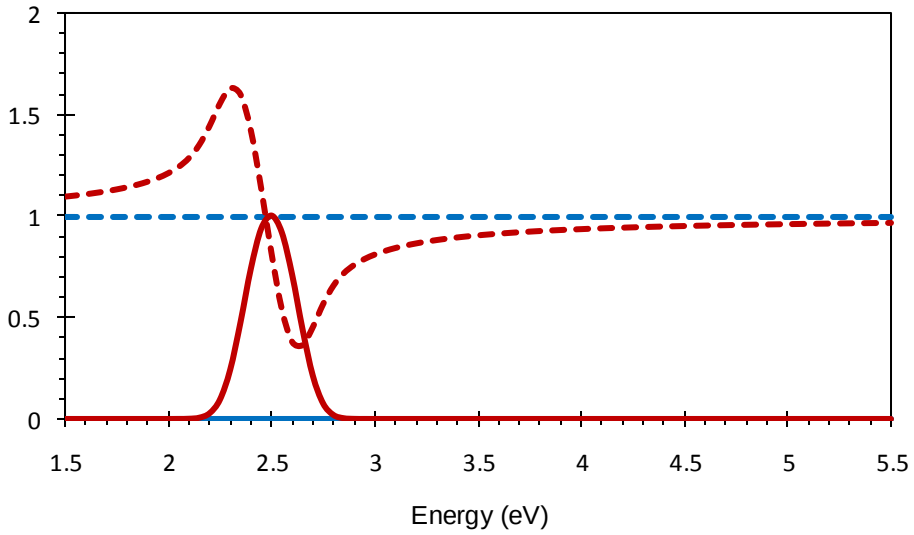

Figure 6.5: *Real (dashed lines) and imaginary (solid lines) parts of the dielectric functions in x (blue) and y (red) of a surface overlayer.*

In order to simulate the effect of the various angular effects an anisotropic model had to be used. In order to keep the system simple a single feature was inserted into a surface overlayer in the *y* direction; as shown in *Figure 6.5* (Gaussian transition shape in the imaginary part of the dielectric function). The dielectric properties in *x* and *z* were kept so that $\varepsilon_x' = \varepsilon_z' = 1$ and $\varepsilon_x'' = \varepsilon_z'' = 0$. Careful consideration was also given to the choice of substrate. A study by Cole et al. [6.14] showed the relationship between the substrate and the dielectric properties of a surface overlayer was given by:

$$\mathrm{Re}\left(\frac{\Delta r}{r}(\omega)\right) = -\frac{2\omega d}{c}\left[A(\omega)\Delta\varepsilon'' + B(\omega)\Delta\varepsilon'\right] \qquad \textit{Eqn. 6.31}$$

where d is the thickness of the surface layer and all other symbols have their usual meanings. Aluminium was chosen because $A(\omega)$ and $B(\omega)$ are simple, following closely the form expected for a free electron gas:

$$A(\omega) = \frac{\omega^2}{\omega_p{}^2} \qquad \textit{Eqn. 6.32}$$

$$B(\omega) = \frac{\omega}{\tau\omega_p{}^2} \qquad \textit{Eqn. 6.33}$$

where ω_p and τ are the plasma frequency and the Drude relaxation time respectively. $A(\omega)$ dominates $B(\omega)$ (see *Figure 6.6*) meaning that the resulting RA response is dominated by a $\Delta\varepsilon''$-like shape as shown in *Figure 6.7*. The optical properties of Aluminum were obtained from Palik [6.15] and a film thickness of 1nm was used.

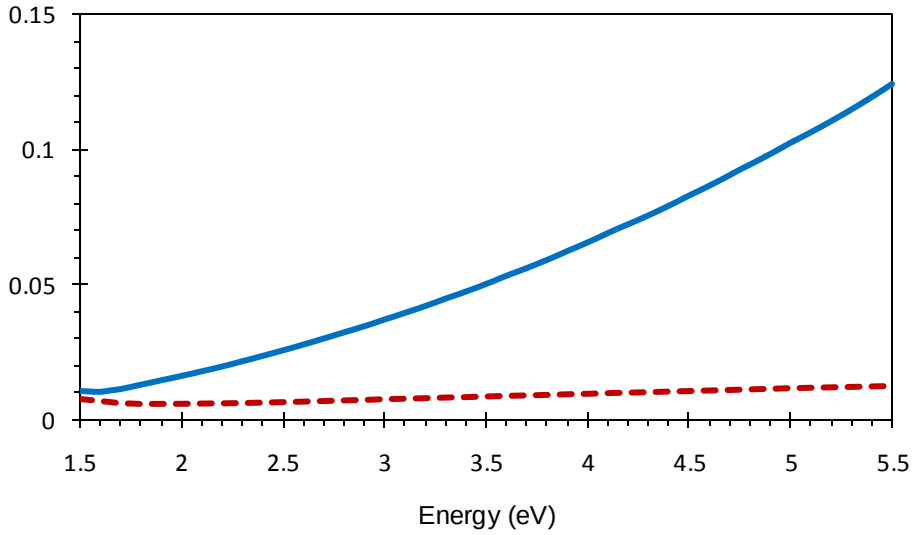

Figure 6.6: *A (solid line) and B (dashed line) functions for Bulk Aluminium.*

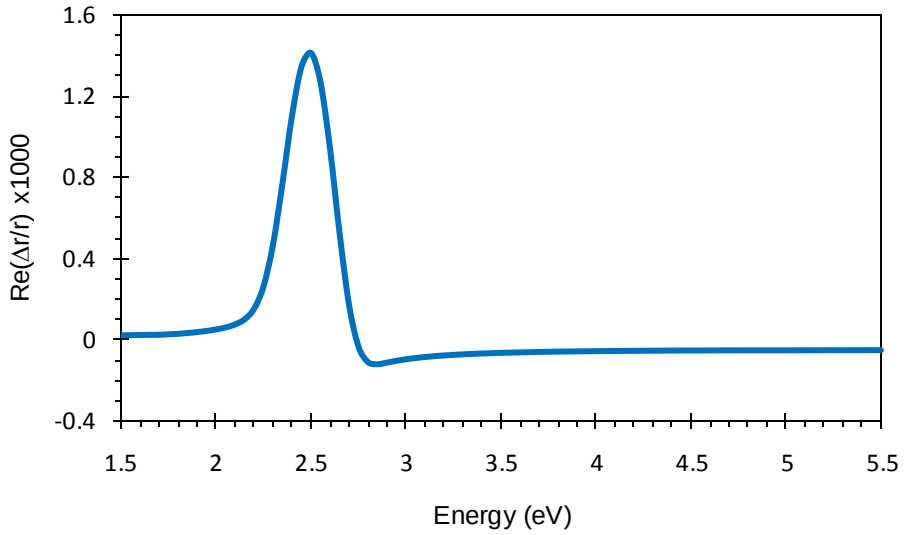

Figure 6.7: *Simulated RA response from a surface overlayer whose dielectric properties are shown in Figure 6.5 on an Aluminium substrate.*

6.7 Sample Rotation

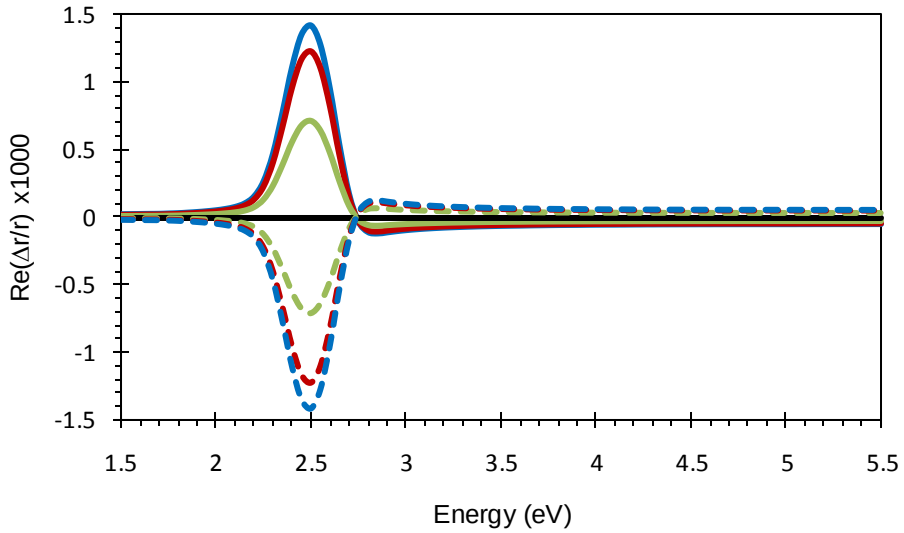

Figure 6.8: *Simulated RA spectra obtained for the Aluminium sample at different azimuthal orientations: 45° (blue solid line), 60° (red solid line), 75° (green solid line), 90° (black line), 105° (green dashed line), 120° (red dashed line) and 135° (blue dashed line).*

As was discussed earlier in *Section 6.5* the rotation of a sample with 2 mirror planes (order 4 rotational symmetry) shows a $\sin 2\theta$ dependence across the spectral range

except at the nodes of $\Re$ where a $\sin 4\theta$ dependence is observed. This behaviour is shown in *Figures 6.8* & *6.9*.

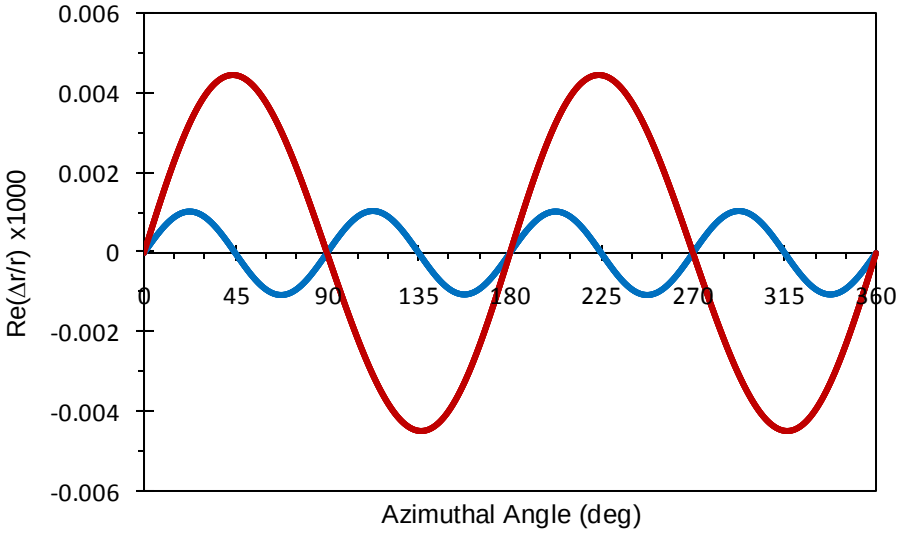

Figure 6.9: *Simulated RA response from rotating the azimuthal angle of the Aluminium sample, at the nodes of $\Re$ (blue) signal x10. Close to the nodes of $\Re$ (red).*

6.8 Tilted Molecule

As mentioned in *Section 6.6* a surface layer possesses three orthogonal dielectric axes. Thus far only the case where one of these axes is parallel to the surface normal has been considered. The system has three degrees of rotational freedom which can be described by three sequential rotations quantified by the Euler angles [6.16] (*Figure 6.10*). The mathematical framework which incorporates this calculation into the optical properties of the system can be found in *Appendix A*. This allows the consideration of cases where the *x* and *y* directions are no longer perpendicular to the surface normal i.e. tilted out of the surface plane; this approach can be used to model tilted molecules.

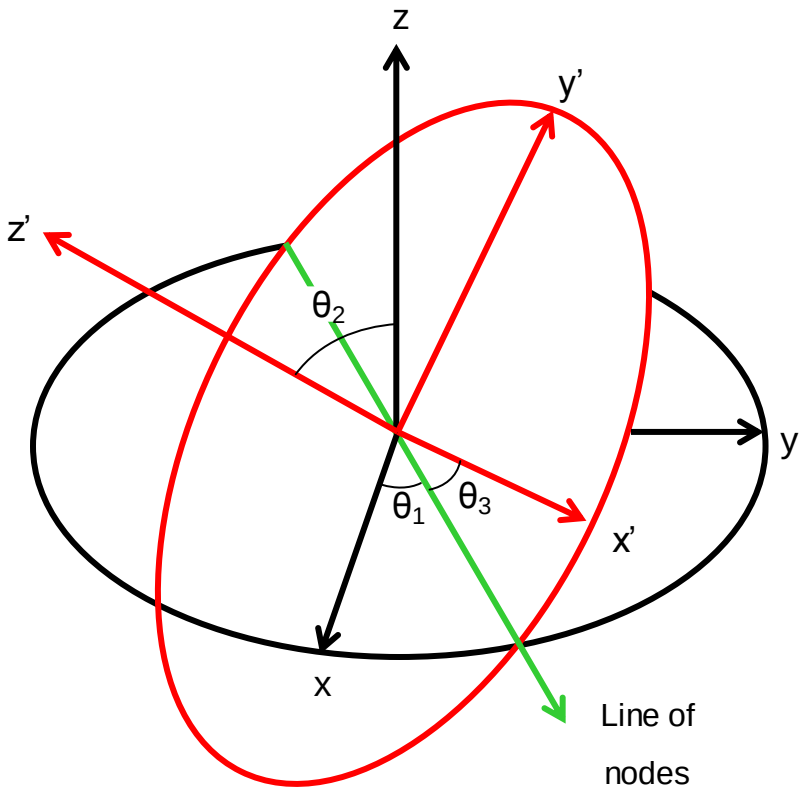

Figure 6.10: *The definitions of the Euler angles.*

The first rotation about *z* keeps both *x* and *y* in the surface plane and for a 3 phase system (with one surface layer and an isotropic bulk) has the same effect as rotating the sample azimuth, and for multilayer systems it rotates the optical axes of a particular layer with respect to the others. The second rotation holds the *x*-axis in position and tilts the *y* and *z* axes about *x*. The third rotation holds the *z*-axis in the tilted position (defined by the 2nd rotation) and allows the rotation of the *x*-*y* plane about it. For most of the work considered in this thesis it is sufficient to consider that the 2nd angle controls the tilt of the molecule out of the surface plane and the 3rd angle controls the alignment of the tilt along either *y* (0°) or *x* (90°) or some arbitrary angle in between. Unless explicitly stated otherwise the Euler angles θ_1 and θ_3 for all the simulations in this chapter are defined to be $\theta_1 = 90°$ and $\theta_3 = 0°$, and the system will be referred to by its tilt angle (θ_2) or "tilt".

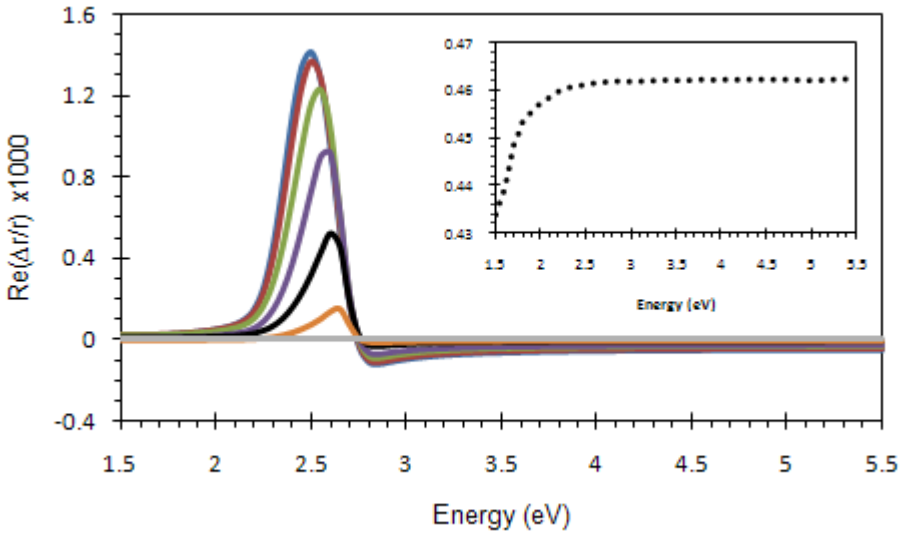

Figure 6.11: *Simulated RA response for a tilt angle of 0° (blue), 15° (red), 30° (green), 45° (purple), 60°(black) 75° (orange) and 90° (grey). Inset: Reflectance of the sample for any tilt angle.*

Figure 6.11 shows the effect on the RA response of a surface overlayer with different tilt orientations, for a fixed azimuthal orientation of θ=45°. For ease of reference it will be assumed that the overlayer represents a molecule with absorption peaks at the appropriate energies, for which a tilt orientation of 0° corresponds to the molecule lying flat on the surface, and a tilt orientation of 90° corresponds to the molecule standing upright on the surface. In the literal case of such an analysis the length of the molecule would be constant; hence the overlayer thickness would vary with tilt angle. This is not considered here, a constant film thickness of 1nm is used throughout. One could equally use the approach to represent stepped surfaces or pre-tilt angles for liquid crystal displays; the molecule orientation is easier to visualise.

The flat orientation is the response that has been considered thus far; and considers anisotropy in the *x*-*y* plane (of the overlayer). This plane is aligned with the probe directions α and β for normal incidence. When the molecule is upright the anisotropy measured by α and β corresponds to the *x*-*z* plane of the overlayer. For angles in between 0° and 90° there are in general contributions from both the *x*-*y* and the *x*-*z* planes. In this model there is only anisotropy in the *x*-*y* plane; the *x*-*z* plane is isotropic. Hence the anisotropic signal is at a maximum for the flat lying orientation

and is zero for the upright orientation, the orientations in between representing differing mixtures of the two.

At this point it is worth drawing the reader's attention to the fact that if the dielectric properties of the overlayer in *x* and *y* were swapped around and the above simulations were repeated the peak as shown for the flat lying molecule would always be present; this is because the anisotropy between the *x*-*y* plane and the *x*-*z* plane would be the same. This illustrates the importance of the conventions used to define the tilt angles and also the significance of orientations of adsorption peaks with respect to this: for a flat molecule studied by RAS, peaks in *x* and *y* are essentially equivalent and for simulation of RA spectra the choice is usually arbitrary. There are occasions when this is not the case but for the majority of cases only the amplitude of the signal is important. For tilted molecules as discussed above these details have great significance.

The effect of having contributions from two planes can be further illustrated by considering the case of a molecule with adsorption peaks in *y* and *z*. The dielectric peaks are shown in *Figure 6.12* and the simulated RA response obtained from such a system is shown in *Figure 6.13*.

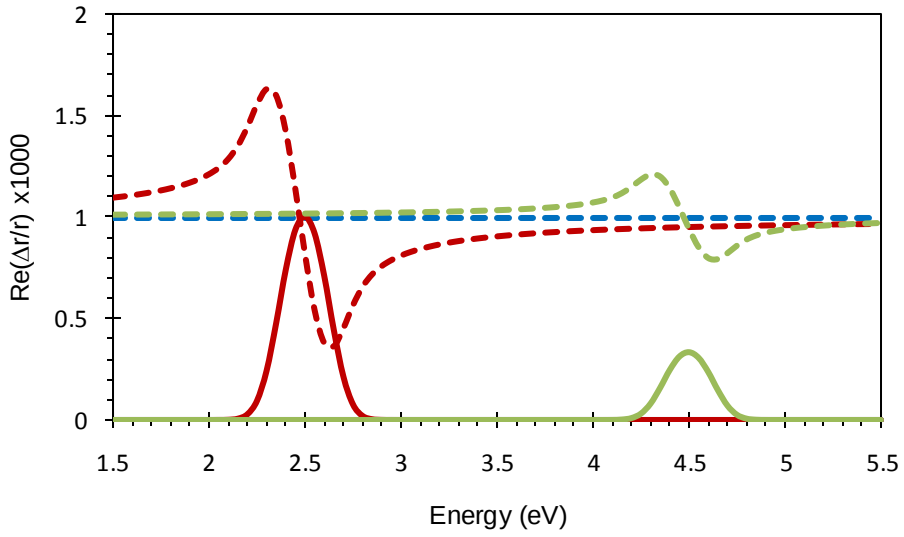

Figure 6.12: *Real (dashed lines) and imaginary (solid lines) parts of the dielectric functions in x (blue), y (red), and z (green) of a surface overlayer.*

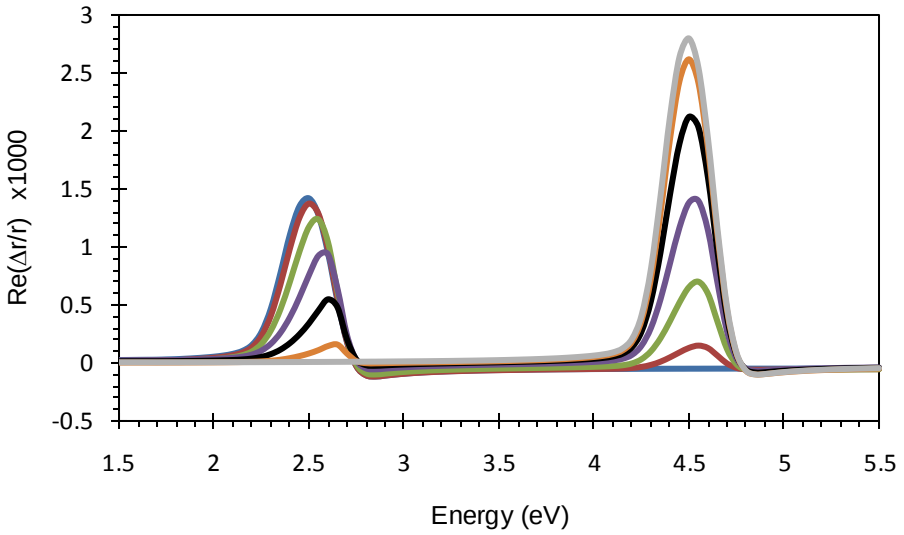

Figure 6.13: *Simulated RA response for a tilt angle of 0° (blue), 15° (red), 30° (green), 45° (purple), 60°(black) 75° (orange) and 90° (grey).*

Figure 6.13 shows that for a flat lying molecule there is no sensitivity to features in the *z*-direction as the spectrum obtained with this system is identical to the spectrum obtained for a molecule with no features in the *z*-direction. For tilted molecules however RAS is sensitive to the anisotropy in multiple planes. This means that a molecule which can change its orientation could give rise to additional features as well as different signal intensities. The maximum intensity of the peak at 4.5eV is larger than the maximum intensity at 2.5eV - despite arising from a smaller dielectric feature because the spectrum scales with photon energy (see *Eqn. 6.31*).

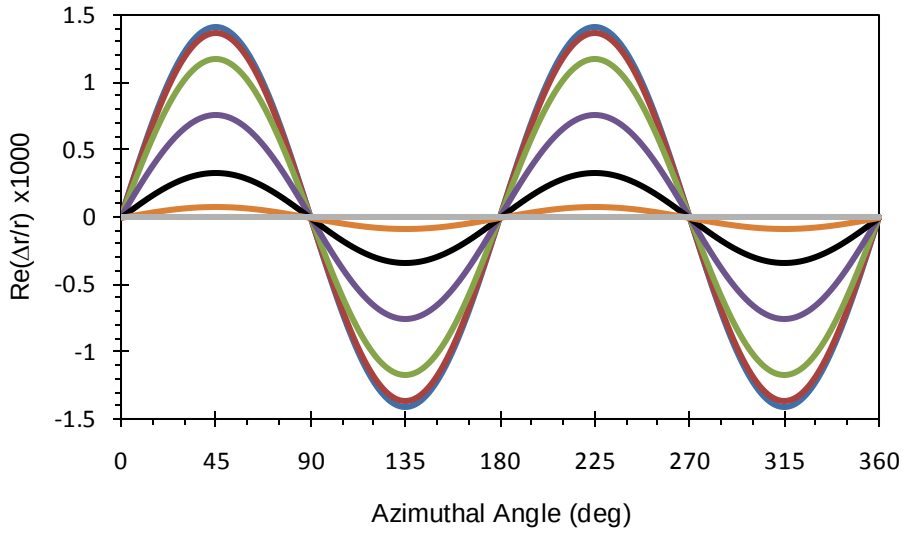

Figure 6.14: *Simulated ADRAS response at 2.5eV for a tilt angle of 0° (blue), 15° (red), 30° (green), 45° (purple), 60°(black) 75° (orange) and 90° (grey).*

Figure 6.14 shows the azimuthal rotations for the different molecule orientations and a sin2θ dependence is observed for all energies (only 2.5eV is shown). This could be expected for the system when the molecule is either in a flat lying orientation or in an upright orientation, as these orientations both possess two mirror symmetry planes. For a molecular tilt which is neither 0° nor 90°, the *x* direction is no longer a mirror plane.

Despite this for the case of strictly normal incidence the sin2θ dependence is preserved because the now 3-dimensional surface is being probed by a 2-dimensional probe, the in and out vectors of α and β (*Eqns 6.2-6.5*) only having non-zero components in the *x* and *y* directions (of the lab frame). Hence the normal incidence probe measures only the components of anisotropy resolved into 2-dimensional space. This being the case and the dielectric axes being perpendicular, a tilt (rotation about the *x*-axis of the molecule) sees the *x*-axis aligned with one of the probe directions and the projection of the *y*-*z* axes aligned with the other probed direction, meaning the eigen-polarisations are perpendicular and the measured response is that of the projection of the dielectric axes in two dimensional space. The projections still possess two mirror planes despite the sample (in 3 dimensional space) only possessing one hence the measured anisotropy is the difference between

the *x* and '*y*-*z* projection'. As the peak at 2.5eV is in the *y* direction it follows that intensity of the peak depends on relative weightings of *y* and *z*.

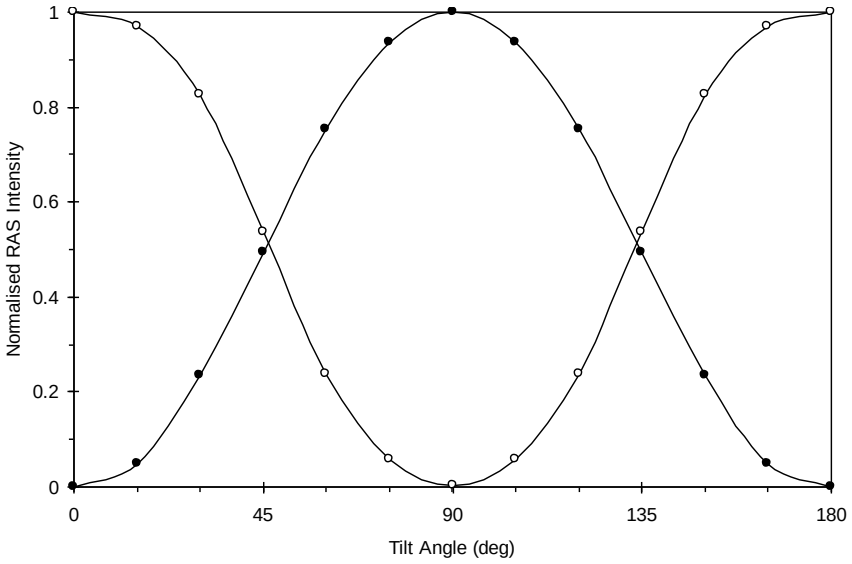

Figure 6.15: *The scaling of the RA intensity of the 2.5eV (open circles) and 4.5eV (filled circles) features with tilt angle.*

The tilting of the molecule causes a scaling of the spectrum by a factor of $\sim \cos^2 \theta_2$ when moving from the *x*-*y* plane to the *x*-*z* plane and $\sim \sin^2 \theta_2$ when moving the opposite way, as shown in *Figure 6.15*. Tilts of θ_2 and 180- θ_2 yield identical spectra at normal incidence as their projections would be the same.

Tilt vs Film Thickness

From observing some of the results obtained by these simulation methods, it becomes apparent (for this sample at least) that although the intensity of features changes significantly the lineshape does not change to the same extent. Reducing the film thickness also has a scaling effect on the intensity of features. It could therefore be difficult (particularly experimentally) to determine if a signal's intensity is due to the tilt of the molecule or a smaller film thickness. Obviously if the film thickness is known this is not a problem and appropriate analysis could allow a tilt to be

determined. However in many cases the film thickness is not known and the sample behaves in a similar manner to that of a flat molecule (of smaller film thickness).

Attempts at studying tilted molecules on surfaces or attempts to determine molecular orientation out of the surface plane with RAS have been made previously theoretically by Mendoza et al. [6.17] and Roseburgh [6.7] and experimentally by Weightman et al [6.18].

Mendoza et al. [6.17] demonstrated the variation of RA spectra with molecular orientation in particular the effect of the local field effect on resonance energy. Roseburgh [6.7] compared different molecular tilts on glass and copper substrates and as well as changes in intensity of the features on both substrates there were energy shifts in the positions of the features. These shifts were found to be different for the glass and the copper substrates, which illustrates that the substrate plays a key role in determining the lineshape of tilted molecules.

Weightman et al. [6.18] and Roseburgh [6.7] both analysed the results of cytosine and cytidine 5'-monophosphate adsorbed onto the Au(110) surface. In an attempt to determine the molecular orientation of the molecule both used different methods and reported different results; Weightman et al. concluded that the molecule was oriented at an angle of no more than 10° from the vertical, while Roseburgh [6.7] reported a tilt of 20-30° to the vertical. These instances demonstrate the difficulty in determining out of surface plane molecular orientation.

6.9 Off Normal Incidence

As discussed earlier in *Chapter 2* other epioptic probes such as Ellipsometry [6.19-6.20] operate at off normal incidence, and obtain surface sensitivity, but unlike RAS, Ellipsometry (in its various forms) is not surface specific, hence there may be additional information which can be obtained using RAS at off normal incidence.

6.9.1 Comparison of different RAS set ups

It is a commonly held belief that only a few degrees off normal incidence can be tolerated and hence when building RA spectrometers every attempt is made to make the angle of incidence as small as possible. This belief is investigated now by simulating two experimental set ups, that of the "standard configuration" discussed previously and the configuration where all the polarization sensitive components are rotated through 45°, referred to as the "rotated 45 configuration". Results from the two set ups for the Aluminium system with peaks in the dielectric properties of *y* & *z* (*Figure 6.12*), for a flat molecule are shown below.

Angle	Standard Configuration	Rotated 45 Configuration
θ_P	0°	45°
θ_S	45°	90°
θ_M	0°	45°
θ_A	45°	90°

Table 6.1: *Orientation of the components for the two RAS set-ups. (Angles are defined in Figure 6.1(b)).*

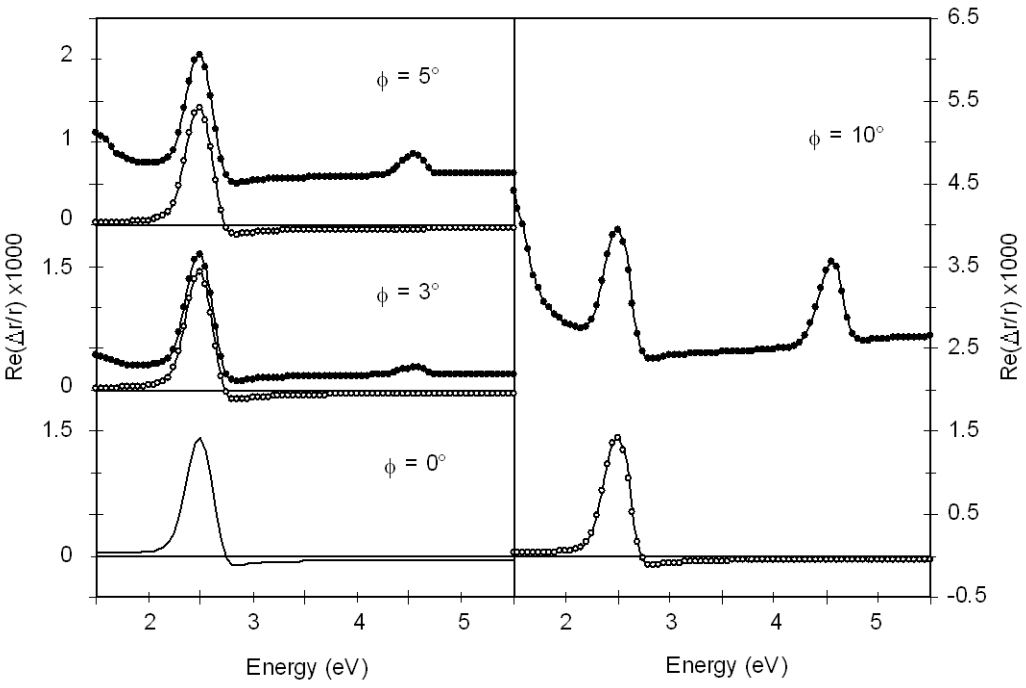

Figure 6.16: *Comparison of the RA response in the standard configuration (open circles) and the rotated 45 configuration (filled circles) for a series of incidence angles. For normal incidence the two spectra are identical and are indicated by a single solid line.*

Observing the simulated spectra using the two configurations (*Figure 6.16*) we can see that at normal incidence the results were identical as would be expected. As the angle of incidence is increased the spectra from the standard configuration set up remain the same shape and for the angles of incidence shown here are indistinguishable from the spectrum at normal incidence. The rotated 45 configuration starts to deviate from the normal incidence signal even at small incidence angles. At 3° incidence there are 3 differences between the two spectra: a small upwards shift of the signal across the spectral range; the development of a peak at 4.5eV; and a change in lineshape at the low energy end of the spectrum. The main feature of the spectrum the 2.5eV peak remains unaffected.

As the incidence angle is increased the amplitude of all 3 of these effects increases, until at large incidence angles, apart from a peak at 2.5eV the spectrum bears little resemblance to that of the standard configuration. The spectrum is then dominated by a *1/reflectance (1/r)* like term.

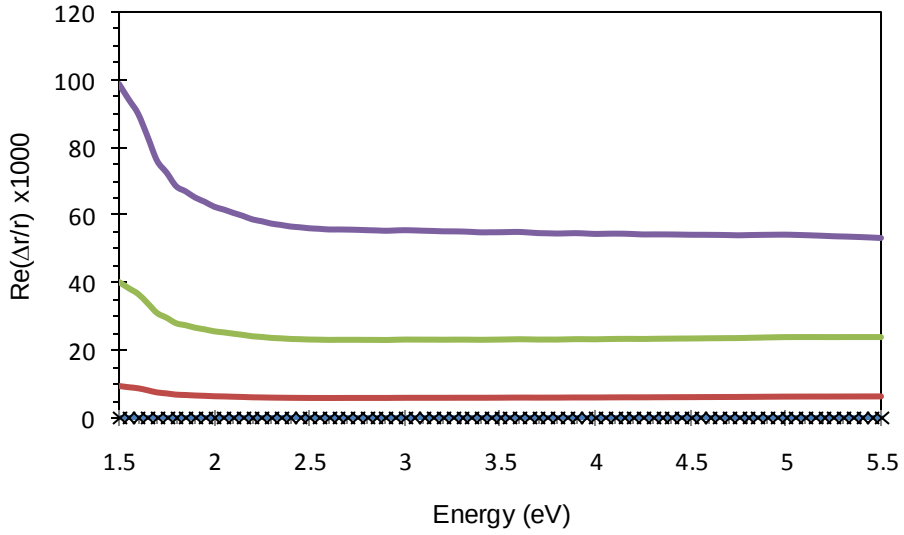

Figure 6.17: *The RA response of an isotopic sample using the rotated 45 configuration at angles of incidence of 0° (blue), 15° (red), 30° (green), and 45° (purple). The crosses denote the response of the same sample in the standard configuration for any angle of incidence.*

If for both arrangements an isotropic sample is used as in *Figure 6.17*, then for any angle of incidence in the standard configuration the RAS signal goes to zero,

whereas in the rotated 45 configuration the signal has a non-zero shape (for non-zero incidence angles) whose intensity varies as a function of incidence angle. This is because the α and β probed directions in the rotated 45 configuration are not balanced in their *s*- and *p*- polarisation ratio and hence an ellipsometric anisotropy is observed. This ellipsometric anisotropy has a dependence on the reflectivity of the sample and hence a large substrate dependence. As mentioned earlier Aluminium was chosen as a substrate because of the simplicity of its dielectric properties; a material with more complex dielectric properties could cause further complications.

The peak at 4.5eV is a combination of material and ellipsometric anisotropy; it is a material effect because it arises due to a peak in the dielectric function at that energy. It is only observed however because of the ellipsometric effect, the imbalance of *s*- and *p*- polarisations in the probe directions.

The results in this section illustrate the importance of choosing the correct spectrometer set-up and show that the standard configuration is the preferable for studying material anisotropy. Even though the set-up is named the standard configuration in this thesis, it is not the configuration used by everyone; a survey of the literature shows a number of groups reporting their set-up as the rotated 45 set up.

6.9.2 The Standard Configuration s- and p- Polarised Light

Figures 6.18 & 6.19 show the simulated RAS and reflectivity signals obtained from the Aluminium sample (whose overlayer dielectric properties are those given in *Figure 6.12*), for *s*- and *p*- polarised light for different angles of incidence. Comparing the two it is clear that both have only one feature in their RA spectrum, which is at 2.5eV (the RA lineshapes are slightly different but that will be discussed later).

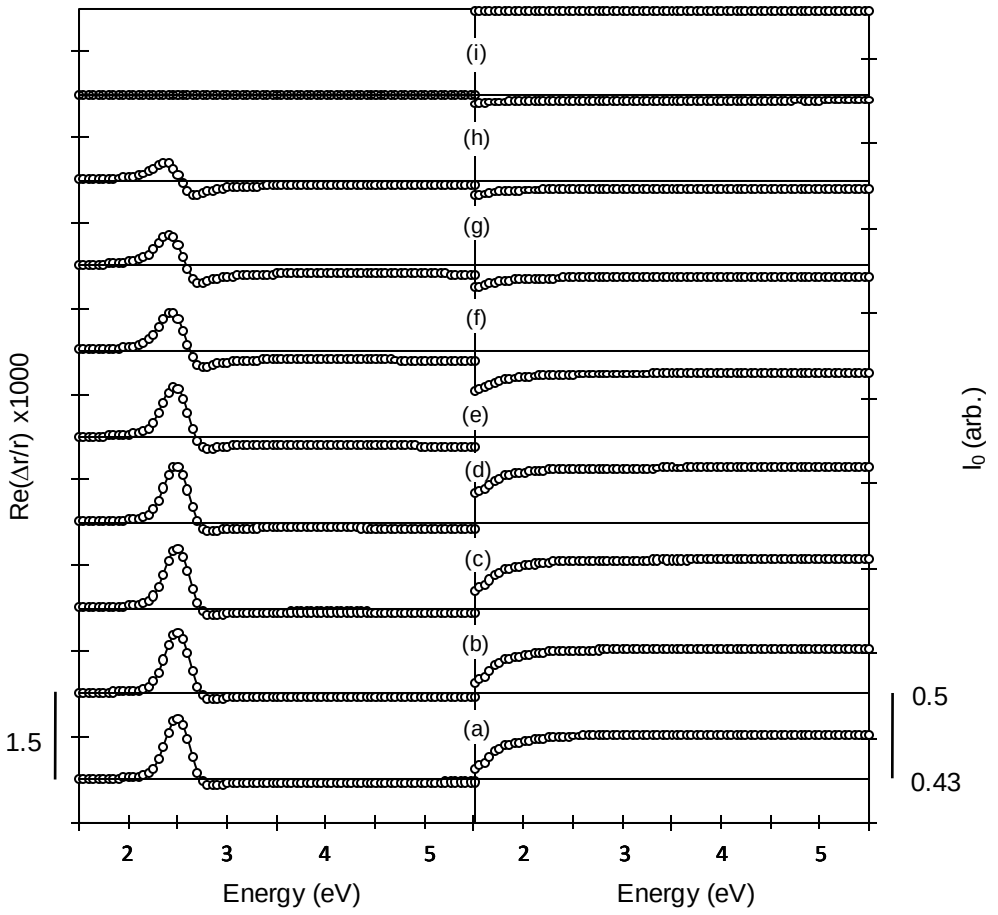

Figure 6.18: *Simulated RA signals (left) and reflectivity signals (right) from spectrometer in the Normal configuration (s- polarised input) for incidence angles of (a) 0°, (b) 15°, (c) 30°, (d) 45°, (e) 60°, (f) 75°, (g) 80°, (h) 85°, (i) 89.9°.*

The reflectivity signals however are different. For the normal incidence case (equivalent for both) the reflectivity is featureless. This remains the case for *s*-polarisations at any angle of incidence, the amplitude of the signal varying proportionally with the reflectance curves for *s*- polarised light across the spectrum. For *p*- polarised light however the reflectivity develops a peak at 4.5eV due to the peak in the *z* dielectric function of the overlayer. This is observed because the *p*-polarised light has a component in the *z*-direction which increases as the angle of incidence increases, hence the feature at 4.5eV feature in the reflectivity spectrum depends on both the reflectance of *p*- polarised light and the magnitude of the *z* component.

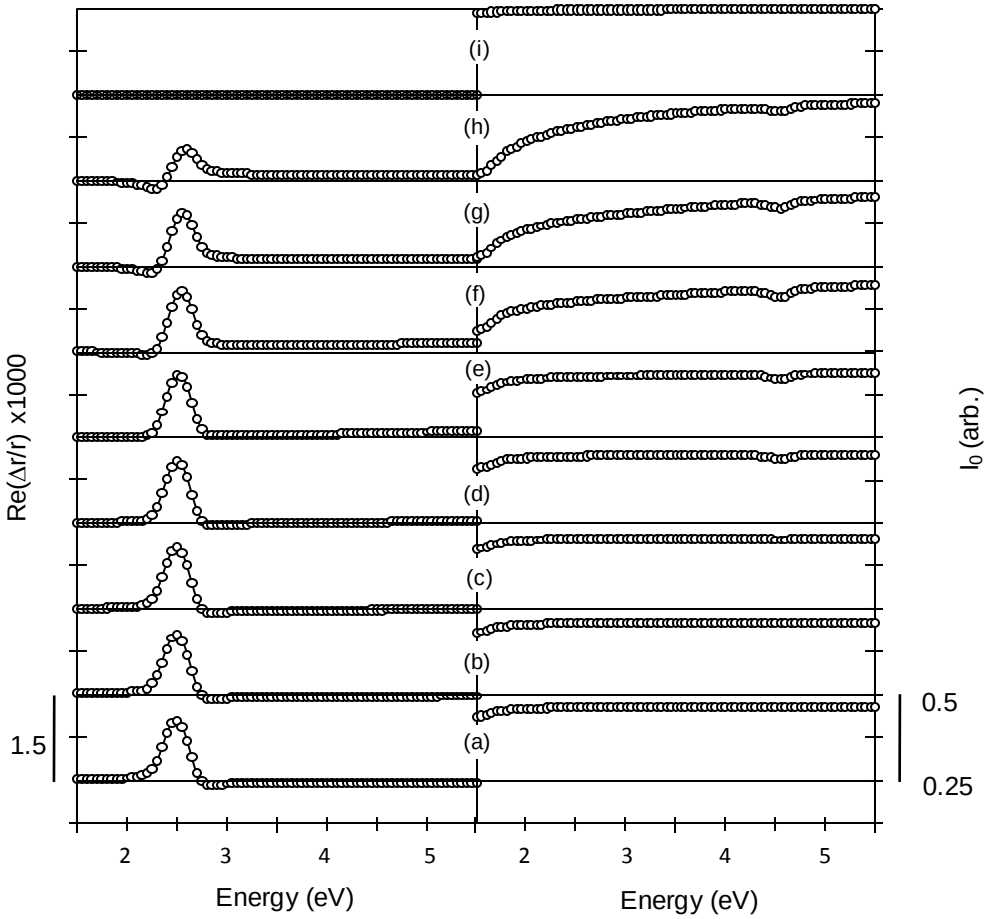

Figure 6.19: *Simulated RA signals (left) and reflectivity signals (right) from spectrometer in the Normal configuration (p- polarised input) for incidence angles of (a) 0°, (b) 15°, (c) 30°, (d) 45°, (e) 60°, (f) 75°, (g) 80°, (h) 85°, (i) 89.9°.*

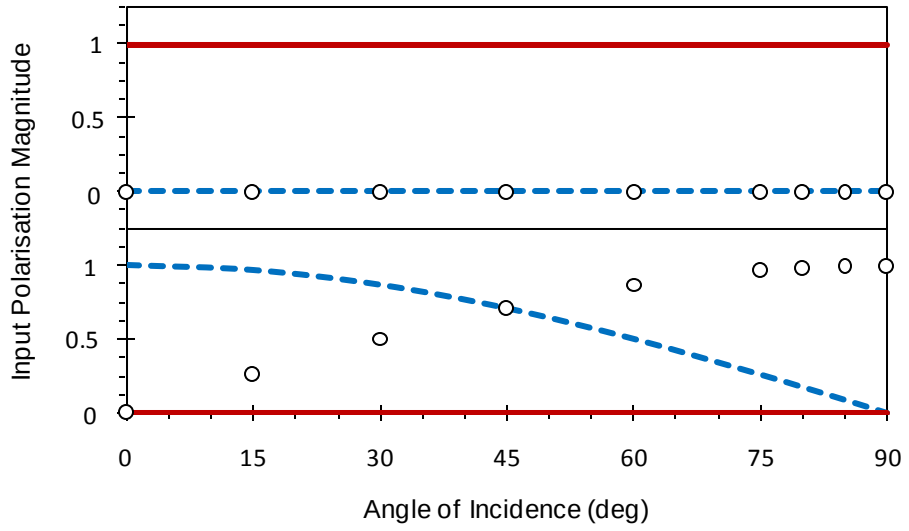

Figure 6.20: *Input polarisation directions for s- (upper panel) and p- (lower panel) polarised light in x (blue dashed lines), y (solid red lines) and z (open circles)*

For the standard configuration using *p*- polarised light the 4.5eV feature is not present in the RA spectrum because the probe directions α and β have the balanced components of *s*- and *p*- polarised light. This *z*-dependence of *p*- is why the 4.5eV peak is present in the rotated 45 configuration. From *Figure 6.20* we can see that the *s*- polarised light has zero *z*-component, whereas the *p*- polarised light has a non-zero *z*-component at off normal incidence angles.

6.9.3 *s*- and *p*- Polarisations Lineshapes

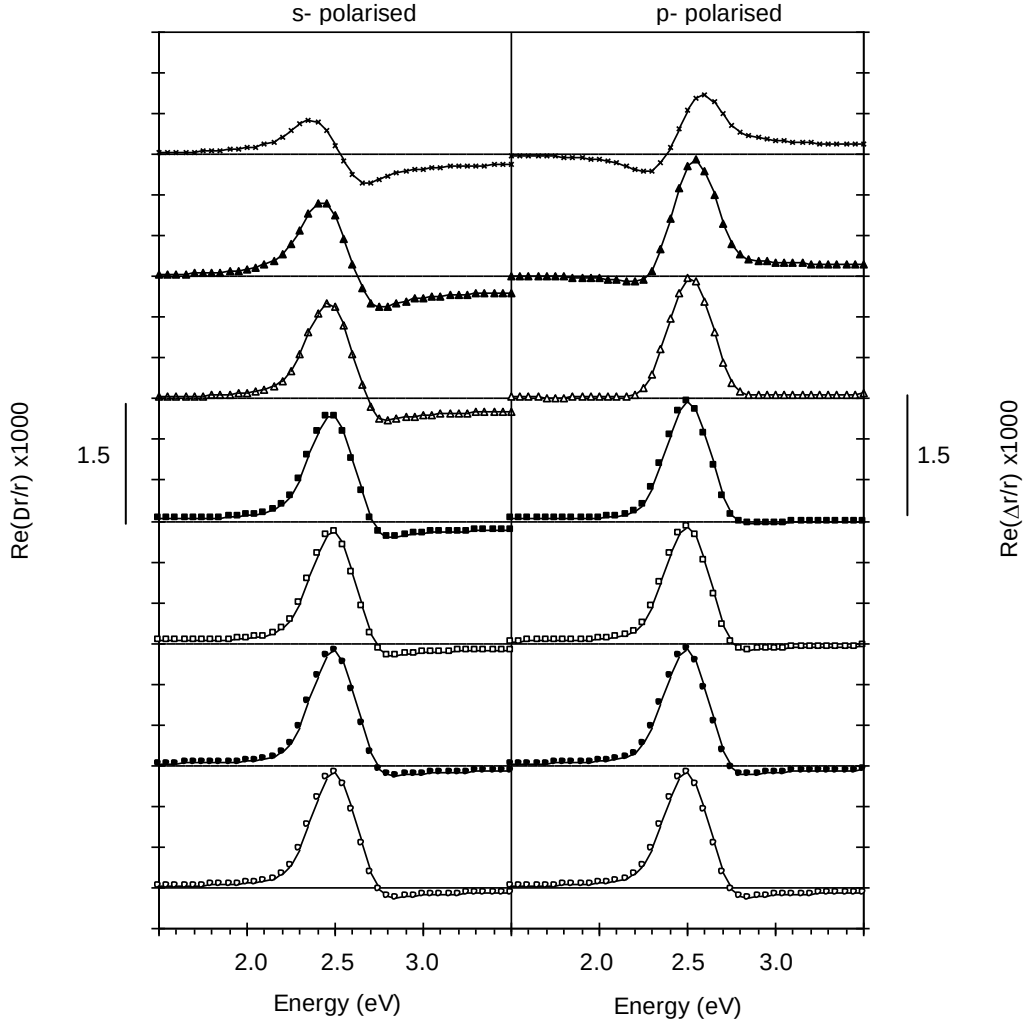

Figure 6.21: *Comparison of RAS lineshape for s- (left) and p- (right) input polarisations for incidence angles of 0° (open circles), 15° (filled circles), 30° (open squares), 45° (filled squares), 60° (open triangles), 75° (filled triangles) and 85° (crosses).*

As suggested by *Eqn. 6.15* and *Eqn. 6.16* for the standard configuration at off normal incidence the *s*- and *p*- polarised input configurations are different therefore the RA spectra obtained from such set ups should not be the same for non-zero incidence angles, hence results for the absorption peaks on Aluminium for *s*- and *p*- polarised input (polariser angles of 0° and 90° respectively) are shown in *Figure 6.21*.

The lineshape for normal incidence is the same for both *s*- and *p*- orientations as would be expected; the two lineshapes at off normal incidence vary differently. The lineshape at normal incidence as discussed earlier is dominated by the peak-like feature in the imaginary part of the dielectric function. As 90° incidence is approached the lineshape is dominated by the real part of the dielectric function, a positive wiggle for *s*- polarisation and a negative wiggle for *p*- polaristaion.

The line shapes in the near peak region can be expressed as a superposition of Cauchy functions and hence the lineshape can be expressed by *Eqn. 6.34* which gives a good match in the near peak region, but a less good fit for some incidence angles away from the peak. The graphical fits to the data are shown in *Appendix C*.

$$\mathrm{Re}\left(\frac{\Delta r}{r}\right) = -\frac{2\omega d}{c}\left[\left(A(\omega)\Delta\varepsilon''\cos\gamma\right) + \left(B(\omega)\Delta\varepsilon'\sin\gamma\right)\right]\frac{R_\phi}{R_0} \qquad \textit{Eqn. 6.34}$$

where γ is the argument, R_φ is the reflectance at an angle of incidence of φ and R_0 is the reflectance at normal incidence, all other values have their usual meanings.

The argument of the function can be represented for *s*- and *p*- polarisations by the Argand diagram shown in *Figure 6.22*. The relationship between the argument and the incidence angle is shown graphically in *Figure 6.23*.

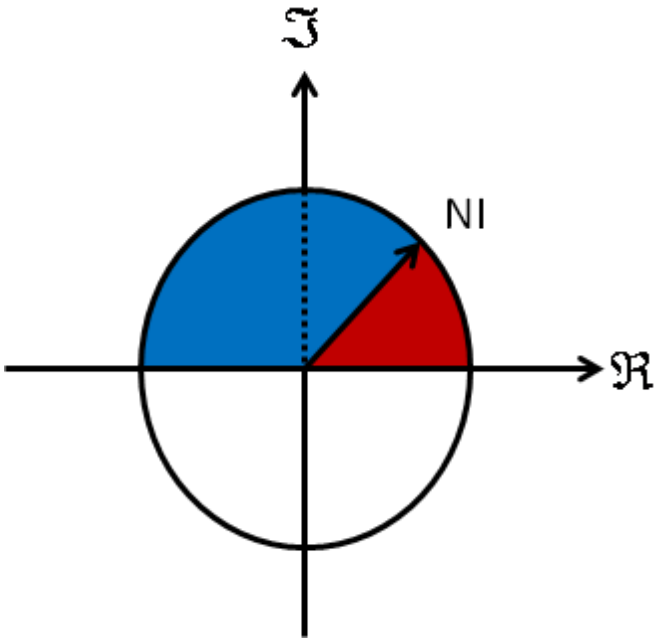

Figure 6.22: *A graphical representation of where the lineshapes of off normal incidence spectra fit on an Argand diagram the red area corresponds to lineshapes obtained from s-polarised light and the blue area p- polarised light.*

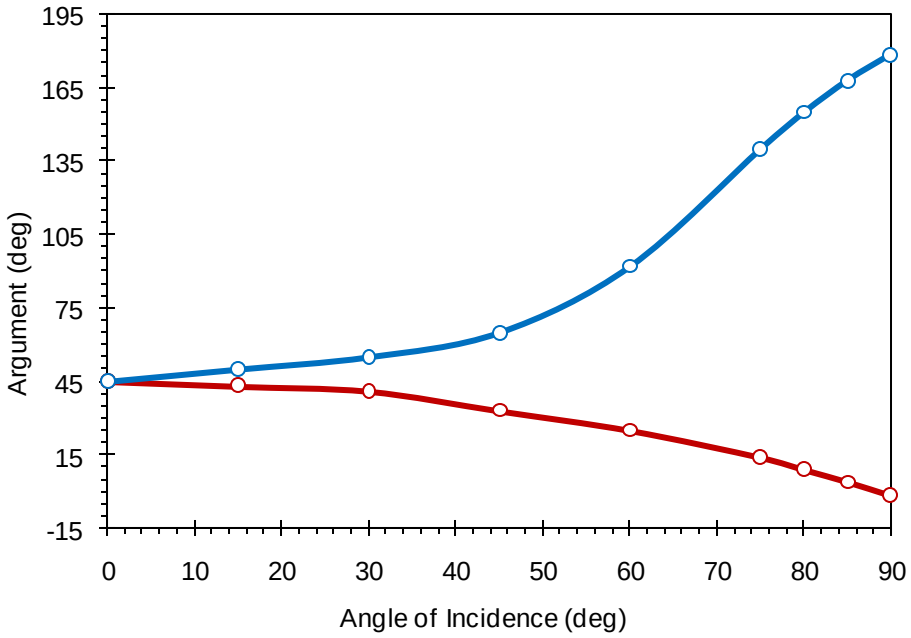

Figure 6.23: *The relationship between the incidence angle and the argument of Eqn. 6.34 for s- (red) and p- (blue) polarisations.*

These results show that for the standard configuration relatively large incidence angles can be tolerated with little effect on either lineshape or intensity. The level of

this tolerance varies with the polarisation; *s*- polarised light can tolerate up to 45° while for *p*- polarised light the value is ~30°. The rotated 45 configuration is much less tolerant of off normal incidence: the lineshape in this configuration is affected significantly at ~3° incidence by the ellipsometric anisotropy, which demonstrates the significance of having the correct balance of *s*- and *p*- polarisations in the probe directions α and β.

6.9.4 Azimuthal Rotations for s- and p- polarisations

The above section has demonstrated the different effects *s*- and *p*- polarised light has on the RAS setup

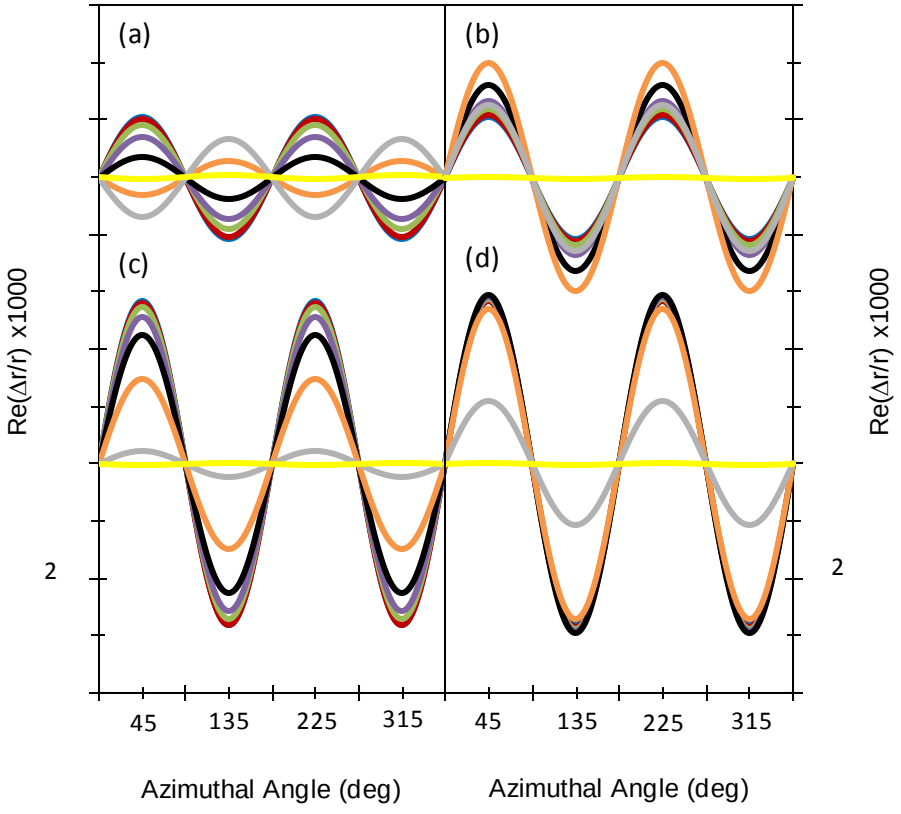

Figure 6.24: *Azimuthal scans at (a): 2.65eV s- pol., (b): 2.65eV p- pol., (c): 2.5eV s- pol., (d): 2.5eV p- pol. For incidence angles of 0° (blue), 15° (red), 30° (green), 45° (purple), 60° (black), 75° (orange), 85° (grey) and 89.9° (yellow).*

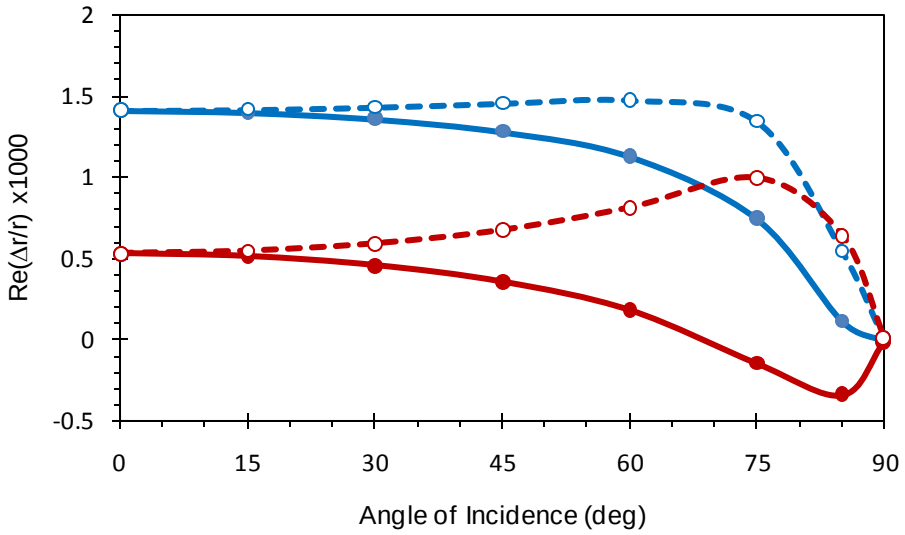

Figure 6.25: *RA intensity of the features at 2.5eV (blue) and 2.65eV (red) for s- (solid lines) and p- (dashed lines) polarised input.*

Figure 6.24 shows the intensity of the spectra at energies of 2.5eV and 2.65eV for both *s*- and *p*- polarised input. *Figure 6.24* shows how these features vary with angle of incidence (for an azimuthal angle of 45°). As would be expected there is different behaviour from *s*- and *p*- polarisations, and the change in line shape causes the RA signal at 2.5eV to change sign for *s*- polarisation as can be seen in *Figure 6.24 (a)*. The way in which the signal varies (see *Figure 6.25*) shows a similarity to the (inverted) shape of reflectance curves. The RA signal has a dependence on *1/r* so this should not come as a surprise. Obviously the scale is a RAS scale not a reflectance scale so is not absolute, and the dependence on Δ skews this effect somewhat as both *r* and Δ are changing, this becomes clearest in the cases *s*- polarised light in the 85-89.9° region where the signal tends towards zero because Δ tends to zero.

6.10 Tilted Molecule at Off Normal Incidence

The effects of a tilted molecule and off normal incidence have both been considered individually and both have been found to have significant effects on the RA spectra obtained. Now the effects of a tilted molecule at off normal incidence will be considered.

6.10.1 Different Tilts at 3° Incidence

As off normal incidence RAS is a new idea with no reported studies in the literature no off normal incidence or variable angle RAS kits exist. However most experimental RAS kits have an incidence angle as close to normal incidence as possible, typically this angle will be ~3°. This being the case it is useful to see what if any effects could be observed using an incidence angle of 3°.

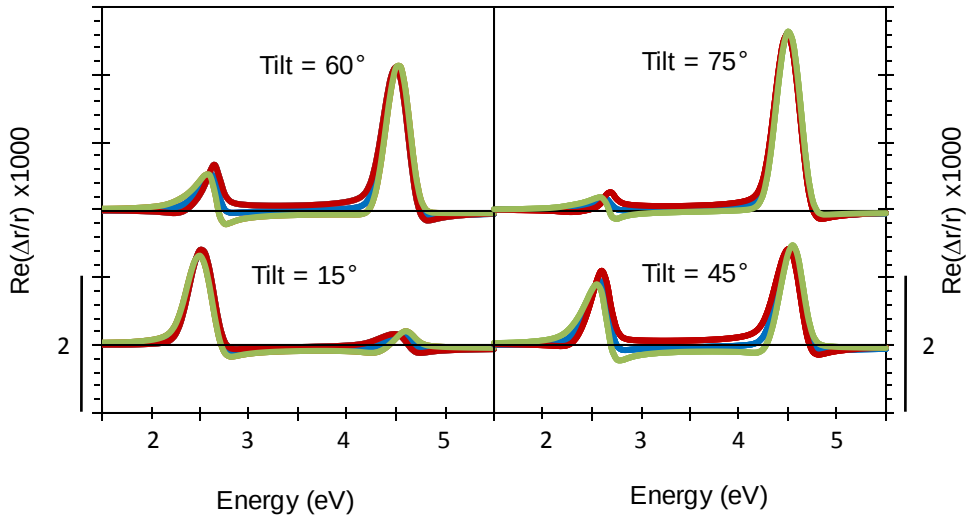

Figure 6.26: *The RA response of a tilted molecule at 3° incidence for s- polarisations (red), p- polarisations (green) compared with normal incidence (blue) for tilts of 15°, 45°, 60° and 75°.*

The spectra in *Figure 6.26* show that for a specific tilt there are differences evident in the lineshapes. The scale of these differences is dependent on the magnitude of the tilt away from its plane, i.e. for a feature in the *x-y* plane small tilt angles see relatively small changes in lineshape, large tilt angles see relatively large changes in lineshape. The same is true of the *x-z* plane - remember the *x-z* corresponds to a tilt of 90°. Hence features at 2.5eV best match normal incidence at low tilt angles 15° (*Figure 6.26 (a)*) and features at 4.5eV best match normal incidence at high tilt angles 75° (*Figure 6.26 (d)*).

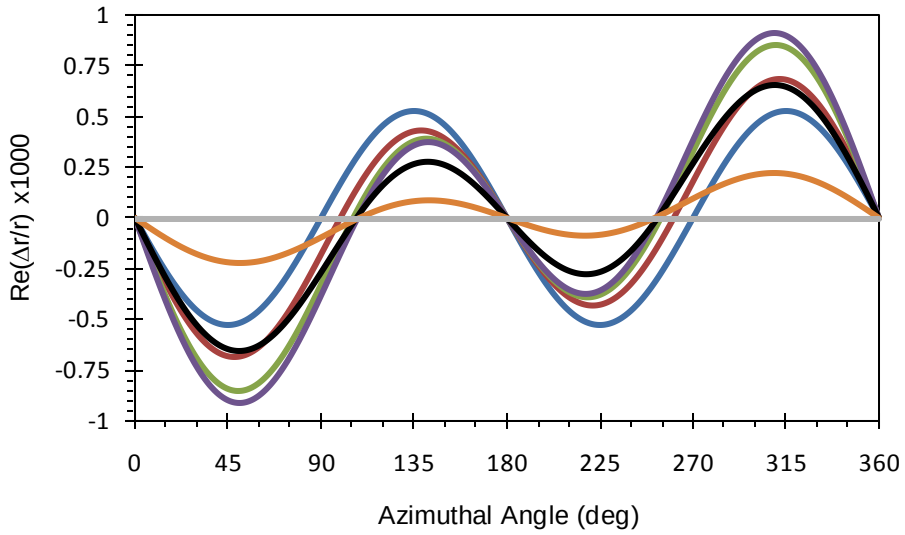

Figure 6.27: *The RA response at 3° incidence for s- polarisations at 2.65eV for a flat molecule (blue), tilts of 15° (red), 30° (green), 45° (purple), 60° (black), 75° (orange) and 90° (grey).*

Figure 6.27 shows the ADRAS curves for different tilts: the flat molecule varies with sin2θ whilst the tilted molecules vary with a distorted sin2θ like shape. The extent of the distortion varies from tilt to tilt.

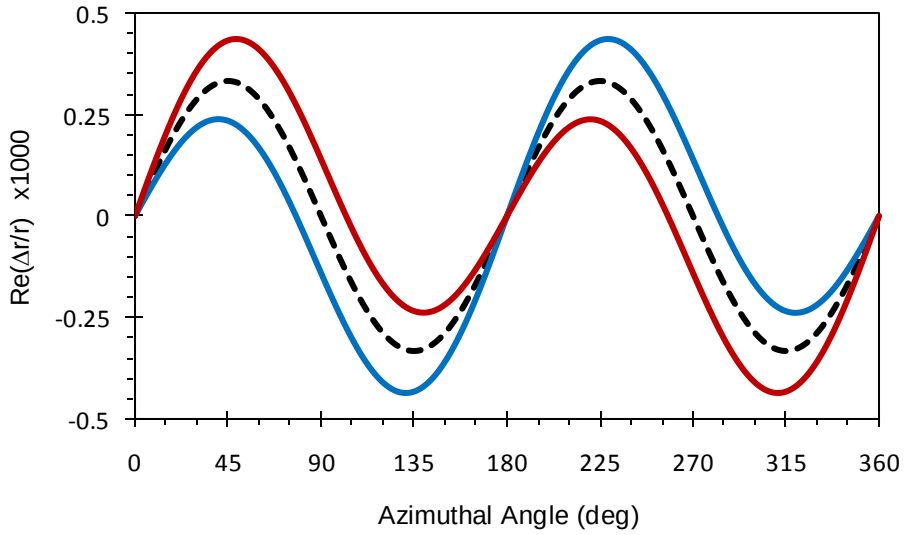

Figure 6.28: *Comparison of azimuthal rotations for s- (blue) and p- (red) polarisations at 3° incidence for a molecule with a tilt of 60°. Black dashed line indicates the same molecule at normal incidence.*

Figure 6.28 shows the azimuthal rotations for a molecule with a tilt of 60° at 3° incidence for both *s*- and *p*- polarised light recorded at an energy of 2.5eV. The *s*- and *p*- polarisations differ by a phase of 180°. The normal incidence rotation corresponds to the mean of the *s*- and *p*- polarisations.

The fact that the curves are not $\sin 2\theta$ in shape as was previously the case indicates a breakdown in symmetry: the new shape (a superposition of $\sin 2\theta$ and $\sin\theta$) indicates the presence of only one mirror plane as opposed to two mirror planes in the $\sin 2\theta$ case.

Although this effect is clearly observed in the data presented in *Figure 6.27*, experimentally it would be much more difficult to identify. In order to observe it the experimentalist must have a molecule with a large tilt (however the tilt is likely to be unknown) and have freedom to rotate the sample through at least 180° and preferably more (often difficult in UHV conditions). If the effect was observed for a rotation through ~180° the asymmetric nature (of the intensity) could easily be assumed to be an experimental artefact or error resulting in a vertical shift in the spectrum (possibly due to a slight misalignment of the polariser). The phase shift in the peak position would also be easy to miss as it is so small (~5° for the case of *Figure 6.28*) because RAS practitioners use azimuthal rotations to find the positions of the dielectric axes, even with complementary data from a system such as LEED a 5° misalignment would be within a likely error of attempting to align a sample by eye.

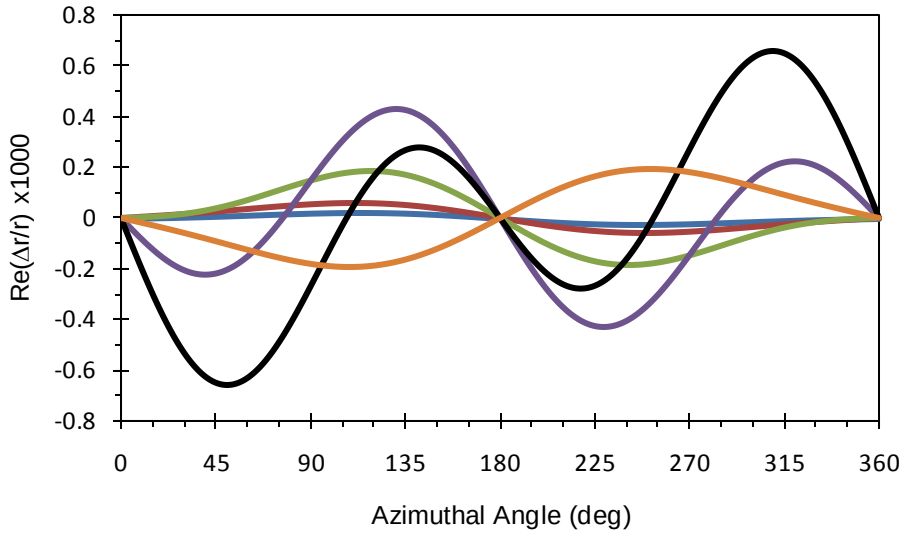

Figure 6.29: *Comparison of azimuthal rotations for a molecule with a tilt of 60° at 3° incidence (s- polarised input) for energies of 1.7eV (blue), 2.05eV (red), 2.3eV (green), 2.5eV (purple), 2.65eV (black) and 3.3eV (orange).*

Figure 6.29 shows the intensity as a function of azimuthal angle for various energies; it is apparent from this figure that the superposition effect that the weightings of the two terms vary with energy. The sin2θ term is observed most strongly at energies where there is a large anisotropy, as the origins of this term are known this is not unexpected. Elsewhere in the spectrum, at energies where the anisotropy is small, this term is difficult to observe as the sinθ term dominates. The curves for 2.65eV and 3.3eV look different to the others as these are at energies where the RAS features have the opposite signs for one of the terms; all such curves can be described by *Eqn. 6.35*:

$$u\sin(\theta)+v\sin(2\theta) \qquad \textit{Eqn. 6.35}$$

where u and v are the energy dependent Fourier components which scale the two terms.

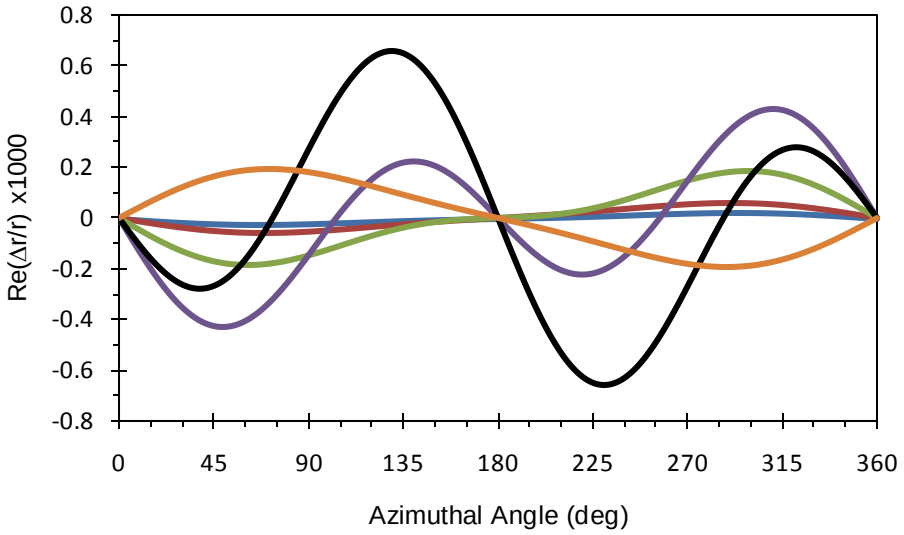

Figure 6.30: *Comparison of azimuthal rotations for a molecule with a tilt of 60° at 3° incidence (p- polarised input) for energies of 1.7eV (blue), 2.05eV (red), 2.3eV (green), 2.5eV (purple), 2.65eV (black) and 3.3eV (orange).*

For *p*- polarised input light similar effects are observed in *Figure 6.30* however they appear to be 180° out of phase with those shown in *Figure 6.29*.

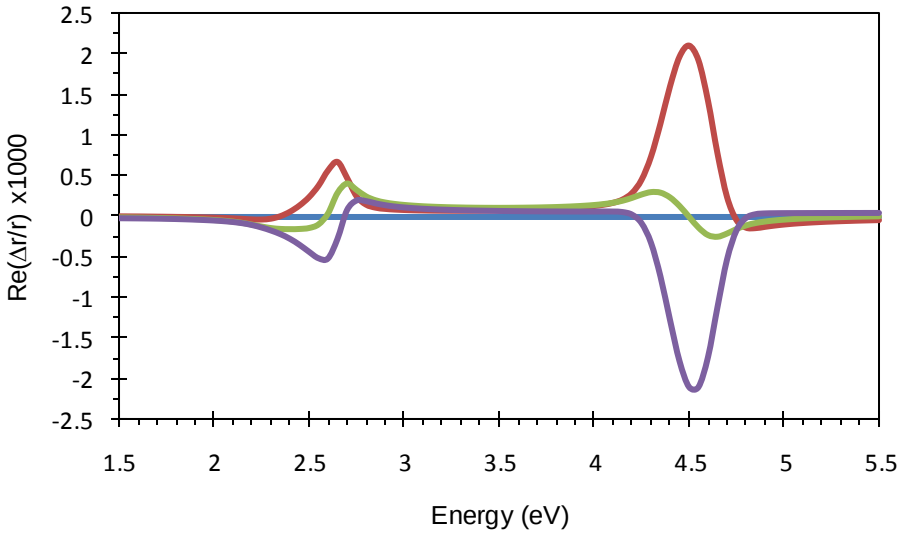

Figure 6.31: *RA spectra from a molecule with a tilt of 60° at 3° incidence for azimuthal angles of 0° (blue), 45° (red), 90° (green) and 135° (purple).*

The non-zero value for the spectrum at an azimuthal angle of 90° in *Figure 6.31* shows an additional source (or cause) of anisotropy that hasn't had to be considered before. The azimuthal angle scans at different energies (*Figures 6.29 & 6.30*) all showing a superposition effect of sinθ and sin2θ suggest this source is always present (at all azimuthal angles), to enable it to be studied it must first be isolated.

Ellipticity

The ADRAS work of MacDonald et al. [6.2] described a situation where ellipticity would be non-zero at normal incidence for a situation where one of the principle dielectric axes of an absorbing biaxial material is not aligned with the surface normal. A similar approach is considered here, the ellipticity is defined in *Figure 6.32*.

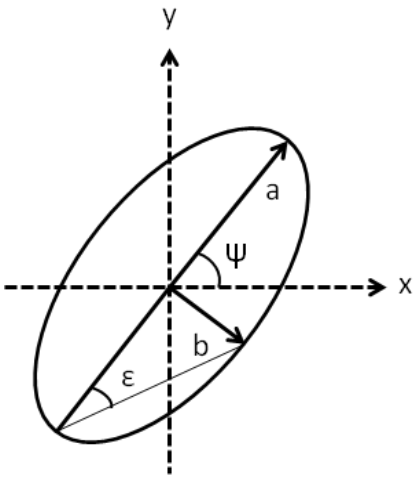

Figure 6.32: *Definitions of an elliptical polarisation state.*

The eigen-polarisations (the polarisations for which the sample acts as an isotropic mirror) have the form $\begin{pmatrix}\chi_+\\1\end{pmatrix}$ and $\begin{pmatrix}\chi_-\\1\end{pmatrix}$ where $\chi_+\chi_- = -1$. These polarisation states have the same ellipticity ε but orthogonal semi major axes. The two elliptical polarisations introduced have Jones Cartesian vectors of the form:

$$e_\alpha = \begin{bmatrix}\cos\psi\cos\varepsilon - i\sin\psi\sin\varepsilon\\ \sin\psi\cos\varepsilon + i\cos\psi\sin\varepsilon\end{bmatrix} \qquad \textit{Eqn. 6.36}$$

$$e_\beta = \begin{bmatrix} \sin\psi\cos\varepsilon + i\cos\psi\sin\varepsilon \\ -\cos\psi\cos\varepsilon + i\sin\psi\sin\varepsilon \end{bmatrix} \qquad \textit{Eqn. 6.37}$$

where ψ is the angle the major axis of e_α makes with *x*-axis, and ε is the ellipticity angle [6.21-6.22]:

$$\varepsilon = \frac{b}{a} \qquad \textit{Eqn. 6.38}$$

and *a* and *b* are the lengths of the major and minor axes respectively.

The Cartesian Jones matrix is given by:

$$R^c = T^{e\to c} R^e T^{c\to e} \qquad \textit{Eqn. 6.39}$$

where R^e is the Jones Matrix in the elliptical frame:

$$R^e = \begin{bmatrix} r_\alpha & 0 \\ 0 & r_\beta \end{bmatrix} \qquad \textit{Eqn. 6.40}$$

and the transformation matrices are given by:

$$T^{e\to c} = \left[e_\alpha \middle| e_\beta \right] \qquad \textit{Eqn. 6.41}$$

$$T^{c\to e} = \left[T^{e\to c} \right]^{-1} \qquad \textit{Eqn. 6.42}$$

From this elliptical frame of reference it is possible to obtain from the simulations the ellipticity of the polarisation eigenstates. However for RAS we are only interested in their difference, which can hence be found for each azimuthal angle and is shown for one such angle in *Figure 6.33*.

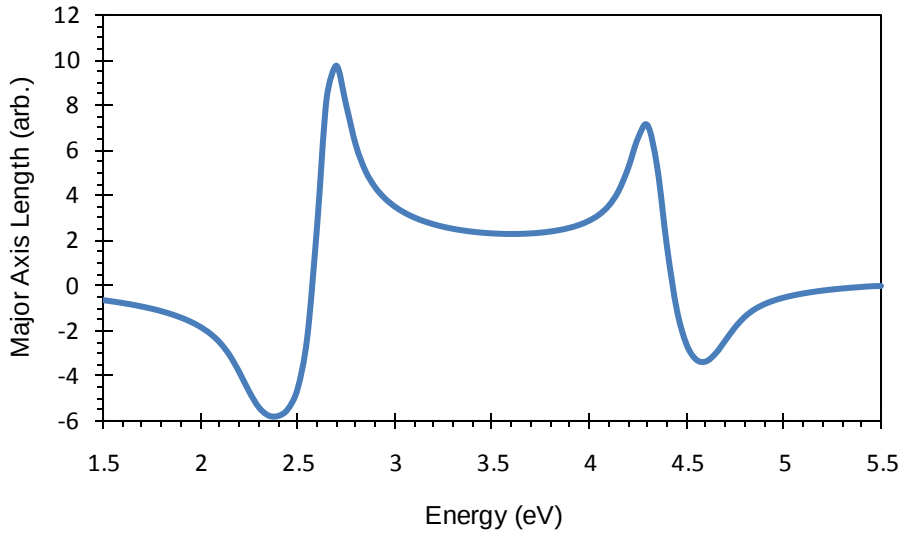

Figure 6.33: *The difference in length of the major axes at an azimuthal angle of 45°.*

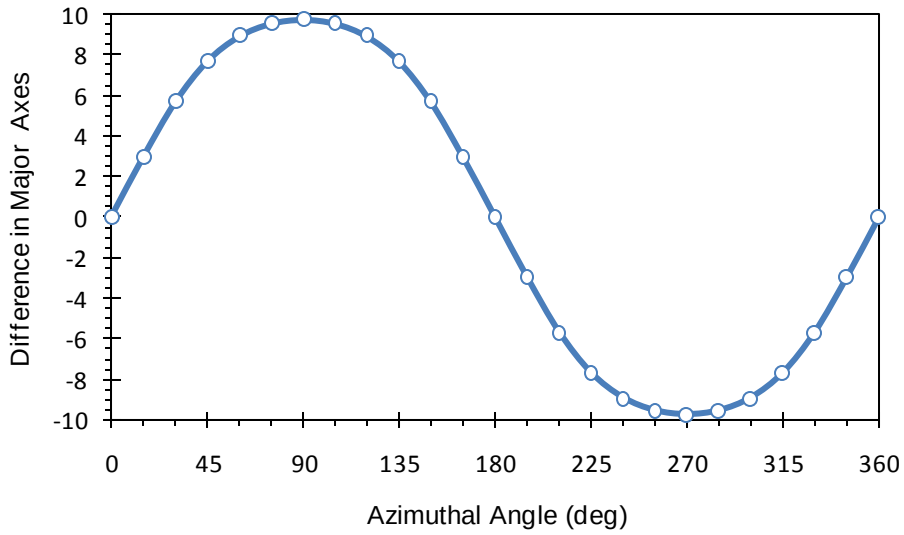

Figure 6.34: *The effect of azimuthal rotation on the difference in length of the major axis of the elliptical eigen-polarisation states at 2.65eV.*

As can be seen from *Figure 6.33* the line shape at an azimuthal angle of 90° of the elliptical components has similar features to that of the RA spectrum observed for the corresponding angle as shown in *Figure 6.31*. Appropriate scaling of these elliptical components with energy and film thickness gives a match to the RAS. *Figure 6.34* also shows that this elliptical signal has a $\sin\theta$ like dependence when rotated about the azimuth which corresponds to the $\sin\theta$ observed above, suggesting

this sinθ term is due to a difference between the elliptical polarisation states, observed due to the tilt at off normal incidence angles.

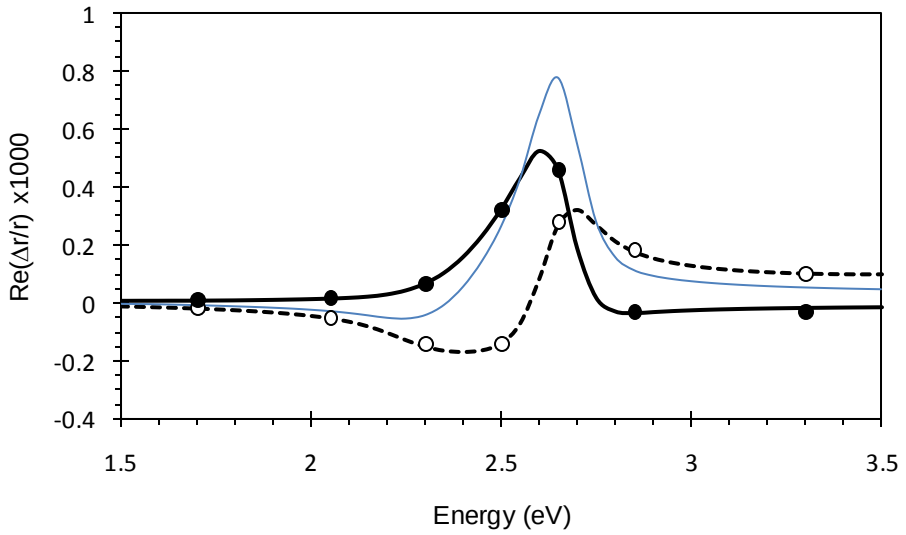

Figure 6.35: *The RA response of a molecule of tilt 60° at 3° incidence (blue line). The Fourier terms u (open circles) and v (filled circles), the elliptical anisotropy (dashed black line) and the non-elliptical anisotropy (solid black line).*

The Fourier terms *u* and *v* from *Eqn. 6.35*, were determined for a series of different energies and are shown in *Figure 6.35*. It is no surprise that the *v* term has a lineshape identical to that of a linear (non-elliptical) anisotropy term, as non-elliptical systems exhibit such behaviour. The *u* term matches the elliptical anisotropy lineshape found from the difference in major elliptical axes, when the non-elliptical sin2θ term goes to zero. This shows conclusively that the RAS signal obtained is therefore a superposition of the elliptical and non-elliptical terms.

6.10.2 Larger Incidence Angles

The simulated results from a 3° incidence angle show that extra information can be obtained from looking at tilted molecules at off normal incidence. Now the case for extending the study to larger incidence angles is considered.

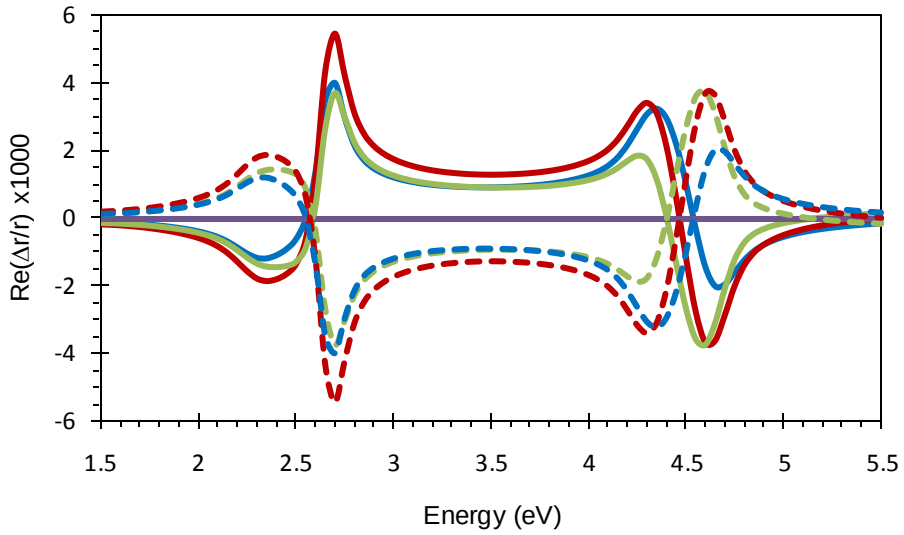

Figure 6.36: *RA response from a molecule of tilt 60° at an angle of incidence of 45° for azimuthal angles of 45° (solid blue line), 90° (solid red line), 135° (solid green line), 180° (solid purple line), 225° (dashed green line), 270° (dashed red line) and 315° (dashed blue line).*

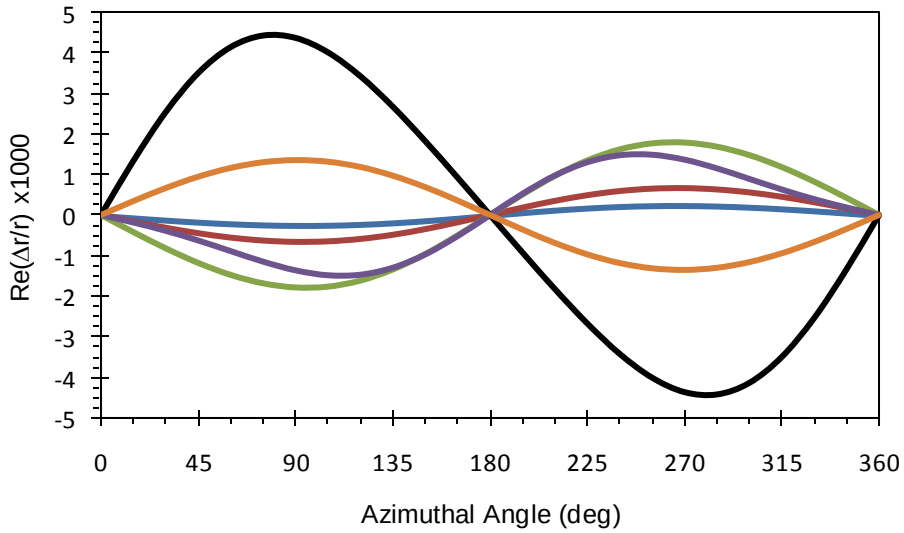

Figure 6.37: *Comparison of azimuthal rotations of a molecule of tilt 60° at an angle of incidence of 45° at energies of 1.7eV (blue), 2.05eV (red), 2.3eV (green), 2.5eV (purple), 2.65eV (black) and 3.3eV (orange).*

Figure 6.36 shows the RA spectra at selected azimuthal angles, and it is clear that the lineshape is now dominated by the elliptical effect. For all azimuthal angles the lineshape is similar to those obtained at 3° incidence for the same molecule at an azimuth of 90° and the spectral intensity is dominated by a $\sin\theta$ variation, as shown

in *Figure 6.37*. Again by determining the Fourier components *u* and *v* at a series of different energies, the lineshape and intensity of the elliptical and non-elliptical anisotropies can be found for this system for different incidence angles.

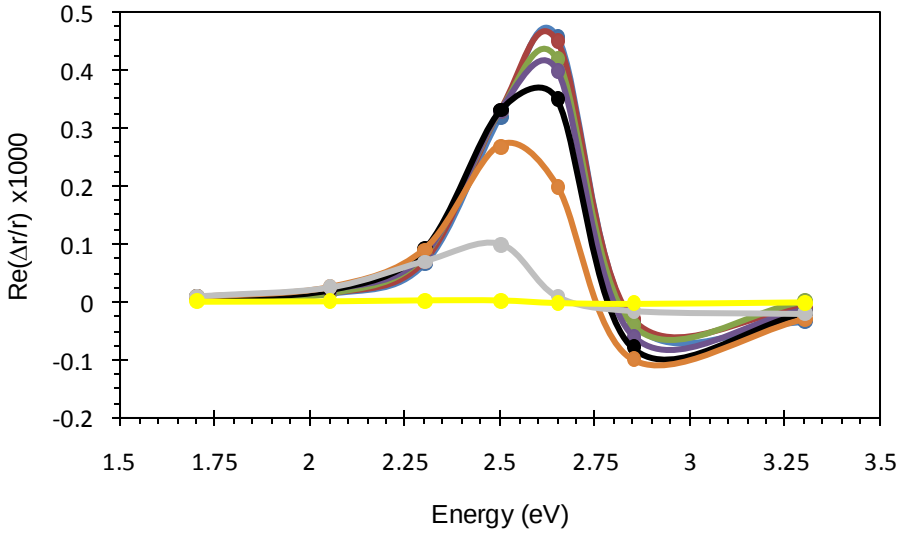

Figure 6.38: *The non-elliptical RA lineshape determined from the Fourier components of the ADRAS curves for a molecule of tilt 60° at incidence angles of 3° (blue), 15° (red), 30° (green), 45° (purple), 60° (black), 75° (orange) 85° (grey) and 89.9° (yellow).*

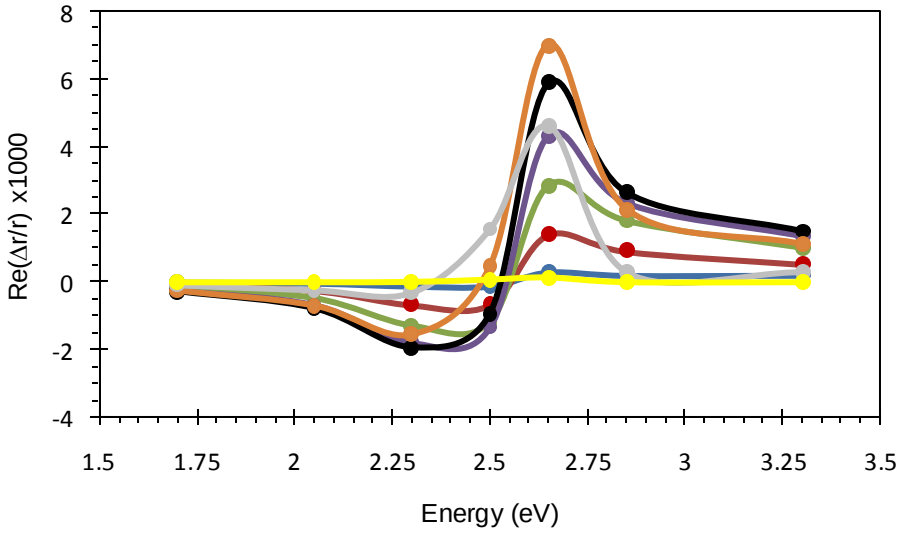

Figure 6.39: *The elliptical RA lineshape determined from the Fourier components of the ADRAS curves for a molecule of tilt 60° at incidence angles of 3° (blue), 15° (red), 30° (green), 45° (purple), 60° (black), 75° (orange) 85° (grey) and 89.9° (yellow).*

Figures 6.38 & 6.39 show how the lineshape of the elliptical and non-elliptical terms vary with incidence angle. For the system shown here the elliptical term dominates the spectrum in all the cases shown except for 3° and 89.9°, suggesting that off normal incidence or variable incidence angle RAS could offer further insight into systems with tilted molecules.

The separation of these different sources of anisotropy allows each to be studied individually. The non-elliptical anisotropy term is the one which is most commonly observed and hence must is known about. The elliptical term merits further investigation and holds information relating to the material's dielectric tensor, which could potentially allow a molecular tilt to be determined using an off normal incidence system.

6.10.3 The effect of non-zero θ_3

Thus far only the value of $\theta_3 = 0$ has been considered (for simplicity reasons); the non-zero effect of θ_3 is now briefly considered.

For a flat molecule ($\theta_2 = 0$) the angles θ_1 and θ_3 have the same definition (see *Appendix A*) and this section has little relevance as the same effects can be modelled using just one angle. However for tilted molecules this is no longer the case, and a non-zero (nor a multiple of 90°) value of θ_3 results in none of the 3 principle dielectric axes being aligned with the surface plane of surface normal. A good example to illustrate the use of this angle would be chiral surfaces. In such an example the 'tilt angle' (θ_2) would be the mis-cut angle, where if $\theta_3 = 0$ the surface would be vicinal and if θ_3 were non-zero (nor a multiple of 90°) the surface would have both steps and kinks.

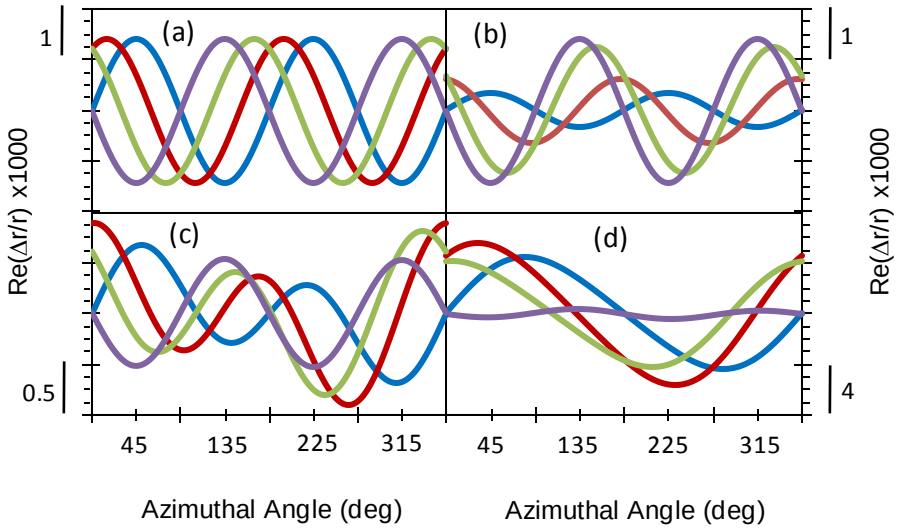

Figure 6.40: *The effects of azimuthal rotations for values of θ_3 of 0° (blue), 30° (red), 60° (green) and 90° (purple); for (a) a flat molecule at normal incidence, (b) a molecule of tilt 60° at normal incidence, (c) a molecule of tilt 60° at 3° incidence, (d) a molecule of tilt 60° at 45° incidence.*

Figure 6.40 shows the effect of varying the value of θ_3; for a flat molecule at normal incidence (*Figure 6.40 (a)*) there is a shift of θ_3 in the peak position of the ADRAS curves. For a tilted molecule at normal incidence (*Figure 6.40 (b)*) there is a shift in position and a change in intensity due to the change in the projections of the dielectric axes onto the probe directions; however the lineshape still varies with $\sin 2\theta$. For a tilted molecule at 3° off normal incidence (*Figure 6.40 (c)*) the azimuthal rotation lineshape is a superposition of $\sin\theta$ and $\sin 2\theta$; again θ_3 varies the phase and amplitude of the signal (the amplitude ratio of $\sin\theta$ and $\sin 2\theta$) as the alignment with the probe directions is different. For $\theta_3 = 90°$ the signal has a $\sin 2\theta$ dependence because for $\theta_3 = 90°$ the dielectric directions aligned with the probe directions are *y* and '*x*-*z*'. At the energy shown (2.65eV) the dielectric properties in the '*x*-*z*' direction are zero meaning no elliptical term arises and hence the signal varies with $\sin 2\theta$. At larger angles of incidence (*Figure 6.40 (d)*) the elliptical term (when present) becomes dominant and hence for the values of $\theta_3 = 0°$, 30° and 60° the shape is dominated by the $\sin\theta$ dependence. For the same reasons as at 3° incidence the $\theta_3 = 90°$ term is still dependent on $\sin 2\theta$.

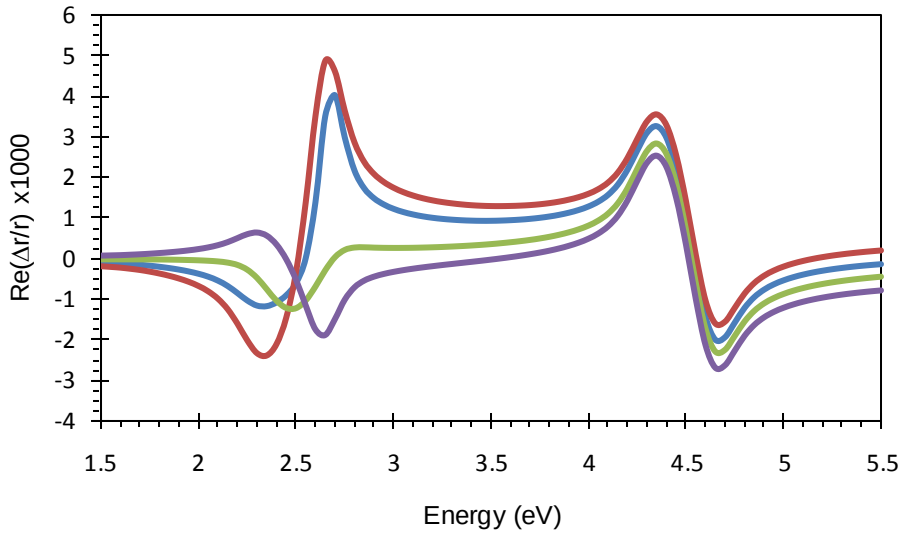

Figure 6.41: *RA response at 45° incidence for a molecule of tilt 60° and with θ_3 of 0° (blue), 45° (red), 90° (green) and 135° (purple).*

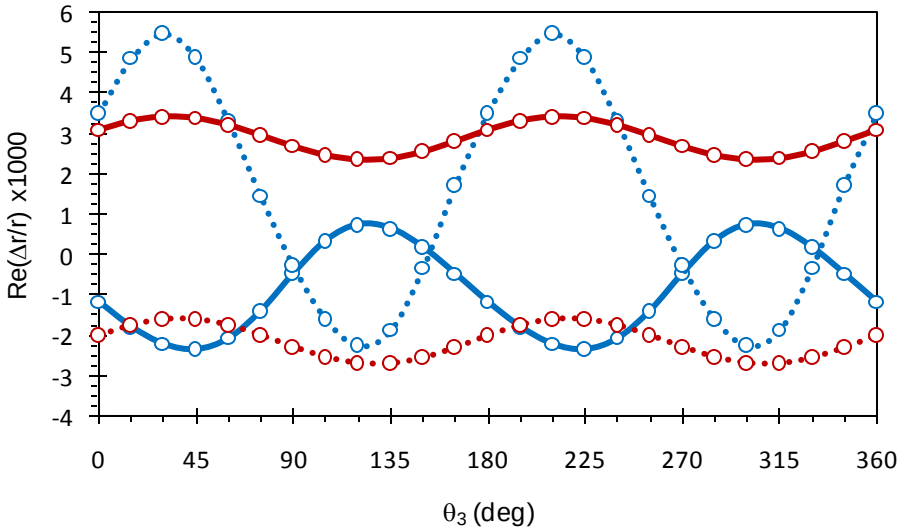

Figure 6.42: *How the RA response at 45° incidence of a molecule of tilt 60° varies with θ3 for 2.3eV (solid blue line), 2.65eV (dotted blue line), 4.3eV (solid red line) and 4.65eV (dotted red line).*

Figure 6.41 shows the effect of θ_3 on the spectra obtained from at tilted molecule at off normal incidence, as would be expected the components with a large *x*-*y* plane dependence vary most as θ_3 is varied. From *Figure 6.42* the difference between the 2.3eV curve and the 2.65eV curve gives a measure of the peak to peak amplitude of the feature arising due to the dielectric features centred at 2.5eV, similarly the 4.3eV

and 4.65eV curves do the same for the *z* based dielectric feature centred at 4.5eV. The peak to peak amplitude of the 2.5eV feature varies as θ_3 changes whilst the peak to peak amplitude of the 4.5eV feature remains constant; this is because the "amount" of *y* measured varies with θ_3 while the "amount" of *z* measured remains constant.

Varying θ_3 changes both the lineshape and amplitude of the features observed in the RA response, but it does not change the origins of the signal. The phase of the ADRAS signal will change due to θ_3, but the information content in it remains the same, hence it should still be possible to determine the dielectric tensor from the elliptical component of the signal; however its form may not be as simple as for the case where $\theta_3 = 0$.

6.11 Summary / Conclusions

The work in this chapter (whilst no means exhaustive) has demonstrated some of the angular effects in RAS and how these affect the spectra obtained. It has demonstrated that there are significant differences between the standard configuration and the rotated 45 configuration for real systems (~3-5° incidence); the latter being prone to ellipsometric anisotropy, due to an imbalance of *s*- and *p*-polarisations in the probe directions. For the standard configuration it has been demonstrated that for a flat molecule large incidence angles can be tolerated with little change to the lineshape obtained.

The study of tilted molecules has demonstrated that normal incidence RAS is only sensitive to the 2-dimensional anisotropy effects. Hence the signal measured is the projections of the material properties onto the probe directions and a $\sin 2\theta$ dependence is observed (to first order) when the sample is rotated. For off normal incidence the signal from the tilted molecule changes significantly; the probe directions have sensitivity in all three directions meaning the breakdown of symmetry can be observed. This is best observed when the sample is rotated as there is a dependence on a superposition of $\sin 2\theta$ and $\sin\theta$, the latter arising from elliptical

effects. This can be observed at even small angles of incidence (3°) and can be isolated by rotating the sample such that the sin2θ term goes to zero, or determined by finding the Fourier coefficients *u* and *v* from *Eqn. 6.35*. Extension to larger incidence angles sees the elliptical term dominate the signal.

The possibility then arises of using this elliptical term to determine the dielectric tensor and hence the molecular tilt of the molecule which could present a strong case for the use of off normal incidence (and variable incidence angle) RAS systems.

6.12 References

[6.1] B.F. MacDonald and R.J. Cole; Appl. Phys. Lett. **80**, 3527 (2002)

[6.2] B.F. MacDonald, J.S. Law and R.J. Cole; J. Appl. Phys. **93**, 3320 (2003)

[6.3] S. Teitler and B. Henvis; J. Opt. Soc. Am. **60**, 830 (1970)

[6.4] D.W. Berreman and T.J. Scheffer; Phys. Rev. Lett. **25**, 577 (1970)

[6.5] D.W. Berreman; J. Opt. Soc. Am. **62**, 502 (1972)

[6.6] M. Schubert; Phys. Rev. B **53**, 4265 (1996)

[6.7] D.S. Roseburgh, *Epioptic Modelling*, PhD Thesis, The University of Edinburgh (2006)

[6.8] B. Koopmans, P.V. Santos and M. Cardona; Phys. Stat. Sol. A **170**, 307 (1998)

[6.9] J. Rumberg, *Development and Optimisation of the Reflectance Anisotropy Spectroscopy (RAS) Technique with Respect to Online Growth Control*, Diploma Thesis, Technische Universität Berlin (1996)

[6.10] C.P. Mansley, C.I. Smith, M.C. Cuquerella, T. Farrell, D.G. Fernig, C. Edwards and P. Weightman; Phys. Stat. Sol. (c) **5**, 2582 (2008)

[6.11] P.D. Lane; *Reflection Anisotropy Spectroscopy (RAS) and Atomic Force Microscopy (AFM) Studies of Biological Molecules*, Masters Dissertation, The University of Liverpool (2004)

[6.12] T. Farrell, P. Harrison, C.I. Smith, D.S. Martin and P. Weightman; Appl. Phys. Lett. **93**, 191102 (2008)

[6.13] K. Schmidegg, L.D. Sun and P. Zeppenfeld; Appl. Phys. Lett. **89**, 051906 (2006)

[6.14] R.J. Cole, B.G. Frederick and P. Weightman; J. Vac. Sci. Technol. A **16**, 3088 (1998)

[6.15] *Handbook of Optical Constants of Solids*, E.D. Palik (Ed.) Academic Press, Orlando/London (1985)

[6.16] H. Goldstein; *Classical Mechanics* 2nd Edition, Addison-Wesley Publishing Reading, Massachusetts/London (1964)

[6.17] B.S. Mendoza and R.A. Vázquez-Nava; Phys Rev B **72**, 035411 (2005)

[6.18] P. Weightman, G.J. Dolan, C.I. Smith, M.C. Cuquerella, N.J. Almond, T. Farrell, D.G. Fernig, C. Edwards and D.S. Martin; Phys. Rev. Lett. **96**, 086102 (2006)

[6.19] J.F. McGilp; Prog. Surf. Sci. **49**, 1 (1995)

[6.20] T.E. Jenkins; J. Phys. D: Appl. Phys. **32**, R45 (1999)

[6.21] R.M.A. Azzam and N.M. Bashara; *Ellipsometry and Polarised Light*, North Holland, Amsterdam (1987)

[6.22] S. Huard; Polarization of Light, Wiley, Chichester (1997)

Chapter 7: Conclusions and Future Work

7.1 Conclusions

The aim of this project was to investigate the effect of nanoscale modifications of the surface; this was done in a number of different manners. The ion bombardment work in *Chapter 4* demonstrated that the time and temperature dependence of RAS signals can be used to determine energy barriers of kinetic processes due to atomic defects on the surface. The deposition of methanthiol on to the Cu(110) surface, in *Chapter 5* allowed the RAS signature of thiolate-Cu linkage to be identified. The multilayer model derived in this chapter provides a simple method of modelling anisotropy from multiple thin films. The simulated angular effects work reported in *Chapter 6* demonstrate the sensitivity of ADRAS to out of the surface plane anisotropy, caused by oriented films or molecular tilt. This chapter also demonstrates the effects of off-normal incidence RAS which has not been reported elsewhere.

In conclusion this work has demonstrated that RAS is sensitive to even small changes on the surface although this may not always appear the case solely from recording spectra.

The Cu(110) and Cu(13,13,1) spectra on initial viewing appear very similar but as demonstrated by studying the 2.1eV feature as a function of bombardment time at low temperatures it is possible to observe the different rates at which processes occur on these two surfaces.

The molecular tilt and off normal incidence work reported in *Chapter 6* shows that small changes to the orientation of overlayer may only have a small impact on the spectral shape but has a large impact on the ADRAS response of the system.

These two examples demonstrate the large information content contained within RAS measurements, which could easily be unnoticed due to their subtlety, and the work in this thesis demonstrates 3 different ways in which these nanoscale changes can be observed; changes in lineshape, changes in time dependence and changes in ADRAS response.

7.2 Future Work

7.2.1 Equipment

While the experimental equipment used in this work has enabled real time measurements for individual energies as a function of time, the time to record a spectrum (with 90 data points) is approximately 2-3 minutes. It would be useful if this time could be cut significantly making it possible to obtain more data on the evolution of peak lineshape with time; for example in this work it would have been useful to record such data during the destruction of the 2.1eV peak during ion bombardment or methanethiol deposition. Groups in Liverpool [7.1] and Berlin [7.2] have developed multi-channel detection 'Rapid RAS' systems although presently these are only reported as having up to 16-channels (allowing only 16 energies to be recorded), and while this is not perfect, appropriate tuning of wavelengths could allow such a system to be used as a peak profiling tool over short spectral ranges. If such systems could be extended to more channels extra information could possibly be obtained about changes in lineshape as well as changes in intensity.

7.2.2 Experiments

The patch argument relating surface state intensity and number of defects seems to provide good fits to the experimental data obtained for defects due to ion bombardment of Cu(110), and thermal defects of Cu(110) (and Ag(110)[7.3]). A range of patch sizes and energy barriers have been identified, although further experimental measurements are required to identify more accurately the values of some of these parameters. Low temperature STM measurements were planned at the new Scottish centre for interdisciplinary surface spectroscopy (SCISS) facility [7.4]

but the availability of this equipment came too later for the timescale of this project; such results however would provide useful statistical information for parameters such as defect coverage and step density. A thorough STM study could also provide information regarding the behaviour of the Cu(110) surface upon bombarding for ~30mins and hopefully provide insight into the behaviour in the 4eV region of the RAS spectrum.

Another variable which is perhaps worth investigating is the choice of bombardment gas. Smentkowski [7.5] reported that for heavier ions the defects created on the surface were localised to the impact site, whilst for lighter gases this was not the case, for a sputtering yield of more than 1 defect per ion this would also affect the patch size calculated.

The RAS results in this thesis show that the 2.1eV feature on Cu(110) is destroyed upon ion bombardment at low temperatures. The IPES results of Heskett et al. [7.6] showed that the unoccupied state giving rise to this transition was destroyed under similar conditions. Sun et al. [7.7] studied the deposition of CO on to Cu(110) and reported the destruction as being due to scattering causing the occupied state to become isotropic. It would perhaps be useful to have both IPES and PES results for both low temperature ion bombarding and deposition studies to understand the origins of surface state behaviour observed in RAS.

Fitting patch size curves for different sized molecules deposited on the system could also be a useful exercise; one might expect that a large molecule would have a more destructive effect on the surface state than a small molecule, however if the molecule size was less than the patch size this may not be the case.

Molecular dynamics studies of such systems could also yield interesting results and take the studies on to a further level by considering clustering effects and different sources of defects.

The multi-layer model derived in *Chapter 5* is potentially very useful for simulating the normal incidence RAS response from multilayered systems without the need for the Berreman algebra, and could be applied to many systems. Similarly the application of the effective medium theory to sub-monolayer adsorbate coverages could also be useful in simulating RA response. Although the model itself is fairly crude it has worked for the S/Cu system in this work. It would be interesting to investigate this model further in an attempt to understand why it seems to work.

The work contained in *Chapter 6* has many potential applications, and it would be interesting to observe the behaviours exhibited in the simulations experimentally. A system which allows control of the molecular tilt would first need to be found, a Langmuir trough could be one potential method of achieving this. Recording off normal incidence RAS measurements is another potential source of substantial results, although obviously this would require the development of an off normal incidence or variable incidence angle RAS kit. ADRAS measurements from tilted molecular systems would also be of interest, and the results in *Chapter 6* show that chiral systems would also provide interesting results.

Further simulation results could provide more insight into which samples might provide the most suitable candidates for experimental investigation. The system used for the work in this thesis was specifically chosen for its simplicity, but an extension of this study to more complex systems could be useful. Further work is also needed to see if a simple method could be developed to use these types of results to determine complete molecular orientation.

7.3 References

[7.1] P. Harrison, T. Farrell, A. Maunder, C.I. Smith and P. Weightman; Meas. Sci. Technol. **12**, 2185 (2001)

[7.2] C. Kaspari, M. Pristov and W. Richter; Phys. Stat. Sol (b) **242**, 2561 (2005)

[7.3] G.E. Isted, P.D. Lane and R.J. Cole; Phys. Rev. B **79**, 205424 (2009)

[7.4] http://www.st-andrews.ac.uk/physics/condmat/sciss/index.html

[7.5] V.S. Smentkowski; Prog. Surf. Sci. **64**, 1 (2000)

[7.6] D. Heskett, D. DePietro, G. Sabatino, M. Tammaro; Surf. Sci. **513**, 405 (2002)

[7.7] L.D. Sun, M. Hohage, P. Zeppenfeld, R.E. Balderas-Navarro and K. Hingerl; Phys. Rev. Lett. **90**, 106104

Appendix A

A.1 2×2 Matrix Representation Method for Isotropic Stratified Media

In *Chapter 2* the 3-phase model was outlined, this model is useful, but addition of multiple reflections becomes more tedious and more impractical as the number of layers in the system is increased. Abelès [A.1] developed an alternative approach by using 2×2 matrix transformations which model the reflection and transmission of polarised light from a system of isotropic stratified layers, a full account of this method is reported by Azzam and Bashara [A.2].

The complex amplitudes of the incident and reflected waves at an arbitrary interface z are defined as $E_+(z)$ and $E_-(z)$ where the ± subscripts denote the directions in which the wave is travelling. The total field at z, $E(z)$ can then be expressed as a 2×1 matrix:

$$E(z)=\begin{bmatrix}E_+(z)\\E_-(z)\end{bmatrix} \qquad \textit{Eqn. A.1}$$

It is then possible to use a transform matrix to relate the field $E(z')$ at z' to the field $E(z'')$ at z'' when z' and z'' are separated by stratified isotropic media.

$$E(z')=TE(z'') \qquad \textit{Eqn. A.2}$$

$$\begin{bmatrix}E_+(z')\\E_-(z')\end{bmatrix}=\begin{bmatrix}T_{11} & T_{12}\\T_{21} & T_{22}\end{bmatrix}\begin{bmatrix}E_+(z'')\\E_-(z'')\end{bmatrix} \qquad \textit{Eqn. A.3}$$

The general transform matrix can be used to represent the overall reflection and transmission properties of the stratified media between z' and z'' and can be expressed as the product of a series of partial transfer matrices (T_{Pn}), corresponding to layer *n*, and transition matrices ($L_{(n-1)n}$) corresponding to the boundaries between layers *n-1* and *n*.

$$T = L_{12}T_{P2}L_{23}T_{P3}L_{34}...T_{Pn}L_{(n-1)n} \qquad \textit{Eqn. A.4}$$

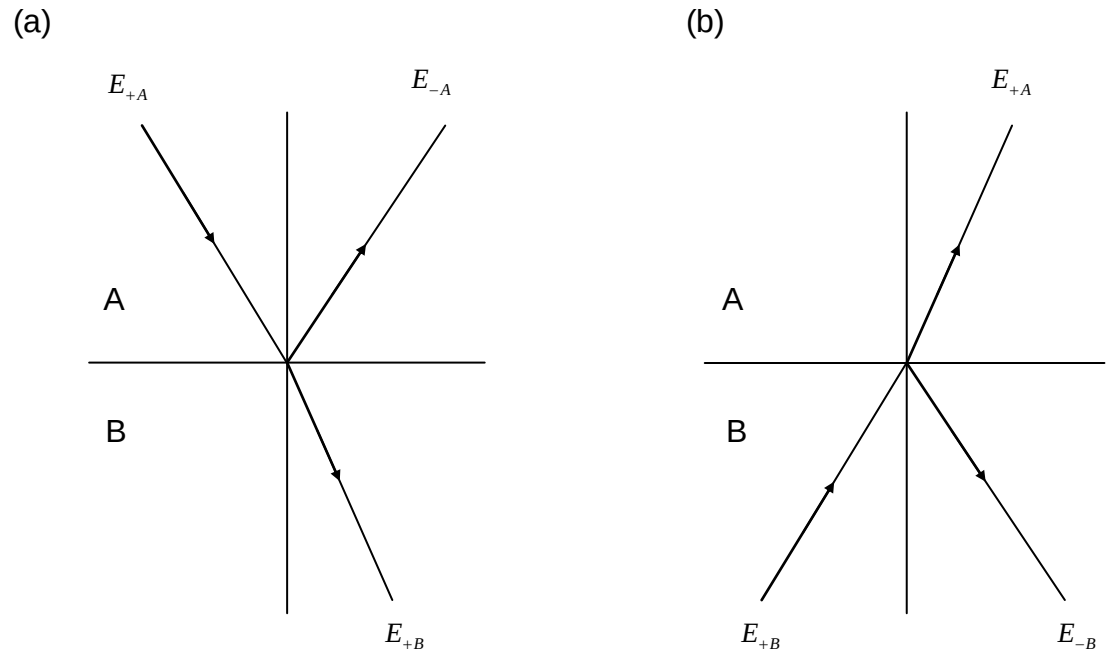

Figure A.1: *The interface between media A and B, showing (a) light incident from medium A and (b) light incident from medium B.*

Figure A.1 shows an interface between two media *A* and *B*. *L* can be used to relate the electric fields of the wave at either side of the interface. The subscripts *A* and *B* denote the medium being considered and r_{AB} and t_{AB} are the Fresnel coefficients for reflection and transmission respectively.

$$\begin{bmatrix} E_{+A} \\ E_{-A} \end{bmatrix} = \begin{bmatrix} L_{11} & L_{12} \\ L_{21} & L_{22} \end{bmatrix} \begin{bmatrix} E_{+B} \\ E_{-B} \end{bmatrix} \qquad \textit{Eqn. A.5}$$

For incident light from medium *A* on the interface *AB* it is known that:

$$E_{+B} = t_{AB} E_{+A} \qquad \textit{Eqn. A.6}$$

$$E_{-A} = r_{AB} E_{+A} \qquad \textit{Eqn. A.7}$$

$$E_{-B} = 0 \qquad \textit{Eqn. A.8}$$

Therefore:

$$\begin{bmatrix} E_{+A} \\ E_{-A} \end{bmatrix} = \begin{bmatrix} 1/t_{AB} & L_{12} \\ r_{AB}/t_{AB} & L_{22} \end{bmatrix} \begin{bmatrix} E_{-B} \\ 0 \end{bmatrix} \qquad \textit{Eqn. A.9}$$

Similarly for incident light from medium *B* on the interface *BA* it is known that:

$$E_{+A} = 0 \qquad \textit{Eqn. A.10}$$

$$E_{-A} = t_{AB} E_{-B} \qquad \textit{Eqn. A.11}$$

$$E_{+B} = r_{BA} E_{-B} \qquad \textit{Eqn. A.12}$$

Therefore:

$$\begin{bmatrix} 0 \\ E_{-A} \end{bmatrix} = \begin{bmatrix} L_{11} & -r_{BA}/t_{AB} \\ L_{21} & \left(t_{AB}t_{BA} - r_{AB}r_{BA}\right)/t_{AB} \end{bmatrix} \begin{bmatrix} E_{+B} \\ 0 \end{bmatrix} \qquad \textit{Eqn. A.13}$$

After manipulation using Fresnel interface coefficients for both propagation directions:

$$L_{AB} = \frac{1}{t_{AB}} \begin{bmatrix} 1 & r_{AB} \\ r_{AB} & 1 \end{bmatrix} \qquad \textit{Eqn. A.14}$$

The propagation through a homogeneous medium results in a phase change of the wave in the direction of travel. This is dependent on the complex refractive index and the thickness of the medium, the angle of incidence and the wavelength of light. The partial transfer matrix is therefore written as:

$$T_P = \begin{bmatrix} e^{i\beta} & 0 \\ 0 & e^{-i\beta} \end{bmatrix} \qquad \textit{Eqn. A.15}$$

where β as previously defined is:

$$\beta = 2\pi N \cos\theta_t \frac{d}{\lambda} \qquad \textit{Eqn. A.16}$$

Knowing that $E_{-B} = 0$ enables *Eqn. A.3* to become:

$$\begin{bmatrix} E_{+A} \\ E_{-A} \end{bmatrix} = \begin{bmatrix} T_{11} & T_{12} \\ T_{21} & T_{22} \end{bmatrix} \begin{bmatrix} E_{+B} \\ 0 \end{bmatrix} \qquad \textit{Eqn. A.17}$$

By expanding this expression the reflection coefficient can be found:

$$r = \frac{E_{-A}}{E_{+A}} = \frac{T_{21}}{T_{11}} \qquad \textit{Eqn. A.18}$$

T_{11} and T_{21} are elements of the general transform matrix. The components for the *s*- and *p*- polarisations are uncoupled meaning that each polarisation can be treated separately – hence distinct matrices are formed for each polarisation.

A.2 4×4 Matrix Representation Method for Anisotropic Stratified Media

The 2×2 matrix formalism has allowed the optical properties of isotropic stratified media to be calculated; but in order to consider anisotropic stratified media a higher rank matrix is required as the *p*- and *s*- components of the magnetic and electric fields are no longer uncoupled. This method was originally developed by Teitler and Henvis [A.3] but is more commonly known for the development by Berreman [A.4-A.5]. A good overview of this is given by Azzam and Bashara [A.2], and has since been refined by Schubert [A.6]. As the code used to perform the simulations is based on that of Roseburgh [A.7] the notation here follows that of Ref [A.7] closely.

By assuming a $e^{i\omega t}$ time dependence Maxwell's equations in differential form can be written as:

$$\begin{bmatrix} 0 & 0 & 0 & 0 & -\partial_z & \partial_y \\ 0 & 0 & 0 & \partial_z & 0 & -\partial_x \\ 0 & 0 & 0 & -\partial_y & \partial_x & 0 \\ 0 & \partial_z & -\partial_y & 0 & 0 & 0 \\ -\partial_z & 0 & \partial_x & 0 & 0 & 0 \\ \partial_y & -\partial_x & 0 & 0 & 0 & 0 \end{bmatrix} \begin{bmatrix} E_x \\ E_y \\ E_z \\ H_x \\ H_y \\ H_z \end{bmatrix} = \frac{1}{c}\frac{\partial}{\partial t} \begin{bmatrix} D_x \\ D_y \\ D_z \\ B_x \\ B_y \\ B_z \end{bmatrix} \quad \textit{Eqn. A.19}$$

Or:

$$\begin{bmatrix} 0 & curl \\ -curl & 0 \end{bmatrix} \begin{bmatrix} E \\ H \end{bmatrix} = \frac{1}{c}\frac{\partial}{\partial t} \begin{bmatrix} D \\ B \end{bmatrix} \quad \textit{Eqn. A.20}$$

$$RG = \frac{1}{c}\frac{\partial}{\partial t} C \quad \textit{Eqn. A.21}$$

If we assume that the medium is linear the R and G can be related by:

$$C = MG \quad \textit{Eqn. A.22}$$

where M is the optical matrix which contains all the information about the optical properties of the medium, and is of the form:

$$M = \begin{bmatrix} \varepsilon & \rho \\ \rho' & \mu \end{bmatrix} \qquad \textit{Eqn. A.23}$$

where ε and μ are the dielectric and magnetic susceptibility tensors and ρ and ρ' are the optical activity or gyroscopic tensors. Each quadrant represents a 3×3 matrix corresponding to the x, y and z directions.

We now need to define the geometry of the system in which we are working. The plane of incidence is defined to be in the x-z plane, meaning that the wave vector of the wave has no y-component. Since our system is homogeneous in the x-y plane the component of the k vector in the x direction k_x is constant. Therefore E (and similarly B, D and H) can be written as:

$$E = E_0 \exp i\left[k_x x + k_z(z) z - \omega t\right] \qquad \textit{Eqn. A.24}$$

and the differential operators as:

$$\partial_x = ik_x \qquad \textit{Eqn. A.25}$$

$$\partial_y = 0 \qquad \textit{Eqn. A.26}$$

$$\frac{\partial}{\partial t} = -i\frac{\omega}{c} \qquad \textit{Eqn. A.27}$$

This allows the curl operator to be rewritten as:

$$curl = \begin{bmatrix} 0 & -\partial_z & 0 \\ \partial_z & 0 & -ik_x \\ 0 & ik_x & 0 \end{bmatrix} \qquad \textit{Eqn. A.28}$$

If we write the generalised field vector G as $G = e^{i\omega t} X$ where X is the spatial part then *Eqn. A.21* becomes:

$$\begin{bmatrix} 0 & 0 & 0 & 0 & -\partial_z & 0 \\ 0 & 0 & 0 & \partial_z & 0 & -ik_x \\ 0 & 0 & 0 & 0 & ik_x & 0 \\ 0 & \partial_z & 0 & 0 & 0 & 0 \\ -\partial_z & 0 & ik_x & 0 & 0 & 0 \\ 0 & -ik_x & 0 & 0 & 0 & 0 \end{bmatrix} \begin{bmatrix} X_1 \\ X_2 \\ X_3 \\ X_4 \\ X_5 \\ X_6 \end{bmatrix} = -i\frac{\omega}{c} MX \qquad \textit{Eqn. A.29}$$

As a result of this it is now possible to write down 4 differential and 2 algebraic equations relating the generalised field vector X to the properties of the medium described in the matrix M.

The differential equations are:

$$\partial_z X_5 = i\frac{\omega}{c} M_{1i} X_i \qquad \textit{Eqn. A.30}$$

$$\partial_z X_4 = -i\frac{\omega}{c} M_{2i} X_i + ik_x X_6 \qquad \textit{Eqn. A.31}$$

$$\partial_z X_2 = -i\frac{\omega}{c} M_{4i} X_i \qquad \textit{Eqn. A.32}$$

$$\partial_z X_1 = i\frac{\omega}{c} M_{2i} X_i + ik_x X_3 \qquad \textit{Eqn. A.33}$$

and the algebraic equations are:

$$k_x X_5 = -\frac{\omega}{c} M_3 X_i \qquad \textit{Eqn. A.34}$$

$$k_x X_2 = \frac{\omega}{c} M_{6i} X_i \qquad \textit{Eqn. A.35}$$

It is now possible using *Eqns. A.34 & A.35* to eliminate two of the variables from the differential equations. Berreman chooses to eliminate X_3 and X_6 which are the z components of the electric and magnetic fields:

$$X_3 = c_{31}X_1 + c_{32}X_2 + c_{34}X_4 + c_{35}X_5 \qquad \textit{Eqn. A.36}$$

$$X_6 = c_{61}X_1 + c_{62}X_2 + c_{64}X_4 + c_{65}X_5 \qquad \textit{Eqn. A.37}$$

where the coefficients c are given by:

$$c_{31}D = M_{61}M_{36} - M_{31}M_{66} \qquad \textit{Eqn. A.38}$$

$$c_{32}D = (M_{62} - ck_x/\omega)M_{36} - M_{32}M_{66} \qquad \textit{Eqn. A.39}$$

$$c_{34}D = M_{64}M_{36} - M_{34}M_{66} \qquad \textit{Eqn. A.40}$$

$$c_{35}D = M_{65}M_{36} - (M_{35} + ck_x/\omega)M_{66} \qquad \textit{Eqn. A.41}$$

$$c_{61}D = M_{63}M_{31} - M_{33}M_{61} \qquad \textit{Eqn. A.42}$$

$$c_{62}D = M_{63}M_{32} - (M_{62} + ck_x/\omega)M_{33} \qquad \textit{Eqn. A.43}$$

$$c_{64}D = M_{63}M_{34} - M_{33}M_{64} \qquad \textit{Eqn. A.44}$$

$$c_{65}D = (M_{35} - ck_x/\omega)M_{63} - M_{33}M_{65} \qquad \textit{Eqn. A.45}$$

where:

$$D = M_{33}M_{66} - M_{33}M_{65} \qquad \textit{Eqn. A.46}$$

Substituting *Eqns. A.36 & A.37* into the differential equations (*Eqns. A.30-A.33*) gives 4 linear differential equations in our chosen parameters.

A.2.1 The Δ Matrix

Now there are first order equations relating the field parameters to the properties of the system, they can now be condensed down into a 4×4 matrix form:

$$\partial_z \begin{bmatrix} X_1 \\ X_5 \\ X_2 \\ -X_4 \end{bmatrix} = i\frac{\omega}{c}\delta \begin{bmatrix} X_1 \\ X_5 \\ X_2 \\ -X_4 \end{bmatrix} \qquad \textit{Eqn. A.47}$$

or more compactly:

$$\partial_z \psi = i\frac{\omega}{c}\delta\psi \qquad \textit{Eqn. A.48}$$

where δ is a 4×4 matrix which is determined by the components of *M*. Note that this work uses the Schubert formulism [A.6] which differs from that of Berreman [A.5] in the definition of the field vector, hence the coefficients of the δ matrix are labelled inconsistently for a conversion between the two formalisms see [A.7].

$$\delta_{11} = M_{51} + (M_{53} + ck_x/\omega)c_{31} + M_{56}c_{61} \qquad \textit{Eqn. A.49}$$

$$\delta_{12} = M_{55} + (M_{53} + ck_x/\omega)c_{35} + M_{56}c_{65} \qquad \textit{Eqn. A.50}$$

$$\delta_{13} = M_{52} + (M_{53} + ck_x/\omega)c_{32} + M_{56}c_{62} \qquad \textit{Eqn. A.51}$$

$$-\delta_{14} = M_{54} + (M_{53} + ck_x/\omega)c_{34} + M_{56}c_{64} \qquad \textit{Eqn. A.52}$$

$$\delta_{21} = M_{11} + M_{13}c_{31} + M_{16}c_{61} \qquad \textit{Eqn. A.53}$$

$$\delta_{22} = M_{15} + M_{13}c_{35} + M_{16}c_{65} \qquad \textit{Eqn. A.54}$$

$$\delta_{23} = M_{12} + M_{13}c_{32} + M_{16}c_{62} \qquad \textit{Eqn. A.55}$$

$$-\delta_{24} = M_{14} + M_{13}c_{34} + M_{16}c_{64} \qquad \textit{Eqn. A.56}$$

$$-\delta_{31} = M_{41} + M_{43}c_{31} + M_{46}c_{61} \qquad \textit{Eqn. A.57}$$

$$-\delta_{32} = M_{45} + M_{43}c_{35} + M_{46}c_{65} \qquad \textit{Eqn. A.58}$$

$$-\delta_{33} = M_{42} + M_{43}c_{32} + M_{46}c_{62} \qquad \textit{Eqn. A.59}$$

$$\delta_{34} = M_{44} + M_{43}c_{34} + M_{46}c_{64} \qquad \textit{Eqn. A.60}$$

$$\delta_{41} = M_{21} + M_{23}c_{31} + (M_{26} - ck_x/\omega)c_{61} \qquad \textit{Eqn. A.61}$$

$$\delta_{42} = M_{25} + M_{23}c_{35} + (M_{26} - ck_x/\omega)c_{65} \qquad \textit{Eqn. A.62}$$

$$\delta_{43} = M_{22} + M_{23}c_{32} + \left(M_{26} - ck_x/\omega\right)c_{62} \qquad \textit{Eqn. A.63}$$

$$-\delta_{44} = M_{24} + M_{23}c_{34} + \left(M_{26} - ck_x/\omega\right)c_{64} \qquad \textit{Eqn. A.64}$$

Eqn. A.48 is a first order differential equation in the generalised field ψ in order to accommodate the thickness of the material d though which the wave propagates. It can be integrated between an initial point z_0 and z where $d = z - z_0$ to give:

$$\psi(z) = \exp\left(i\frac{\omega}{c}d\delta\right)\psi(z_0) \qquad \textit{Eqn. A.65}$$

The prefactor T is the transfer matrix and it projects the initial wavevector through the material, and it is defined by the power series expansion:

$$T = \exp\left(i\frac{\omega}{c}d\delta\right) = \sum_{n=0}^{\infty}\left(i\frac{\omega}{c}d\delta\right)^n \qquad \textit{Eqn. A.66}$$

A.2.2 The M Matrix

So far we have the relationship between waves at different points within the sample related to the components of *M*. The *M* matrix as defined in *Eqn. A.23* consists of 4 quadrants each consisting of a 3×3 matrix.

The first quadrant to consider is the dielectric tensor ε which relates the displacement field to the electric field and for a general anisotropic case takes the form:

$$\varepsilon_0 = \begin{bmatrix} \varepsilon_{0x} & 0 & 0 \\ 0 & \varepsilon_{0y} & 0 \\ 0 & 0 & \varepsilon_{0z} \end{bmatrix} \qquad \textit{Eqn. A.67}$$

when x, y and z are parallel to the principal optical axes of the medium. For the isotropic case $\varepsilon_{0x} = \varepsilon_{0y} = \varepsilon_{0z}$ and the dielectric tensor would be $\varepsilon_0 = \varepsilon I$, where I is the identity matrix. However if the co-ordinate system is such that the optical axes

and the geometric axes are no longer parallel then rotation tensor must be applied such that:

$$\varepsilon = R^{-1}(\theta_3)R^{-1}(\theta_2)R^{-1}(\theta_1)\varepsilon_0 R(\theta_3)R(\theta_2)R(\theta_1) \qquad \textit{Eqn. A.68}$$

where $R(\theta_3,\theta_2,\theta_1)$ are the tensors describing the rotation, and $\theta_3,\theta_2,\theta_1$ are the Euler angles as described by Goldstein [A.8].

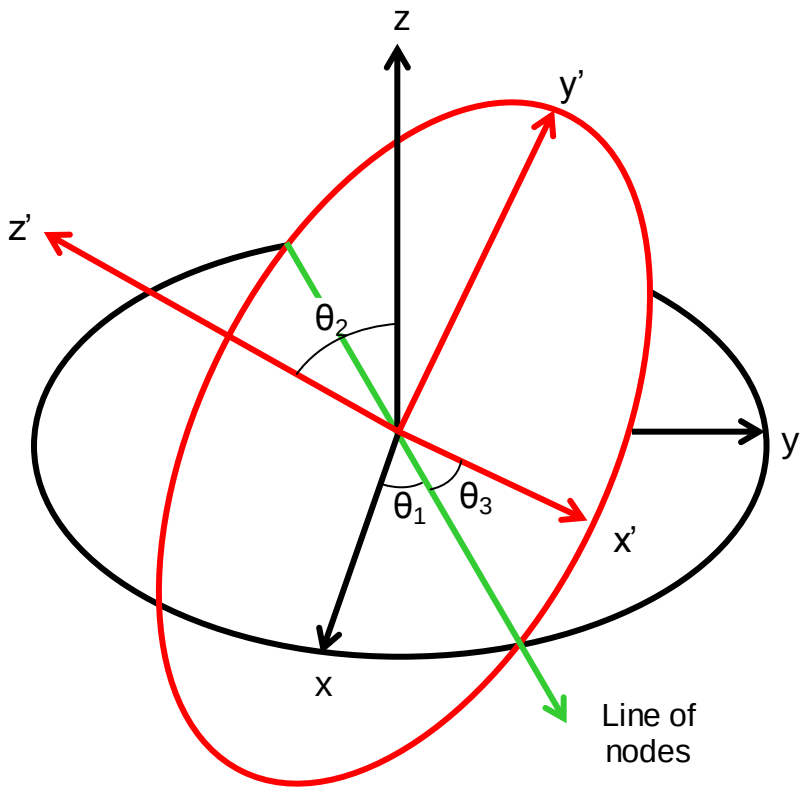

Figure A.2: *The Euler angles.*

The transformations to obtain the *x'*, *y'*, *z'* co-ordinate system from the initial *x*, *y*, *z* system must be carried out by sequential clockwise rotations: firstly about the z-axis, secondly about the new *x*-axis (shown as line of nodes in *Figure A.2*), and thirdly about the new *z*-axis (*z'* axis). In experimental terms the first rotation is the sample azimuth, the second the surface/adsorbate molecule tilt, and the third the orientation

of the molecule. (Note for an un-tilted molecule the first and third rotations are equivalent.)

$$R(\theta_1)=\begin{bmatrix}\cos\theta_1 & \sin\theta_1 & 0\\ -\sin\theta_1 & \cos\theta_1 & 0\\ 0 & 0 & 1\end{bmatrix} \qquad \textit{Eqn. A.69}$$

$$R(\theta_2)=\begin{bmatrix}1 & 0 & 0\\ 0 & \cos\theta_2 & \sin\theta_2\\ 0 & -\sin\theta_2 & \cos\theta_2\end{bmatrix} \qquad \textit{Eqn. A.70}$$

$$R(\theta_3)=\begin{bmatrix}\cos\theta_3 & \sin\theta_3 & 0\\ -\sin\theta_3 & \cos\theta_3 & 0\\ 0 & 0 & 1\end{bmatrix} \qquad \textit{Eqn. 6.71}$$

This results in the ε quadrant of the M matrix becoming:

$$M_\varepsilon=\begin{bmatrix}\varepsilon_{11} & \varepsilon_{12} & \varepsilon_{13}\\ \varepsilon_{21} & \varepsilon_{22} & \varepsilon_{23}\\ \varepsilon_{31} & \varepsilon_{32} & \varepsilon_{33}\end{bmatrix} \qquad \textit{Eqn. A.72}$$

Since we are dealing exclusively with non-magnetic materials the μ quadrant M_μ is isotropic and is hence described by the identity matrix:

$$M_\mu=\begin{bmatrix}1 & 0 & 0\\ 0 & 1 & 0\\ 0 & 0 & 1\end{bmatrix} \qquad \textit{Eqn. A.73}$$

Also we are not dealing with optically active materials hence the remaining two quadrants are:

$$M_\rho=M_{\rho'}=0 \qquad \textit{Eqn. A.74}$$

A.2.3 Multi-layered Systems

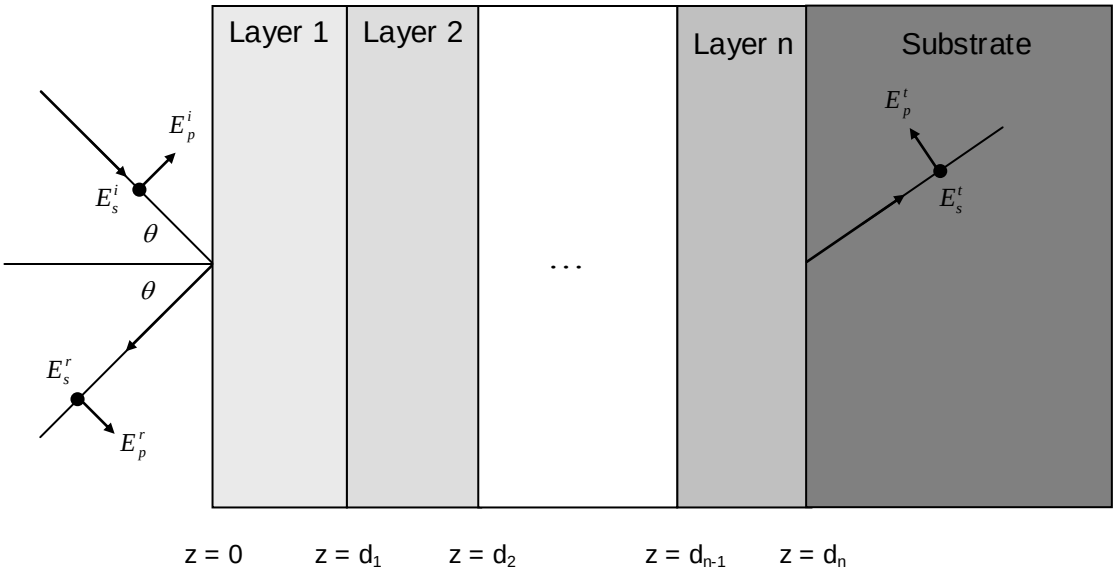

Figure A.3: *The geometry of a multi-layered system of the Schubert 4×4 matrix formulism.*

The transfer matrix as defined in *Eqn. A.65* can be used to calculate the optical response of a system of stratified media. Since this transfer matrix projects the wavevector through one medium, propagation through a sequence of media is described as a product of transfer matrices, where one matrix represents each layer. Schubert [A.6] defined the incident field vector as: (Note: the notation used here is that of Roseburgh [A.7] not that of Schubert [A.6], this is merely for consistency and simplicity, as the two are equivalent)

$$\Psi = \begin{bmatrix} E_s^i \\ E_s^r \\ E_p^i \\ E_p^r \end{bmatrix} \qquad \textit{Eqn. A.75}$$

Relating it to the transmitted field vector via a general transfer matrix gives:

$$\begin{bmatrix} E_s^i \\ E_s^r \\ E_p^i \\ E_p^r \end{bmatrix} = \begin{bmatrix} T_{11} & T_{12} & T_{13} & T_{14} \\ T_{21} & T_{22} & T_{23} & T_{24} \\ T_{31} & T_{32} & T_{33} & T_{34} \\ T_{41} & T_{42} & T_{43} & T_{44} \end{bmatrix} \begin{bmatrix} E_s^t \\ 0 \\ E_p^t \\ 0 \end{bmatrix} \qquad \textit{Eqn. A.76}$$

The second and fourth components of the right hand side are zero because there is no back travelling through the substrate medium.

Eqn. A.76 gives the relationship between the polarised components on either side of the stack of surface layers as shown in *Figure A.3*, from this the reflection and transmission coefficients can be obtained as these are defined as the ratio of the reflected or transmitted waves to the incident waves and these can be expressed in terms of the general transfer matrix as shown below:

$$r_{pp} = \left(\frac{E_p^r}{E_p^i} \right) = -\frac{T_{41}T_{13} - T_{11}T_{43}}{T_{11}T_{33} - T_{13}T_{31}} \qquad \textit{Eqn. A.77}$$

$$r_{ss} = \left(\frac{E_s^r}{E_s^i} \right) = \frac{T_{21}T_{33} - T_{23}T_{31}}{T_{11}T_{33} - T_{13}T_{31}} \qquad \textit{Eqn. A.78}$$

$$r_{ps} = \left(\frac{E_s^r}{E_p^i} \right) = \frac{T_{21}T_{13} - T_{23}T_{11}}{T_{11}T_{33} - T_{13}T_{31}} \qquad \textit{Eqn. A.79}$$

$$r_{sp} = \left(\frac{E_p^r}{E_s^i} \right) = \frac{T_{41}T_{33} - T_{43}T_{31}}{T_{11}T_{33} - T_{13}T_{31}} \qquad \textit{Eqn. A.80}$$

By comparison to the 2×2 matrix method the uncoupled components r_{pp} and r_{ss} is equivalent to the expression given in *Eqn. A.18*. If in the 2×2 matrix method the *s*- and *p*- were calculated individually the would be denoted as r_s and r_p rather than r_{ss} and r_{pp}. In the 2×2 matrix method there are no equivalent terms for r_{sp} and r_{ps} as the system is isotropic and there no conversion between *s*- and *p*- polarisations occurs.

A.3 References

[A.1] F. Abelès, Ann. Phys. (Paris) **5**, 596 (1950)

[A.2] R.M.A. Azzam and N.M. Bashara; *Ellipsometry and Polarised Light*, North Holland, Amsterdam (1987)

[A.3] S. Teitler and B.W. Henvis; J. Opt. Soc. Am. **60**, 830 (1970)

[A.4] D.W. Berreman and T.J. Scheffer; Phys. Rev. Lett. **25**, 577 (1970)

[A.5] D.W. Berreman; J. Opt. Soc. Am. **62**, 502 (1972)

[A.6] M. Schubert; Phys. Rev. B **53**, 4265 (1996)

[A.7] D.S. Roseburgh; *Epioptic Modelling*, PhD Thesis, The University of Edinburgh (2006)

[A.8] H. Goldstein; *Classical Mechanics* 2nd Edition, Addison-Wesley Publishing Reading, Massachusetts/London (1964)

Appendix B

B.1 Signal to Noise Analysis

This appendix details the method used to calculate the signal to noise ratio obtained when the analyser is rotated from its normal position in the standard configuration to a position where it is almost crossed with the polariser.

B.1.1 Theoretical Signal

The theoretical signal recorded in RAS can be written as:

$$x(t) = DC + AC_1 \sin(2\pi\omega t) + AC_2 \cos(4\pi\omega t) + AC_3 \sin(6\pi\omega t) + \ldots$$

Eqn. B.1

where t is the time, T is the period of the wave and ω is the angular frequency $2\pi f$, f is the modulator frequency 50kHz. The DC signal varies differently upon rotation of the analyser from the modulated AC signals, as described by *Eqns. 6.19 & 6.20*. Therefore to first order in Δ/r it can be written:

$$DC = |r|^2 \cos^2 \theta_A \qquad \textit{Eqn. B.2}$$

$$AC_n = |r|^2 2 J_n \Delta \sin 2\theta_A \qquad \textit{Eqn. B.3}$$

where θ_A is the analyser angle, J_n is the n^{th} order Bessel function, r and Δ are chosen such that $\Delta/r \sim 0.001$. Assuming x is measured in millivolts, values of $\Delta = 1$ and $r = 1000$ give realistic AC and DC measurements. The values of the Bessel functions are given in *Table B.1*.

	Value
J_0	0
J_1	0.51911
J_2	0.431783
J_3	0.199032
J_4	0.064763
J_5	0.016395
J_6	0.003406

Table B.1: *The amplitudes of the Bessel functions.*

B.1.2 Noise Generation

Noise can then be added to the signal. The maximum value of statistical noise on a signal a is proportional to $\sqrt{a}$. Hence the noise is a randomly assigned percentage of this signal, and the noise generated on the signal *x(t)* is:

$$Noise = cR\sqrt{x(t)} \qquad \textit{Eqn. B.4}$$

where c is a constant and R is a random number; -1 < R < +1 with a probability weighted towards a normal distribution. Choosing $c = 1$ gives the noise on the overall signal as ~3% which appears comparable to typical experimental conditions.

The measured signal can hence be written as:

$$I(t) = x(t) + Noise \qquad \textit{Eqn. B.5}$$

B.1.3 Measured Signal

The measured DC and AC components of interest are now determined in the same way as the lock in amplifier determines them:

$$DC_{measured} = \frac{\sum_{t=0}^{t=tc} I(t)}{n_{tc}} \qquad \textit{Eqn. B.6}$$

$$AC_{measured} = \frac{2}{NT}\int_0^{tc} I(t)\cos\left(\frac{2n\pi t}{T}\right)dt \qquad \textit{Eqn. B.7}$$

where t_c is the time constant (or experimental integration time), n_{tc} is the number of data points recorded in the time t_c. N is the number of periods T of the fundamental frequency in the time t_c. The periodic term is the reference wave outputted by the modulator.

The measured RAS signal can hence be determined:

$$RAS_{measured} = \frac{1}{J_2}\frac{\sin(2\theta)}{\cos^2(\theta)}\frac{AC_{measured}}{DC_{measured}} \qquad \textit{Eqn. B.8}$$

The signal to noise ratio (SNR) can then be determined by:

$$SNR = 10\log_{10}\left(\frac{RAS_{measured}}{RAS_{noise}}\right) \qquad \textit{Eqn. B.9}$$

where

$$RAS_{noise} = RAS_{measured} - RAS_{Theory} \qquad \textit{Eqn. B.10}$$

As would be expected the SNR for smaller values of t_c was lower than for higher values. For the typical experimental value of t_c = 300ms the signal to noise against analyser angle is given in *Figure B.1*.

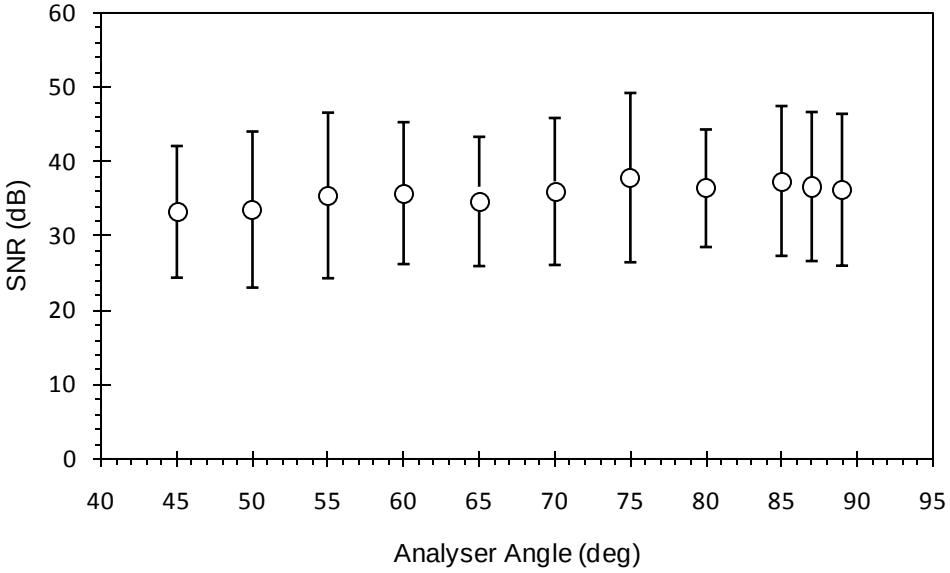

Figure B.1: *The mean SNR averaged over 100 data points, (open circles), error bars denote the standard deviation.*

As can be seen from *Figure B.1* rotating the analyser has little effect on the SNR value. The results shown were from a signal composed of 6 harmonics. Further results were obtained in which a low pass filter was applied, to cut out higher frequencies; this yielded very similar results to those shown.

As would be expected reducing the integration time sees a decrease in the SNR value.

Appendix C

C.1 Complex Angle fits of Off-Normal Incidence Spectra

This appendix contains fits of the off normal incidence RA spectra to the complex angle formula outlined in *Chapter 6 (Eqn. 6.34)*.

$$\mathrm{Re}\left(\frac{\Delta r}{r}\right) = -\frac{2\omega d}{c}\left[\left(A(\omega)\Delta\varepsilon''\cos\gamma\right) + \left(B(\omega)\Delta\varepsilon'\sin\gamma\right)\right]\frac{R_\phi}{R_0}$$

C.1.1 Normal Incidence

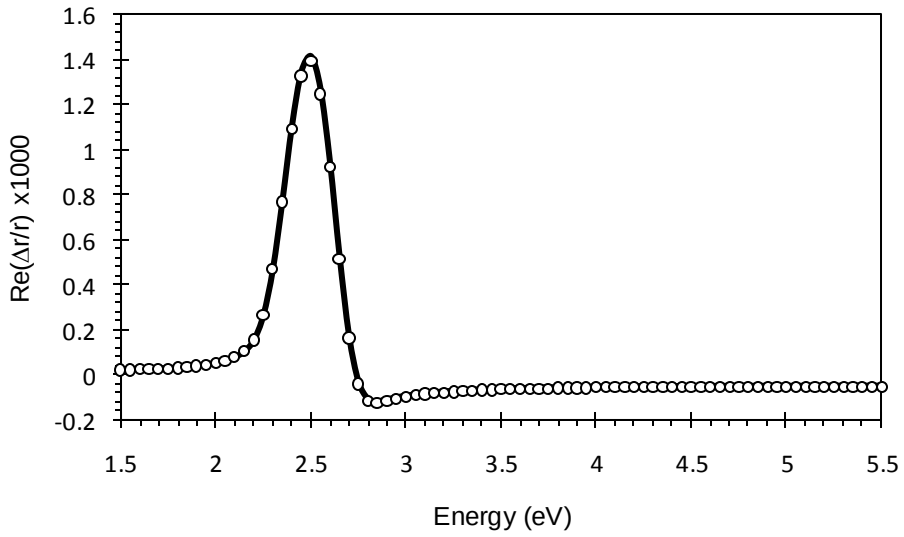

Figure C.1: *The RA response of the sample (solid line) and the complex angle fit γ = 45° (open circles) at normal incidence.*

The case of normal incidence is fairly trivial as $R_\varphi = R_0$, but it demonstrates that the complex angle equation describes the RA lineshape well.

C.1.2 s- Polarised Light

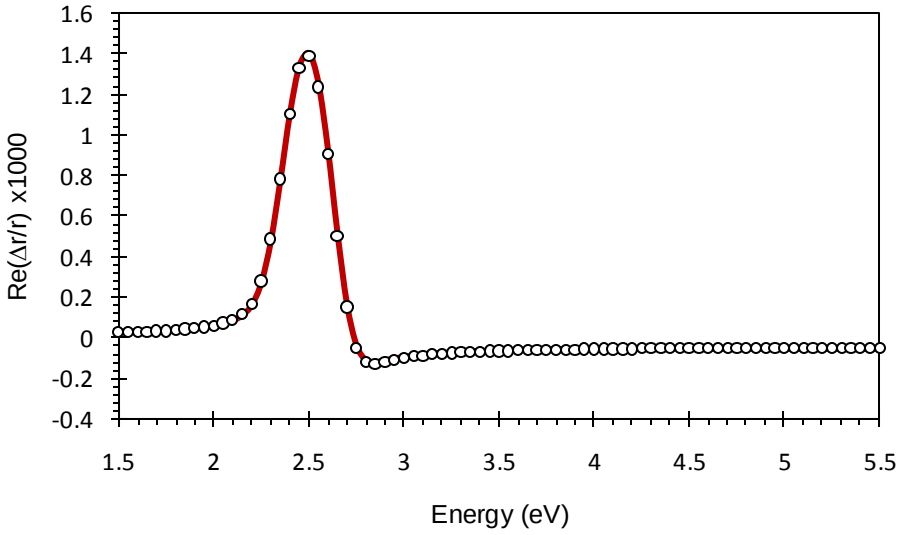

Figure C.2: *The RA response of the sample (solid line) and the complex angle fit $\gamma = 43°$ (open circles) at 15° incidence.*

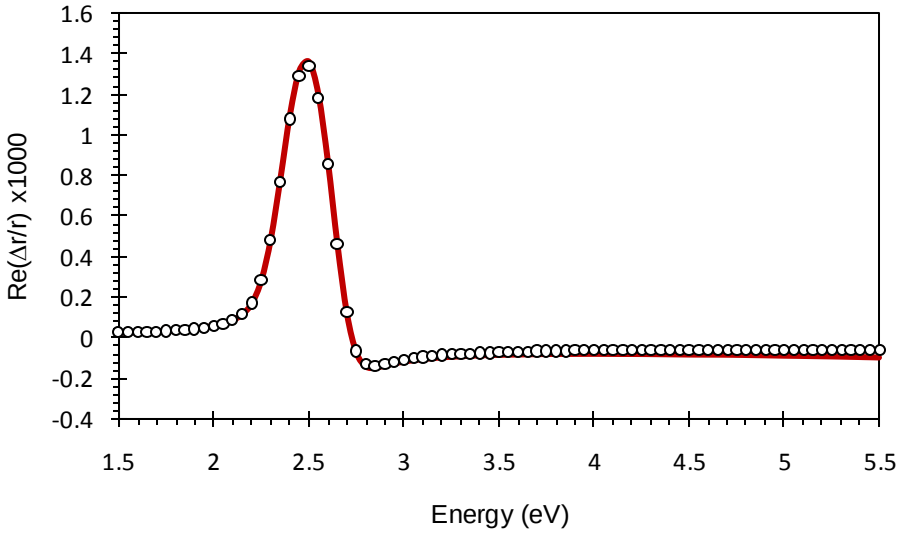

Figure C.3: *The RA response of the sample (solid line) and the complex angle fit $\gamma = 41°$ (open circles) at 30° incidence.*

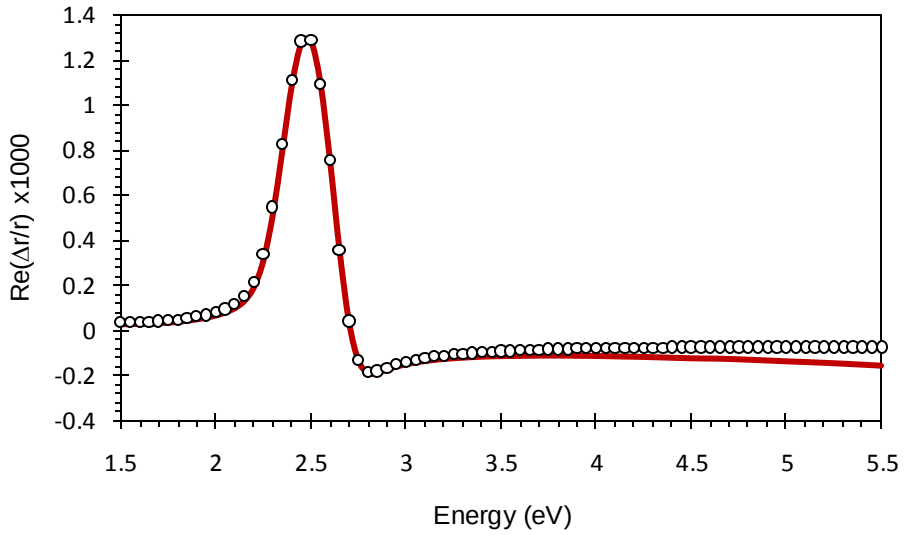

Figure C.4: *The RA response of the sample (solid line) and the complex angle fit* $\gamma = 33°$ *(open circles) at 45° incidence.*

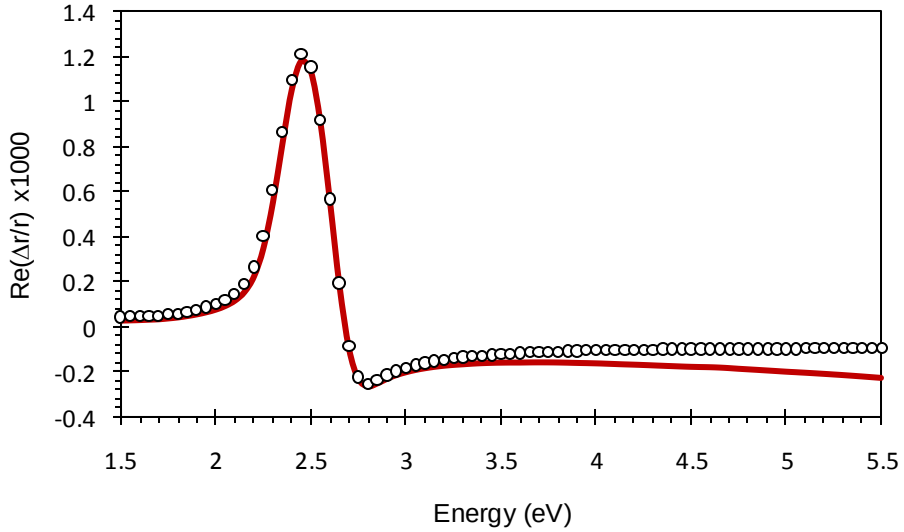

Figure C.5: *The RA response of the sample (solid line) and the complex angle fit* $\gamma = 25°$ *(open circles) at 60° incidence.*

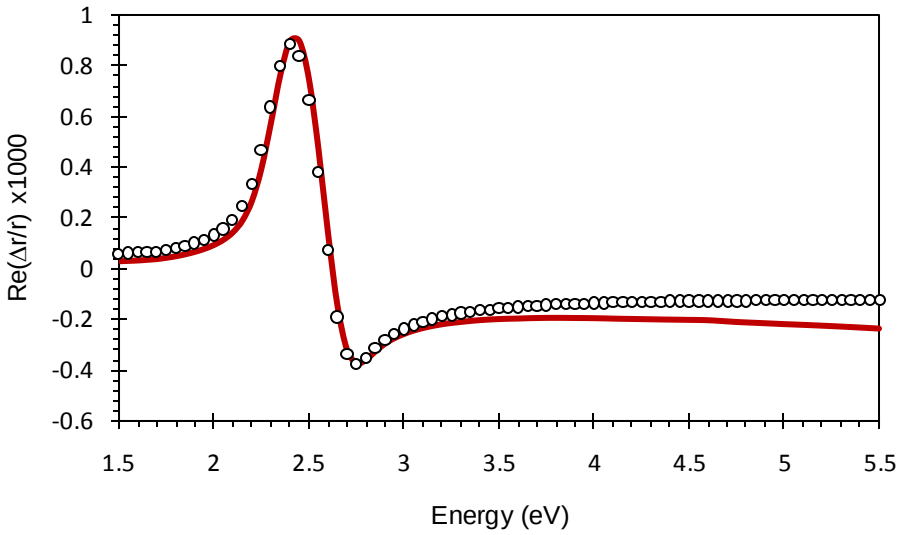

Figure C.6: *The RA response of the sample (solid line) and the complex angle fit $\gamma = 14°$ (open circles) at 75° incidence.*

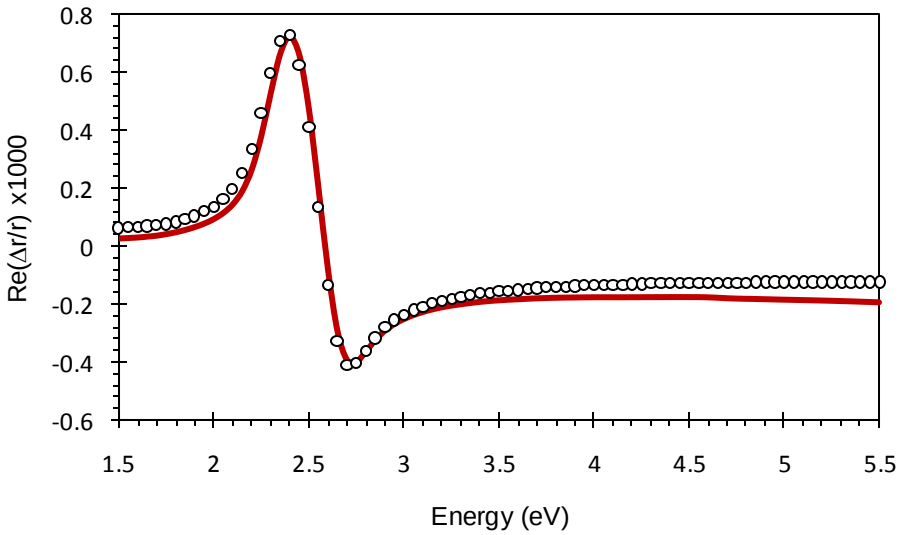

Figure C.7: *The RA response of the sample (solid line) and the complex angle fit $\gamma = 9°$ (open circles) at 80° incidence.*

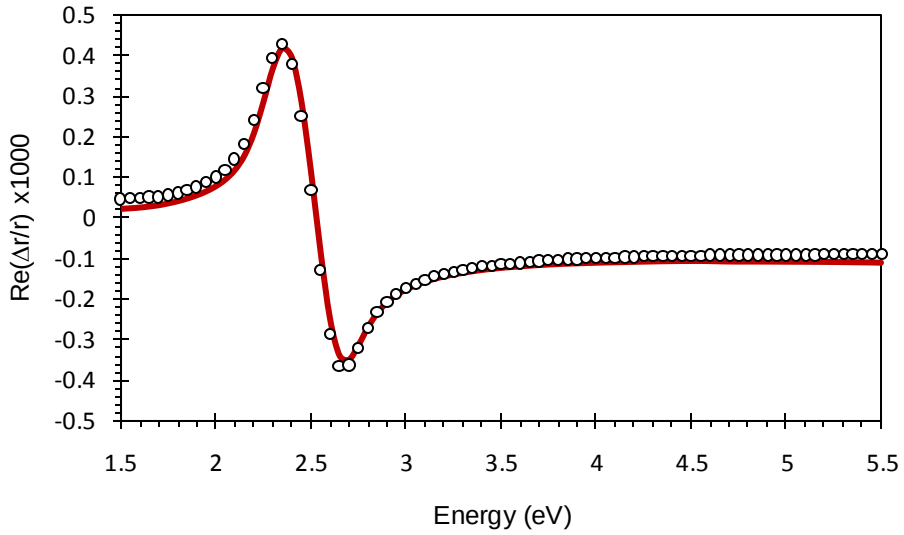

Figure C.8: *The RA response of the sample (solid line) and the complex angle fit γ = 4° (open circles) at 85° incidence.*

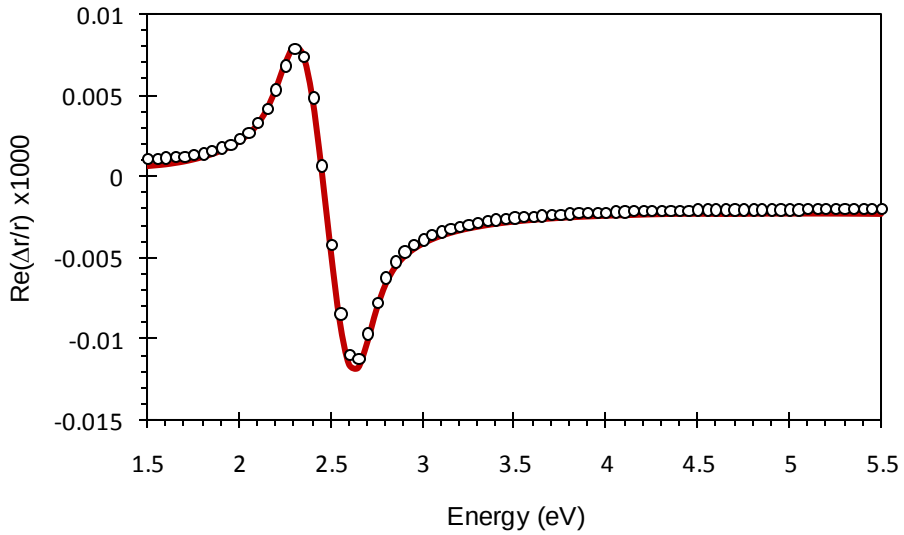

Figure C.9: *The RA response of the sample (solid line) and the complex angle fit γ = -1.5° (open circles) at 89.9° incidence.*

C.1.3 p- Polarised Light

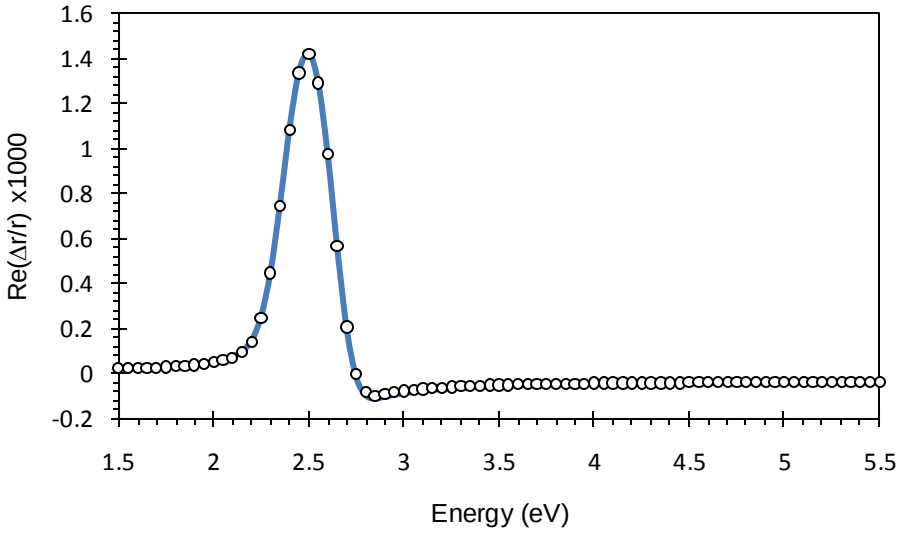

Figure C.10: *The RA response of the sample (solid line) and the complex angle fit $\gamma = 50°$ (open circles) at 15° incidence.*

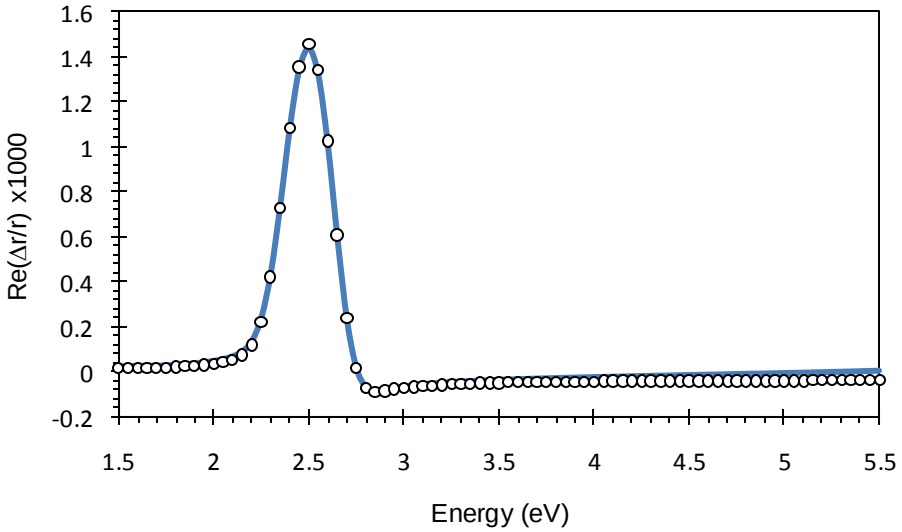

Figure C.11: *The RA response of the sample (solid line) and the complex angle fit $\gamma = 55°$ (open circles) at 30° incidence.*

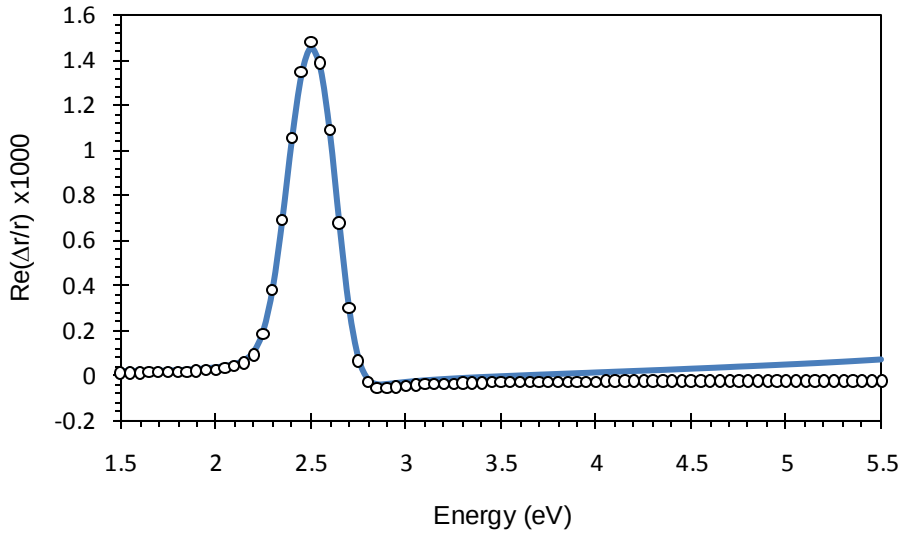

Figure C.12: *The RA response of the sample (solid line) and the complex angle fit $\gamma = 65°$ (open circles) at 45° incidence.*

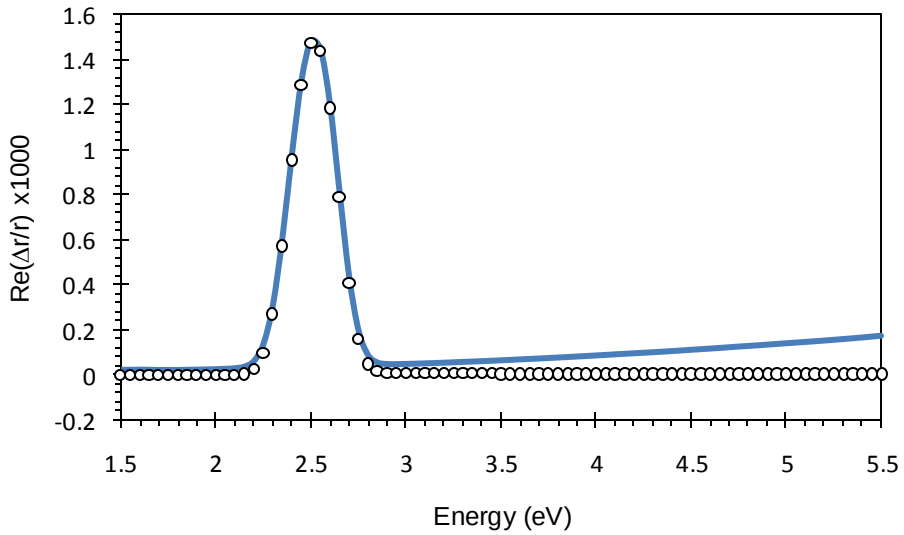

Figure C.13: *The RA response of the sample (solid line) and the complex angle fit $\gamma = 92°$ (open circles) at 60° incidence.*

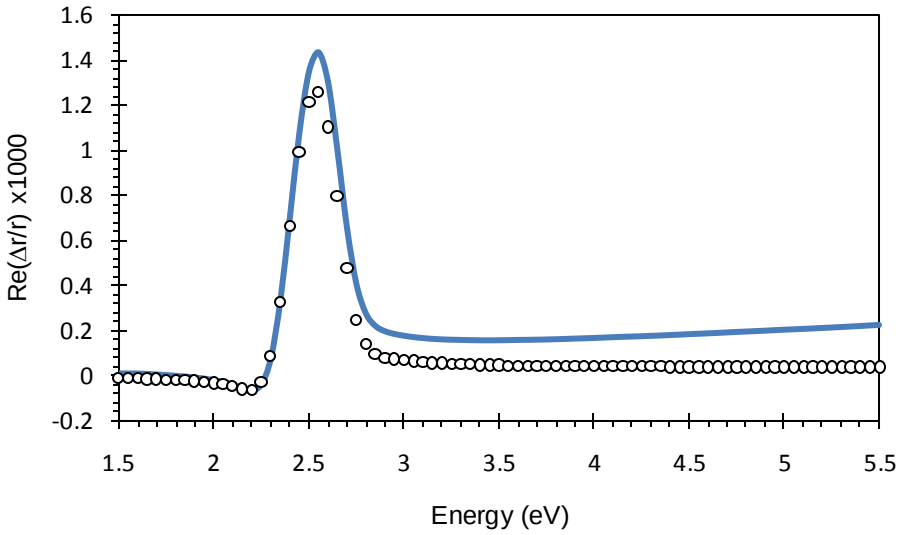

Figure C.14: *The RA response of the sample (solid line) and the complex angle fit γ = 140° (open circles) at 75° incidence.*

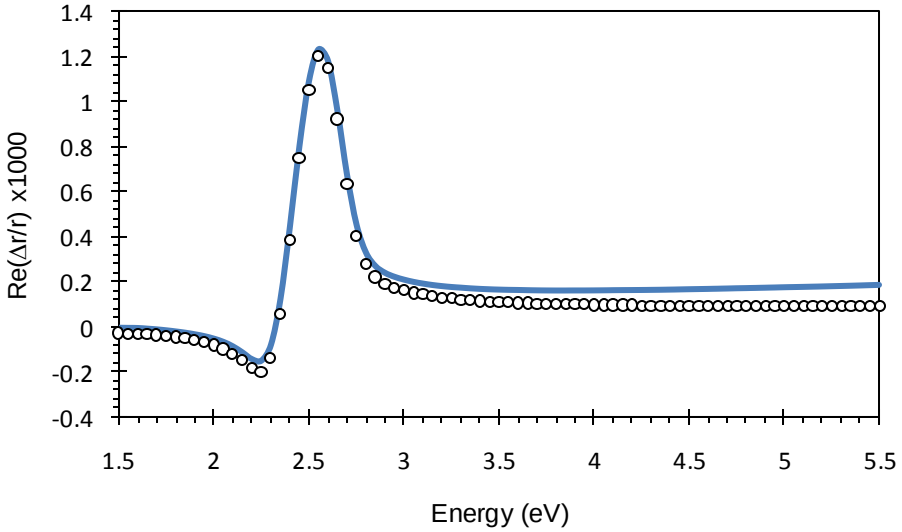

Figure C.15: *The RA response of the sample (solid line) and the complex angle fit γ = 155° (open circles) at 80° incidence.*

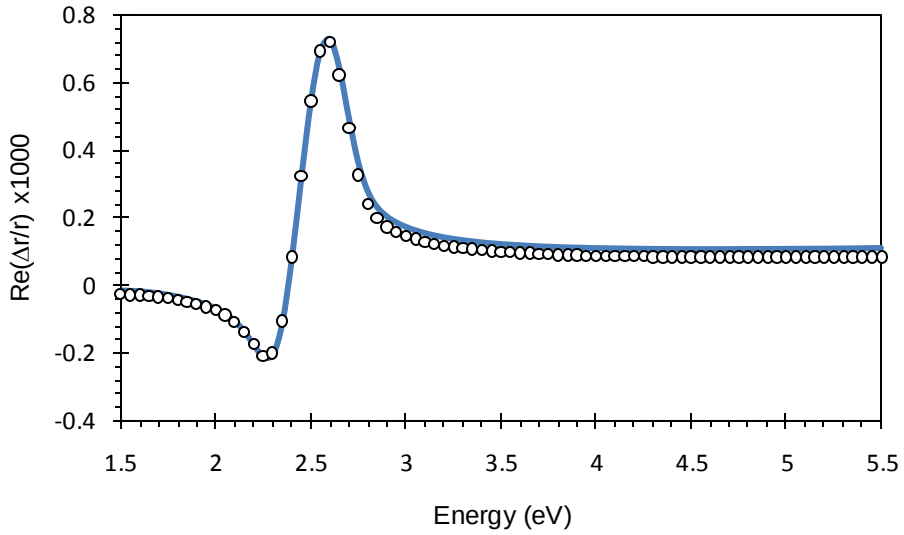

Figure C.16: *The RA response of the sample (solid line) and the complex angle fit γ = 168° (open circles) at 85° incidence.*

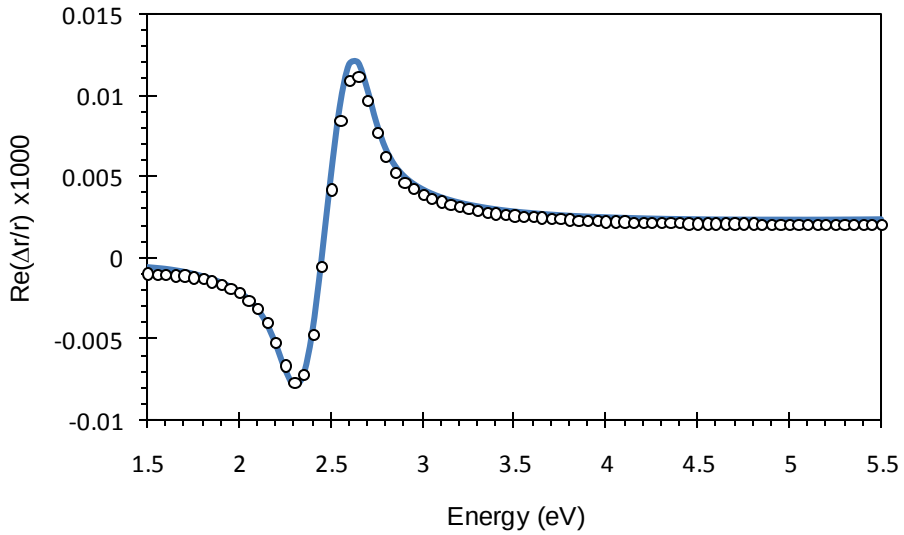

Figure C.17: *The RA response of the sample (solid line) and the complex angle fit γ = 178.5° (open circles) at 89.9° incidence.*

Appendix D

D.1 Published Work

The simulation of the RAS response of sulphur on Cu (110) using effective medium theory.

P.D. Lane, G.E. Isted, R.J. Cole and D.S. Martin

Epioptics -10 proceedings of the 43rd course of the international summer school of solid state physics, Edited by A. Cricenti (World Scientific) (In Press)

The effect of thermally induced surface defects on the optical anisotropy of Ag (110).

G.E. Isted, P.D. Lane and R.J. Cole

Phys. Rev. B **79**, 205424 (2009)

Azimuthal dependent reflection anisotropy of oriented thin films.

P.D. Lane, G.E. Isted, D.S. Roseburgh and R.J. Cole

(Submitted)

An optical signature of the thiolate-Cu linkage: methanethiol and L-Cysteine adsorption on Cu (110).

D.S. Martin, P.D. Lane, G.E. Isted, R.J. Cole and N.P. Blanchard

(In Preparation)